

CRANFIELD UNIVERSITY

DARINA FIŠEROVÁ

NUMERICAL ANALYSES OF BURIED MINE
EXPLOSIONS WITH EMPHASIS ON EFFECT OF
SOIL PROPERTIES ON LOADING

DEFENCE COLLEGE OF MANAGEMENT AND
TECHNOLOGY

PHD THESIS

CRANFIELD UNIVERSITY

DEFENCE COLLEGE OF MANAGEMENT AND
TECHNOLOGY

ENGINEERING SYSTEMS DEPARTMENT

PHD THESIS

ACADEMIC YEAR 2005-2006

DARINA FIŠEROVÁ

NUMERICAL ANALYSES OF BURIED MINE
EXPLOSIONS WITH EMPHASIS ON EFFECT OF
SOIL PROPERTIES ON LOADING

SUPERVISOR: DR. AMER HAMEED

JANUARY 2006

© Cranfield University 2006. All rights reserved. No part of this publication may be reproduced without the written permission of the copyright owner.

Abstract

DURING ARMED CONFLICTS or peace-support operations, most casualties are attributed to vehicle-landmine accidents and thus, mine protection features are a prerequisite for vehicles serving in these areas. Previously, mine protection research was predominantly experiment driven and focussed on structural deformation. Soil parameters were not observed and the influence of soil was not considered. Accurate soil modelling is necessary because experimental studies have shown that soil, in particular saturated soil, has a significant effect on the magnitude of landmine blast loading on a vehicle. This research describes a numerical modelling approach for studying soil-blast interaction in landmine explosions. The numerical analysis is carried out using the non-linear dynamic analysis software, AUTODYN. The research progressed from (1) the explosion of hemispherical charge laid on a rigid surface, through (2) the study of the explosion of mine deployed in dry sand, to (3) the validation of the mine explosion in cohesive soil for different setups.

A framework for deriving the model for soil with varying moisture contents was proposed. The subject of the study is prairie soil (cohesive soil). Standard soil laboratory data are used to determine soil properties that are then used to define a numerical soil model. Validity of the modelling procedure was ascertained by comparison with experimental results from the horizontal pendulum series that were conducted at Defence R&D Canada – Suffield. The applicability of the model was ascertained for (i) different soil types, (ii) varying moisture content, (iii) different mine deployment, and (iv) various high explosive. The numerical results are in reasonable agreement for all observed range of the moisture content. The model and the methodology is generic and extensible and it is argued that such models greatly complement mine experiments.

Tátovi a mámě

To Suresh

Acknowledgments

THE AUTHOR WISHES TO extend her thanks to Mr. Paseka¹ and to Ms. Hlady² who were kind enough to go beyond their call of duty to share information. Mr. Paseka agreed to share an internal report on soil properties which provided the author with much needed data and insight. Ms. Hlady decided to share both the soil test data as well as the internal report of the explosion experiments. This helped the author to understand the large task of experimental work and to validate reliably the soil modelling methodology.

Financial support from Alvis Vickers Ltd. (now BAE Systems, Land Systems) Newcastle-upon-Tyne, for providing (i) a dedicated computer for running the simulations, and, (ii) one year maintenance grant for the author is gratefully acknowledged.

Big thank you to everyone who helped in different ways and not realising how much they actually helped.

Thank you.

Děkuji svým rodičům a sourozencům bez jejich podpory bych to těžko zvládla. Táta má u mne velkou pusou a máma velký zmrzlinový pohár. Kamila, Marina a Ota dostanou masala dosa.

Amma, Appa, Satheesh to whom the middle czech sentence is extended, with Satheesh's choice.

¹Brno Technology University, Brno, The Czech Republic

²DRDC - Suffield, Canada

Contents

Abstract	ii
Acknowledgements	vi
Abbreviations	xxi
1 Introduction	1
1.1 Motivation	1
1.2 Research rationale	2
1.3 Background	5
1.4 Research specification	8
1.5 Work disseminations	9
1.6 Thesis outline	10
2 Literature survey	11
2.1 Experimental findings related to the mine explosion phenomenon . . .	12
2.1.1 Experimental techniques for measuring the mine explosion output	13
2.2 Numerical simulation dedicated to mine explosions	15
2.2.1 Numerical modelling of explosion process	19
2.2.2 Numerical modelling of vehicles with crew	20
2.3 Soil-blast interaction	21
2.4 Summary	22
3 Review of soil properties and theory	25
3.1 Description of soil	26
3.1.1 Particle size distribution	26
3.1.2 Density	27
3.1.3 State consistency of soil	28
3.1.4 Concluding remarks on soil description	30

3.2	Soil strength	30
3.2.1	Stresses in soil	31
3.2.2	Compressive strength	32
3.2.3	Shear strength	33
3.2.4	Mechanism of deformation	33
3.3	Standard soil tests for stress-strain relationships	34
4	Modelling of physical process using AUTODYN	37
4.1	Solution methods in AUTODYN	39
4.2	Solvers	43
4.2.1	Lagrange solver	43
4.2.2	Euler solvers	43
4.3	Material modelling	44
4.3.1	Failure model	46
4.4	Features	46
4.5	Description of materials used in simulations	48
4.6	AUTODYN procedure to setup a model	49
4.7	Summary	50
5	Soil model derivation	53
5.1	Statistical soil properties data	55
5.2	Properties of prairie soil	56
5.3	Deriving model for prairie soil	58
5.3.1	Equation of state: Compaction	59
5.3.2	Strength model: Granular	63
5.3.3	Failure model: Hydro-tensile criterion	67
5.3.4	Concluding remarks on prairie soil modelling	68
5.4	Deriving model for sand	68
5.4.1	Laine's sand model	69
5.4.2	Modified Laine's model	69
5.4.3	Sand model for varying moisture content	70
5.4.4	Concluding remarks on sand modelling	71
5.5	Summary	71
6	Experiments for validating numerical solutions	73
6.1	Experimental data for hemispherical surface explosion (CONWEP)	74
6.1.1	Methodology of experiments	76
6.1.2	Results	77
6.1.3	Comments on CONWEP	78

6.2	Small-scale experiments in dry sand	78
6.2.1	Methodology of experiments	78
6.2.2	Results	80
6.2.3	Comments on small-scale experiments	80
6.3	MIP deployment and moisture effect	84
6.3.1	Methodology of experiments	84
6.3.2	Results	86
6.3.3	Comments on the MIP experiments	89
6.4	Summary	89
7	Results of modelling in AUTODYN	91
7.1	Getting started with AUTODYN	92
7.1.1	Setup of hemispherical surface explosion	92
7.1.2	Hemispherical surface explosion results	93
7.1.3	Effect of deployment in sand	98
7.1.4	Discussions	102
7.1.5	Concluding remarks	104
7.2	Small-scale explosion in dry sand	105
7.2.1	Setup of small-scale explosion in dry sand	105
7.2.2	Deployment effect in dry sand	106
7.2.3	Sensitivity analysis of the setup parameters	115
7.2.4	Discussions	120
7.2.5	Concluding remarks	123
7.3	Cohesive soil model validation using MIP	124
7.3.1	Setup of the MIP model	125
7.3.2	Rigid surface model	130
7.3.3	Prairie soil model and its sensitivity analysis	130
7.3.4	Derived sand models	137
7.3.5	Effect of explosives type	139
7.3.6	Effect of deployment in prairie soil	141
7.3.7	Discussions	141
7.3.8	Concluding remarks	146
7.4	Summary	147
8	Discussions and future directions	149
8.1	Modelling high explosives	149
8.2	Modelling cohesive soils	150
8.2.1	Modelling methodology for soil	150
8.2.2	Validation of soil models	151

8.2.3	Advantages of proposed methodology	153
8.2.4	Directions in modelling soil	154
8.3	Comments on scaling	155
8.4	Mine explosion output	158
8.4.1	Directions in experiments	159
8.5	Summary	160
9	Conclusions	163
A	Description of soil laboratory tests	181
A.1	Tests for determining physical properties of soil	181
A.1.1	Particle size distribution	181
A.1.2	Density	182
A.1.3	Moisture content	182
A.1.4	State consistency of soil	182
A.2	Tests for determining mechanical properties of soil	183
A.2.1	Compression tests	184
A.2.2	Direct shear tests	186
A.2.3	Pressuremeter test	187
B	Autodyn features	189
B.1	Other solvers	189
B.1.1	Interface tracking in Euler solver	190
B.2	Additional features in material modelling	191
B.3	Material models used in simulations	194
C	Mine impulse pendulum	197
C.1	Mine impulse pendulum – rotational movement	197
C.2	Surrogate MIP – straight-line motion of the plate	198
C.3	Plate parameters equivalent to the horizontal pendulum	199
D	Prairie soil laboratory data	203
D.1	Physical properties	203
D.2	Mechanical properties	205
E	Prairie soil modelling	209

List of Figures

1.1	Research focus.	3
1.2	Branches of science relevant to enhancement of landmine protection.	4
1.3	Approaches to deal with the problem.	5
1.4	Representative antitank blast mine: TM-72 [2].	6
1.5	The scheme of mine deployment.	7
2.1	Dimple gauge. Reproduced from Joynt [77].	15
2.2	Non-deformable gauges measure the impulse delivered to the structure.	15
3.1	Soil composition.	26
3.2	Grading curves. Reproduced from Berry <i>et al.</i> [24].	28
3.3	Atterberg limits.	29
3.4	Plasticity chart.	29
3.5	Concept of total and effective stresses in soil.	32
3.6	Mohr-Coulomb failure criterion applied for prairie soil triaxial data.	33
4.1	Geometric representation of the finite difference formulae for the first derivatives.	41
4.2	Mesh discretization from AUTODYN manual [32].	41
4.3	Lagrange computation scheme from AUTODYN manual [32].	42
4.4	Description of solvers from AUTODYN manual [32].	43
4.5	Setting models in AUTODYN: a two-step procedure for MIP models.	51
5.1	The composition of prairie soil at the initial stage - MIP trials, triaxial test and oedometer test specimen.	60
5.2	Equations of state for prairie soil having 7.7, 15 and 28.7% moisture content.	64
5.3	Triaxial test results for prairie soil (Mohr's circle).	65

5.4	Strength model: Yield surface parameters varying with moisture content.	66
5.5	Variation of yield surface for prairie soil having 15 % moisture content.	66
5.6	Sand models: Laine's model and its modification.	70
5.7	Sand models: EOS for different moisture contents.	71
6.1	Pressure-time history of airblast.	75
6.2	Scaling law explained, after Smith <i>et al.</i> [108].	76
6.3	Blast-wave parameters for spherical TNT explosion in free air with respect to the scaled distance. Reproduced from CONWEP [115].	77
6.4	Experimental setup of small-scale experiments in dry sand. Reproduced from Bergeron <i>et al.</i> [22].	79
6.5	Maximum pressure with respect to distance above the ground caused by the explosion of 100 g C-4 in dry sand.	81
6.6	Maximum specific impulse with respect to distance above the ground caused by the explosion of 100 g C-4 in dry sand.	81
6.7	Time development of the height of ejecta caused by the explosion of 100 g C-4 in dry sand.	82
6.8	Time development of the width of crater caused by the explosion of 100 g C-4 in dry sand.	82
6.9	Time development of the detonation product cloud caused by 100 g C-4 in dry sand.	83
6.10	The mine impulse pendulum experiments. Reproduced from Bues <i>et al.</i> [30].	84
6.11	The schematic representation of the mine impulse pendulum [mm	86
6.12	MIP experiments: influence of soil properties on impulse delivered to the pendulum. [C-4, DOB = 50 mm]	87
6.13	MIP experiments: influence of depth of burial on impulse delivered to the pendulum. [C-4, Prairie soil]	87
6.14	MIP experiments: influence of explosive types on impulse delivered to the pendulum. [Prairie soil, DOB = 50 mm]	88
7.1	The scheme of initial model for hemispherical surface explosion.	93
7.2	Pressure-time histories for TNT charge placed on rigid surface.	95
7.4	Pressure-time histories for rigid- and sand-surface models.	96
7.3	Influence of equation of state of explosives on blast-wave parameters. Dashed line indicates extrapolated CONWEP data.	97
7.5	Influence of sand surface against rigid surface on blast-wave parameters. Dashed line indicates extrapolated CONWEP data.	99

7.6	Model setup for a charge buried in sand. Notice the gauge positions and origin of the co-ordinates.	100
7.7	Material location for charge in various deployments in dry sand.	101
7.8	Influence of the deployment on the maximum pressure in different directions with respect to the surface laid charge.	103
7.9	Influence of the deployment on the specific impulse in different directions with respect to the surface laid charge.	103
7.10	Mine deployment – simulation configuration: (a) buried charge, (b) flush charge.	106
7.11	Sand modelling by Wang and Laine.	108
7.12	Blast-wave parameters for both the mine deployments at measuring points of 300 mm and 700 mm above the ground surface.	110
7.13	Time development of the height of ejecta caused by the explosion of 100 g C-4 in dry sand.	111
7.14	Time development of the width of crater caused by the explosion of 100 g C-4 in dry sand.	112
7.15	Time development of the detonation product cloud caused by 100 g C-4 buried in dry sand.	113
7.16	Time development of the detonation product cloud caused by 100 g C-4 laid flush in dry sand.	114
7.17	Sensitivity parameters: (a) Position of detonation point, (b) Position of transducers: X horizontal and Y vertical deviations.	116
7.18	Sensitivity of detonation point position: pressure with respect to horizontal position of transducers at 300 mm above the ground.	118
7.19	Sensitivity of detonation point position: specific impulse with respect to horizontal position of transducers at 300 mm above the ground.	118
7.20	Sensitivity of transducer vertical deviation: pressure with respect to transducer horizontal deviation, charge initiated in the CENTRE.	119
7.21	Sensitivity of transducer vertical deviation: specific impulse with respect to transducer horizontal deviation, charge initiated in the CENTRE.	119
7.22	Evaluation of predicted damage factors, where p_{max} is the maximum overpressure, I is the specific impulse and DN is the damage number.	121
7.23	Sensitivity analysis of the setup parameters: the band of the results.	123
7.24	The modelling phases of the MIP experiments. (a, b) 1 st step: without plate, (c) 2 nd step: inserting the plate, (d, e, f) Pressure contours are shown.	127

7.25	Mesh sensitivity: the influence of mesh size on the impulse delivered to the plate. [1 kg C-4, Prairie soil, DOB = 50 mm, D_{clc} = 400 mm]	133
7.26	Poisson's ratio: influence of Poisson's ratio on the impulse delivered to the plate. [1 kg C-4, Prairie soil, DOB = 50 mm, D_{clc} = 400 mm]	134
7.27	Yield surface: influence of yield surface parameters on the impulse delivered to the plate. [1 kg C-4, Prairie soil, DOB = 50 mm, D_{clc} = 400 mm]	136
7.28	Failure criterion: the influence of hydro-tensile limit on the impulse delivered to the plate. [1 kg C-4, Prairie soil, DOB = 50 mm, D_{clc} = 400 mm]	138
7.29	Sand models: the influence of sand properties on the impulse delivered to the plate. [1 kg C-4, Sand, DOB = 50 mm, D_{clc} = 400 mm]	138
7.30	High explosives: influence of high explosive type on the impulse delivered to the plate. [1 kg C-4/TNT/Composition B, Prairie soil, DOB = 50 mm, D_{clc} = 400 mm]	140
7.31	Surface-laid charge: impulse delivered to the plate. [1 kg C-4, Prairie soil, DOB = -50 mm, D_{clc} = 400 mm]	142
7.32	Charge buried at 100 mm: impulse delivered to the plate. [1 kg C-4, Prairie soil, DOB = 100 mm, D_{clc} = 400 mm]	142
7.33	Specific impulse versus distance from symmetric axis and the MIP total impulse delivered to MIP. [1 kg C-4, Prairie soil, DOB = 50 mm, D_{clc} = 400 mm]	146
8.1	Fine impulse structure captures the total impulse delivered to the trolley, and local impulse in the small areas (protrusions). Reproduced from Joynt [78].	160
A.1	The shrinkage curve for determining shrinkage limit w_p .	183
A.2	The schematic representation of compressive strength tests.	184
A.3	The schema of the shearbox used in small shearbox tests.	187
A.4	The evaluation of shearbox test.	187
B.1	Stochastic distribution.	192
B.2	Definition of cumulative damage failure criterion. After AUTODYN manual [32].	194
C.1	Schematic pendulum and plate.	200
D.1	Grading curve for prairie soil.	204

D.2	The composition of prairie soil at the initial stage - MIP trials, triaxial test and oedometer test specimens.	204
D.3	Calculation of the friction angle and cohesion for prairie soil.	207

List of Tables

2.1	Overview of numerical modelling of a mine explosion. Air is modelled using ideal gas EOS in every case.	18
3.1	Definition of soil physical properties.	27
3.2	Definitions of particle size.	27
3.3	Plasticity in compliance with ČSN and BS.	29
3.4	Soil consistency in compliance with ČSN.	30
3.5	Summary of soil description.	31
3.6	Summary of standard soil tests.	35
4.1	Governing equations: laws of conservation.	38
4.2	Supplementary equations for modelling.	38
4.3	Definitions and units of variables.	39
4.4	Finite difference formulae.	40
5.1	Properties for clay with low plasticity (CL), after Vrtek [119].	56
5.2	Data from triaxial tests used to determine the equation of state for the solid phase.	62
6.1	MIP experiments matrix, the pendulum arm is positioned at 400 mm distance above the surface.	85
7.1	Model description for hemispherical charge explosion.	94
7.2	Maximum overpressure for rigid-surface models with HE modelled with different EOS and different mesh size.	96
7.3	Maximum overpressure for rigid- and sand-surface models.	98
7.4	Specific impulse for rigid- and sand-surface models.	98
7.5	Model description for small-scale explosion in dry sand.	107

7.6	Input parameters for material modelling.	107
7.7	Blast-wave parameters for different deployments in dry sand for 100 g C-4 charge.	109
7.8	MIP experiments matrix, distance above surface 400 mm.	125
7.9	Model description of the recreated mine impulse pendulum experiments.	128
7.10	Impulse delivered to the plate caused by the explosion of 1 kg C-4 charge laid on the rigid surface.	130
7.11	Parameter analysis conducted on the prairie soil model. (φ is the friction angle, c is the cohesion.)	131
7.12	Mesh sensitivity: impulse delivered to the plate caused by the explosion of 1 kg C-4 buried at 50 mm in prairie soil.	132
7.13	Poisson's ratio: impulse delivered to the plate caused by the explosion of 1 kg C-4, charge buried at 50 mm in prairie soil.	134
7.14	Yield surface: impulse delivered to the plate caused by the explosion of 1 kg C-4, charge buried at 50 mm in prairie soil.	136
7.15	Failure criterion: impulse delivered to the plate caused by the explosion of 1 kg C-4, charge buried at 50 mm in prairie soil.	137
7.16	Sand models: impulse delivered to the plate caused by the explosion of 1 kg C-4 buried at 50 mm in sand.	139
7.17	High explosives: impulse delivered to the plate caused by the explosion of 1 kg HE buried at 50 mm in prairie soil.	140
7.18	Deployment: impulse delivered to the plate caused by the explosion of 1 kg C-4 for various deployment in prairie soil.	143
8.1	TNT equivalent factors for air blast and buried charges.	156
8.2	Introduction to the scaling problem. Charge deployed in dry sand (Laine's model). S and E denotes numerical simulation and experimental results, respectively.	157
B.1	Model of air using an ideal gas equation of state.	194
B.2	Model of high explosives using Jones-Wilkins-Lee equation of state.	195
B.3	Model of Iron Armco.	195
C.1	Dimension of the mine horizontal pendulum.	201
C.2	Dimension of the plate as surrogate MIP.	201
D.1	Particle size distribution for prairie soil.	203
D.2	Prairie soil properties at the initial and final stage of triaxial tests.	206
D.3	Stresses at triaxial tests for prairie soil.	206

E.1	Summary of equations for deriving cohesive soil model.	211
E.2	Derivation of model for prairie soil with 7.7% moisture content. . . .	212

Abbreviations

AP	anti-personnel
AT	anti-tank
BS	British Standard
CFD	Computational Fluid Dynamics
ČSN	Czech Standard
DRDC	Defence Research and Development Canada
EOS	equation of state
FD	finite difference
FE, FEM	finite element, finite element method
HE	high explosives
JWL	Jones-Wilkins-Lee (equation of state for explosive)
MIP	Mine impulse pendulum

Once peace is declared the landmine
does not recognise that peace.

— Jody Williams,
Nobel Peace Prize Laureate in 1997

Chapter 1

Introduction

THIS PHD THESIS will look at near-field explosion in soil by using numerical techniques. Numerical techniques are cost-effective and easier to setup and run (when compared with experiments). Numerical simulations can recreate scenarios and physical parameters and allow flexibility in a way experiments cannot. The key question is “Does all this flexibility yield credible results?” This thesis says: “Yes, it does”. In fact, the findings of this thesis suggest that, if properly used, the benefits of such a study can complement experiments.

In this Chapter, the rationale and background of the subject is presented. The work done in this area shows the missing gap that this research covers. The research aims are proposed. The Chapter concludes with the thesis outline.

1.1 Motivation

The Mine Ban Treaty of 1999 has not put a stop, in any way, to the global landmine crisis, as an estimated 100 million mines lay strewn in around 60 countries all over the world. Furthermore, landmines are actively used in recent conflicts (Hefernan [56]). Around 26,000 civilians are killed or maimed every year by mine-fields (Schlein [104]). Beside the human life lost, the medical treatment of landmine injuries is an expensive hidden landmine effect for the society. *Morbidity and mortality weekly report* [31] has reported the expenses of up to US\$ 1 million on medical service for the humanitarian coordinator.

Furthermore, the medical, psychosocial, environmental and economic impacts inevitably scale up further tension and armed conflict in the affected areas. In the

mine-affected countries, scarcity of adequate medical services, safe water and food has led to dependency on the international community for humanitarian and development assistance. International and non-governmental organizations, coordinated by the United Nations, are extensively undertaking mine clearance efforts and humanitarian aid logistics, but mine contamination of infrastructure disrupts relief supplies from reaching their intended destination.

In addition, the military aspect of the mine threat cannot be omitted in this domain. In World War II, 20% of tank casualties were attributed to mines. In Vietnam, US armour casualties attributed to mines were 70% and French forces lost about 85% of tanks in Indo-China (Sloan [106]). In the more recent conflicts, US military losses attributed to landmines were 59% in the Persian Gulf War and 60% in Somalia (Bird [25]). Although there are no final statistics of the losses in the recent conflicts in Iraq and Afghanistan, about 28% of fatalities are caused by the mines and improvised explosive devices (IED) (iCasualties [7], by 3rd November 2005).

1.2 Research rationale

Due to the reasons mentioned, mine protection features are a prerequisite for armoured fighting, personnel carrier or transport vehicles. These aspects have developed into active research interests. Within the last few years, some initiatives have been undertaken to study and understand mine blast and loading behaviour in order to enhance the design of vehicles used in mine infested zones. The research has been conducted in three independent areas:

- **Prediction of the blast load** – dealing with shock wave propagation through soil and air by taking into account the characteristics of the explosive and the nature of the soil, such as moisture content, soil particle sizes and their linkages.
- **Response of the vehicle** – investigating the structural and kinematic responses of the vehicle, including the shape of the vehicle’s chassis and blast attenuation materials.
- **Vulnerability of human beings** – assessment of the effects caused by the high shock pressures, spalling of fragments and vertical or lateral motion of the vehicle resulting from the explosion.

Figure 1.1 shows how these “independent” areas of research are actually *interdependent*. The research focus appears shaded in the figure. Reducing crew mortality

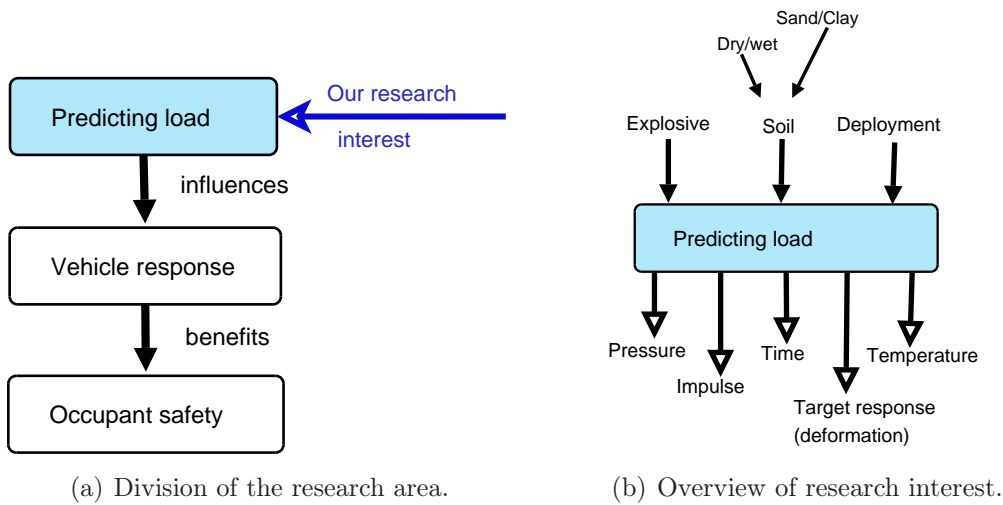


Figure 1.1: Research focus.

remains a great challenge for vehicle manufacturers such as GIAT [33], BAE Systems (includes Alvis Vickers, Ltd.) [55], MOWAG [52], and PLASAN SASA [101].

In addition, understanding the process of explosion in soil and prediction of loading are beneficial for manufacturers of demining equipment and personnel protective equipment used in clearance of anti-personnel mines [2].

Branches of science involved

The research of enhancing landmine protection and reducing human casualties bring several branches of science to work together. Figure 1.2 represents the main branches involved. The science of mathematics and physics is underlying and experimental (measurement) experience is other subject of its own. In this thesis, chemistry is studied through explosion development and soil mechanics is studied in order to understand the soil and its properties.

Approaches for problem solving

Solutions to technical problems posed in academia or industry can take two different forms. The first is the empirical solution, obtained by repeated solving of the problem and plotting the observed trend. The second is the theoretical solution where a mathematical model of the problem is constructed and a numerical solution is derived for the same. The *pros* and *cons* of these approaches are given below:

- (a) *Experimental approach* is a good benchmark to evaluate response of vehicles to blast loading. However, the setup itself can be physically demanding and

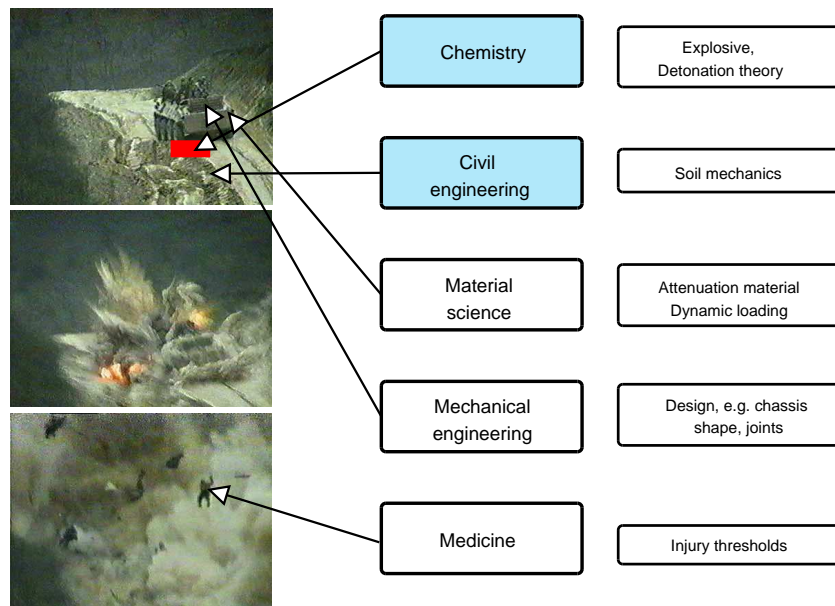


Figure 1.2: *Branches of science relevant to enhancement of landmine protection. (Photos depict the Chechnyan insurgency operation against Russian armed forces [114].)*

expensive to conduct. Moreover, multiple experiments need to be conducted to confirm findings – adding to the costs.

- (b) *Theoretical approach* can be described by using numerical simulation since computational power has significantly increased [23]. This is used to facilitate understanding of the explosion process as well as interaction with surrounding materials, namely air and soil. The set-up as well as running is flexible, non-destructive and highly iterative. However, assumptions and abstractions need to be made in order to initiate this form of study.

In the real life the lines are blurred between the two approaches. Figure 1.3 shows how the approaches are linked with each other. The numerical modelling cannot survive without the 'moment of truth' when the benchmark numerical results are compared with experimental data. On the other hand, experimental work and understanding the phenomena can be improved using the numerical modelling as it will be seen in the sensitivity analyses (Chapter 7, Section 7.2 and 7.3).

Both approaches have been undertaken in this area of research field in recent years. Since experiments have mostly investigated the response of a plate under explosion, the soil characteristics have not been measured and considered. This approach is represented by Bird [25], Nell [93], and Alem *et al.* [12]. Bergeron

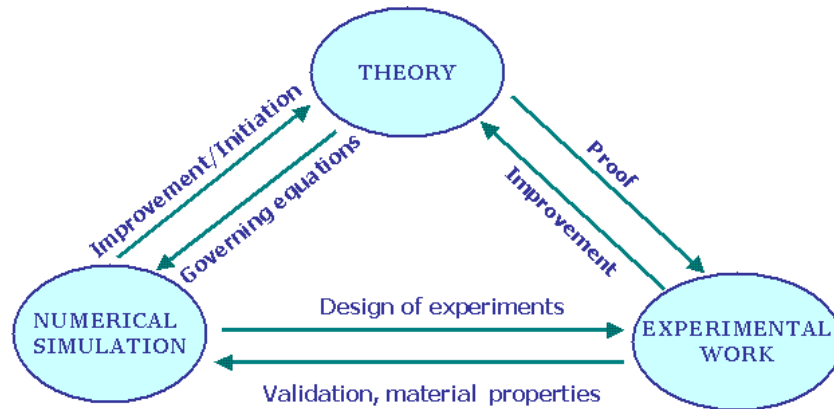


Figure 1.3: Approaches to deal with the problem.

et al. [19, 20, 22] have experimentally investigated the effect of soil properties on loading. Numerical modelling approaches of Laine *et al.* [83] and Fairlie *et al.* [44] benchmarks this experimental finding. These are some of the few systematic studies to investigate the explosion process and are not merely studies of the response of plates to explosions.

Earlier modelling approaches tended to simplify the problem of mine explosion. For instance, soil was not considered in the modelling problem by Cheng *et al.* [34] and Niekerk [94]. Williams *et al.* [125, 127] incorporated empirical relations for explosion in soil into the finite element LS-DYNA software. However, subsequent approaches by Laine *et al.* [83], Fairlie *et al.* [44] and Wang [121] incorporate sand (but not cohesive soil) in their modelling. The significance of these observations is addressed in ensuing chapters.

1.3 Background

Since their first use against Kublai Khan's Mongol invaders in 1277 A.D., landmines have gone through several development stages that are evident in its modern day impact. Mines have evolved and grown specialised in terms of their intended target and subsequent destructive effect. This specialisation has led to the classification of landmines as *antitank* (AT), *antipersonnel* (AP), *antihelicopter* and *off route* varieties. With changing battlefield scenarios, the design of the mine has been adjusted to suit those needs, and thus landmines are chiefly classified based on their destructive effect, as follows:

- *Blast* – the dominant destructive force is the shock-wave propagating through air and material causing disruptive overpressure and impulse.

- *Fragmentation* – the destructive elements are the fragments that are propelled towards the target in high velocity.
- *Shaped charge* – the formed jet travelling at a great speed penetrates armour and causes *behind armour* effect. A variation of this shaped charge is the *Misznay Schardin charge* whose self-forging fragment travels at a lower velocity than the aforementioned jet.

Fragmentation and shaped charge effect is concisely covered in terminal ballistics [1]. Shaped charges have been under investigation over many years for various applications in military and civilian sectors. Walters *et al.* [120] have comprehensively covered this phenomenon. Several computer software packages such as TEMPS, DESC-3 have been developed for shaped charge design and effect. Moreover, several researchers, such as Smith *et al.* [107] and Adamik *et al.* [9], have also employed commercial finite element software to formulate design parameters.

The focus of the present research is on the antitank blast mine. The Russian antitank mine TM-72 shown in Figure 1.4 demonstrates the main features of AT mine design.

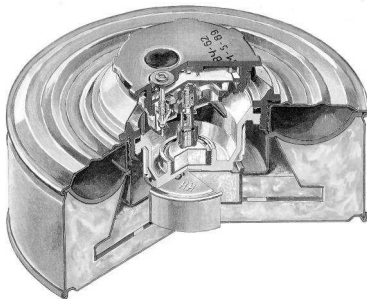


Figure 1.4: *Representative antitank blast mine: TM-72 [2].*

Antitank blast mine. The main charge is housed in a thin outer casing and is initiated by a fusing system. The charge consists of a high explosive, in particular, TNT or Composition B of mass 1.5 kg to 13 kg. Casings are mainly made of plastic, although metal, wooden and cardboard casings have been used in older designs. These mines often have antipersonnel mines around them or explicitly fitted *anti-lift devices* to prevent clearance by personnel.

A detailed overview of landmines is given in *Jane's mines and mine clearance* [2], Sloan [106] and Courtney-Green [37].

The degree of loading varies depending on the way a mine is deployed. Figure 1.5 summarises the various forms of mine deployment: mines are either (a) spread on the ground surface, (b) laid flush with the ground level or (c) buried in the soil (20 mm – 60 mm, [3]). Finally, two or more mines may be stacked in the same place.

In every deployment, the soil condition has an important influence. Although part of the explosive energy is dissipated into the soil, the soil material impinging on the vehicle significantly contributes to the loading [19, 68]. Depth of burial as

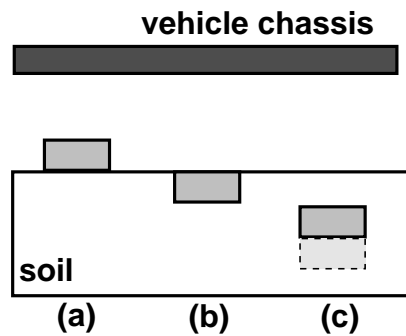


Figure 1.5: The scheme of mine deployment.

well as soil composition plays a role in the loading magnitude. Soil is composed of air, water and solid particles. Soil can be divided into the following two categories, each displaying different characteristics:

- *Cohesionless soil* consists of coarse particles. Frictional forces prevail among the particles, for example sand.
- *Cohesive soil* is composed of fine particles with dominant cohesion forces which attribute inherent constitutive strength, for example clay.

Since study of cohesionless soil has been undertaken by several researchers, such as Sadd *et al.* [103], Laine *et al.* [82] and Adushkin [10], this research deals with cohesive soil. The investigation includes the effect of soil composition on vehicle loading.

The other distinctive feature is the dimensional setup. The vehicle under attack is situated in the *fireball zone*. In other words, the vehicle is located in an unstable area where the explosion parameters are highly influenced by the detonation products. Therewith shock-wave anomalies were observed by Nykl *et al.* [95]. Joynt [76] describes these anomalies as “fingers of fire”. These aspects are not well documented and therefore, bring further uncertainty into the study.

Soil subjected to explosion has been under investigation for a few decades [67]. However, the research was confined to other areas such as mining, excavation of irrigation systems and response of buildings. Empirical formulae have been derived in each of these cases. In other words, empirical relations between parameters of cratering, compaction, ground shock represent the soil-blast interaction in most cases (Ambrosini *et al.* [13] and Vovk *et al.* [118]). In another approach, soil is treated as an elastic-plastic continuum medium and the soil particle movement is translated into pressure and impulse delivered to the buried structure (Smith *et al.* [108] and Tennant *et al.* [112]).

1.4 Research specification

Although numerical analysis is a generic term, in the present case, it means to employ the commercially available software AUTODYN [32] and through the choices of methods of solution and material modelling options:

To propose a numerical model that captures the principles of the explosion process and reliably recreates the interaction among soil, air and explosion products in the near region to the initiation point.

This allow us to answer a key research question and to understand the software better for the later research stages. The other key question that is worthwhile answering is the reliability of the answers that the hydrocode might return. Therefore, the problem statement is extended into:

To validate numerical solutions against documented experimental studies and to ensure adherence to same, within some acceptable tolerance levels.

The model that satisfies the two criteria mentioned above is restricted if it cannot accommodate any changes of the physical parameters that are parts of the explosion process, such as, soil condition, method of deployment, type of high explosive. So, the final challenge would require:

The ability to extend the numerical model to include and to modify these physical parameters that form the constituents and obtain consistent results in terms of behaviour.

The aim of this thesis can be briefly summarised as follows:

Numerical simulation and validation of landmine explosion taking into account soil properties, in particular, soil composition (by varying the moisture content).

The research was conducted in three stages with increasing complexity:

Stage I. Hemispherical surface explosion in air.

In this study, the charge was located on the *rigid surface*, i.e., perfect reflection, and shock-wave propagates in air. Numerical results were validated by comparison with experimental data obtained from CONWEP [115].

Stage II. Small-scale explosion in dry sand.

This phase introduced sand into the modelling. The charge was either flush or buried in dry sand. Sand model derived by Laine *et al.* [82] was used. The simulation was validated against experimental data by Bergeron *et al.* [22].

Stage III. Mine Impulse Pendulum Study.

A methodology was developed to derive the model for soil of varying composition. The methodology was applied to *prairie soil* (cohesive soil) whose moisture content ranged from 7.7% to 28.7%. The model was comprehensively validated for several setups. Mine impulse pendulum experiments [19] were used for validation.

1.5 Work disseminations

The research findings were presented in the following peer-reviewed conferences and journals:

- FIŠEROVÁ, D., *et al.*. Systematic study of simulated mine explosions using AUTODYN. In *6th International seminar on New trend in research of energetic materials* (Pardubice, The Czech Republic, April 2003).
- FIŠEROVÁ, D., *et al.*. Evaluating numerical approaches in explosion modelling using a surface-laid mine. *Journal of Battlefield Technology* 7, 2 (July 2004), 1 – 5.
- FIŠEROVÁ, D., *et al.*. Numerical simulations as a reliable alternative for landmine explosion studies: The AUTODYN approach. *International Journal of Impact Engineering*. submitted, under review.
- FIŠEROVÁ, D., *et al.*. The use of numerical simulations to analyse soil behaviour and the contribution made to target effects by soil, following the explosion of buried mines. In *7th International conference on Shock and impact loads on structures* (Perth, Australia, December 2005).

The work was further disseminated in the form of (in)formal presentations to industrial researchers. The comments that arose from these presentations were from an application point of view (i.e., expectations from industry based researchers) were valuable and kept the research investigations in perspective. The presentations are listed below:

- AUTODYN Users' Meeting, UK, December 2003,
- Alvis Vickers¹, Ltd., March 2004,
- DSTL and Qinetiq, October 2005,
- BAE Systems, Land Systems, November 2005.

¹Alvis Vickers, Ltd. is a part of BAE Systems, Land Systems since September 2004.

1.6 Thesis outline

The remaining part of the thesis deals with the following topics:

Chapter 2. Literature survey

The work performed in the area of landmine explosion in terms of experiments and numerical simulations is presented.

Chapter 3. Soil mechanics

The theory of soil mechanics and laboratory tests for determining soil properties necessary for this study are explained.

Chapter 4. Research methodology AUTODYN

The features of AUTODYN that are used in the models are explained.

Chapter 5. Soil modelling

A methodology is proposed for deriving soil models based on soil composition. The available soil properties data from laboratory tests are introduced.

Chapter 6. Experiments for validating numerical solutions

As the numerical simulations needed to be validated to be deemed as reliable, the experiments that complement the numerical simulation research are presented in this chapter.

Chapter 7. Results of modelling in AUTODYN

The work that progressed from simple simulations to more complex models is presented. The results for the three case studies are given. The derived soil model is extensively validated. The numerical results are compared with the experimental evidence.

Chapter 8. Discussions and future directions

The salient features of the proposed methodology is presented. The findings from the research are discussed from the perspective of applications. The problems encountered with existing scaling laws are highlighted. Some alternative approaches to modelling are briefly presented.

Chapter 9. Conclusions

The thesis concludes with contribution to the knowledge and proposals for the future work.

We feel that even when all possible scientific questions have been answered, the problems of life remain completely untouched.

— Ludwig Wittgenstein (1889-1951)

Chapter 2

Literature survey

THE TOPIC OF MINE EXPLOSION and its simulation has grown steadily and evolved in the last few years. For instance, one can find literature regarding explosion process from numerical solutions (Brode [28], Mader [88]) to experimental findings (Held [59, 62, 63], Kingery *et al.* [79]). The literature coverage can be grouped into the following broad categories:

- The internal problem of an explosion process – deals with the processes taking place in the high explosive namely, detonation theories and elemental chemical composition of explosive and detonation products (Fickett *et al.* [45], Brown [29]).
- The external problem of an explosion process – examines the processes occurring in the surrounding medium namely, the effect of stress and shock waves propagation in various materials for the reasons cited below:
 - response of buildings subjected to internal and external blast load (Smith *et al.* [108], Baker *et al.* [15]),
 - high-strain rate loading and dynamic behaviour of metallic and composite material (Zukas *et al.* [129], Meyers [91]),
 - explosions in air and underwater (Kinney *et al.* [80], Henrych [67]), and,
 - mining, rock blasting (Persson *et al.* [98]).

This chapter is not aimed to be an exhaustive literature review of the explosion process and mine protection design. The concentration is on the study of the particularities of landmine explosions in order to understand the progress made in this

area and thus state the important issues that are necessary to investigate onward. The ensuing sections deal with relevant research areas, such as recent developments in mine explosion simulation and relevant experimental work. The topic of soil-blast interaction is briefly presented in this chapter. Public domain sources were available to the author.

2.1 Experimental findings related to the mine explosion phenomenon

Although mine research is extensively experimental, i.e., vehicle being subjected to mine explosion as part of manufacturers' research, these trials do not determine (quantify) the explosion output. The work dedicated to study the mine explosion output in different soil and deployments setups are a few: small scale experiment (Bergeron *et al.* [22]), mine impulse pendulum (MIP) (Bergeron *et al.* [19], Bues *et al.* [30]), piston (Hlady *et al.* [68]), momentum gauges (Held [63]). From these, small scale experiments and MIP were selected to validate the numerical simulations, therefore, these experiments are described in details in Chapter 6.

In Bergeron *et al.* [22], it was observed that the depth of burial considerably influences the measured parameters. The influence of the deployment is more pronounced in maximum pressure than in specific impulse. The flush charge in dry sand gave 19 times higher maximum pressure than the charge buried at 80 mm, whereas the specific impulse increases only 2.4 times in the same case. The impulse delivered to the mine impulse pendulum from a charge buried in wet soil is 2.5 times higher than a surface-laid charge. In Held [63], the impulse, that was measured using momentum gauges, from a charge flush and buried mine in sand was about 50 % and 90 %, respectively, higher impulse than surface-laid mine.

The other parameter that significantly affects the magnitude of the loading is the moisture content. In Bergeron *et al.* [19], the impulse delivered to the pendulum when the mine is buried in saturated prairie soil is two times higher than from the mine buried in dry soil. In Hlady *et al.* [68], the energy transfer in wet prairie soil was five times higher than in dry soil. The cohesiveness of wet prairie soil allows the formation of large clumps of soil in the ejecta; these large clumps carry significant energy [68]. At overburdens of 0 and 20 mm, less soil is available to become ejecta; the trend of increasing impulse with increasing moisture is much less pronounced for these cases [69]. Dry sand subjected to an explosion behaves like a homogeneous material and does not form clumps. Dry prairie is less homogeneous than sand, and few small clumps are formed.

Multiple spike gauges (Joynt [76]) were employed to investigate the energy spread above surface caused by the explosion of buried anti-tank mine. The investigation was to confirm (or refute) the “fingers of fire” effect, that was observed on high-speed camera of explosion of AT under the vehicle. The experiments showed that the distribution of the impulse forms an irregular pattern. In vertical direction, the difference in impulse was up to 14 times. The details of setup and soil properties are not presented.

The fine impulse structure (Joynt [78]), the large scale facility (Coffey *et al.* [35]), and the vertical impulse measurement fixture (Skaggs *et al.* [105]) were developed to investigate the effect of mine explosion on vehicle loading for various setups. However, the details and findings are not available.

Vehicle response. Several trials, Absil *et al.* [8], Niekerk [94], Bird [25], Nell [93] and Alem *et al.* [12], were conducted to study response of vehicle subjected to mine explosion. The goals of these tests were (i) to analyse gross motion and damage on the vehicle in order to identify the most vulnerable components, (ii) to assess the effect on occupants and (iii) to evaluate attenuation materials (Holland [70]). In conclusion, vehicle design proposals have been made from tests and these include a V-shaped hull, double floor, deflector plates fitted under wheel wells, fuel tank placement in rear part of vehicle, energy absorbing seat and control of vehicle manufacture process, primarily welding. Nell [93] measured the soil parameters during trials, namely resistance of the ground by *Dynamic cone penetrometer*, density and moisture content, but their influence on mine blast output has not been presented. Other research groups have investigated the plate deformation in order to validate numerical simulation (Persson *et al.* [97], Williams *et al.* [127]).

Human vulnerability. The experiments conducted in order to assess the human response, widely use automotive crash-test dummies (also termed Hybrid-III mannequin) for mine research purposes [25, 94]. However, a question that has arisen is “Does the Hybrid-III mannequin have sufficient fidelity to evaluate human injury criteria during land mine explosions?” [94]. This has led to development of *frangible synthetic leg* [21, 25] that is able to represent the response of human leg reliably.

2.1.1 Experimental techniques for measuring the mine explosion output

The experiments to measure mine explosion output are not easy to perform as the area of the interest is located in fireball and soil clumps can destroy the measuring

equipment. It was observed that the pressure transducers are not a feasible option to measure the mine explosion output as it does not include the soil contribution to the loading (Bergeron *et al.* [22], Blaney *et al.* [26]). The difficulties in developing cheap and robust pressure gauges in order to measure internal detonation tests are described in Dirlwanger [40].

Similarly, studies on measurement techniques which work on mechanical principle such as conservation laws of energy and momentum have been conducted in order to capture the soil contribution. This can be divided as follows:

- *Deformable gauges* – The main measuring part is deformed. Some calibration is needed to link the part deformation to transformed pressure/impulse. For example, spikes and dimple gauges, tins [60].
 - **Multiple spike gauges.** (Joynt [76]) The measuring device consists of the hemispherical dome-like structure pierced by spikes in several directions. The spikes have a sharp point that penetrates a soft aluminium cylinder. This cylinder is thrown upwards by the explosion energy. The change in distance is linked to the impulse delivered.
 - **Dimple gauge.** (Joynt [77, 78]) This method was used in the mine boot experiments. The dimple gauge consists of the steel anvil and thin aluminium plate. The plate is placed in front of the anvil with holes. The impulse presses the plate to the holes of anvil, making a “dimple” on the plate. The deformation is related to the energy that caused it, and this is determined by a calibrating procedure. Figure 2.1 shows the anvil and the plate after experiments. This method was scaled up to measure the response of vehicle wheel subjected to explosion of 7 kg TNT [78].
- *Non-deformable gauges* – The explosion energy is delivered to the part which does not deform. The explosion energy is transformed into kinetic energy (movement) of the gauge. Figure 2.2 schematically represents these gauges.
 - **Straight-linear movement:** The displacement is directly related to the imparted impulse. The movement is in either vertical [68], horizontal [65, 110, 111], or inclined [78] direction.
 - **Rotational movement:** The angle is linked to the delivered impulse. The movement is in either vertical (pendulum) [72], or horizontal (MIP)[30, 19] direction.
 - **Free flying objects:** The energy is transformed to the kinetic energy of steel blocks which fly in free air. The positions of the blocks are captured

in two different time frames and the imparted momentum is calculated – momentum gauges [63, 62].

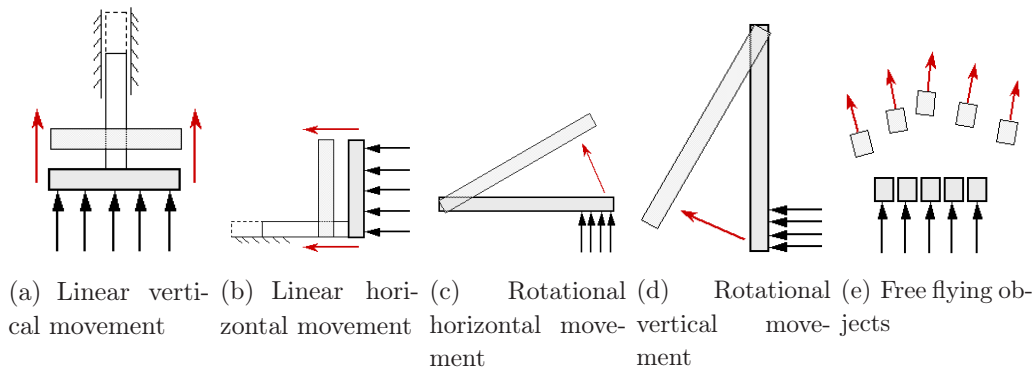


(a) The anvil of the dimple gauge



(b) Plate after experiments. The numbers written on the dimples are mm of deflection.

Figure 2.1: Dimple gauge. Reproduced from Joynt [77].



(a) Linear vertical movement (b) Linear horizontal movement (c) Rotational horizontal movement (d) Rotational vertical movement (e) Free flying objects

Figure 2.2: Non-deformable gauges measure the impulse delivered to the structure.

2.2 Numerical simulation dedicated to mine explosions

Finite element method (FEM) studies are widely used in defence related engineering analyses, such as high-velocity impact and penetration [57, 81]. In preliminary works, explosion was implemented in simulation using empirical formulae [54, 126]. Recently, bespoke numerical procedures have been developed which allow the study of the explosion process from the initiation of explosive charge [44, 121].

Responses of the vehicle being subjected to various blast loading can be iteratively modelled using computers and appropriate numerical techniques. This approach reduces the cost of expensive field trials. Researchers employ numerical simulation to study various tasks with different focus such as (i) injury of occupants, (ii) design of vehicle components and (iii) attenuation material. Simulations dealing with mine explosion are summarised in Table 2.1. The table focusses on parameters dominant to explosion loading. The model of plate is not crucial and is therefore not included in the table. The paragraphs that follow, review this table and the findings in detail.

Numerical analyses of the effect of soil conditions and the depth of buried mines undertaken by Laine *et al.* [83] yielded the following conclusions: A buried mine gives a much lower maximum pressure acting over a long duration than the flush and surface-laid mine. In contrast, the incident impulse of a buried mine was the highest at distances above the ground less than 1 m. Loading caused by a buried mine is concentrated in the vertical direction more than a surface mine that is more spatially spread. The buried mine in fully saturated clay yielded about 25% higher pressure and impulse than the mine buried in sand. Thus, it can be stated that the effect of soil condition has a great influence on the pressure and impulse. However, these numerical simulations were not validated by experimental data and details on soil were not presented.

A methodology for simulating mine explosion is presented by Fairlie *et al.* [44]. Firstly, two approaches in AUTODYN-2D were investigated for modelling high explosive: (i) multi-material Euler solver employing Jones-Wilkins-Lee, (JWL) equation of state (EOS) for detonation products, and, (ii) single-material Euler solver employing *ideal gas* equation of state for detonation products. It was observed that prediction of the target momentum is consistent. Therefore, further analysis used the *ideal gas* equation of state approach for detonation products. Also, in this setup, the *pendulum* used in the experiments conducted by Bergeron *et al.* [19] was modelled (using 5 subgrids) in AUTODYN-3D. The Lagrangian grid was filled using the sand model derived by Laine *et al.* [82]. By comparing the numerical findings (sand model) with experimental data (dry sand and prairie soil), it was concluded that the impulse from a mine buried in dry sand and prairie soil was overestimated by 24% and 3% respectively by the numerical model. Therefore, varying soil parameters, namely moisture content and initial density amplifies the impulse generated by the mine.

Numerical results obtained by Wang [121] were compared with experiments performed by Bergeron *et al.* [22]. Comparison shows that the numerical predictions of positive phase duration and the displacement of ejecta front overestimated experi-

ments by 36% and 10% respectively. The peak of the overpressure was underestimated by 50%. The findings are on the same plane in the case of a surface mine as well. Apart from the peak pressure and positive phase duration, the simulation agrees well with experiments. Further analysis is suggested by Wang in area of cell size sensitivity and the feasibility of an empirical JWL EOS.

The response of a box-like structure to a mine blast was studied by Cheng *et al.* [34]. The soil was considered as a rigid surface which allowed reflection but no refraction. This assumption simplified the analysis. Authors assumed that this simplification would result in a greater loading of the structure over a model that incorporates soil in its parameters. In the contrast, Laine *et al.* [83] and Bergeron *et al.* [19, 22] observed that buried mines have given higher loading and larger deformation than the surface mine. Numerical analysis has not been supported by experimental evidence. Full details about the structure and metallic material are not available.

Williams *et al.* [126] investigated the floor deflection of a vehicle using a simple empirical impulse model for soil. This was used to generate an initial velocity boundary condition, in spite of their using an FEM software, LS-DYNA-3D. The only variable soil parameter of the model was density ($\rho_{soil} = 2170 \text{ kg.m}^{-3}$). No other soil characteristics were incorporated in the model to predict pressure loading and momentum transfer. This setting resulted in a plate deformation of 578 mm, while experimental results showed a deformation of 287 mm. It is believed that this obvious discrepancy was due to the fact that energy absorption mechanism of soil was not implemented into the empirical model used. Another notable effort, Gupta [54], is an algorithm derived from the empirical-based code CONWEP and implemented into the FEM software LS-DYNA, in order to generate blast overpressure loading on a panel.

When results of simulations that focused on the response of a plate are not in good agreement with experimental data, i.e. the value of deformation, it has been concluded that further study of the plate model needs to be carried out or simple scale-up of the explosive charge is done. In each case, the detonation model or the shock wave propagation has not been analysed and confronted.

Table 2.1: Overview of numerical modelling of a mine explosion. Air is modelled using ideal gas EOS in every case.

Source	Code	Cell size [mm]	Explosive EOS	Soil	Distance above-ground [m]	Note
Laine <i>et al.</i> [83]	AUTODYN	8	10.4 kg position B – JWL EOS	Sand – Laine [82]; saturated clay	0.4 till 1; 100 mm soil coverage	Analysis of pressure and impulse magnitude were conducted for buried, flush and surface-laid charge.
Fairlie <i>et al.</i> [44]	AUTODYN	25 (air)	1 kg C-4: Ideal Gas EOS	Sand – Laine [82]	0.4; 50 mm soil coverage	Total momentum imparted to the pendulum was observed and compared with experiments.
Wang [121]	LS-DYNA		100 g C-4: JWL EOS	Sand – ‘Soil and foam failure’ model [unpublished]	0.3 and 0.7, ($Z=0.63$; $1.48 \text{ m.kg}^{-1/3}$)	Pressure and ejecta forming were investigated and compared with experiments (Bergeron <i>et al.</i> [22]).
Cheng <i>et al.</i> [34]	AUTODYN & MSC.Dytran	10	5 kg TNT – JWL EOS	rigid surface	0.56	Output parameter was the deflection of box.
Williams <i>et al.</i> [126]	LS-DYNA		7.5 kg C-4	$\rho = 2170 \text{ kg.m}^{-3}$ Westine <i>et al.</i> [123]		Blast was introduced through initial velocity boundary condition obtained from <i>empirical impulse</i> model. Output parameter was floor deflection.
Gupta [54]	LS-DYNA		907.2 g Pentolite		1.52	CONWEP algorithm was implemented into LS-DYNA to generate blast pressure loading. Response of composite panel was investigated.
Niekerk [94]	MSC.Dytran		800 g Pentolite	rigid surface	0.5/ 0.505	Pressure analysis resulted into 24% underestimated prediction. Experiment data varies from 38 to 81 MPa.
Absil <i>et al.</i> [8]	AUTODYN	2	475 g Composition B		0.2	Impact of fragments from steel casing on aluminium plates was investigated.
Dorn <i>et al.</i> [43]	FLUENT & LS-DYNA	Methodology paper without quantitative and qualitative data. Presents interaction of blast wave with flat and angled geometry of chassis, kinematic response of vehicle and occupant injuries (DYNAMAN model)				
Jacko <i>et al.</i> [74]	AUTODYN		500 g TNT			Response of the homogenous armour plate and armour plate with Kevlar layer subjected contact explosion was studied.
Person <i>et al.</i> [97]	AUTODYN		0.125 / 0.5 / 1 / 4 kg PETN		0.25 / 0.5	Maximum deflection and velocity of steel plate of 5, 10 or 20 mm thickness. Compared with experiments [97].
Rhijnsburger [102]	LS-DYNA		10 kg TNT	rigid surface		

2.2.1 Numerical modelling of explosion process

In conventional use, a mine is generally laid above, flush or buried in soil (commonly categorised between sand and clay). Upon initiation, the detonation wave propagates through the explosive material, generating high pressures and temperature in the detonation products. These products expand violently, forcing the surrounding material (soil and air) out of the occupied volume and create a pressure shock-wave propagating through the surrounding material in all directions from the charge. As soil is pressed out forming ejecta, the detonation products break through the surface. Soil gains kinetic energy and moves upwards. After impinging on the target, soil falls back and a crater is formed. It is to be noted that the detonation products expand to a scaled radius of about $0.8 \text{ m.kg}^{-1/3}$ [116], where scaled distance is defined as $Z = R/W^{1/3}$, R [m] is the distance from charge centre and W [kg] is the TNT equivalent charge mass. The whole of the compressive wave propagates in air beyond a scaled radius of $1.6 \text{ m.kg}^{-1/3}$. Hence analyses focusing up to this region must take into account both the explosive products and air.

Explosions are numerically described by a general system of conservation equations. The equations consist of laws of conservation of mass, momentum, energy, supplementary equation and material models for explosive, air and soil. A supplementary equation expresses suitable working hypothesis, also termed as *detonation theory*. The simplest detonation theory is expressed by the Chapman-Jouguet (CJ) equation $D = u + c$, where D is the detonation wave front velocity, u is the particle velocity and c is the sound speed. The Chapman-Jouguet ideal detonation theory is described as one-dimensional laminar flow with instantaneous chemical reaction, such that the shock wave travelling through explosive is planar and propagates through the explosive unchanged. Fickett *et al.* [45] explains ideal detonation theories while Brown [29] overviews non-ideal detonation theories.

Material models play an important role linking stress to deformation and internal energy. Fluids and gases (in the presented modelling studies, detonation products and air) are sufficiently modelled using an *equation of state* (EOS), which expresses a relationship between the pressure p , specific volume v and specific energy e . Details of the governing equations of explosion are discussed by Henrych [67]. Mader [88] and Oran *et al.* [96] have comprehensively dealt with numerical methods for modelling of explosions.

High explosives are modelled using an equation of state for explosive products that can be classified into two types as follows:

- Equations of state *without explicit chemistry* are based on experimental data for a particular composition from which the formulae are derived, for an example, Jones-Wilkins-Lee [41].

- Equations of state *with explicit chemistry* contain individual EOS for component molecules and rules for their combining to give an EOS for any composition, for an example, BKW, RUBY [129].

The particular application, the required accuracy and the solution methodology are the main factors that influence the decision of the choice of appropriate EOS for explosive products. Souers *et al.* [109] has stated that the chemical equations of state predict unsatisfactory results, and are difficult to incorporate into finite element software. On the other hand, Mader [88] has argued that “*JWL fit to a cylinder test may be useful for describing that particular cylinder test, but it will not be useful for describing anything else.*” Overview of EOS is listed in Zukas *et al.* [129].

The empirical Jones-Wilkins-Lee (JWL) equation of state is widely used in mine blast calculations (see Table 2.1). It is implemented in codes, such as LS-DYNA and AUTODYN. The cylinder expansion test was developed to derive the JWL EOS for explosive products [41]. In this test, a copper tube containing explosive is detonated, and the cylinder wall acceleration caused by the explosive products expansion is recorded with a high-speed camera until the cylinder has expanded to about three times the original diameter. The resulting empirical equation is a pressure-volume relationship that is independent of temperature. The JWL equation is implemented in AUTODYN in the form given below

$$p = A \left(1 - \frac{\omega}{R_1 V} \right) e^{-R_1 V} + B \left(1 - \frac{\omega}{R_2 V} \right) e^{-R_2 V} + \frac{\omega E}{V} \quad (2.1)$$

where A [Pa], B [Pa], R_1 [-], R_2 [-] and ω [-] are coefficients which depend upon the composition of the explosive. The variable $V = v/v_0$ [-] is the expansion of the explosive products and E [J.m⁻³] is the detonation energy per unit volume. The values of JWL’s coefficients have been derived by various authors such as Dobratz *et al.* [41], Finger *et al.* [46] and Souers *et al.* [109].

2.2.2 Numerical modelling of vehicles with crew

Simulations that studied the deformation of a vehicle part and simplified vehicle have been successfully performed, such as Persson *et al.* [97], Absil *et al.* [8], Niekerk [94], Cheng *et al.* [34] and Williams *et al.* [127]. As the main aim of the mine protection vehicles is crew-survivability, the numerical simulation should be extendable to incorporate the human body. Possibilities exist to incorporate human body to the numerical simulation in the studies of mine explosion. Examples are (i) Articulated total body [ATB] in MSC-DYTRAN [94], (ii) GEBOD in LS-DYNA [125], and (iii)

DYNAMAN developed by Frazer-Nash Consultancy Limited [43]. The development in software and hardware shows that it is possible to model more complex problems. For instance, Williams *et al.* [125] performed a numerical analysis of the effect of 6 kg C-4 mine detonated under the wheel with 4 crew members in the Cougar crew compartment.

2.3 Soil-blast interaction

Civil engineering has reported on soil under explosion for a few decades (Henrych [67]), for various purposes such as excavation of irrigation systems, elimination of soil sagging at construction sites, deposition of highway embankments in marshlands and response of buried structures. The contemporary resources and application requirements have affected the solving approaches. Thus, experimental approach has prevailed in this domain. The empirical formulae have been derived for given problems and continuum mechanics have been applied to soil movements. The issues can be summarised as follows:

Cratering. Empirical relations between apparent crater volume (diameter) and charge weight is derived for the forensic sciences (accidental explosion) and mining industry. Moreover, these relations are applied to a set of explosive charges for excavating irrigation systems. Experiments investigate varying moisture content, depth of burial or height of burst. It was observed that the rise in the moisture content caused decrement of the optimum and critical depth of burial. Feasibility of scaling cratering effect is discussed. This research area has been studied by several authors such as Ambrosini *et al.* [13], Dick *et al.* [39] and Nakayama *et al.* [92]. Gu *et al.* [53] examines the feasibility of using numerical analyses LS-DYNA to predict cratering effects arising from near-field, shallow-buried explosion, in numbers, 20 kg TNT buried at 2 m in dry sand.

Compaction. Explosion methods have been studied in order to prepare foundations for structure. Empirical formulae of the compacted zone were derived for the dimension of charge and its layout. Soil was incorporated through density and experimental coefficients. Moisture content was recommended to be about 16%. This approach is represented by Henrych [67], Vovk *et al.* [118].

Ground Shock. Attenuation of shock-wave in a soil mass is investigated in order to assess damage to buried structures. Soil particle movement is translated

into pressure and impulse delivered by soil to target. Plasticity theory is applied to soil mass. Baker *et al.* [15] and Smith *et al.* [108] have investigated this area. The attenuation of airblast energy in soil has been studied by Madshus *et al.* [89], but the scaled distances exceeded $100 \text{ m.kg}^{-1/3}$ and measurement techniques used to analyse ground response to propagating airblast were dissimilar to methods at the close-in distances from explosion. Soil-blast interaction in far-field demonstrates the following: (i) pressure was measured by microphones and reaches magnitude in order of hundreds Pascal, (ii) ground displacements were recorded by geophones and seismometers with amplitude of order of micrometers, (iii) time is in order of seconds. Numerical simulations of response of buried structures were performed, for example, by Akers *et al.* [11], and Leong *et al.* [85].

Mining. Since formation of detonation wave front play a important role, the non-ideal theories have been introduced in order to explain processes in long cylindrical charges which dominate in rock blasting and mining industry. Although rock can be described as a rigid linearly elastic material, it also displays anisotropic behaviour imposed by crack properties such as its dimension and filling. Persson *et al.* [98] have comprehensively covered this phenomenon.

In many approaches, only empirical formulae have been derived for soil type and particular system when looking at final results of soil-blast interaction. In the other cases, soil is treated as an elastic-plastic continuum medium and investigated behaviour of soil is dissimilar to the mine explosion loading.

The most relevant study of soil-blast interaction has been conducted by Laine *et al.* [82] who investigated mechanical properties of *dry sand*. Suitable model was derived in order to incorporate into numerical procedures, namely AUTODYN. Triaxial compression tests data were used to derive Compaction equation of state and Granular strength model. The influence of moisture content on mechanical properties, consequently numerical model, has not been investigated.

2.4 Summary

- ◆ Soil moisture content and depth of burial have a significant influence on vehicle loading.
- ◆ Numerical simulations were mostly performed to assess the deformation of plate.

- ◆ Sand model exists. But it is not extended for different moisture content.
- ◆ Experimental studies are the prevailing medium of validation and thus were called on for validation purposes in this thesis.

Weather is not as important as good soil, and good soil is not as important as human harmony.

— Chinese proverb

Chapter 3

Review of soil properties and theory

SOIL IS A COMPLEX structure consisting of skeleton of solid particles and interconnected spaces. Spaces between particles, termed *voids*, are filled by water and gases, usually air. Two forces, namely *gravitational* and *surface forces*, act in the areas of contact between the particles. The surface forces derived from electro-chemical activity are dominant between clay particles which have large surface-area to volume ratio. These forces result in “cohesion” between particles and this attributes plasticity to soil. General term *cohesive soil* refers to soil with significant quantity of clay particles which exhibit the characteristics of cohesion and plasticity. The gravitational (frictional) forces related to the mass of particles occur mainly at coarse grained soils. The dominant influence of frictional forces results in a non-stiction between particles and thus soil is termed as *cohesionless soil*.

The properties of soil, as any other material, are attributed to composition of the material. The section that follows, presents soil physical properties and soil classification as standardised in civil engineering. The sections that follow, deal with mechanical properties and briefly describe laboratory tests for obtaining stress-strain relations, which are needed for soil modelling. Standard laboratory procedures were proposed throughout in order to keep the cost to a minimum (due to repeatability of procedure and no need of special equipment). The presented knowledge focusses on soil behaviour and properties needed for soil-blast interaction.

3.1 Description of soil

Soil may be regarded as a three-phase medium consisting of solid particles, water and air.

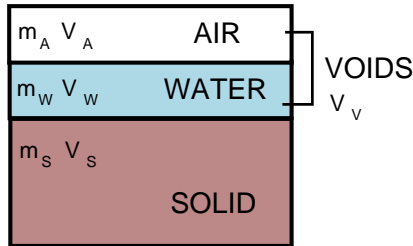


Figure 3.1: Soil composition.

Parameters specifying phase configuration of soil are *moisture content*, *voids ratio*, *porosity* and *degree of saturation*. Their definitions are presented in Table 3.1. Figure 3.1 depicts the soil phases and their mass and volume notation.

$$\alpha_a + \alpha_w + \alpha_s = 1 \quad (3.1)$$

where α is the relative volume of the relevant phase. Throughout the thesis, subscripts a, w, s denote air, water and solid particles, respectively. The relative volume is defined as,

$$\alpha_a = \frac{V_a}{V_{total}} \quad (3.2)$$

Moisture content is the basic soil parameter as this term is also referred in other soil characteristics, such as Atterberg limits. Moisture content expresses the amount of water in soils and is defined by a proportion of the mass of dry soil (solid):

$$w = \frac{m_w}{m_s} \times 100 \quad [\%] \quad (3.3)$$

The solid phase configuration is described by particle size distribution which is also part of soil classification. The other basic physical parameter is density. Plasticity and consistency attributed to fine soils are other parameters for specifying soil type. These properties are covered subsequently.

3.1.1 Particle size distribution

The physical characteristic of soils is determined by the distribution of various particle sizes in granular soil and by the cohesion and plasticity in clay soil. The definitions of particle size classification are given in Table 3.2. The limits of particle size vary with applied standards. (There is no internationally agreed size for particle size distribution.) The distribution of particle size of soil is expressed in terms of the *particle size distribution curve*, also called *grading curve*. Figure. 3.2 shows typical grading curves. The curve is obtained by combining two procedures: **sieving methods** for cohesionless soil with fractions of silt and clay, and **sedimentation methods** for the fine particles.

Table 3.1: Definition of soil physical properties.

Parameter	Symbol	Units	Definition		Relationship
Moisture content	w	%	$\frac{\text{mass water}}{\text{mass solid}}$	$\frac{m_w}{m_s}$	
Void ratio	e	–	$\frac{\text{volume voids}}{\text{volume solids}}$	$\frac{V_a+V_w}{V_s}$	$e = \frac{\rho_s}{\rho_d} - 1$
Porosity	n	–	$\frac{\text{volume voids}}{\text{total volume}}$	$\frac{V_a+V_w}{V_a+V_w+V_s}$	$n = \frac{e}{1+e}$
Specific volume	v	–	$\frac{\text{total volume}}{\text{volume solids}}$	$\frac{V_a+V_w+V_s}{V_s}$	$v = 1 + e$
Degree of saturation	S_r	%	$\frac{\text{volume water}}{\text{volume voids}}$	$\frac{V_w}{V_a+V_w}$	$S_r = \frac{w \rho_s}{e}$
Air voids content	A_v	–	$\frac{\text{volume air}}{\text{total volume}}$	$\frac{V_a}{V_a+V_w+V_s}$	$A_v = n(1 - S_r)$
Particle density	ρ_s	kg.m ⁻³	$\frac{\text{mass solids}}{\text{volume solids}}$	$\frac{m_s}{V_s}$	$\rho_s = G_s \rho_w$
Specific gravity	G_s	–	$\frac{\text{solids density}}{\text{water density}}$	$\frac{m_s}{V_s} \frac{1}{\rho_w}$	$G_s = \frac{\rho_s}{\rho_w}$
Bulk density	ρ	kg.m ⁻³	$\frac{\text{total mass}}{\text{total volume}}$	$\frac{m_a+m_w+m_s}{V_a+V_w+V_s}$	
Dry density	ρ_d	kg.m ⁻³	$\frac{\text{mass solids}}{\text{total volume}}$	$\frac{m_s}{V_t}$	
Limits liquid, plastic, shrinkage	w_L, w_P, w_S	–			
Plasticity index	I_P	–			$I_P = (w_L - w_P)$
Liquidity index	I_L	–			$I_L = \frac{w-w_P}{w_L-w_P}$
Consistency index	I_C	–			$I_C = \frac{w_L-w}{w_L-w_P}$

Table 3.2: Definitions of particle size in various standards (BS – British standard, ČSN – Czech standard, ASTM – American society for testing materials, USCS – Unified soil classification system (US)).

Group symbol		G	S	M	C
Particle description		Gravel	Sand	Silt	Clay
Particle size [mm]	BS, ČSN	60 – 2	2 – 0.06	0.06 – 0.002	< 0.002
	ASTM	> 4.75	4.75 – 0.075	0.075 – 0.005	0.001 – 0.005
	USCS	75 – 4.75	4.75 – 0.075	< 0.075 fines	

3.1.2 Density

Three terms of density are introduced as the main characterisation of mass per volume involving different components of soils. The *bulk density*, ρ , is fundamental mass per unit volume of soil with all three components, particularly solids, water and air. The bulk density is expressed by equation:

$$\rho = \frac{m}{V} = \frac{m_s + m_w + m_a}{V_s + V_w + V_a} \quad (3.4)$$

The second term is the *dry density*, ρ_d , which is mass per unit volume of dry soil, i.e. without water. Algebraically:

$$\rho_d = \frac{m_s + m_a}{V_s + V_a} \quad (3.5)$$

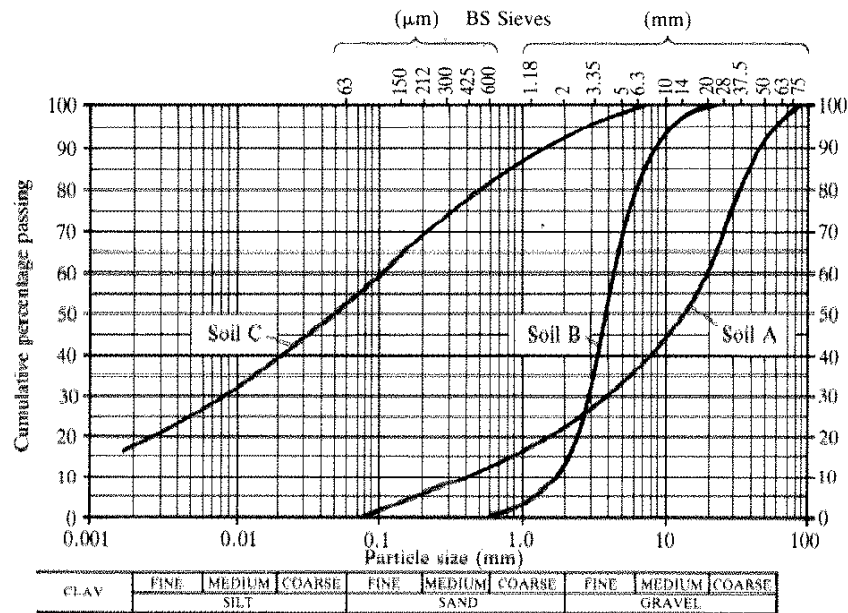


Figure 3.2: Grading curves. Reproduced from Berry et al. [24].

Note, that the mass of air is negligible with respect to the mass of water and solid particles. Relationship between bulk density and dry density is for a known moisture content w , and is expressed as follows:

$$\rho = \rho_d(1 + w) \quad (3.6)$$

The *particle density*, ρ_s , depends on mineral compositions of soil particles and is given by a ratio of mass of solid particles to volume of solid particles :

$$\rho_s = \frac{\text{mass solids}}{\text{volume solids}} = \frac{m_s}{V_s} \quad (3.7)$$

3.1.3 State consistency of soil

Plasticity of soil is another important physical characteristic of soil. To express it, moisture content has been taken as a limiting criterion. State consistency of soil is termed by the *Atterberg limits* which are composed of (see Figure 3.3):

- *The liquid limit*, w_L , expresses the moisture content at which a soil changes from the plastic to the liquid state.
- *The plastic limit*, w_P , empirically determines the moisture content at which a soil passes from the non-plastic to the plastic state.

- The *shrinkage limit*, w_S , corresponds to the moisture content at which soil changes from the solid state to the non-plastic state, in other words soil at this moisture content stops shrinking. The shrinkage caused by drying is more significant in clays than in silt and sand.

The plastic and liquid limits are the parameters to express how much plasticity is acquired by soil. This relation is depicted in the *plasticity chart* as shown in Figure 3.4. In the chart, the line between clay and silt is of equation:

$$w_P = 0.27 w_L + 14.6[\%] \quad (3.8)$$

Plasticity chart divides the soil further to five categories of plasticity: low, intermediate, high, very high and extremely high. In Table 3.3, the terms are summarised.

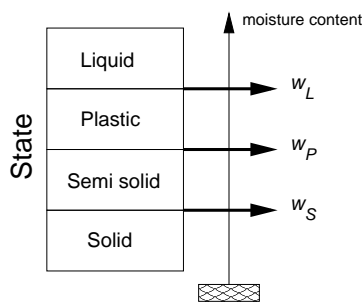


Figure 3.3: Atterberg limits.

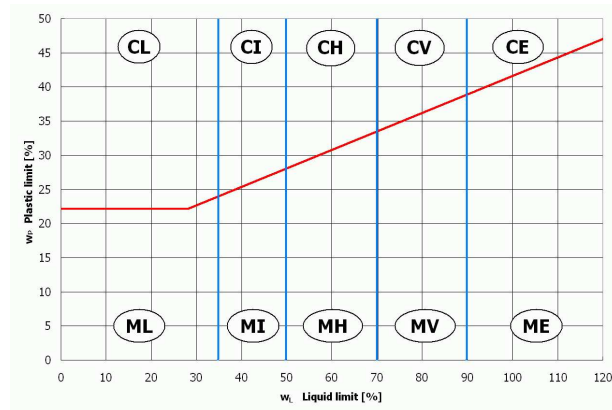


Figure 3.4: Plasticity chart.

Table 3.3: Plasticity in compliance with ČSN and BS.

Symbol Clay / Silt	Term	Liquid limit w_L
CL/ ML	low	< 35 %
CI/ MI	intermediate	35 – 50 %
CH/ MH	high	50 – 70 %
CV/ MV	very high	70 – 90 %
CE/ ME	extremely high	> 90 %

The *plasticity*, *liquidity* and *consistency indexes* are parameters derived from the Atterberg limits. Their formulae are presented in Table 3.1. The *plasticity*

index expresses the range of the moisture content where soil is in plastic state. The *liquidity index* determines if the soil condition is close to the liquid or the plastic limit. For I_L nearing 100% the soil is near the liquid limit, and for I_L nearing 0% the soil is near the plastic limit. The *consistency index* is used for defining the soil states as presented in Table 3.4.

Table 3.4: Soil consistency in compliance with ČSN.

	I_C	Note
very soft	< 0.05	$w = w_L$, flows between fingers when clenched in fist
soft	$0.05 - 0.50$	easily moulds in fingers
firm	$0.5 - 1$	hard to mould in fingers
stiff	> 1	$w = w_P$, cannot be moulded in fingers, possible to imprint nail
hard		$w < 7\%$, dried-up, crumbles when hit by hammer

3.1.4 Concluding remarks on soil description

Table 3.5 summarises the description and parameters that allow to identify soil unambiguously. This mean that following parameters need to be determined by soil laboratory tests:




- particle size distribution – classified soil as sand, silt, or clay,
- Atterberg limits – determine plasticity and consistency,
- bulk density, particle density, and moisture content.

From these parameters, the other parameters that describe the ratio of different phases can be calculated using formulae presented in Table 3.1. For instance, parameters of relative volume α_s , α_w , α_a , were needed to derive the soil model (Chapter 5). The soil laboratory tests, in compliance with British Standard BS 1377 [27], are briefly described in Appendix A.

3.2 Soil strength

Soil subjected to the explosion process is subjected to shear and compression loading. Tension is not considered as soil cannot bear large tensile stresses [17]. Accordingly, this thesis explains the various technical terms and definitions used to describe soil

Table 3.5: Summary of soil description.

PARTICLE SIZE				
C – Clay	M – Silt	S – Sand	G – Gravel	
 increasing particle size				
PLASTICITY				
CL, ML	CI, MI	CH, MH	CV, MV	CE, ME
low	intermediate	high	very high	extremely high
 increasing plasticity				
CONSISTENCY				
hard	stiff	firm	soft	very soft
 increasing moisture content				
Parameters				
Bulk density	Particle density		Moisture content	

behaviour under this loading. These concepts are explained in greater detail within soil mechanics texts [24, 17, 84].

3.2.1 Stresses in soil

When discussing the concept of soil mechanics, it is necessary to introduce the concept of the following stresses. Schematically, these are shown in Figure 3.5:

Total stress, σ , acts on a plane (faces of element). Soil is assumed to be a solid material. It is an “external” stress to the soil element.

Pore water pressure, u_w , is given by the pressure in water that fills the void spaces. Pore water pressure has the same value in all directions, i.e., hydrostatic. The *water table* level is the level in which the pore water pressure is equal to atmospheric pressure, ($u_w = p_a$). The soil below the water table is fully saturated and the pore pressure depends on the depth below the water table h_w ; algebraically, $u_w = \rho g h_w$. The soil above the water table is assumed to have zero pore pressure, $u_w = 0$, although this is conservative and simplifying approach. The pore pressure is a component of internal soil structure, namely water.

Effective stress, σ^{ef} , is given by the stress existing within the mineral grain structure. It is related to the interparticle forces which can appear in two forms: (a)

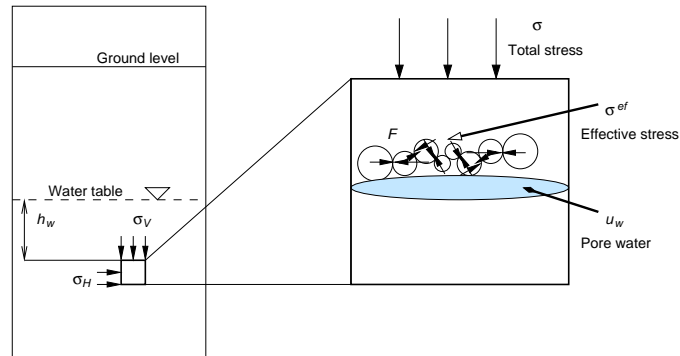


Figure 3.5: Concept of total and effective stresses in soil.

direct contact in sand, or, (b) the electrochemical forces in the clay. This principle applies only to fully saturated soil, i.e., soil below water table. Effective stress is a contributor to the total stress provided by the skeleton.

The relationship between these three stresses is captured by the following relation:

$$\text{total stress} = \text{effective stress} + \text{pore water pressure} \quad (3.9)$$

$$\sigma = \sigma^{ef} + u_w \quad (3.10)$$

3.2.2 Compressive strength

In soil mechanics, the process of soil compression is the gradual reduction of the volume in the time frame of days, months, even years. The following terms are commonly used in soil mechanics:

Compressibility is given by volume changes in a soil when subjected to pressure, compressibility parameters determine the amounts of deformation under applied stresses.

Consolidation describes the rate of volume change with time, consolidation parameters predicts the time that is needed to produce the required deformation.

Compaction is the expulsion of air from soil.

This behaviour does not sufficiently represent dynamic loading of soil subjected to explosion.

3.2.3 Shear strength

The failure of soil integrity depends on its ability of bearing shear stress. The system of stress, i.e., shear and isotropic, is resisted together by soil skeleton and pore water. As water has no shear strength, the applied shear stress is sustained solely by the soil skeleton that is manifested through the frictional interaction between the particles. The Mohr-Coulomb failure criterion expresses the relationship between frictional and cohesive elements of the soil through this relation:

$$\tau_f = c + \sigma \tan \varphi \quad (3.11)$$

where c is the *cohesion* of the soil, σ is the normal stress, φ is the *angle of friction* of the soil (for granular material $c = 0$). Equation 3.11 can be expressed in effective terms σ^{ef} , c^{ef} , φ^{ef} which correspond to properties of the soil skeleton. This relationship is graphically represented in Figure 3.6. The data from triaxial test carried out on prairie soil are used. The parameters, c_u , ϕ_u refer to soil in undrained condition. The line is the tangent to the Mohr's circles obtained using triaxial compression test data. Parameters c^{ef} , φ^{ef} are determined from the direct shear test or the triaxial compression test.

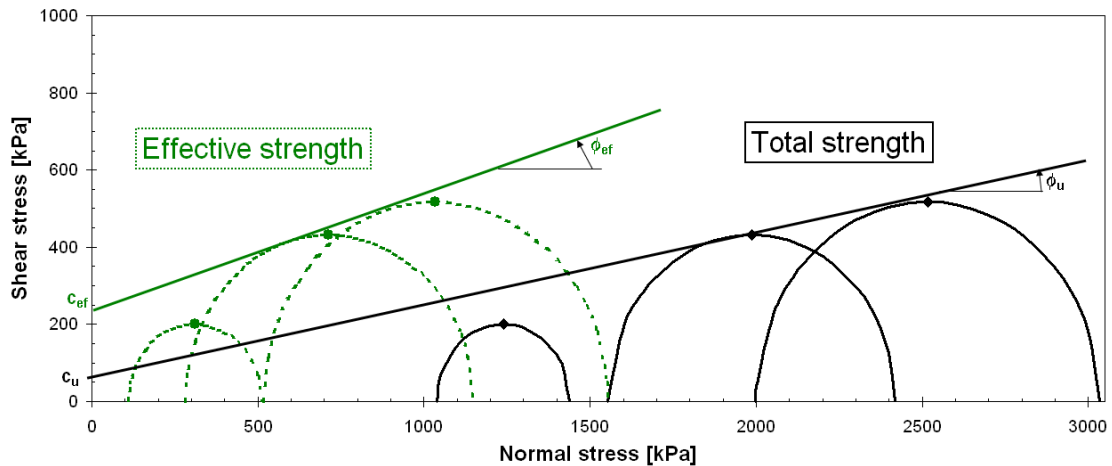


Figure 3.6: Mohr-Coulomb failure criterion applied for prairie soil triaxial data.

3.2.4 Mechanism of deformation

From Henrych [67], the mechanism of deformation in cohesive soils can be divided into two types: ① *the soil skeleton deformation*, and, ② *the deformation of all the soil phases*. At high pressures, the soil skeleton deformation is given by the plastic

deformation of bond and grain displacements. Volume compression of all soil phases plays a role in the deformation of all the soil phases. Both mechanisms are always proceeding at the same time during soil compression. From a particular point during compression, one of the mechanisms becomes dominant to such a degree that the other becomes negligible.

In dry soil, compressibility of water and air is greater than the skeleton compressibility, thus with static and dynamic loading the soil skeleton deformation ① increases and mechanism ② becomes insignificant. When pressure increases, grain bond distortion and soil compaction occur. The mechanism ② becomes more dominant and in this phase, mechanism ① becomes negligible.

In water-bearing soil subjected to slow static loading, water and air are pressed out from the voids and the mechanism ① determines soil compressibility. With a rapid dynamic loading the deformation ② becomes dominant because the compressibility of water and air is higher than the skeleton grain bonds. The solid phase compresses at high pressures.

Macroscopic deformations of sandy soils are described in Luong [87]. The main deformation mechanisms are *compaction*, *distortion* and *attrition*. In compaction mechanism, the voids are pressed out and the solid particles are nearer to one another, thus the soil bulk density increases. Distortion mechanism is characterised by sliding grains and energy dissipation by heat. In attrition mechanism, the grains are crushed under high pressure.

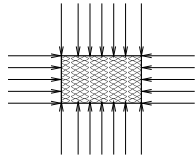
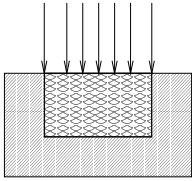
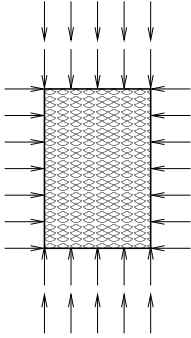
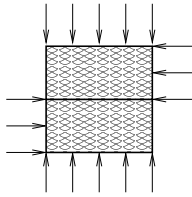
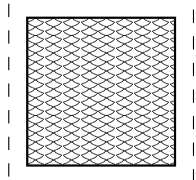
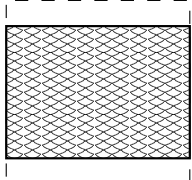
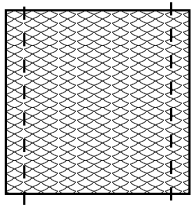
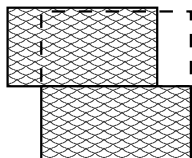
The loading of saturated cohesive soil caused by an explosion is a dynamic process where water and air are not pressed out from the voids, therefore the deformation mechanism of cohesive soil is dominated by deformation of all soil phases, mainly the water and air. This is due to the higher resistance of water and air than the skeleton particle linkages. The solid phase deformation becomes active at high pressures. In dry cohesive soil, deformation is dominated by particle linkage distortion and soil compaction. As soil naturally exhibits non-uniform distribution of soil phases and its linkage, it leads to stochastic distortion of soil. This non-homogeneity does not manifest itself in soil response where the soil mass is dominant factor.

3.3 Standard soil tests for stress-strain relationships

Soil laboratory procedures are standardised in British Standard BS-1377 [27]. These procedures are used to determine the soil mechanical properties for civil engineering purposes. From these procedures, the tests that are the most relevant to the research are briefly introduced. Table 3.6 summarises the testing mechanism and deformation. Data from these standard soil tests were used to derive a numerical

model for soil in Chapter 5.

Table 3.6: Summary of standard soil tests.

Test	Isotropic compression	One dimensional compression	Triaxial compression	Direct shear
Loading				
Deformation				
Notes		also referred as oedometer test, constrained modulus D	Friction angle and cohesion	Friction angle and cohesion in effective terms

One dimensional compression test. Other terms for this test are the *oedometer test*, the *confined compression test* and the *consolidation test*. The soil specimen is subjected to incremental vertical axial force. The soil is allowed to drain. The deflection of the soil specimen is measured and recorded with respect to time (for about 50 hours). The constrained modulus D (also termed as oedometer modulus E_{oed}) can be obtained from this test.

Direct shear test. The test consists of applying shear stress to a soil specimen at different normal stress levels. The drainage of the specimens is not controlled, i.e., the moisture content at the initial and final stages can vary. The effective values of friction angle and cohesion are determined.

Triaxial test. A cylindrical soil specimen is subjected to shear stresses by changing the principal stresses σ_1 and σ_3 . Commonly, the triaxial cell pressure σ_3 is kept constant, and the axial (vertical) stress σ_1 is increased until soil fails. The specimen is confined by the membrane in order to keep the soil water content unchanged (undrained tests) or allow water to dissipate (drained tests). Therefore, total and effective values of friction angle and cohesion can be obtained. The axial deformations for stress increments are measured.

For more details on soil tests refer to British Standard BS 1377 [27] and Appendix A for their brief description.

The whole is often more than the
sum of its parts.

— Aristotle

Chapter 4

Modelling of physical process using AUTODYN

EXPLOSIONS ARE NUMERICALLY described by a general system of differential equations. The equations consist of laws of conservation of mass, momentum, energy, supplementary equation and material models for explosive, air and soil. A supplementary equation expresses suitable detonation theory. Material models play an important role linking stress to deformation and internal energy. Fluids and gases (in the present modelling study, detonation products and air) are sufficiently modelled using an *equation of state* (EOS), which expresses a relationship between the pressure p , specific volume v and specific energy e . Additional components are needed for modelling of solids (in the presented studies, soil) because solids bear shear strength. Tables 4.1 and 4.2 present these governing and supplementary equations, respectively. These equations have to be solved simultaneously. Numerical techniques have been developed to solve these equations, such as finite difference, finite volume, finite elements [96, 113, 128, 18]. Due to the number of mathematical operations involved, software solutions are the only feasible method to provide solutions [36]. Commercial softwares are available for various applications. As shown in Table 2.1, the software AUTODYN has been used for mine explosion simulations. Therefore, AUTODYN was chosen to carry out the numerical analyses in this research. This chapter explains AUTODYN principles and features that were employed in the present studies.

Table 4.1: Governing equations: laws of conservation.

Law of conservation	Lagrangian description	Eulerian description
Mass	$\frac{d\rho}{dt} + \rho \frac{\partial v_i}{\partial x_i} = 0 \quad (4.1)$	$\frac{\partial \rho}{\partial t} + \frac{\partial(\rho v_i)}{\partial x_i} = 0 \quad (4.2)$
Momentum	$\frac{dv_i}{dt} = f_i + \frac{1}{\rho} \frac{\partial \sigma_{ij}}{\partial x_j} \quad (4.3)$	$\frac{\partial v_i}{\partial t} + v_j \frac{\partial v_i}{\partial x_j} = f_i + \frac{1}{\rho} \frac{\partial \sigma_{ij}}{\partial x_j} \quad (4.4)$
Energy	$\frac{dE}{dt} = -\frac{p}{\rho} \frac{\partial v_i}{\partial x_i} + \frac{1}{\rho} s_{ij} \dot{\epsilon}_{ij} \quad (4.5)$	$\frac{\partial E}{\partial t} + v_i \frac{\partial E}{\partial x_i} = \frac{p}{\rho^2} \left(\frac{\partial \rho}{\partial t} + v_i \frac{\partial \rho}{\partial x_i} \right) + \frac{1}{\rho} s_{ij} \dot{\epsilon}_{ij} \quad (4.6)$

Table 4.2: Supplementary equations for modelling.

Stress tensor	$\sigma_{ij} = -(p + q) + s_{ij} \quad (4.7)$
Equation of state	$p = f(\rho, e) \quad (4.8)$
Constitutive model	$\sigma_{ij} = g(\epsilon_{ij}, \dot{\epsilon}_{ij}, E, D) \quad (4.9)$
Explosion	$h(p, \rho, v, T, x, t) = 0 \quad (4.10)$

Table 4.3: Definitions and units of variables.

Symbol	Unit	Definition
t	s	Time
v	m.s ⁻¹	Velocity
x	m	displacement
D		Damage
E	J	Internal energy
p	Pa	Hydrostatic pressure
s	Pa	Deviatoric stress
T	K	Temperature
q	Pa	Pseudo-viscous pressure
GREEK		
ρ	kg.m ⁻³	Density
σ	Pa	Stress
ε	–	Strain
SUBSCRIPT		
i, j, k		
0		initial state
SUPERSCRIPIT		
dotted		Time derivative

4.1 Solution methods in AUTODYN

The software AUTODYN [32] has been developed to solve non-linear problems in dynamics, especially for large strain and deformations. Governing differential equations are derived from the laws of conservation of mass, momentum and energy (see Table 4.1). These laws are satisfied at every timestep. In addition, a constitutive law is required for material modelling that links stress to deformation and internal energy. This system of differential equation is solved in AUTODYN using a combination of finite volume, finite element and mesh free solver technologies. The solution methodology is based on explicit time integration.

Detonation of high explosive is implemented in such a way, that the fraction of explosive energy is inserted into cell at the arrival time of the detonation wave. It is recommended that the detonation wave front is spread over several cells as the burn fractions need several time steps. By this procedure, the high explosive is assumed to be completely detonated and converted into explosive products. This procedure is termed *burn on time*.

The differential equations are solved as a set of algebraical equations that are

obtained by discretization techniques. AUTODYN follows the discretization method developed by Wilkins [124] with changes in some details. This method is based on explicit central difference method which is second order accurate. For reference, finite difference formulae are presented in Table 4.4 and its geometric representation is shown in Figure 4.1. In explicit methods¹, the solution at the new time step $t + 1$ is directly computed with known quantities at a previous time step t . Explicit schemes are conditionally stable. The limitation is on the time step which has to satisfy the Courant-Friedrich-Levy (CFL) condition. The CFL condition states that the time step must be kept small enough that the information has enough time to propagate through the space discretization. In practical implementation, the CFL condition is expressed that the time step is smaller than the time taken for a sound wave to cross the smallest element, in mathematical notation:

$$\Delta t \leq \frac{kl}{c} \quad (4.11)$$

where k is the smallest mesh dimension (cell/element size), l is the stability fraction (typically 0.6 – 0.9 [96]), c is the speed of sound. In AUTODYN, the stability fraction equals 0.6666 in default. The parameter can be set in Controls → Timestep options → Safety factor.

Table 4.4: *Finite difference formulae.*

Derivative	FD	Name	Order of accuracy
$\left(\frac{\partial u}{\partial t}\right)_{t=t_i}$	$\frac{u_{i+1}-u_i}{\Delta t}$	Forward difference (Upwind scheme)	First
	$\frac{u_i-u_{i-1}}{\Delta t}$	Backward difference (Downwind scheme)	First
	$\frac{u_{i+1}-u_{i-1}}{2\Delta t}$	Central difference	Second
$\left(\frac{\partial^2 u}{\partial t^2}\right)_{t=t_i}$	$\frac{u_{i+1}-2u_i+u_{i-1}}{\Delta t^2}$	Central difference	Second

The spatial discretization in AUTODYN is on structured mesh², i.e. rectangular mesh in IJK space. Figure 4.2 depicts the mesh element and the assignment of the

¹Implicit schemes are stable, but more complex than the explicit method. In the implicit schemes, the solution at the new time step $t + 1$ is determined by coupled sets of equations that use known (t) and unknown ($t + 1$) quantities.

²AUTODYN version 6 (released during 2005) included the unstructured concept, i.e., the elements can be hexahedral, pentahedral, tetrahedral.

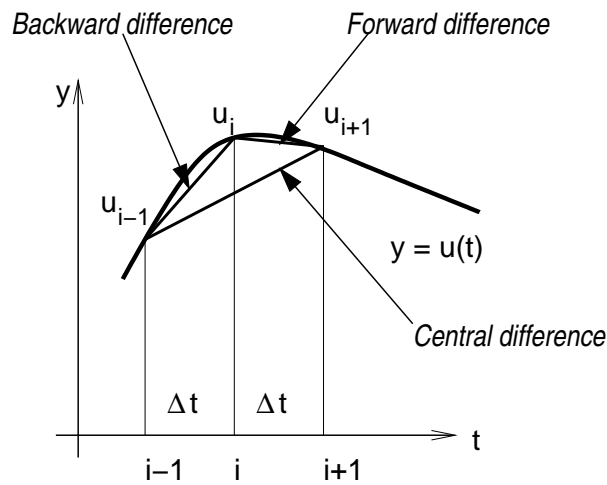


Figure 4.1: Geometric representation of the finite difference formulae for the first derivatives.

variables in element. The mesh represents the geometry of interest. The material, boundary conditions and initial conditions are assigned to a mesh.

The material deformation (the position of each particle in a continuum) can be described with respect to initial coordinates or current position of vector. The first is Lagrangian representation, the latter Eulerian. Both representations are commonly used in hydrocode. The principle of the solving the differential equations is shown on Lagrangian computation.

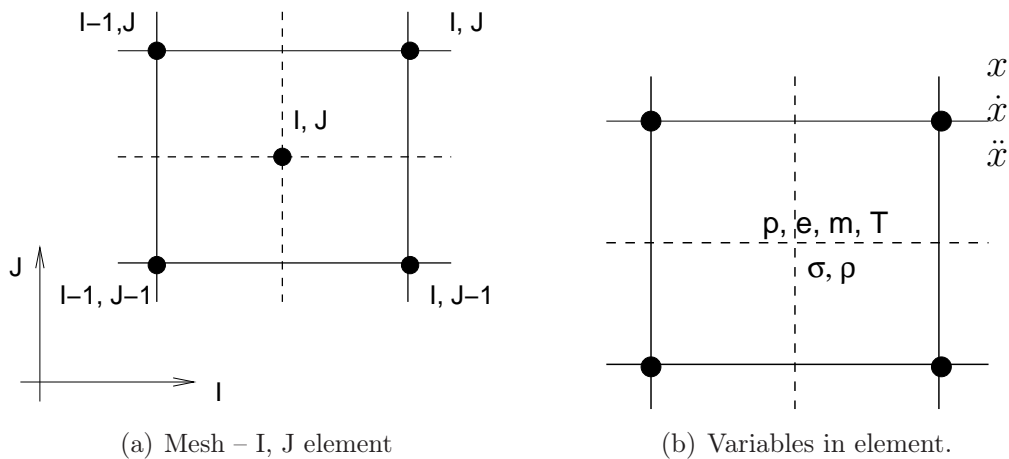


Figure 4.2: Mesh discretization from AUTODYN manual [32].

Lagrangian computation scheme

In the Lagrangian representation, material remains in the element under any deformation. In other words, material does not flow in and out. Figure 4.3 schematically represents the series of calculations computed at every timestep. In the first step, the boundary and/or interactive forces are updated and joined with the forces for inner elements that were calculated in previous timestep. Then the accelerations of the nodes are calculated using the momentum equation. Subsequently, the velocities and positions of the nodes are determined through integration. The strain rates and change in volume are calculated. Then, the pressures, stresses and energies are determined using the material model and law of conservation of energy. With application of law of conservation of momentum, the forces are calculated that are the input for the next integration cycle. The variables are defined in manner shown in Figure 4.2(b). The velocities and accelerations relate to the nodes positions, and thus these variables are defined at the nodes. Other material variables, such as pressure, stress, energy, density, mass, are defined in the centre of element.

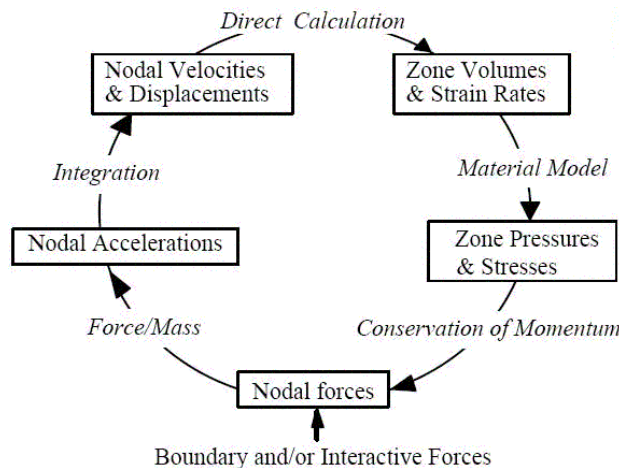


Figure 4.3: Lagrange computation scheme from AUTODYN manual [32].

Errors can occur within the calculation algorithms and the introduction of alleviative schemes (such as anti-tangle forces). This can prevent the absolute conservation of mass, momentum and energy. Therefore, the sums of mass, volume, energy and momentum are evaluated for each element at every timestep. By default, five per cent error is allowed. When the value is exceeded the calculation terminates with warning “Energy error is too large”. It is possible to increase this value at Controls → Wrapup criteria → Energy fraction. The question that is remaining “what is the tolerable error for the model?”.

4.2 Solvers

With the various structural dynamic applications, different needs arise to cover in the hydrocode. As AUTODYN tends to cover a wide spectrum of the dynamic applications, the following solvers have been implemented.

4.2.1 Lagrange solver

The Lagrangian representation keeps material in its initial element. The numerical mesh moves with the material flow velocity and distorts. There is no transport of material from element to element. This behaviour is represented in Figure 4.4(a). This approach is suitable for modelling solid materials. The Lagrange solver runs on structured IJK mesh. Elements are quadrilateral (2D) and brick-type (3D). The disadvantage of the Lagrangian representation is that the mesh highly distorts with large material movements. This can lead to inaccurate and inefficient solution, sometimes leading into termination of the calculation. Therefore the rezoning option and erosion technique are available in AUTODYN in order to simulate accurately, large deformation phenomena.

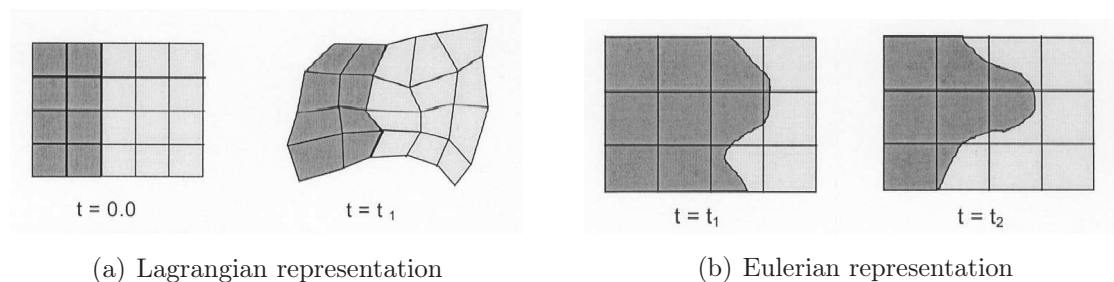


Figure 4.4: Description of solvers from AUTODYN manual [32].

4.2.2 Euler solvers

The Eulerian representation allows materials to flow from cell to cell while the structured IJK numerical mesh is spatially fixed. This is depicted in Figure 4.4(b). This treatment is suitable for modelling fluids, gases and large deformation of structural materials. Three Euler solvers are implemented in AUTODYN. The solvers use different algorithm to solve continuity equation as follows:

- **Euler** – employs the first-order upwind differencing scheme to solve continuity equation (convective transport). The implementation allows several materials

in a cell. The Euler solver is the original/oldest implementation of Euler solvers. The Euler solver is in AUTODYN-2D and 3D. The Euler solver is suitable for applications with fluid-structure interaction, as this solver can be coupled with Lagrange meshes.

- **Euler Godunov** – implements higher-order Godunov scheme with strength. This scheme is multimaterial. The Euler Godunov is implemented in AUTODYN-3D. The Euler Godunov is suitable for calculation of purely fluid and gas dynamic problems or large deformation of structural materials.
- **Euler FCT** – uses higher-order scheme which is termed *Flux-corrected transport*. This solver allows only a single material in a cell. Thus, this solver is suitable for the gas dynamic calculations. The Euler FCT is implemented in AUTODYN-3D.

The Euler solvers apply a control volume method to solve the governing conservation equations. In a control volume method, the integral equations are discretized over finite volumes. Each finite volume has a node(vertex) in the middle. The finite-difference equations are solved in two steps numerical procedures: The first step is Lagrangian step where the mesh follows the material flow and distorts. The second step is advection step where the solution is mapped from the deformed mesh back onto the initial mesh, which is spatially fixed.

The Smooth particle hydrodynamic (SPH), Arbitrary Lagrange-Euler (ALE) and Shell solvers are briefly introduced in Appendix B.

4.3 Material modelling

Material model consists of following parts:

- **Equation of state (EOS)** – expresses the relationship between the pressure p , density ρ and specific energy e . It is the hydrostatic component of the stress tensor (Equation 4.7). In hydrostatic loading, all three normal stresses are equal.
- **Strength model** – formulates material resistance to shear. This relation of transition between elastic and plastic regime is represented by yield criterion which is a function of material properties such as strain, strain rate and/or energy.

- Failure model – is introduced into material model because material cannot withstand tensile stress exceeding the tensile limit. The failure model defines the onset of fracture which can be determined by a critical variable for a flow variable (for example pressure or effective plastic strain).
- Erosion – overcomes the problem of large distortion of Lagrange grid. The element is removed from the calculation when a strain exceeds a specified limit.

In AUTODYN, several models of equation of state, strength model, as well as failure model are incorporated for various material behaviours. It is also possible to introduce user's model through custom subroutines. A new material model for granular materials (powders) – this includes soil – is now available. This model was developed for Nammo, Raufoss, Norway ³ to enable improved modelling of effects observed in physical experiments. The model consists of a Compaction equation of state and a Granular Strength model.

Compaction EOS

The compaction equation of state is described by the plastic compaction curve. This is given by the relationship between the pressure and density as a ten point piecewise linear curve. The first data set corresponds to the loose soil. The last data set corresponds to the compacted soil, i.e., theoretical maximum density. The elastic loading and unloading compaction curve is given by the density dependent bulk soundspeed as follows:

$$p = c^2(\rho) \rho. \quad (4.12)$$

Granular strength model

The nonlinear behaviour of the soil is represented by assuming that the shear modulus G is non-linearly dependent on the level of soil compaction and the yield strength is both density and pressure dependent. Thus, the yield surface is given by the relation:

$$Y = f_1(p) + f_2(\rho) \quad (4.13)$$

These assumptions are described via a ten point piecewise linear curve for (a) the pressure p and the yield stress Y , (b) the density ρ and the yield stress Y , and (c) the density ρ and the shear modulus G .

³The Medium and Large Caliber Division, <http://www.nammo.com>

4.3.1 Failure model

For onset of failure, the failure model is introduced into material model because material cannot withstand tensile stress exceeding the tensile limit. The failure models can be divided into the three categories:

- *Bulk failure* – The flow variable, namely the hydrodynamic tensile pressure or bulk strain, is set as a critical variable of material. Material is viewed as isotropic.
- *Directional failure* – As the failure can depend on the directions, the appropriate criteria are incorporated that test on principal stress or strain or on material stress or strain. These criteria enable to model delamination, spalling, plugging, petalling. This failure criterion is not applicable to Euler solver and Shell solver.
- *Damage* – This criterion covers the inelastic behaviour of material whose strength is affected by the crushing. The strength parameters, like yield, shear modulus, can be reduced with the damage as calculation proceeds. These materials are for example concrete and ceramics.

Hydro-tensile limit

The bulk failure occurs when the hydrodynamic pressure exceeds the specified limit. This criterion can be expressed as follows:

$$p > p_{min}^{tensile} = \text{const.} \quad (4.14)$$

Then, the pressure is set to zero, i.e., $p = 0$ and the internal energy is recalculated. By this procedure, the material is rehealed and can sustain negative pressure in the next time step. This criterion is simple and allows calculation to proceed for a long time. The tensile wave can propagate in the modelled system. This criterion can be suitable for modelling cavitation and spalling effects. However, it is recommended not to draw conclusions from details in the spalling and cavitated regions.

4.4 Features

The simulations presented in this thesis used other features available in AUTODYN, that are explained as follows:

Boundaries

Flow out boundary condition was used throughout the presented simulation. This condition allows material to leave computational domain, i.e., reflection is not permitted on this boundary. This boundary condition can be applied only to material employing Euler solver. Other boundary options assign the constraints for different parameters. In AUTODYN, these boundary conditions are available Stress, Velocity, Bending, Flow in, Transmit.

Gauges

Measurement points, termed **gauges** in AUTODYN, can be assigned in a model to measure the parameters at any interested point of the mesh. The gauges are spatially defined by x, y, z or I, J, K coordinates. Two types of gauges are available in AUTODYN as follows:

- Fixed gauges are “fixed” in the space, i.e. the coordinates do not change with time.
- Moving gauges are “moving” with the flow.

The parameters can be viewed in **History**. Relationships between various parameters can be graphically analysed.

Interaction

When two or more **parts** are employed in a model, **interaction** between the parts is desired. AUTODYN provides following possibilities of interaction:

- Euler-Lagrange coupling: allows the interaction between parts modelled using Euler and Lagrange solvers.
 - Automatic – This option enables to couple automatically any Euler and Lagrange solvers without assigning the polygons to the Lagrangian parts. This is a new feature in version 5 and above.
 - Polygons – Polygons must be assigned to the Lagrangian parts.
- Lagrange-Lagrange interaction: enables the interaction between parts modelled using Lagrange solver. It is possible to retain inertia of eroded nodes.

4.5 Description of materials used in simulations

Air

Since air is a gas, the strength model and the failure model are not needed. Air is sufficiently described by an equation of state. The surrounding air is assumed to be an *ideal gas* whose equation of state is in the form

$$p = (\gamma - 1)\rho e \quad (4.15)$$

where γ is the adiabatic exponent, ρ is the density of air and e is the specific internal energy. The specific internal energy of air is the function of temperature T ,

$$e = \frac{R T}{\gamma - 1} \quad (4.16)$$

where $R = 287.1 \text{ J.kg}^{-1}.\text{K}^{-1}$ is the individual gas constant, $\gamma = 1.4$ is the adiabatic exponent. For $T = 288.15 \text{ K}$ ($t = 15^\circ\text{C}$), the specific internal energy equals $206.82 \times 10^3 \text{ J.kg}^{-1}$. The parameters of air, which were inserted into models, are presented in Appendix B.

High explosive

High explosives are modelled using an equation of state for explosive products. The Jones-Wilkins-Lee, (JWL) empirical equation of state for explosive products is widely used in mine explosion calculations (see Table 2.1). It is implemented in many codes, such as LS-DYNA and AUTODYN. The JWL equation is implemented in the AUTODYN in the form given below:

$$p = A \left(1 - \frac{\omega}{R_1 V}\right) e^{-R_1 V} + B \left(1 - \frac{\omega}{R_2 V}\right) e^{-R_2 V} + \frac{\omega E}{V} \quad (4.17)$$

where A, B, R_1, R_2 and ω coefficients depend upon the composition of the explosive. The variable $V = v/v_0$ is the expansion of the explosive products and E is the detonation energy per unit volume. The values of JWL's coefficients have been derived by various authors such as Dobratz *et al.* [41], Finger *et al.* [46] and Souers *et al.* [109]. The commonly used explosives are included in AUTODYN material library. The parameters for high explosives used in simulations are given in Appendix B.

Iron

When recreating the mine impulse pendulum experiments, the target plate is made of iron. The plate serves as a “momentum trap”, i.e., to capture the momentum delivered to the plate. The stresses and deformation of the plate are not investigated. A material model for iron was taken from the AUTODYN material library. In particular, IRON-ARMCO was selected for faster computation with the linear equation of state, Johnson-Cook strength model and no failure model. The parameters of iron are presented in Appendix B.

4.6 AUTODYN procedure to setup a model

The two-step procedure (when the plate is also incorporated in latter study) is depicted in Figure 4.5. The description is given as follows. It is noted that this – “**Materials**” – represents the button(tab) which is in AUTODYN.

1st step

1. **Materials**
 Retrieve materials from the AUTODYN library by pressing **Load**. Create a **New** material when the numbers are manually filled to chosen type of EOS, strength model and failure model. The material properties can be modified in **Modify**.
 ◇ *In the MIP study:* air, C-4/TNT, sand, prairie soil (manually inserted)
2. **Boundaries**
 Creating a boundary option, which in the later step is applied to the computational domain.
 ◇ *In the MIP study:* Flow out
3. **Parts**
 Define the solver of the part and determine the geometry and mesh of the part.
 - **New** – create a new part, choose solver (Euler), Define geometry - Box, and size of the cells (Mesh grading is possible in x, y -axis directions).
 - **Fill** with material (in xy coordinate or IJ).
 - **Boundary** – assign boundary condition to the computational domain.
 - **Gauges** – insert measurement points in the area of interest.
 ◇ *In the MIP study:* at 400 mm distance above the ground – this distance is the position of bottom of the plate.
4. **Detonation**
 set the detonation **Point** – give x and y coordinates of explosion initiation. Limit range of application – include region where the HE is located in IJ coordinates.
5. **Controls**

- Wrapup criteria terminates calculation at either time or cycle limit.
 - ◇ *In the MIP study*: 0.3 to 0.8 ms according to mine deployment
 - Gravity can be set to x and y axis.
6. **Output**
Define refreshment and saving of file in increment of time or cycles.
- 2nd step**
7. **Materials**
Retrieve material from library.
 - ◇ *In the MIP study*: Iron-ARMCO
8. **Parts**
Create a new part: *Plate* using Lagrange solver. Define box geometry. In **Activation** set time when the pressure wave reaches the location of the plate. This is read from the history file for 1st step.
9. **Interaction**
Select Automatic option in Euler/Lagrange tab.
10. **Controls**
Wrapup criteria are changed to terminate the calculation at either time or cycle limit.
 - ◇ *In the MIP study*: about 30 ms according to deployment

4.7 Summary

- ◆ The numerical tool used in this research was explained.
- ◆ The procedure of setting-up the model in AUTODYN was presented.
- ◆ For more details on topics other than those discussed here, refer to AUTODYN manuals.

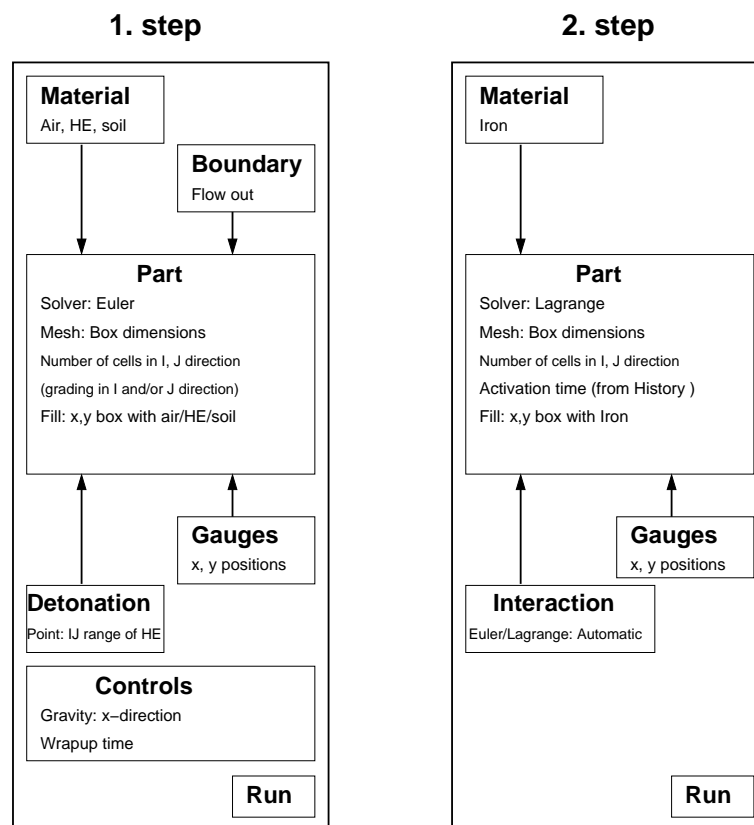


Figure 4.5: Setting models in AUTODYN: a two-step procedure for MIP models.

The road to wisdom is plain and simple to express:
Err and err and err again, but less and less and less.

— Piet Hein (1905-1996)

Chapter 5

Soil model derivation

FROM THE PREVIOUS Chapters, it is clear that several types of soil exist and different properties are held by soil, and the moisture content influences the magnitude of the explosion loading. Recall that, there exists a sand model derived by Laine *et al.* [82] for sand with 6.57% moisture content. There is no procedure, so far, on extending this model for different moisture contents. In addition, there is no model for cohesive soil. This shortcoming is addressed in this thesis. The novelty of the thesis is to derive a soil model that incorporates the various soil compositions, in particular, moisture content.

Numerical simulation of the explosion of a mine buried in soil should be reliable and extensible. This requirement brings the necessity of two sets of experiments:

- *Soil properties* – for deriving numerical model of soil. This includes determining soil description and mechanical properties.
- *Explosion experiments* – for validation of the numerical results. The explosion experiments need to investigate the explosion loading as a function of soil conditions.

For deriving the soil model we need to know the soil properties, which are generally determined through laboratory tests. As this can be performed by any commercial soil laboratory (for civil engineering) the laboratory tests should preferably be standard ones. The standard tests are cost effective as they do not require any special equipment and devices (as opposed to [14, 51, 82]). In addition, soil testing can be conducted worldwide in adherence to the same quality standards. The standard laboratory procedures for soil testing are described in BS 1377 [27]. The

relevant laboratory methods are briefly presented in Chapter 3 and Appendix A. At an early stage of the research, there was collaboration to perform soil experiments in the soil laboratory at Brno University of Technology, The Czech republic, as they are an accredited laboratory, with excellent facilities. This turned out to be beneficial, as a unique collection of soil properties data (Vrtek [119]) was obtained. This report is a collection of more than 3,000 experiments performed in compliance with Czech standards ČSN (equivalent to British standard BS). Data are presented in Section 5.1.

For validating the numerical results, experiments need to evaluate the loading caused by the explosion of a charge buried in cohesive soil. The measuring techniques need to be able to capture the contribution of soil towards the loading. In addition, consistency in setup and measuring the soil parameters, for each trial, all play an important role. Survey of existing literature has yielded the experimental work by Bergeron *et al.* [19] describing the Mine Impulse Pendulum (MIP). Very briefly, this work deals with the mine explosion in a manner that is relevant to the present research. Here, a horizontal ballistic pendulum measures the effective impulse transfer from a landmine explosion as a function of soil conditions, geometry and explosive. Trials were carried out on cohesive soil (referred to as *prairie soil*). Therefore, DRDC-Suffield, Canada was contacted by the author in order to obtain the experimental results. Besides the experimental explosion data, reports on soil laboratory tests were received for this research purpose. The explosion experiments are described in Chapter 6, Section 6.3. Soil properties data of prairie soil are presented in Section 5.2.

MIP explosion data and soil properties from the experiments make the modelling reliable as well as relevant to the physical conditions of the process, in every aspect. Thus, a methodology was derived for developing the numerical model of prairie soil that allows moisture content to be varied. These modelling principles were then extended to develop a *sand model*. This demonstrated the extensibility of the present approach, i.e., cohesive and cohesionless soil were analysed using the same methodology. These modelling ideas are examined and validated in Chapter 7, Section 7.3. The modelling methodology as well as preliminary results were published at the *7th International Conference on Shock and Impact Loads on Structures* [49].

To summarise:

- Soil properties data – presenting experimental data used for soil modelling:
 - Statistical soil data in Section 5.1,
 - Prairie soil properties in Section 5.2.

- Soil modelling – deriving models for soil with varying moisture content:
 - Prairie soil model in Section 5.3,
 - Sand model in Section 5.4.

5.1 Statistical soil properties data

The report by Vrtek [119] is a personal endeavor of Mr. František Vrtek summarising his 38-year expertise and knowledge working in engineering geology. This report, of which few copies exist, was handed out personally by the author to his colleagues in industry and academia. Data were collected from over 3,000 laboratory tests. Tests were conducted in compliance with the Czech standards series ČSN 72 10 (equivalent to BS 1377). Data are organised with respect to soil type as follows:

- clays of different plasticity (CL, CI, CH, CV, CE),
- silts of different plasticity (ML, MI, MH, MV, ME),
- sands and gravels of different particle size.

Soil groups are further subdivided into:

- silts and clays for different consistencies – **soft**, **soft-firm**, **firm**, **firm-stiff**, **stiff**. Consistency is related to the moisture content. That makes 25 types of clay and 25 types of silt.
- sand and gravel for **damp** and **wet**, and different compaction degree – **loose**, **medium compact**, **compact**.

For each group, the report presents the following physico-mechanical parameters:

- Bulk density,
- Friction angle and cohesion, undrained and effective values, and
- Oedometric modulus¹ for stresses of 100, 200 and 300 kPa, respectively.

The parameters presented are the average, minimum and maximum measured values. Table 5.1 represents data for clay of low plasticity (CL).

¹Also termed as constrained modulus, D . The modulus is obtained from one dimensional confined compression test.

Table 5.1: *Properties for clay with low plasticity (CL), after Vrtek [119].*

		Density	Friction	Cohesion	E_{oed} for		
		ρ	angle φ_u	c_u	100	200	300
		[kg.m ⁻³]	[°]	[kPa]	[kPa]	[kPa]	[kPa]
SOFT	minimum	1,799	0	7	1,100	2,900	5,200
	average	1,983	3	24	3,800	5,300	8,100
	maximum	2,111	4	38	6,300	8,600	12,000
SOFT-FIRM	minimum	1,414	0	16	1,700	2,600	6,200
	average	2,021	3	33	3,900	6,300	9,100
	maximum	2,225	9	48	7,500	11,700	13,000
FIRM	minimum	1,668	0	21	2,000	4,000	4,500
	average	1,999	9	50	4,300	7,000	10,600
	maximum	2,235	29	104	7,800	11,100	30,000
FIRM-STIFF	minimum	1,696	3	27	2,800	3,400	4,900
	average	2,003	14	62	6,400	9,100	12,800
	maximum	2,198	26	153	13,100	16,600	23,000
STIFF	minimum	1,508	14	10	2,400	4,400	5,100
	average	1,921	26	67	6,400	9,700	11,300
	maximum	2,203	35	130	14,800	14,800	17,400

Soil mixture. The presented experimental data are for basic types of soils. However, a variety of soils can be found in nature. These soils are combinations of the basic soil types (eg. a sandy silt, silty sand) and their properties can be derived. The soil mixture properties cannot be determined correctly by laboratory procedures. For instance, a triaxial test is conducted for soil particle size less than 4 mm and thus the gravel and coarse sand phase is taken out and does not contribute to the soil parameters. Therefore, several mixture theories have been developed. In the report by Vrtek [119], the mixture theory is consistent with the collected data and has been verified in practice.

5.2 Properties of prairie soil

Prairie soil forms the research interest because prairie soil is cohesive and no models exist for cohesive soil. We have experiment data for validation purposes, on account of the MIP tests being conducted in prairie soil. The experiments themselves investigated the effect of the soil condition on the magnitude of impulse delivered. Bulk density and moisture content were measured for each soil trial. Moisture content ranged from 7.7% to 28.7%. Several tests, including triaxial and consolidation tests, were performed on a prairie soil sample. This section outlines the prairie soil

properties as presented in [4, 6, 5]. Appendix D gives detail of the soil properties obtained from different laboratory soil tests.

Description. The prairie soil is described as a sandy, silty, low plastic, brown clay containing roots².

Particle size distribution. Sieve analysis showed 100% of particles passing at 10 mm sieve size and 45% passing at 0.08 mm. This means that the sample was roughly 45% fine soil, i.e., silt and clay.

Physical properties. For each soil trial, bulk density and moisture content were determined. From the bulk density and moisture content it can be calculated relative volume of each phase, i.e. $\alpha_s + \alpha_w + \alpha_a = 1$, where s, w, a denote the solid, water and air phase, respectively. The relative volume is determined using equations given in Table 3.1. Figure 5.1 shows the relative volume for each MIP trial. Solid particle density was 2680 kg.m⁻³.

Mechanical properties.

- *Triaxial undrained tests* – were carried out on three specimens of 14.6, 18.3 and 17.1% moisture content, respectively. The triaxial test determined the cohesion and friction angle³. Mohr’s circles are used to determine these parameters. Appendix D presents the procedure in detail. Figure 5.3 depicts the Mohr’s circles.
- *One dimensional consolidation test* (Oedometer) – one sample having 13.6% moisture content was tested. This test determines the oedometric modulus and compression parameters with respect to time (several hours/days). These test data were not used in soil model derivation as water was allowed to drain. This condition does not correspond with the soil behaviour under the explosion process.
- *Direct shear test* determined the effective cohesion and effective friction angle. These test data were not used in soil model derivation as the total cohesion and

²Although description states the soil is categorised as low plasticity, the Atterberg limits were not determined to support this observation.

³These parameters correspond to the total stress (including pore water pressure). Therefore, they should be correctly termed as *total* or *undrained*. *Effective* parameters describe the properties of soil skeleton.

total friction angle shall be used to represent soil behaviour under undrained condition, that occurs during explosion process.

5.3 Deriving model for prairie soil

In the previous sections, the properties of prairie soil and statistical data of soil, have been laid out. In this section, information from the preceding sections is used to develop a numerical model for a cohesive type of soil, i.e., *prairie soil*. These modelling ideas are tested and validated in Chapter 7, Section 7.3.

Recall from Chapter 4 that in order to be able to model soil as an entity, the following relations are necessary:

- *Equation of state* – describing hydrostatic behaviour,
- *Strength model* – characterising the resistance to shear stress,
- *Failure model* – defining the onset of fracture.

After analysing the existing modelling components in AUTODYN, it was concluded that the following AUTODYN features represent cohesive soil behaviour from the soil mechanics standpoint⁴:

- Equation of state: **Compaction**,
- Strength model: **Granular**,
- Failure model: **Hydro-tensile limit**.

The derivation of the soil model has been an iterative process. The main difficulty was to find the way in which to extend the prairie soil laboratory data to different moisture contents. It will be recalled, that triaxial tests were carried out for three specimens having 14.6, 18.3 and 17.1% moisture content. A soil model is required ranging from 7.7% to 28.7% moisture content in order to be able to validate the numerical results with the mine impulse experiments. The statistical data [119] have been included into modelling. One challenge was to incorporate all this isolated information so that it forms a coherent modelling methodology that can be applied for any soil in the future.

⁴In addition, the sand model derived by Laine *et al.* [82] uses the same AUTODYN features.

5.3.1 Equation of state: Compaction

The EOS Compaction is described by a plastic compaction curve, which is given as a piecewise linear curve with ten points, namely density as a function of pressure, i.e., $\rho = f(p)$. In addition, the elastic loading and unloading compaction curve is given by the density dependent bulk soundspeed, i.e., $\rho = f(v_c)$. Material is compacted to the reference density ρ_{ref} , which corresponds to the solid particle density. Thus, the following relationships are needed:

$$\rho = f(p) \quad (5.1)$$

$$\rho = f(v_c) \quad (5.2)$$

A. EOS: Pressure vs. density relationship

In this work, the approach presented in Henrych [67] was adopted. Soil is a three-phase medium consisting of solid particles, water and air; the EOS reflects this variation in the soil composition in principle as follows:

$$\text{EOS} = \alpha_s \text{EOS}_s + \alpha_w \text{EOS}_w + \alpha_a \text{EOS}_a \quad (5.3)$$

where subscripts s , w , a denote the solid particles, water and air, respectively, and α is the relative volume of the relevant phase. Thus, innumerable variations of soil composition can be modelled with this approach. This is important because it was observed within the MIP data that it is possible to achieve different phase ratios for soil for the same moisture content. Another issue that is also worth mentioning is that moisture content alone does not determine the phase ratio of soil. Figure 5.1 shows the phase ratios of prairie soil for triaxial data specimens and MIP specimens. Thus, by using Henrych's relation, one can work with soil properties derived from experiments, and still gain insight into the phase ratio for that experiment.

For air, the equation of state EOS_a was considered in an adiabatic form:

$$p = p_0 \left(\frac{V_{a0}}{V_a} \right)^{k_a} = p_0 \left(\frac{\rho_a}{\rho_{a0}} \right)^{k_a} \quad (5.4)$$

where p_0 is the atmospheric pressure, ρ_{a0} is the density of air at atmospheric pressure, ρ_a is the density of air at the pressure p and k_a is the adiabatic coefficient. ($p_0 = 101.3 \text{ kPa}$, $\rho_{a0} = 1.2255 \text{ kg.m}^{-3}$, $k_a = 1.4$).

For water, the equation of state EOS_w was taken from Henrych in the form:

$$p = p_0 + \frac{\rho_{w0} c_{w0}^2}{k_w} \left[\left(\frac{\rho_w}{\rho_{w0}} \right)^{k_w} - 1 \right] \quad (5.5)$$

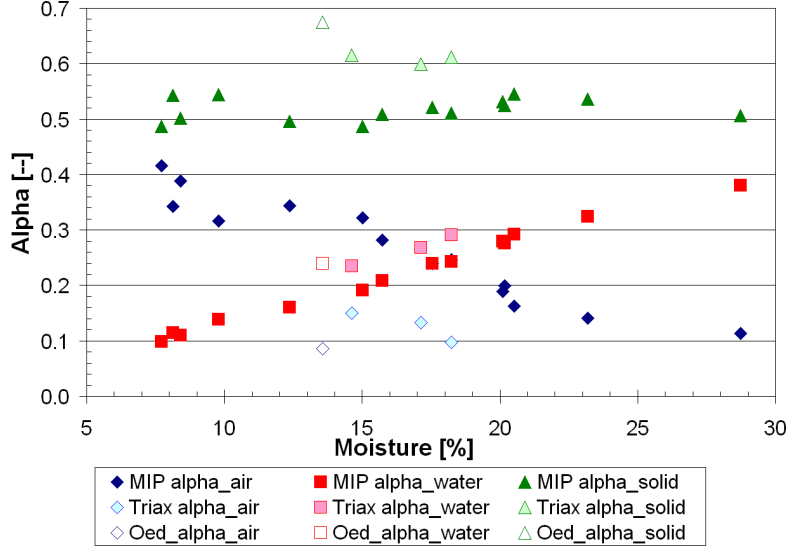


Figure 5.1: The composition of prairie soil at the initial stage - MIP trials, triaxial test and oedometer test specimen.

where p_0 is the atmospheric pressure, ρ_{w0} is the density of water at atmospheric pressure, ρ_w is the density of water at the pressure p , c_{w0} is the speed of sound at atmospheric pressure condition, and k_w is the exponent. ($p_0 = 101.3 \text{ kPa}$, $\rho_{w0} = 1000 \text{ kg.m}^{-3}$, $c_{w0} = 1415 \text{ m.s}^{-1}$, $k_w = 3$).

Let subscript 0 denote the parameters at the initial stage (before compression). Then, the following relationship is valid:

$$\alpha_{s0} + \alpha_{w0} + \alpha_{a0} = 1 \quad (5.6)$$

where the relative volume, for example, of air is given as

$$\alpha_{a0} = \frac{V_{a0}}{V_0} \quad (5.7)$$

where V_0 is the total volume of soil, i.e. $V_0 = V_{s0} + V_{w0} + V_{a0}$.

At the pressure p , the relative volumes of soil phases are defined with respect to the initial total volume (Henrych [67]), i.e., for air:

$$\alpha_{ap} = \frac{V_a}{V_0}. \quad (5.8)$$

As the soil phases compress at a different rate, their relative volume at pressure p is changed from their initial values at the atmospheric pressure p_0 . Substituting

Equations 5.7 and 5.8 and applying the law of conservation of mass, Equation 5.4 can be rewritten as

$$\frac{p}{p_0} = \left(\frac{\frac{\alpha_{a0}}{\rho_0}}{\frac{\alpha_{ap}}{\rho_0}} \right)^{k_a} \quad (5.9)$$

Rearranging, the relative volume of air changes with pressure as follows:

$$\alpha_{ap} = \alpha_{a0} \left(\frac{p}{p_0} \right)^{-1/k_a} \quad (5.10)$$

Similar to Equation 5.10, the relative volume of water changes with pressure as follows:

$$\alpha_{wp} = \alpha_{w0} \left(\frac{p - p_0}{\rho_{w0} c_{w0}^2} k_w + 1 \right)^{-1/k_w} \quad (5.11)$$

As soil is composed of the sum of relative volume of all phases, it can be written (using similar principles as Equation 5.8) as:

$$\alpha_{sp} + \alpha_{wp} + \alpha_{ap} = \frac{V_s}{V_0} + \frac{V_w}{V_0} + \frac{V_a}{V_0} = \frac{V}{V_0} \quad (5.12)$$

Applying the law of conservation of mass, the density of a three-phase medium at pressure p is now given by:

$$\rho = \frac{\rho_0}{\alpha_{sp} + \alpha_{wp} + \alpha_{ap}} \quad (5.13)$$

α_{ap} and α_{wp} can be substituted from Equations 5.10 and 5.11. Thus Equation 5.13 expresses the relation between the pressure and the soil density.

The equation of solid phase shall be particular for the soil properties (given by the location and soil nature). Therefore the EOS_s is determined using the laboratory data. Derivation of α_{sp} is discussed in subsequent sections. As presented in Section 5.2, two sets of test were performed on the prairie soil (i) undrained triaxial test, and (ii) one-dimensional compression test. The undrained triaxial test represents the explosion loading of soil more accurately than the one-dimensional compression test, as during the explosion process there is no time for water drainage compared to the oedometer test procedure where the water is allowed to drain. Thus the triaxial data are used to derive the solid phase EOS.

Solid phase EOS derived from triaxial test data

For the solid phase, the equation of state EOS_s was derived using triaxial test data. Triaxial data are presented in Table 5.2 where total stress and density are measured

Table 5.2: Data from triaxial tests used to determine the equation of state for the solid phase.

Specimen No.	Total stress	Bulk density	α_{ap}	α_{wp}	α_{sp}
	[kPa]	[kg.m ⁻³]	Eq. 5.10 [-]	Eq. 5.11 [-]	Eq. 5.14 [-]
1	101.3	1841.0	0.165712	0.235081	0.599206
	1439.3	2062.7	0.024895	0.235081	0.632543
2	101.3	1887.5	0.112691	0.291960	0.595348
	2418.5	2062.7	0.011686	0.291960	0.611418
3	101.3	1832.2	0.148230	0.268201	0.583569
	3033.4	2097.4	0.013074	0.268201	0.592283

parameters and respective α_p were calculated in the following manner. The relative volumes of water and air, α_{wp} , α_{ap} were calculated using their respective Equations 5.10 and 5.11. The remaining was attributed to the solid phase, as in Equation 5.13 α_{sp} is unknown, and therefore can be calculated as follows:

$$\alpha_{sp} = \frac{\rho_0}{\rho} - \alpha_{wp} - \alpha_{ap} \quad (5.14)$$

The obtained values of α_s were plotted and the curve of the form

$$\frac{\alpha_{sp}}{\alpha_{s0}} = C (p - p_0)^{k_s} \quad (5.15)$$

was fitted through the calculated points. For the prairie soil, the equation is

$$\frac{\alpha_{sp}}{\alpha_{s0}} = 1.514347 (p - p_0)^{-0.050123} \quad (5.16)$$

This function was used to calculate the compression of solid phase throughout the numerical simulations, i.e. for the high pressure region as well. As data for high pressure region are not available, this extrapolation was used and implemented into soil modelling. The simulation results presented in Chapter 7 demonstrate the feasibility of this approach.

It is noted that at low pressure the relative volume of solid phase increased, this can be attributed to (i) the phenomenon of clay swelling in the triaxial tests⁵, (ii) the loading is resisted by the particle linkage (see Chapter 3).

⁵Personal discussion with Assoc. Prof. Pruska, PhD, Technical University, Prague.

B. EOS: Density vs soundspeed relationship

Assuming isotropic material, the velocity of wave propagation (soundspeed) is defined as follows:

$$v = \sqrt{v_L^2 - \frac{4}{3}v_S^2} \quad (5.17)$$

where v_L is the longitudinal (bulk) component of velocity, and v_S is the shear component of velocity. The velocity components are given (after Horák [71]):

$$v_L = \sqrt{\frac{3 K (1 - \nu)}{\rho (1 + \nu)}} \quad (5.18)$$

$$v_S = \sqrt{\frac{G}{\rho}} \quad (5.19)$$

where K is the bulk modulus, G is the shear modulus, and ν is the Poisson's ratio. These moduli are derived in the next section. The Equations 5.17, 5.18 and 5.19 give the density vs soundspeed relationship, as demonstrated in Appendix E.

It is noted that the calculated velocity is lower than velocity of earthquake (wave) propagation presented in [117]. The reason for this discrepancy is explained in Section 5.4.2.

Closure

With this procedure, the input parameters for the **Compaction EOS** in AUTODYN are obtained. The **Compaction EOS** consists of piecewise linear relationships between density and pressure and between density and sound speed. The equations of state for prairie soil are illustrated for soil having 7.7, 15 and 28.7% moisture content in Figure 5.2. The pressure-density curves, obtained from this calculation, correspond with the soil behaviour. Dry soil is more compressible than wet soil. This is represented by slowly rising curve in the low pressure area. In contrast, the curve of wet soil is steep from the beginning.

5.3.2 Strength model: Granular

The **Granular** strength model consists of following relationships:

- Yield surface is dependent on the pressure p and density ρ as follows: $Y = f_1(p) + f_2(\rho)$. This is inserted into AUTODYN as piecewise linear curves with ten points of (i) the pressure p and the yield stress Y , and (ii) the density ρ and the yield stress Y ,

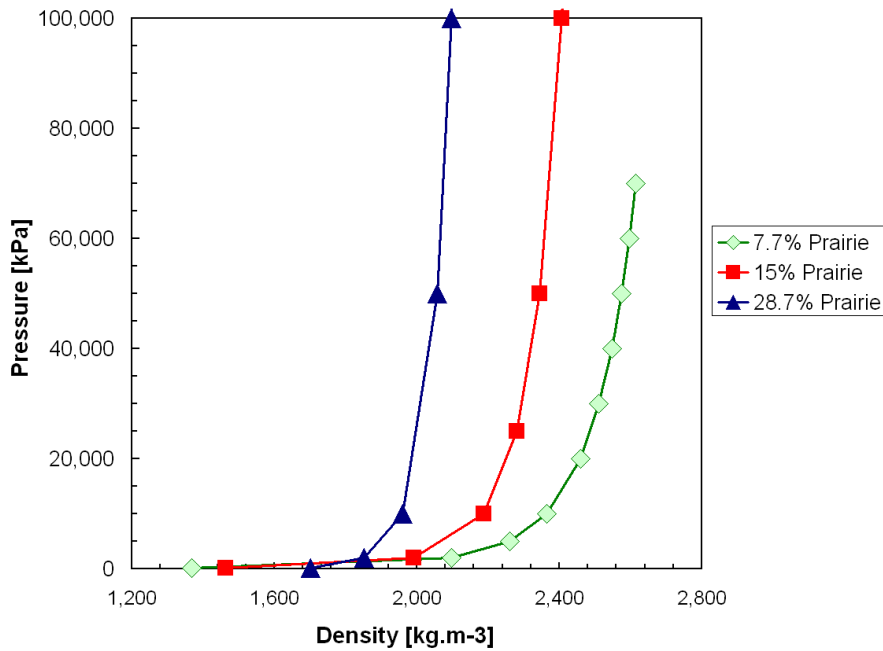


Figure 5.2: Equations of state for prairie soil having 7.7, 15 and 28.7% moisture content.

○ The shear modulus G is dependent on the density ρ .

In soil mechanics widely used Mohr-Coulomb yield criterion (Equation 3.11) was adapted to determine the yield surface. The Mohr-Coulomb criterion expresses the relationship between frictional and cohesive properties of soil by the equation:

$$Y = c + p \tan \phi$$

where c is the cohesion, p is the normal stress, ϕ is the angle of friction. The values of cohesion and friction angle can be obtained from the triaxial tests; this criterion is graphically represented by the tangent line to the Mohr's circles. The procedure of derivation is described in Appendix D.

Figure 5.3 depicts the Mohr's circles for prairie soil. The cohesion obtained from triaxial tests was negative (see dashed line in Figure 5.3), which is not feasible. Because the relationships of cohesion and friction angle with respect to soil composition are needed to determine the yield surface, the statistical soil data obtained from triaxial tests [119] were consulted. It was observed that the friction angle depends on the void ratio; the amount of probable contacts among the solid particles determines the friction properties. Figure 5.4(a) depicts this relationship for statistical data of the same particle distribution as the prairie soil (sandy clay with low

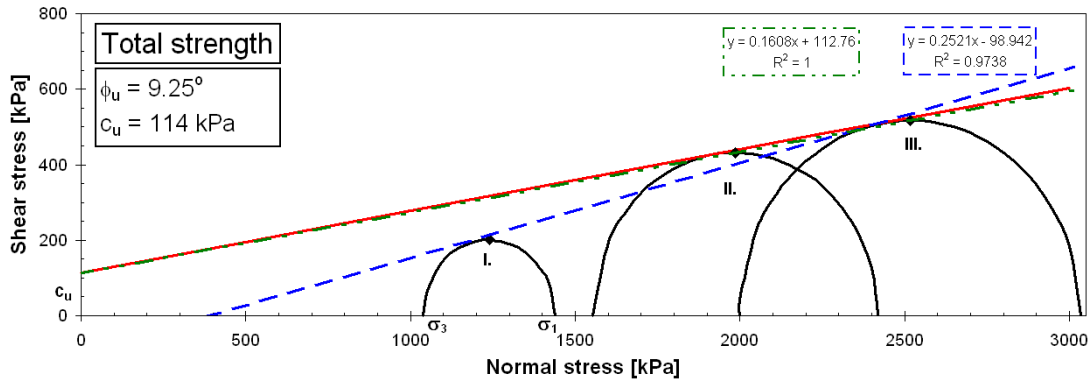


Figure 5.3: Triaxial test results for prairie soil (Mohr's circle). Dashed line: all three tests included, cohesion is negative. Solid line: the first circle omitted, $\phi = 9.25^\circ$, $c = 114$ kPa (for $w = 17.6\%$).

and intermediate plasticity, abbreviated as CLS and CIS, respectively) and incorporates values for MIP and triaxial samples. It will be observed, that the friction angle determined from triaxial test of prairie soil coincides with the observed trend. Simulation began with the minimum values of cohesion and friction angle from statistical data (see Figure 5.4); the influence of these parameters (yield surface) on the soil behaviour was found by adopting the maximum values from the statistical soil data. For instance, Figure 5.5 shows the difference in yield surface for soil having 15% moisture content. It can be observed, that the change in cohesion does not significantly vary the yield surface. Conversely, the friction angle considerably changes the yield surface.

Shear modulus was determined using an EOS from which the bulk modulus K was calculated as follows:

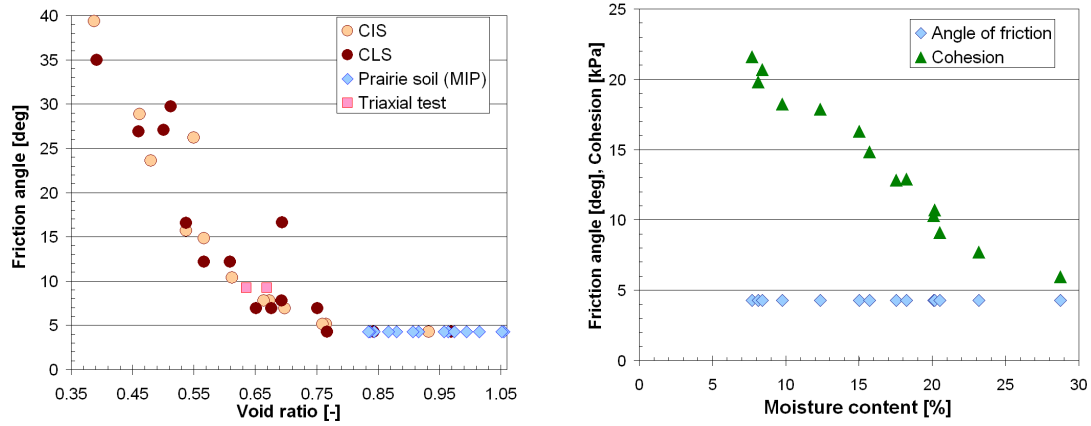
$$K = \frac{\sigma_2 - \sigma_1}{\varepsilon_2 - \varepsilon_1} \quad (5.20)$$

Then, the shear modulus G can be obtained as follows:

$$G = K \frac{3}{2} \frac{1 - 2\nu}{1 + \nu} \quad (5.21)$$

where ν is the Poisson's ratio. This is another parameter needed to be determined.

Poisson's ratio is defined as the ratio of transverse strain to longitudinal strain of solid specimen. This ratio determines the compressibility of the material, as materials can be compressible or incompressible. The Czech standard ČSN assigns Poisson's ratio to be 0.35 for fine soil. Fine soil is of wide grouping and its consistency (moisture content) is not taken into account. In [84, 100], it is presented that soil in undrained condition behaves like incompressible material. That is represented by



(a) Relationship of friction angle with respect to void ratio.

(b) Friction angle and cohesion for prairie soil.

Figure 5.4: Strength model: Yield surface parameters varying with moisture content.

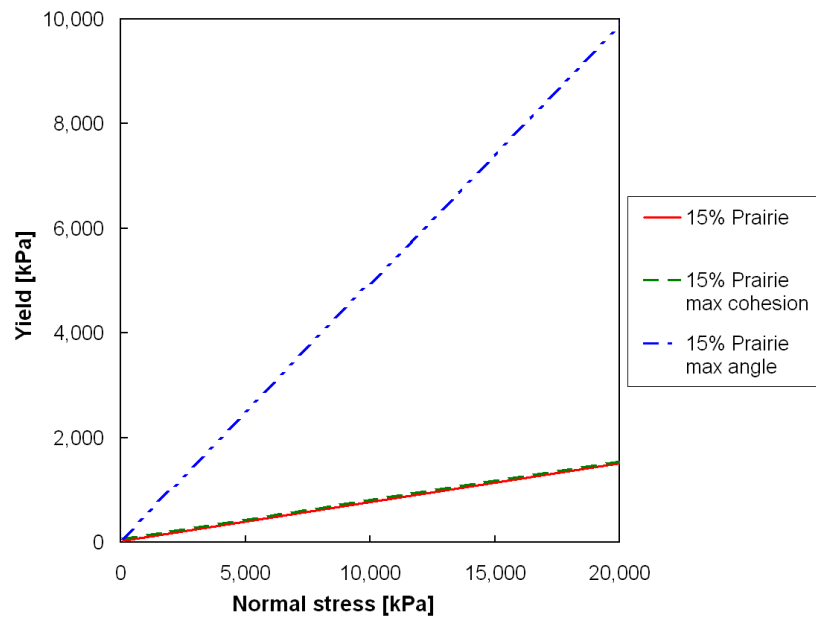


Figure 5.5: Variation of yield surface for prairie soil having 15% moisture content.

Poisson's ratio as:

$$\nu = 0.499 \quad (5.22)$$

From the literature [100, 67], it was observed, that Poisson's ratio varies from 0.2 to 0.45 where the first value is for dry soil and the latter for wet soil. These values indicate that the Poisson's ratio for soil relates to the moisture content, but there is no relationship representing this. Therefore, it was proceeded to derive this relationship.

Since water is commonly treated as an incompressible material and air is easily compressible, it was assumed that $\nu_w = 0.4999$ and $\nu_a = 0.0001$ for *computational purposes only*. This led to the reasoning that the overall compressibility of soil is given by the sum of the compressibility of respective soil phases. Algebraically,

$$\nu = \nu_s \alpha_{s0} + \nu_w \alpha_{w0} + \nu_a \alpha_{a0} \quad (5.23)$$

where subscripts s , w , a denote the solid particles, water and air, respectively, and α_0 is the relative volume of the relevant phase in the initial stage. The Poisson's ratio for solid particle was assumed to range from 0.25 to 0.35, as these values represents the rock and dense soil properties [84, 66]. Thus, Equation 5.23 can be rewritten as:

$$\nu = (0.25 \text{ to } 0.35) \alpha_{s0} + 0.4999 \alpha_{w0} + 0.0001 \alpha_{a0} \quad (5.24)$$

This equation gives the Poisson's ratio corresponding to values found in literature. For prairie soil, the Poisson's ratio varies between 0.2196 and 0.3670.

Closure

With this procedure, the input parameters for Granular strength model in AUTODYN were obtained. The Granular strength model for prairie soil consists of piecewise linear relationships of pressure vs yield surface, and shear modulus vs density. The parameters were derived using the data from standard soil laboratory tests. A parametric study of yield surface and Poisson's ratio was performed in numerical simulations.

5.3.3 Failure model: Hydro-tensile criterion

The tensile stress that a material can sustain determines the failure model. As soil cannot sustain large tensile stresses [17], the Hydro-tensile criterion was used with this limit:

$$p_{MIN} = -c \quad (5.25)$$

where c is the cohesion. The underlying idea is that failure occurs when soil cohesion turns negative, i.e. no longer sticking. The effect of the value of tensile limit was analysed in numerical simulations by progressively decreasing the cohesion values from Eq. 5.25.

5.3.4 Concluding remarks on prairie soil modelling

In this Chapter, a methodology was proposed for an extensible numerical soil model and was applied for prairie soil. The following parameters were examined in Chapter 7 to ascertain their effect on overall soil behaviour under explosion loading:

- Poisson's ratio,
 - Compressible soil: $\nu = f(\alpha_{s0}, \alpha_{w0}, \alpha_{a0})$ as given in Equation 5.24,
 - Incompressible soil: $\nu = 0.499$.
- Yield surface:
 - friction angle – maximum value from statistical soil data [119],
 - cohesion – maximum value from statistical soil data,
 - friction angle and cohesion obtained from triaxial test data; these parameters correspond to prairie soil having 17.5% moisture content.
- Hydro-tensile limit:
 - $p_{MIN} = -c$
 - $p_{MIN} = 0$
 - $p_{MIN} = -5c$

The model is validated in Chapter 7, Section 7.3. Appendix E summarises the relations used during derivation and presents examples.

5.4 Deriving model for sand

The methodology that was presented above is now applied, to derive a numerical model of sand (cohesionless soil). Since the mechanical properties of sand (in which MIP experiments were carried out) are not available, the derivation is based on data of Laine's sand model. Therefore, the sand model derived by Laine *et al.* [82] is briefly presented and subsequently, a model is derived for sand having the same moisture content as Laine's. The sand model is extended for sand with varying moisture content using the statistical soil data [119].

5.4.1 Laine's sand model

The sand model (Laine *et al.* [82]) was derived for sand having 6.57% moisture content. Laine's sand model employs the same AUTODYN features as are used in the prairie soil model. The model was derived using the triaxial cell test *bender elements* that allowed the measurement of wave velocities in the sand specimen. A brief description of the sand model is presented below:

Equation of state: **Compaction**

Pressure vs density, $p = f(\rho)$, was derived from the triaxial test data. Relationship density vs soundspeed, $\rho = f(v_c)$, was derived using longitudinal and shear wave velocities that were measured using bender elements. Figure 5.6(a) depicts this relationship. Red line "6.57% Sand" in Figure 5.7 shows the pressure-density relationship.

Strength model: **Granular**

Yield surface, Y , was derived using triaxial test data. The friction angle $\phi = 50.8^\circ$ and cohesion $c = 0$ kPa. Shear modulus was calculated (Eq. 5.19) using the shear wave velocity that was measured. Figure 5.6(b) presents this parameter with respect to the density.

Failure model: **Hydro-tensile limit**

Hydro-tensile limit was assumed to be $p_{MIN} = -1$ kPa. This is virtually zero. Sand is commonly assumed to possess zero cohesion.

5.4.2 Modified Laine's model

Laine's model was modified by applying the methodology that was derived to develop a numerical model for prairie soil. The changes in Laine's sand model are as follows: Equation of state $p = f(\rho)$ and yield surface Y were maintained without change. The bulk and shear moduli were calculated using Equations 5.20 and 5.21, respectively. In these equations the Poisson's ratio was determined by applying the equation (after Jaky [75]):

$$\nu = \frac{1 - \sin \phi}{2 - \sin \phi} \quad (5.26)$$

where $\phi = 50.8^\circ$ is the friction angle. The velocity of sound was determined using Equation 5.17.

Applying this procedure the resulting velocity and shear modulus differed to those presented by Laine *et al.* [82]. Figure 5.6 shows these differences. The calculated velocity and shear modulus have lower values than in Laine's model (measured). This apparent "discrepancy" in the obtained values between the two models

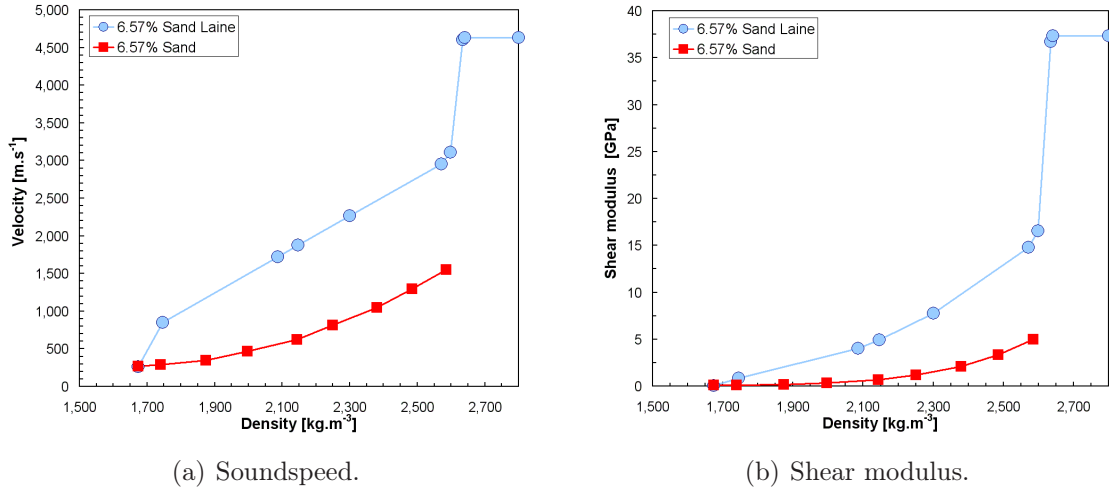


Figure 5.6: Sand models: Laine's model and its modification.

can be clearly explained: Laine *et al.* have used the bender elements method for measuring the velocity of sound. This is a relatively new technique in soil research, and results in higher values for the soil properties in small-strain deformation region, see Viggiani *et al.* [117] and, more recently, Mašín *et al.* [90]. In other words the bulk and shear moduli and consequently, velocity at small-strain deformation, are by order higher than those obtained from standard triaxial tests, which were used throughout this thesis. This new technique can be incorporated to extend the current work, and is discussed in greater detail in Chapter 8.

5.4.3 Sand model for varying moisture content

As the mine impulse pendulum experiments were performed with sand having 0.5 and 16 % moisture content, the sand model was extended to cater for varying moisture content. The properties of sand are not available, therefore the Laine's sand model and statistical soil data are used in derivation of a sand model. The EOS for solid phase was derived using the Laine's sand model and applying Equation 5.13. The EOS for solid phase resulted in the following:

$$\frac{\alpha_{sp}}{\alpha_{s0}} = 3.343408(p - p_0)^{-0.099171} \quad (5.27)$$

Then, the procedure as in derivation of prairie soil model is followed. Yield surface parameters are given by cohesion $c = 0$ kPa and the friction angle determined using Equation 5.26.

5.4.4 Concluding remarks on sand modelling

The methodology derived for prairie soil model was applied to develop sand model. Figure 5.7 illustrates the equations of state for sand of 0.5, 6.57 and 16 % moisture content. The results of the simulation using sand models are presented in Chapter 7, Section 7.3.

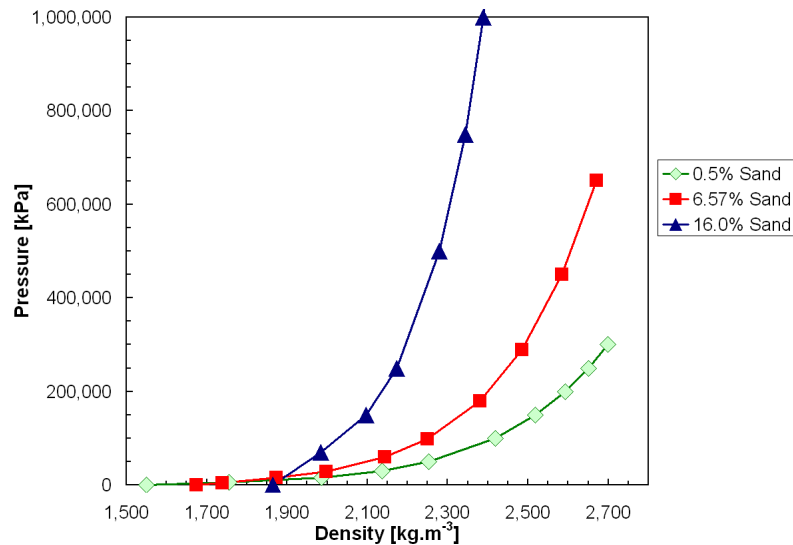


Figure 5.7: Sand models: EOS for different moisture contents.

5.5 Summary

- ◆ Prairie soil properties and statistical soil data are presented. Data were obtained from the standard soil laboratory tests.
- ◆ The methodology for derivation of cohesive soil model was developed. The methodology enables to model soil for varying moisture content. This is the key feature in this thesis.
- ◆ The methodology was applied to derive a sand model.
- ◆ The numerical models of prairie soil and sand were validated using experimental data. The results are presented in Chapter 7, Section 7.3.

If I have a thousand ideas and only one turns out to be good, I am satisfied.

— Alfred Bernhard Nobel (1833-1896)

Chapter 6

Experiments for validating numerical solutions

FOR NUMERICAL SOLUTIONS to gain credence, the results obtained *must* be consistent with data that result from conducting experiments similar to those that are simulated. Published experimental work was carefully chosen to validate the numerical models. In this selection, we were also partly aided by the fact that DRDC-Suffield, Canada has produced some commendable experimental work in the field of mine explosions (c.f., [19, 20, 22, 30, 68]).

To contextualise the presented work, brief, yet substantial description of the experiments are provided in this Chapter. The experiments, as well as numerical results in the ensuing chapters, are presented in the order of increasing complexity. The first experiment, and study, deals with explosions in the air. This study has served as an introduction to the topic as well as gaining familiarity with the software AUTODYN and its methods. The second study then introduces sand into the simulation. The experiments in discussion here, were originally conceived with the aim to provide high-quality data for validating numerical simulations. Finally, the effect that *moisture content* in clayish soil has on the impulse delivered to the test structure, is also presented and validated against the numerical model. It is this experimental work that forms the crucial foundation of this research.

Summarising, the following experiments are referred to in the subsequent sections:

- *Hemispherical surface explosion* – experimental data collated in CONWEP [115] are presented in Section 6.1.

- *Small-scale experiments in dry sand* – experimental results published in papers by Bergeron *et al.* [19, 20, 22] are introduced in Section 6.2.
- *Mine impulse pendulum* (MIP) – study of the design of the pendulum is described in Bues *et al.* [30]. The effects of soil properties and mine deployment were published in Bergeron *et al.* [19]. This experimental work is described in Section 6.3.

Each section is structured to provide the background of the experiments. The experiments are briefly described; in particular, the setup and measurement techniques are discussed. The results from experiments are also presented. Each section recapitulates the salient features in the experiment discussed.

6.1 Experimental data for hemispherical surface explosion (CONWEP)

Explosions in air are well covered in literature (see Baker *et al.* [15], Henrych [67], Kinney and Graham [80], Smith and Hetherington [108]), and were used for getting familiar with the software as well as evaluating numerical techniques used in AUTODYN. One such comprehensive collection of experimental results is CONWEP [115]. CONWEP is a software program that features a collection of conventional weapons effects calculations. CONWEP is described in greater detail in the publication included in software [115]. The airblast data are based on the report Kingery and Bulmash [79]. This collection is based on experimental data of spherical explosions and hemispherical surface explosions. A relationship between blast-wave parameters and scaled distance is developed and implemented in the code. Hence, it is possible to obtain blast-wave parameters for a particular mass of explosive at a given scaled distance.

Blast-wave parameters

The blast-wave profile of an explosion in air is depicted in Figure 6.1. The blast wave is mainly described by the following parameters:

- *Arrival time*, t_a , is the time interval starting from initiating the explosive, until the blast-wave reaches the measuring point.
- *Maximum overpressure*, p_{max} , is the maximum overpressure of the blast wave.

- *Specific incident impulse, I* , is the area under the pressure-time history. Thus, the impulse depends on the shape of the pressure-time curve, namely, the maximum overpressure, the rate of decay of the pressure and the duration of the blast wave.
- *Positive phase duration, t_p* , is the time interval when the pressure is higher than atmospheric pressure. The interval ends when the pressure falls below the atmospheric pressure.

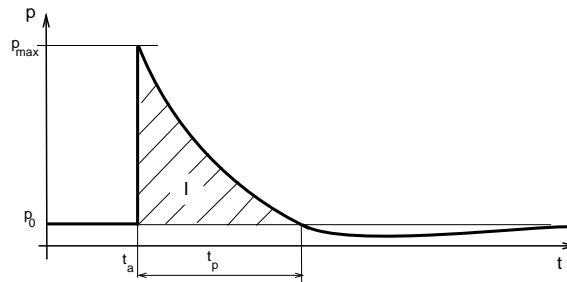


Figure 6.1: Pressure-time history of airblast.

Scaling blast waves

Scaling laws allow a compact and efficient representation of blast wave data for a wide range of situations. The Hopkinson-Cranz scaling law is commonly used and states (after Baker *et al.* [15]):

Self-similar blast waves are produced at identical scaled distances when two explosive charges of similar geometry and of the same explosive but different sizes are detonated in the same atmosphere.

This law is commonly described as *cube-root* scaling and is given by

$$\lambda = \frac{d_2}{d_1} = \left(\frac{W_2}{W_1} \right)^{1/3} \quad (6.1)$$

where λ is the scale factor, W_1 and W_2 are the masses of the charges of diameter d_1 and d_2 , respectively. As depicted in Figure 6.2, the ratio of the distances R at which the same overpressure occurs, as well as the specific impulse ratio and positive phase duration ratio, is equal to the scaling factor:

$$\lambda = \frac{R_2}{R_1} = \frac{I_2}{I_1} = \frac{t_{p2}}{t_{p1}} = \left(\frac{W_2}{W_1} \right)^{1/3} \quad (6.2)$$

This leads to the scaled distance formulation:

$$Z = \frac{R}{W^{1/3}} \quad (6.3)$$

where W is the mass of the charge, usually in terms of TNT equivalent.

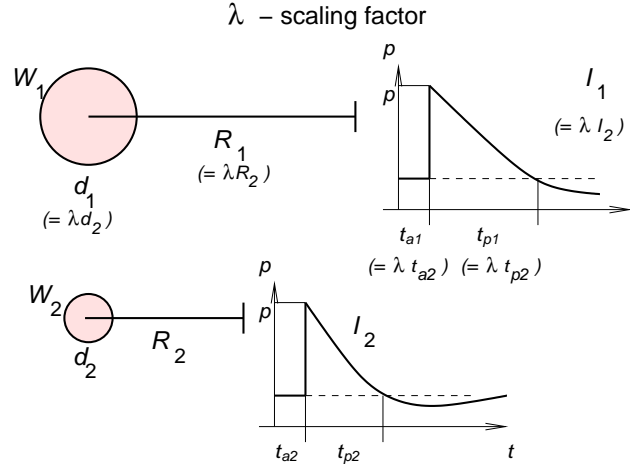


Figure 6.2: Scaling law explained, after Smith et al. [108].

The Sachs scaling law should be applied when the effects of local ambient conditions (eg. high altitude) are significant in determining the blast wave parameters. The Sachs scaling law states that the dimensionless pressure and impulse are unique functions of a dimensionless scaled distance. Thus, the scaling factors take into account differences in atmospheric conditions as follows:

$$\text{Pressure: } S_p = \frac{p_a}{p_0} \quad (6.4)$$

$$\text{Distance: } S_R = \left(W_2 \frac{p_0}{p_a} \right)^{1/3} \quad (6.5)$$

$$\text{Impulse: } S_I = (W_2)^{1/3} \left(\frac{p_0}{p_a} \right)^{2/3} \left(\frac{T_0}{T_a} \right)^{1/2} \quad (6.6)$$

where p_a is the ambient atmospheric pressure, $p_0 = 101.3 \text{ kPa}$ is the standard sea level atmospheric pressure, T_a is the ambient temperature in [K], $T_0 = 288 \text{ K}$ is the standard temperature. For normal sea level condition, the Sachs scaling factors reduce to the factors encountered in the Hopkinson-Cranz approach.

6.1.1 Methodology of experiments

As the experimental data were taken from many sources (see Reference list in Kingery *et al.* [79]), the general description of experimental techniques used is de-

scribed in the report. High speed photography and blast switches were employed to measure blast wave arrival time. The arrival time can also be determined from pressure transducer recordings. The maximum overpressure was directly measured by pressure transducers or derived from the velocity of the blast-wave front. The overpressure impulse was calculated from the pressure-time history records. The experimental results obtained were scaled to standard atmospheric sea level conditions for 1 kg of explosive using Hopkinson and Sachs scaling laws.

6.1.2 Results

Polynomial functions of the blast parameters that represent the experimental data are shown in Figure 6.3. It has been observed from Kingery *et al.* [79] that the function representing positive phase duration is not in good agreement with the experimental data. Therefore, the author has decided that the maximum overpressure and specific impulse will be used for the validation of the numerical results. In addition, it is noted that CONWEP is unable to provide data for scaled distances below $0.18 \text{ m.kg}^{-1/3}$. Maximum overpressures and specific impulses at scaled distances below this value are evaluated by extrapolation, therefore, the waveform may be inaccurate. Data for the case modelled in Chapter 7, Section 7.1 were extracted from CONWEP.

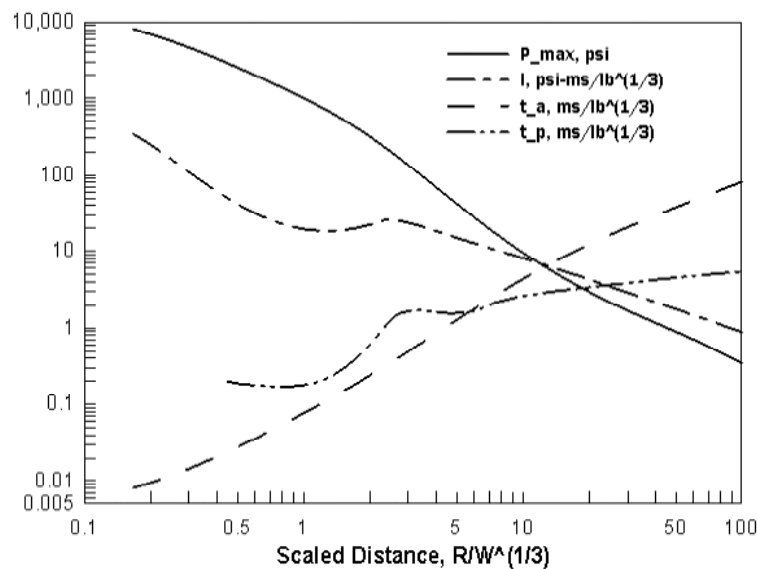


Figure 6.3: Blast-wave parameters for spherical TNT explosion in free air with respect to the scaled distance. Reproduced from CONWEP [115].

6.1.3 Comments on CONWEP

CONWEP provides reliable experimental data for spherical air burst and hemispherical surface explosions for scaled distances exceeding $0.18 \text{ m.kg}^{-1/3}$. In particular, maximum overpressure and specific impulse can be obtained for a particular explosive at a given distance. It is assumed that the charge is placed on the *rigid* surface, i.e. surface of perfect reflection. These blast parameters serve as a benchmark for the numerical simulations described in Chapter 7, Section 7.1.

6.2 Small-scale experiments in dry sand

The explosion process of an antipersonnel mine deployed in dry sand was investigated in order to obtain high-quality data for validation of numerical simulations, such as Wang [121]. The blast parameters, namely maximum overpressure, time of arrival, specific impulse, were determined for different depths of burial. Other (important, and catalogued) experimental data describe the soil displacement and development of the detonation product cloud. For full details of this experimental work refer to the technical report by Bergeron *et al.* [22]. The results are published in [19, 20]. It is to be noted that Wang [121] used this experimental work to validate his numerical solutions obtained using LS-DYNA software [86].

6.2.1 Methodology of experiments

Setup

The experimental setup consists of a bucket and fixings for pressure transducers. It is depicted in Figure 6.4. The bucket was filled with dry sand and was refilled after each trial shot in order to retain the same properties of sand. The explosive charge was 100 g of C-4 that simulated an antipersonnel mine. To ensure consistency in dimensions and mass the explosive was placed into a disc-shaped thin-walled plastic container ($\phi 64 \text{ mm} \times 20 \text{ mm}$). Pressure transducers were fitted on the symmetric axis of the charge at 5 different positions above sand surface. These distances were 300, 700, 1100, 1500 and 1900 mm.

It can be observed from the report that the researchers attempted to maintain experiment repeatability. For example, spatial accuracy was assured by using auxiliary devices for setting the charge into a particular depth and for aligning the charge centre to the axis of the pressure transducers in each case.

Soil type

Dry sand was used throughout the experiments to retain the same properties. The

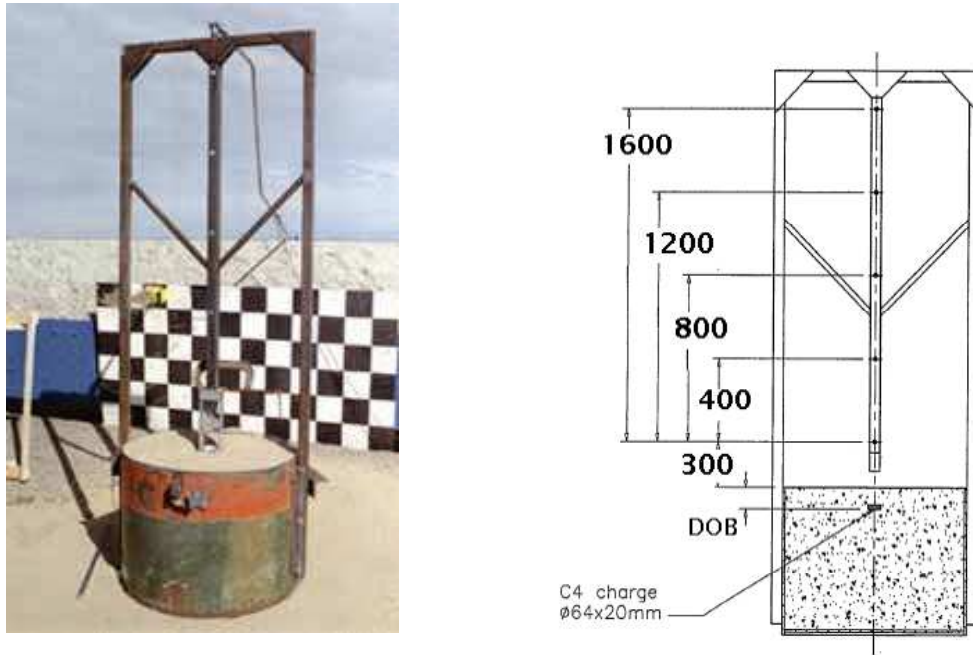


Figure 6.4: *Experimental setup of small-scale experiments in dry sand. Reproduced from Bergeron et al. [22].*

majority (96.2%) of the sand particles were graded in the interval 160 to 630 μm . Dry density was about $1,572 \text{ kg}\cdot\text{m}^{-3}$ and moisture content ranged from 0.1 to 0.4%. The bulk density of sand filled in the bucket was about $1,636 \text{ kg}\cdot\text{m}^{-3}$.

Measuring techniques

In the early stage of the explosion, soil moves upwards forming an ejecta. The height of the ejecta and the crater width developing in time were determined using flash X-ray photography. An alignment procedure was carefully carried out to ensure that photographs kept the same datum.

Propagation of the blast wave in air was captured using pressure transducers. The pressure-time histories were measured directly above the charge at various distances from the surface (see Figure 6.4). The following air-blast parameters were derived from this measurement: (1) time of arrival, (2) maximum pressure, and (3) specific impulse. It is noted that the pressure is side-on, i.e., pressure from air alone and does not include pressure from soil particles.

The entire explosion process was recorded using high-speed photography. From these frames, detonation product expansion was identified, namely, height and width of detonation product cloud with the passage of time.

6.2.2 Results

The experimental results from an explosion of 100 g of C-4 deployed at various depths of burial in dry sand are discussed:

- Shock-wave parameters – maximum pressure and specific impulse for distances above the surface are depicted in Figures 6.5 and 6.6, respectively.
- Displacement parameters – the development of ejecta with passage of time is shown in Figure 6.7. The crater creation is depicted in Figure 6.8. The width and height of detonation product cloud with respect to time are given in Figure 6.9.

In general, it was observed that the depth of burial significantly influences the measured parameters (see Figures 6.5 and 6.6). The side-on maximum pressure and impulse decrease with the distance above the surface. The influence of the depth of burial is more pronounced on the maximum pressure. The flush charge gives 19 times higher maximum pressure than the charge buried at 80 mm, whereas the specific impulse increases only 2.4 times in the same case. With increased depth of burial, soil starts moving upwards with greater delay, with smaller height of ejecta being the result (see Figure 6.7). The width of the crater increases with the depth of burial as shown in Figure 6.8. After breaking through the soil cap, detonation products expand in the air. With the increased depth of burial the detonation product cloud gets smaller in its height and width (see Figure 6.9).

6.2.3 Comments on small-scale experiments

This is a fairly general experimental set up, designed to provide data for the validation of numerical models (in this case, LS-DYNA by Wang [121]). For repeatability, every effort was made to retain as many parameters as possible during this experimental work. This includes the geometric accuracy and sand properties. Despite these efforts, the variation in results was in the range 20% to 80%. These experimental results were used for validation of numerical simulations described in Chapter 7, Section 7.2.

The observations and experience from conducting this experiment were applied to develop appropriate measuring techniques that would also include the energy transferred into soil ejecta. In other words, the soil that impinges on the structure (vehicle) contributes to the total loading. This led to the design of the mine impulse pendulum that is described in the ensuing section.

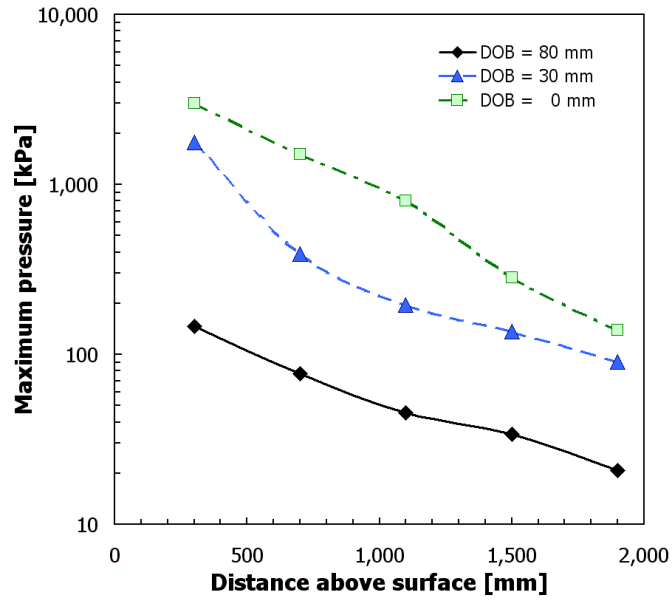


Figure 6.5: Maximum pressure with respect to distance above the ground caused by the explosion of 100 g C-4 in dry sand.

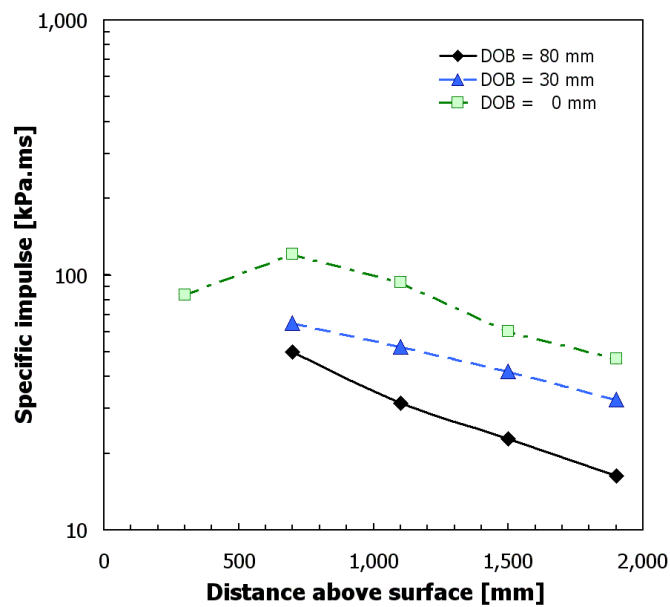


Figure 6.6: Maximum specific impulse with respect to distance above the ground caused by the explosion of 100 g C-4 in dry sand.

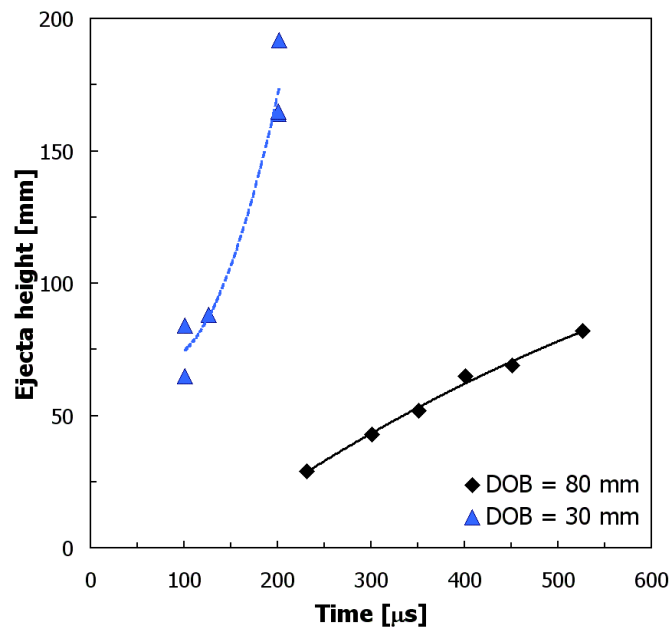


Figure 6.7: Time development of the height of ejecta caused by the explosion of 100 g C-4 in dry sand.

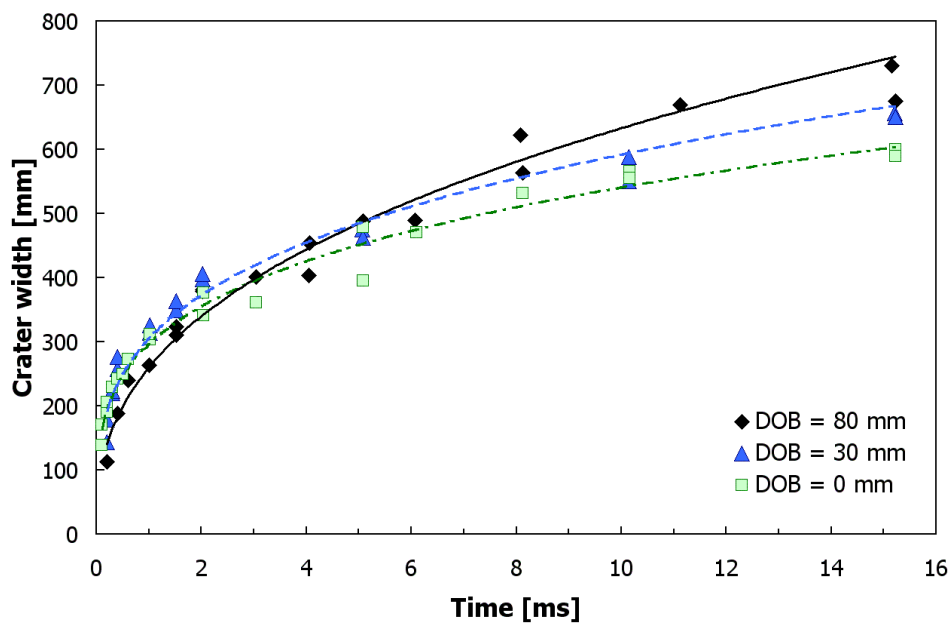
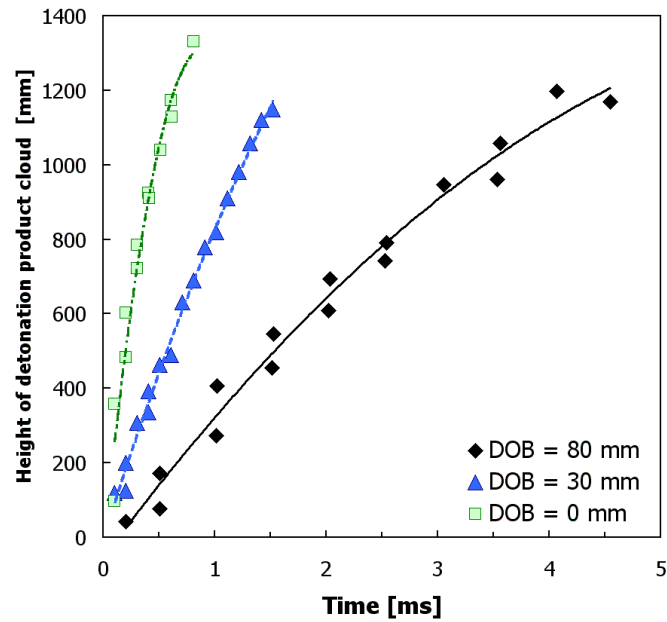
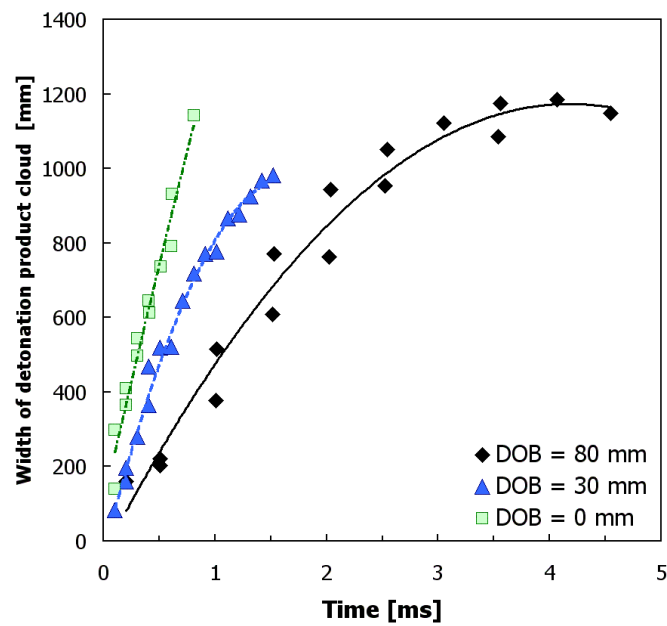


Figure 6.8: Time development of the width of crater caused by the explosion of 100 g C-4 in dry sand.



(a) Height of detonation product cloud



(b) Width of detonation product cloud

Figure 6.9: Time development of the detonation product cloud caused by 100 g C-4 in dry sand.

6.3 Mine impulse pendulum (MIP) experiments: deployment and moisture effect

Experience with the previous set of experiments, along with other trials at DRDC-Suffield [35], was used to develop the mine impulse pendulum (MIP), which determines the impulse/energy imparted to the plate. The MIP work was conducted over a four-year period, resulting in more than 100 tests. The theory and implementation was published in the technical report by Bues *et al.* [30]. The preliminary results were reported by Bergeron *et al.* [19]. However, a technical report that discusses all the test results is in progress at DRDC-Suffield, Canada. The MIP experiments were performed to study the effect of soil type, soil moisture content, depth of burial, and explosive type on mine blast output.

6.3.1 Methodology of experiments

Setup

The Mine Impulse Pendulum is a horizontal ballistic pendulum (see Figure 6.10), which measures the effective impulse and kinetic energy transfer from a landmine explosion as a function of soil conditions, geometry and explosive [30]. There are two main parts to the MIP: the base and arm. The MIP is portable; for each trial it is moved to undisturbed soil. During a trial, the base is held in place by inertia (water is added for ballast). The arm consists of two long I-beams, cross braces and a target plate. The mass of the arm is 1483 kg, the total length is 4.87 m. The arm is free to rotate about a pivot attached to the base. The distance from the pivot point to the centre of the target is 4.37 m. The force of the mine blast and ejecta impact the target plate, causing the arm to rotate. The maximum angle of rotation is used to calculate the impulse and kinetic energy transferred to the target.

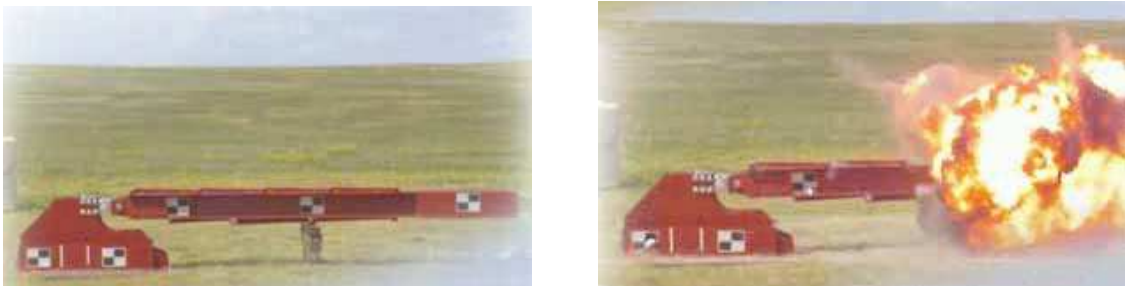


Figure 6.10: *The mine impulse pendulum experiments. Reproduced from Bues et al. [30].*

Table 6.1: *MIP experiments matrix, the pendulum arm is positioned at 400 mm distance above the surface.*

Deployment	Sand	Prairie soil	Steel
Surface-laid		C-4	C-4
Flush (DOB = 0 mm)		C-4	
Buried at 50 mm	C-4	C-4 TNT Comp-B	
Buried at 100 mm		C-4	

The landmine was usually simulated by an explosive charge of 1 kg C-4. The charge was placed into the disc-shaped plastic casing of ϕ 134 mm and 45 mm height. In some experiments, 1 kg charges of Composition-B and TNT were tested. The mine was laid on the surface or buried at one of three overburdens (0, 50 mm, or 100 mm). Overburden is the amount of soil from the top of the mine to the surface of the ground. Mines were laid in or on either prairie soil, sand or a steel plate. Table 6.1 shows the setup combinations under investigation in the course of the experiments.

Soil type

Trials were conducted on undisturbed soil on the range. This soil will be referred as *prairie soil*. Bulk density and moisture content were measured for every soil trial. Moisture content ranged from 7.7% to 28.7%. The prairie soil is described as a sandy, silty, low plastic, brown clay containing roots. The sieve analysis showed 100% of particles passing at 10 mm sieve size and 45% passing at 0.08 mm. Thus the sample consists of 55% of sand particles and 45% of silt and clay particles. Solid particle density was $2610 \text{ kg}\cdot\text{m}^{-3}$. Appendix D outlines the soil properties obtained from different laboratory soil tests.

Measuring techniques

The principle of a pendulum was applied in order to capture the momentum imparted to the target during a mine explosion. The implementation led to the design of the mine impulse pendulum which is pictured in Figures 6.10 and 6.11. The mine blast force acts on the target plate and causes the arm to move upwards. The maximum angle of arm deflection corresponds to the impulse (energy) delivered to the target. The maximum arm deflection was measured using a high speed video, and mechanical gauges.

Total impulse delivered by a mine explosion to the mine impulse pendulum is

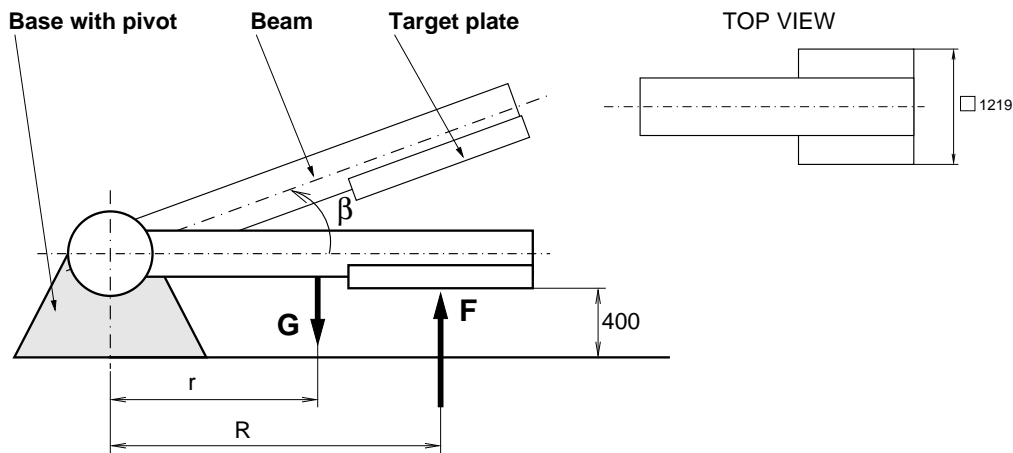


Figure 6.11: .

[The schematic representation of the mine impulse pendulum [mm]. (Not to scale.)
Reproduced from Bues *et al.* [30].

determined from

$$I_{MIP} = \sqrt{\frac{2mgrJ_0 \sin \beta}{R^2}} \quad [N.s] \quad (6.7)$$

where m is the mass of the pendulum arm, g is the gravitational constant, r is the distance from pivot point to the centre of gravity of the arm, J_0 is the moment of inertia of the pendulum arm about the pivot point, β is the maximum angle reached by the pendulum arm, R is the distance from the pivot point to the application point of the momentum. Appendix C describes the derivation of Equation 6.7 and parameters of the pendulum.

6.3.2 Results

For the purposes of this document, experimental data, i.e., impulse delivered to the pendulum, have been organised in such a way to show the influence of

- the various soil properties as given in Figure 6.12,
- depth of burial as depicted in Figure 6.13, and,
- explosive type as shown in Figure 6.14.

This arrangement further clarifies the idea that the case studies form a logical progression. In other words, it was possible to extend the numerical model to include additional functionality as required in each case study. This approach allows us to

have different set of experiments (conducted in different conditions) to validate the model, while demonstrating the extensibility of the numerical model as well.

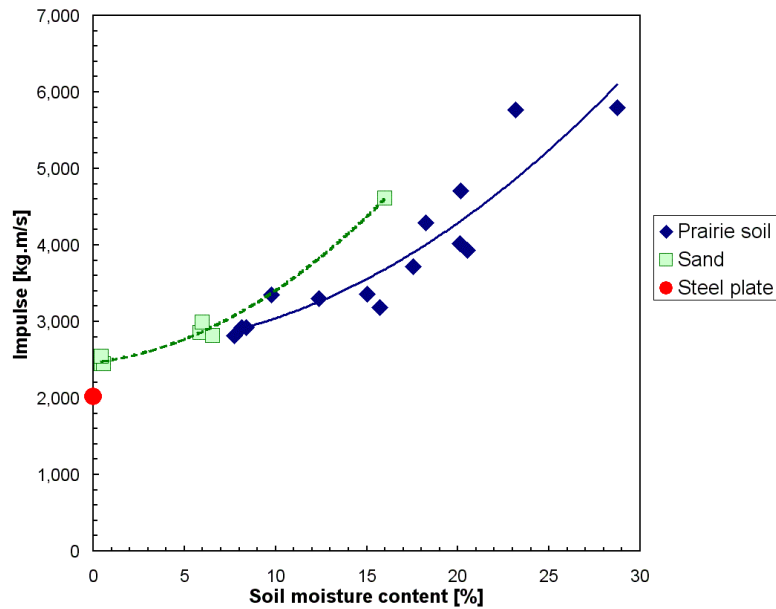


Figure 6.12: MIP experiments: influence of soil properties on impulse delivered to the pendulum. [C-4, DOB = 50 mm]

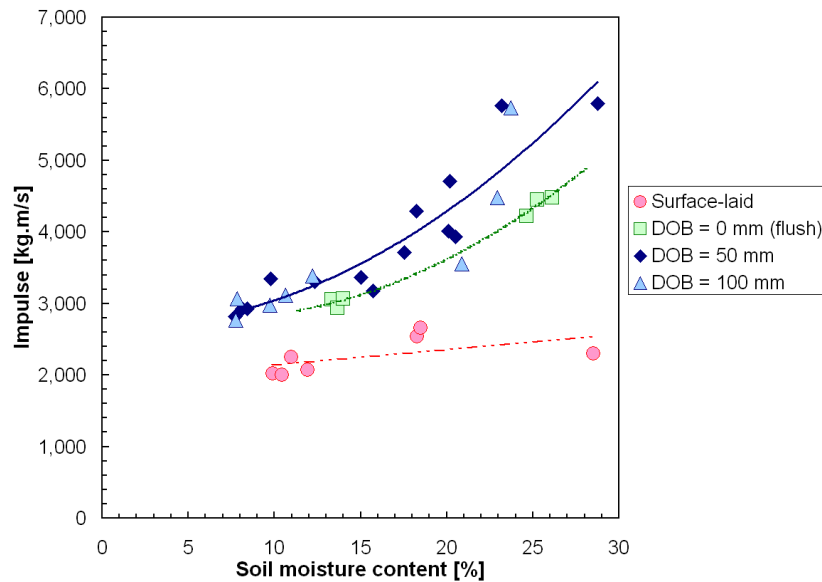


Figure 6.13: MIP experiments: influence of depth of burial on impulse delivered to the pendulum. [C-4, Prairie soil]

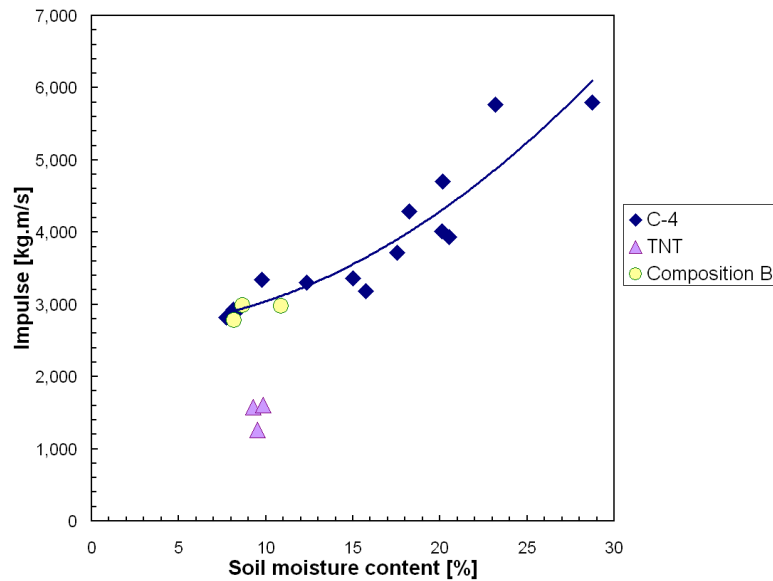


Figure 6.14: *MIP experiments: influence of explosive types on impulse delivered to the pendulum. [Prairie soil, DOB = 50 mm]*

The variation in the impulse measured with increase in moisture content is plotted in Figure 6.12. Data was collected for C-4 explosive and 50 mm overburden. Two types of soil, namely sand and prairie soil, were used in the experiment. It can be seen that, in both cases, the data obtained follows a quadratic¹ fit. It is evident that the impulse increases with increase in soil moisture content. The charge buried in wet prairie soil gives 1.76 times higher impulse than in dry soil. In addition, the single result obtained from the explosion of the charge located on the steel plate is plotted. The steel plate represented a *rigid surface*. The explosion from the charge detonated on the steel plate gives lower impulse than buried charges.

Figure 6.13 shows the influence of the depth of burial on the impulse generated while varying the soil moisture content. Data was collected for C-4 explosive and prairie soil. The lowest impulse is obtained from the explosion of a surface laid charge. Also, the surface laid explosions do not significantly vary with increasing soil moisture content. In contrast, the impulse obtained from charges buried in prairie soil is dependent on the soil moisture content. Generally, the impulse from buried charges is higher than that from surface laid charges. The difference between impulses is most pronounced in saturated soil. The impulse from a charge buried in wet soil is 2.5 times higher than a surface laid charge. Similarly, the difference in impulse between a flush charge and a charge buried in dry soil is 1.5 times.

¹usage of this term, solely to aid visualisation

Influence of the different explosive types on mine blast output is depicted in Figure 6.14. Three types of explosives were investigated in the course of the MIP experiments; namely, TNT, C-4 and Composition B. The experiments were carried out for a charge buried at 50 mm in prairie soil. The trials for TNT and Composition B charges were conducted for soil with about 10% moisture content, whereas moisture content varied from 7 to 28% for C-4 charge. The TNT charges yield the least impulse. The charges made from C-4 and Composition B yielded similar results. The impulse obtained from TNT charges are about 2 times lower than C-4 and Composition B, for the same setup (soil moisture content).

6.3.3 Comments on the MIP experiments

The mine impulse pendulum experiments represent a significant body of work. It comprehensively deals with several parameters influencing mine blast loading, in particular, soil properties and mine deployment. The measuring method has been able to capture the impulse transfer from explosion to the target, including energy from soil particles. The number of trials performed was extensive (over 100 tests in all) and to date, only part of the results have been disseminated. A set of technical reports documenting this work is in the process of being compiled. DRDC, Canada is continuing its work on experiments related to blast loading from mine explosions. For instance, the preliminary results of *piston experiments* were presented by Hlady [68].

6.4 Summary

- ◆ Three sets of experiments were presented. Trial setup, measuring techniques and soil type were shown. The experimental results were analysed in each case.
- ◆ Successive increase in the complexity of the experiments, i.e., from simple air-blast to mine explosion performed for clayish soil having different moisture contents.
- ◆ The experiments discussed here were modelled in the course of the research to lend credence to the work. The results obtained by numerical simulations using AUTODYN are presented subsequently in Chapter 7 and compared with experiment data.

Case I – CONWEP

Charge:	any mass, hemispherical
Deployment:	surface-laid
Soil type:	rigid surface
Distance above the ground:	above $0.18 \text{ m.kg}^{-1/3}$
Measured parameters:	<ul style="list-style-type: none"> ○ maximum overpressure ○ specific incident impulse

Case II – Small-scale experiment in dry sand

Charge:	100 g C-4, disc-shaped
Deployment:	<ul style="list-style-type: none"> ● flush ● 30 or 70 mm buried
Soil type:	dry sand
Distance above the ground:	0.3, 0.7, 1.1, 1.5 and 1.9 m (scaled distance from $0.595 \text{ m.kg}^{-1/3}$)
Measured parameters:	<ul style="list-style-type: none"> ○ maximum overpressure ○ specific incident impulse ○ time of arrival ○ height of ejecta ○ height and width of detonation product cloud ○ width of crater

Case III – Mine impulse pendulum (MIP)

Charge:	1 kg C-4, disc-shaped
Deployment:	<ul style="list-style-type: none"> ● surface-laid ● flush ● 50 or 100 mm buried
Soil type:	<ul style="list-style-type: none"> ○ sand ○ prairie soil
Distance above the ground:	400 mm (scaled distance $0.368 \text{ m.kg}^{-1/3}$)
Measured parameters:	impulse delivered to the pendulum [N.s]

What we see depends on mainly what we look for.

— Sir John Lubbock, (1834 – 1913)

Chapter 7

Results of modelling in AUTODYN

THIS CHAPTER PRESENTS the numerical simulations performed using the AUTODYN software¹. The validity of the models was verified by the experiments discussed in Chapter 6. The simulations are described with its setup, and the results are presented and discussed at the end of each main section. The simulations were performed with increasing levels of complexity. Three sets of simulations are presented with various aspects being studied in each set:

- *Hemispherical surface explosion* – familiarisation with the AUTODYN software. A hemispherical charge laid on a rigid or sand surface was modelled. Mine deployment is analysed based on the numerical results. This is described in Section 7.1.
- *Small-scale explosion in dry sand* – introducing sand model into the numerical simulation. The effect of deployment – flush as well as buried charge, was validated. More importantly, a sensitivity analysis, a novelty, was performed. This set of simulations is presented in Section 7.2.
- *Cohesive soil model validation using mine impulse pendulum [MIP]* – The impulse delivered to the plate caused by the explosion of the charge buried in clayish soil or sand was modelled. The models of *prairie soil* and sand, whose

¹An explanation of how to use AUTODYN for landmine explosion modelling is given in Chapter 4.

derivation was described previously (in Chapter 5), were used. The simulations are described in Section 7.3.

The third set of simulations is the most important as they confirm the validity of the proposed methodology.

7.1 Getting started with AUTODYN

The first step in designing mine-resistant vehicles is to determine the loading on the vehicle caused by a mine explosion. Although soil-blast interaction makes a significant contribution to the total loading, the first task undertaken was to simulate the blast wave propagation in surrounding air in order to gain familiarity with the AUTODYN software and ascertain the numerical procedures in AUTODYN. The numerical findings were compared with experimental data obtained from CONWEP. The initial findings of this research were presented at the *6th International seminar on New trend in research of energetic materials* [50] and *Journal of Battlefield Technology* [48].

The explosive content of an anti-tank mine varies between 1.5 and 13 kg [2]. Most vehicles have a ground clearance which ranges between 200 and 600 mm [3]. Therefore a numerical model was established which used a hemispherical TNT charge of mass 10.19 kg, and the resulting blast wave parameters at distances between 200 and 800 mm were examined. These distances correspond to scaled distances² from 0.092 up to 0.369 m.kg^{-1/3}. Two studies are presented:

- i. Hemispherical surface explosion models were compared with CONWEP data. The results are presented in Section 7.1.2.
- ii. Analysis of the effect of mine deployment in dry sand. The charge was laid on surface, flush, or buried. The results are given in Section 7.1.3.

7.1.1 Setup of hemispherical surface explosion

A two-dimensional axi-symmetric model was developed using the multi-material flow solver (Euler) in AUTODYN to investigate the effect of:

- *Rigid surface* – a solid boundary with a perfect reflection as shown in Figure 7.1(a).

²Scaled distance is defined as $Z = R/W^{1/3}$, where R [m] is the distance from charge centre and W [kg] is the TNT equivalent charge mass.

- *Sand surface* – the charge was placed on a sand surface as shown in Figure 7.1(b). The sand model derived by Laine *et al.* [82] was used.

Throughout the study, the terms rigid-surface model and sand-surface model will be used to denote the preceding definitions, respectively. Boundary conditions were applied to the computational domain such that no reflections were permitted (see Figure 7.1). The surrounding air was assumed to be an *ideal gas*. The explosive charge was modelled using two approaches for the equation of state of the detonation products:

- *Ideal gas EOS* – simplified model proposed in analysis by Fairlie *et al.* [44].
- *Jones-Wilkins-Lee (JWL) EOS* – empirical EOS widely used in mine blast simulation (refer to Table 2.1).

For the rigid surface model, two equations of state for detonation products, namely Jones-Wilkins-Lee and ideal gas EOS, were analysed. While cell sizes of 5, 3, 1, 0.5, 0.1 and 0.05 mm were used to study the mesh sensitivity. A sand-surface model was run only using JWL EOS for detonation products. A summary of the model setup is presented in Table 7.1.

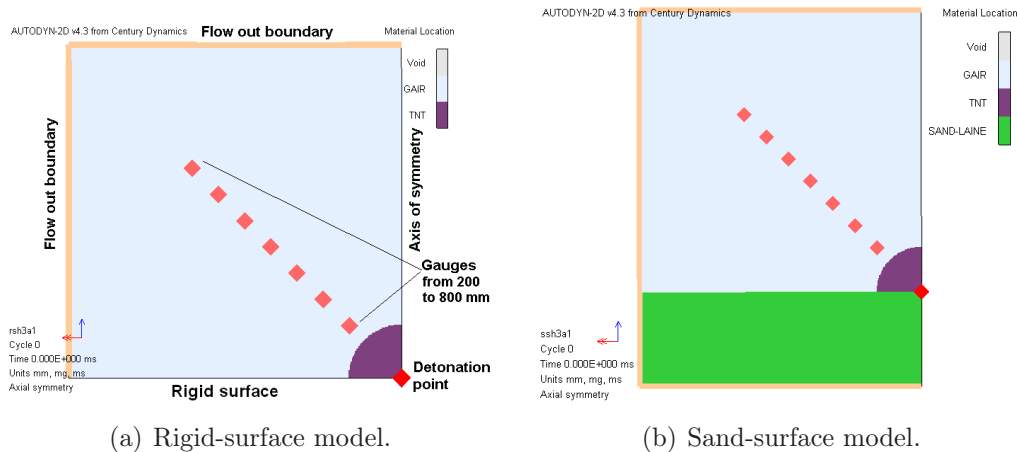


Figure 7.1: The scheme of initial model for hemispherical surface explosion.

7.1.2 Hemispherical surface explosion results

Two blast wave parameters: maximum overpressure and specific impulse, were evaluated for different distances using both the above EOS for different mesh sizes. The

Table 7.1: Model description for hemispherical charge explosion.

	Parameter	Notes
	2D axi-symmetric model	
Solver	Euler	
Units	mm, mg, ms	
Mesh dimension ((x_1, x_2) \times (y_1, y_2)) [mm]	(i) (0, 900) \times (0, 900) (ii) (-300, 900) \times (0, 900)	
Cell size	5, 3, 1, 0.5, 0.1, 0.05 mm	
Boundary conditions	Flow out	
Detonation point (x, y)	(0.0, 0.0)	
Gravity x-axis	- 9.80665	
Explosive dimension EOS	TNT circle radius 144 mm (a) JWL (b) Ideal gas	10.19 kg $e_{int} = 3.681 \times 10^6 \text{ kJ.kg}^{-1}$
Surrounding material EOS	Air Ideal gas	$e_{int} = 192 \times 10^3 \text{ kJ.kg}^{-1}$
Soil EOS Strength model Failure model	Sand Compaction Granular Hydro $p_{MIN} = -1 \text{ kPa}$	Laine <i>et al.</i> [82]
Deployment	(i) Rigid surface (ii) Sand surface	
Measured parameter	Maximum pressure Specific impulse	

numerical results were compared with empirical data from CONWEP [115]. CONWEP generates overpressure and specific impulse data for a particular explosive and given scaled distance. It is noted that CONWEP is unable to provide data for scaled distances below $0.18 \text{ m.kg}^{-1/3}$. Maximum overpressures and specific impulses at scaled distances below this value are evaluated by extrapolation. Details about CONWEP are stated in Chapter 6, Section 6.1.

The results are presented in this order:

- A. Effects of EOS and mesh sensitivity – JWL and *ideal gas* equations of state for modelling the detonation products are analysed along with the mesh sensitivity.
- B. Surface analysis – the effect of rigid and sand surface is investigated.

A. Effects of EOS and mesh sensitivity

Overpressure-time histories extracted from the analyses using *ideal gas* are shown in Figure 7.2(a), and those from the JWL analysis are plotted in Figure 7.2(b). The overpressure-time histories were recorded at the distances from 200 mm to 800 mm with an increment of 100 mm. Maximum overpressures at a particular scaled distance for the various mesh sizes considered and for both EOS are presented in Table 7.2, which is graphically interpreted in Figure 7.3(a).

For the models using the *ideal gas* EOS, it was observed that cell size had little influence on the magnitude and shape of the resulting blast waves. Comparison with CONWEP indicated that maximum overpressures were underestimated by 50 – 30% at the distances exceeding 400 mm, as shown in Figure 7.3(a). The CONWEP data below 400 mm were extrapolated and therefore were ignored in this comparison. The specific impulse results over the same range were in closer agreement with CONWEP. Plots of specific impulse against distance are presented in Figure 7.3(b).

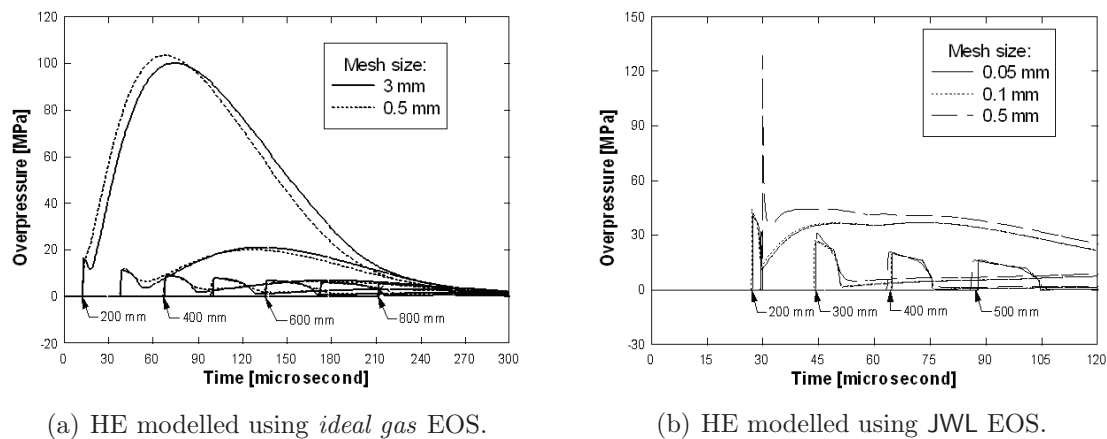


Figure 7.2: Pressure-time histories for TNT charge placed on rigid surface.

Results obtained using the JWL EOS were observed to be highly dependent upon the mesh size. For the largest cell size, maximum overpressures were up to 8 times those of the fine mesh analysis at the distance of 200 mm. It was also observed that for cell sizes of 0.1 and 0.05 mm, maximum overpressures were convergent and comparable with CONWEP data over the whole range considered, including the extrapolated region. Interestingly, opposite trends were observed with respect to the specific impulse. Fine meshes resulted in the greatest underestimation of specific impulse (up to 70%), while coarser meshes predicted specific impulses only 25% lower at the distances exceeding 400 mm (see Figure 7.3(b)). Examination of the *ideal gas*

and JWL pressure records (Figures 7.2(a) and (b)) shows that the compressive shocks were sharp in the case of JWL, while they were flat and rounded in the case of *ideal gas*.

Table 7.2: Maximum overpressure for rigid-surface models with HE modelled with different EOS and different mesh size.

Distance <i>R</i>	Maximum overpressure									
	CONWEP	JWL EOS						Ideal Gas EOS		
		5 mm	3 mm	1 mm	0.5 mm	0.1 mm	0.05 mm	5 mm	3 mm	0.5 mm
[mm]	[kPa]	[kPa]	[kPa]	[kPa]	[kPa]	[kPa]	[kPa]	[kPa]	[kPa]	[kPa]
200	41 650 ^a	333 914	241 910	160 573	128 930	44 349	41 738	98 584	103 429	100 213
300	27 090 ^a	71 756	68 005	36 148	31 747	27 392	27 498	20 747	20 083	20 999
400	19 150	42 028	25 158	22 543	21 088	20 315	20 656	9 912	9 802	9 512
500	14 420	18 571	18 265	15 634	16 256	16 059	16 314	8 289	8 168	8 160
600	11 360	14 752	12 933	12 247	13 196	13 005	— ^b	7 112	7 018	7 228
700	9 230	11 137	10 114	9 990	10 963	10 680	— ^b	6 240	6 225	6 494
800	7 667	8 549	8 189	8 310	9 221	8 866	— ^b	5 528	5 581	5876

^aScaled distance is out of range for duration calculation. Waveform may not be accurate.

^bThese distances were not modelled due to limitations of hydrocode.

B. Surface analysis

To study the surface effect, a rigid and a sand surface, was modelled. JWL EOS was used for the explosive in the sand surface model. Since mesh size of 3 and 1 mm gave the same trend for both the rigid and the sand surface models, the discussion below focusses on the 1 mm mesh size.

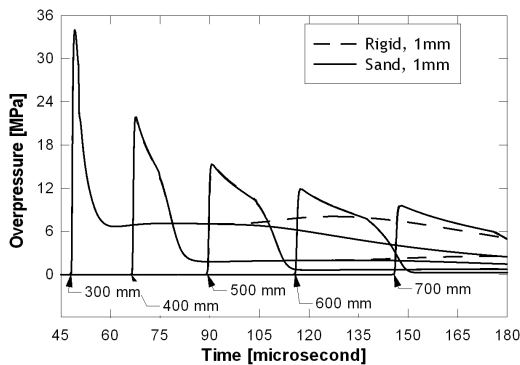
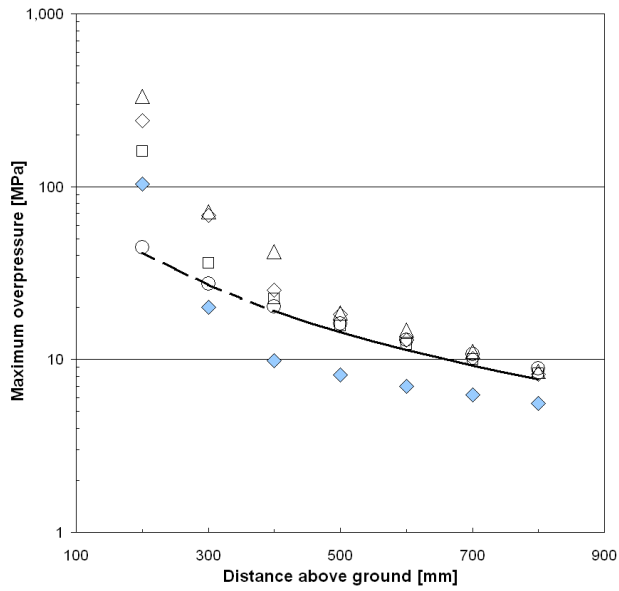
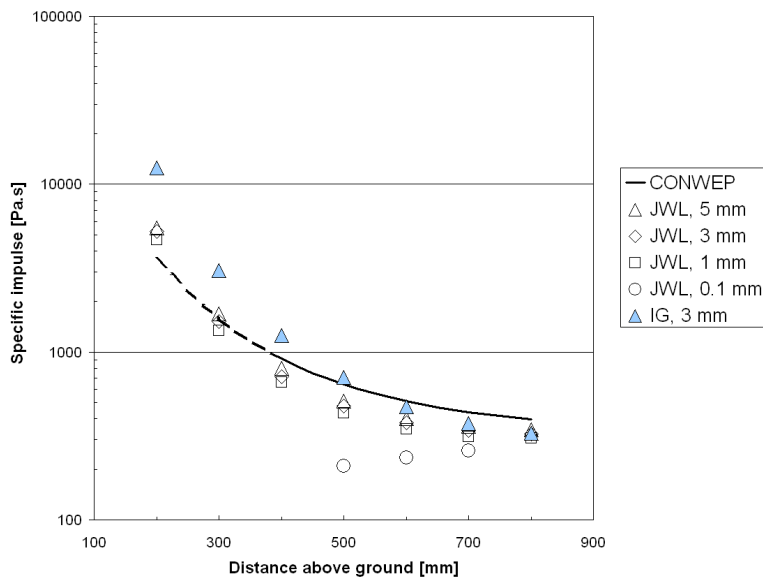


Figure 7.4: Pressure-time histories for rigid- and sand-surface models.

Overpressure-time histories extracted from the analysis of the rigid and sand surface models are shown in Figure 7.4. The time histories were recorded at the distances from 200 mm to 800 mm with an increment of 100 mm. It was observed that overpressure-time histories are largely coincident. A tabulation of the maximum overpressure and specific impulse against scaled distances for various mesh sizes considered are presented in Tables 7.3 and 7.4, respectively. These tables are graphically interpreted in subsequent Figures 7.5(a,b).



(a) Maximum pressure.



(b) Specific impulse.

Figure 7.3: Influence of equation of state of explosives on blast-wave parameters. Dashed line indicates extrapolated CONWEP data.

It was observed that the type of surface within the region considered did not influence the maximum overpressure and time of arrival. The magnitude of specific impulse was less in the case of the sand surface model (see Figure 7.5(b)). Reductions of approximately 23 % were noted at the distances of 300 and 400 mm. This was because of the fact that some of the explosion energy was consumed by sand compaction and crater formation. At the distances greater than 600 mm, the difference in the magnitude of specific impulse is not significant.

Table 7.3: *Maximum overpressure for rigid- and sand-surface models.*

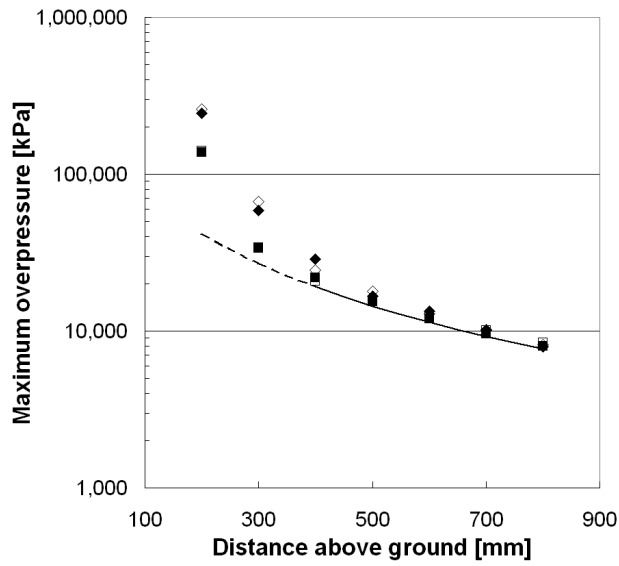
Distance	Scaled distance	Maximum overpressure				
		CONWEP	Rigid 3 mm mesh	Rigid 1 mm mesh	Sand 3 mm mesh	Sand 1 mm mesh
[mm]	[m.kg ^{-1/3}]	[kPa]	[kPa]	[kPa]	[kPa]	[kPa]
200	0.092	41,650	256,675	136,141	245,534	137,268
300	0.138	27,090	57,443	33,987	58,820	33,982
400	0.184	19,150	28,432	21,808	28,619	21,975
500	0.231	14,420	16,684	15,307	16,679	15,362
600	0.277	11,360	13,421	12,055	13,418	11,925
700	0.323	9,230	10,204	9,647	10,162	9,599
800	0.369	7,667	7,993	8,032	7,916	8,027

Table 7.4: *Specific impulse for rigid- and sand-surface models.*

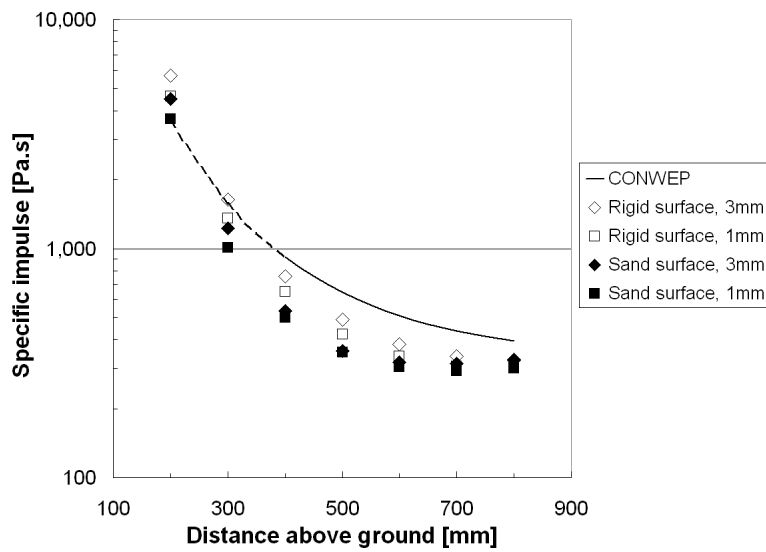
Distance	Scaled distance	Specific impulse				
		CONWEP	Rigid 3 mm mesh	Rigid 1 mm mesh	Sand 3 mm mesh	Sand 1 mm mesh
[mm]	[m.kg ^{-1/3}]	[kPa.ms]	[kPa.ms]	[kPa.ms]	[kPa.ms]	[kPa.ms]
200	0.092	3,586	5,415	4,551	4,512	3,687
300	0.138	1,572	1,536	1,316	1,227	1,008
400	0.184	917	669	634	534	499
500	0.231	644	424	421	357	353
600	0.277	509	353	340	319	304
700	0.323	437	332	311	314	293
800	0.369	396	335	308	326	300

7.1.3 Effect of deployment in sand

Building on the analyses in the previous section, a 10 kg TNT charge was deployed in sand having moisture content of 6.57 % in order to study the effect of mine



(a) Maximum pressure.



(b) Specific impulse.

Figure 7.5: Influence of sand surface against rigid surface on blast-wave parameters. Dashed line indicates extrapolated CONWEP data.

deployments. The sand model was derived by Laine *et al.* [82]. The following deployment methods were investigated:

- *Surface-laid charge* – the charge was laid on the sand surface.
- *Flush charge* – the top of the charge was in level with the sand surface.
- *Buried charge* – the charge was buried in sand at the depth of 20 mm and 60 mm, further referred as $DOB = 20$ mm and $DOB = 60$ mm, respectively.

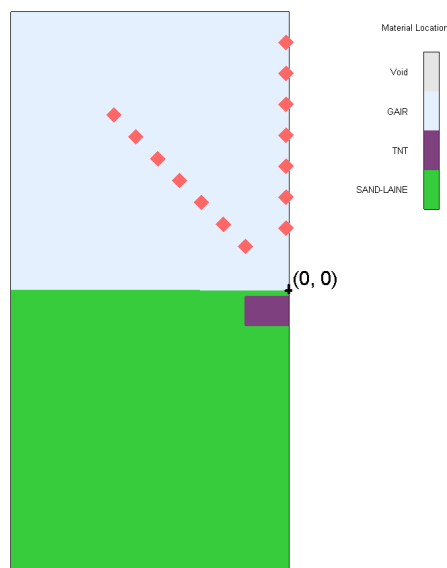
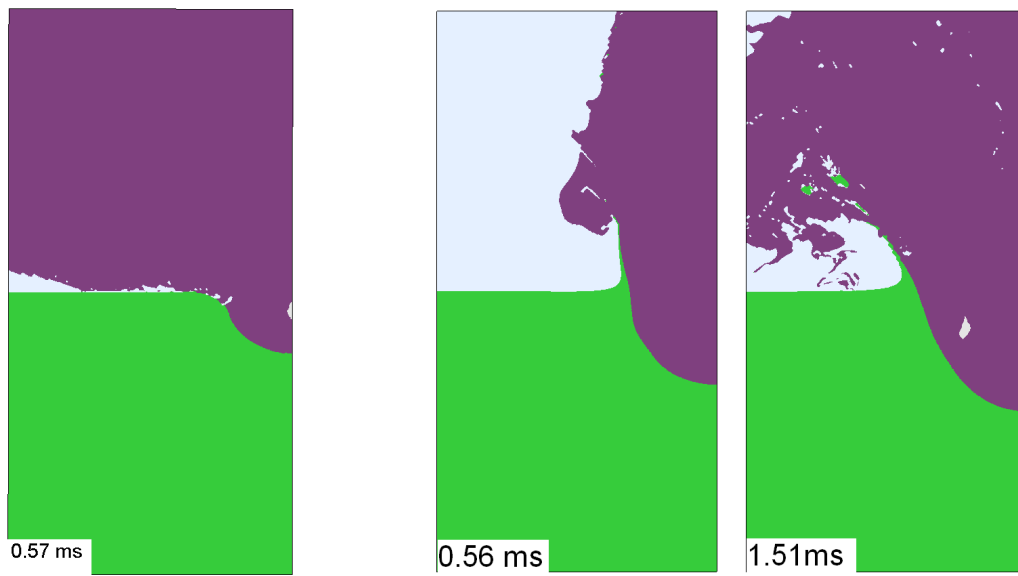


Figure 7.6: Model setup for a charge buried in sand. Notice the gauge positions and origin of the co-ordinates.

The models were consistent with the model presented in Table 7.1. The mesh size was 3 mm. Maximum pressure and specific impulse were analysed at distances from 200 to 800 mm with a 100 mm increment in both vertical and diagonal directions. The gauge positions are shown in Figure 7.6. The origin of co-ordinates (0,0) is located in the intersection of the sand surface and the axis of symmetry.

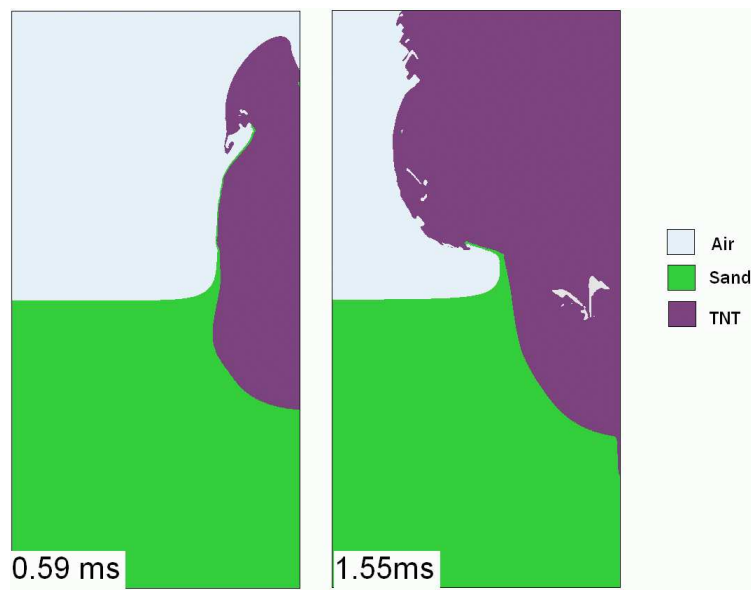
The progress of the explosion for different deployments is captured in Figure 7.7. It is observed that the affected area from buried charges (b) and (c) is more confined to the upward direction when compared with the hemispherical distribution of the surface laid charge (a). A similar trend was observed in the distribution of maximum pressure and specific impulse.

The maximum pressure and specific impulse from the buried charges were compared with the surface-laid charge parameters. This is expressed by sensitivity



(a) Surface-laid.

(b) Buried at 20 mm.



(c) Buried at 60 mm.

Figure 7.7: Material location for charge in various deployments in dry sand.

coefficients as follows:

$$S_i^f = \frac{f(i) - f(\text{surface-laid})}{f(\text{surface-laid})} \quad (7.1)$$

where $f(i)$ is either the maximum pressure or specific impulse of the respective deployment i . The difference of maximum pressure of the flush and buried charges with respect to the surface-laid charge is presented in Figure 7.8(a,b) for vertical and diagonal directions, respectively. The sensitivity of the specific impulse is depicted in Figure 7.9.

In the vertical direction, the maximum pressure from the charge buried at 20 mm is about 60 % higher than the surface-laid charge at the distances 300 and 400 mm. The maximum pressure from the flush charge is higher than the surface-laid charge at the distances greater than 400 mm. The maximum pressure from the charge buried at 60 mm is lower than the surface-laid charge in all observed distances. The highest maximum pressure was obtained at the distances of 300 and 400 mm, where the maximum pressure from charge buried at 60 mm was about 20 to 30 % lower than the surface-laid charge. In the diagonal direction, the maximum pressure from flush and both buried charges was considerably lower than the surface-laid charge. In particular, the maximum pressure is between 5 and 20 % of the surface-laid charge.

The effect of deployment is significantly pronounced on the specific impulse in the vertical direction. The specific impulses from charges buried at depths of 20 and 60 mm are up to 8 and 6 times higher, respectively, compared to the surface-laid charge. The maximum impulse occurred between 300 and 500 mm.

7.1.4 Discussions

Hemispherical surface explosion

Convergence of the numerical results with CONWEP data occurs with increased distance away from the charge centre, for both equations of state. The model which used the *ideal gas* EOS does not agree with the blast wave parameters of CONWEP at close distance, where the blast wave parameters are highly influenced by the detonation products. Therefore, the *ideal gas* representation will not be considered in future studies.

Results obtained from the JWL EOS model were not consistent for all the region observed. Fine meshes gave consistent maximum overpressures but underestimated impulses, while the large mesh sizes resulted in pressure overshoots at the close-in distances and specific impulses 25% lower. Huntington-Thresher *et al.* [73] concluded from experimental analysis that CONWEP overestimated specific impulse by 20-25%. Taking this into consideration, specific impulses predicted by the model using JWL

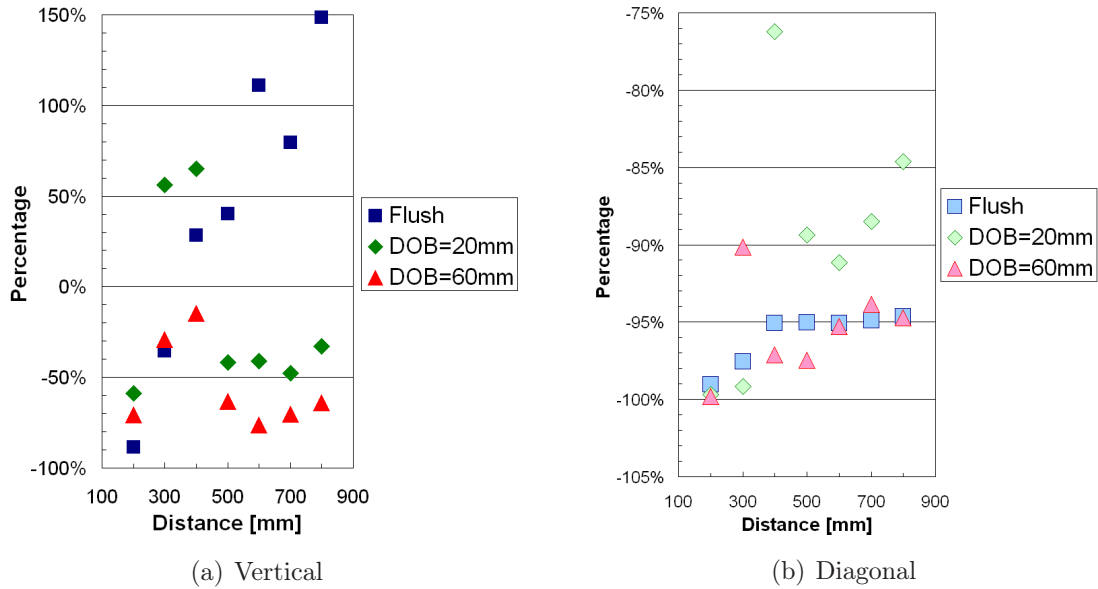


Figure 7.8: Influence of the deployment on the maximum pressure in different directions with respect to the surface laid charge.

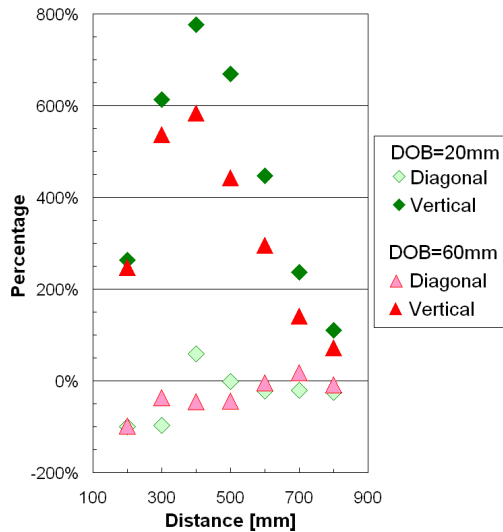


Figure 7.9: Influence of the deployment on the specific impulse in different directions with respect to the surface laid charge.

with a coarse mesh were in good agreement with experiments.

The surface which the charge laid on did not influence maximum overpressure and time of arrival. There was a difference in the specific impulse. The sand surface model predicted about 23 % lower impulse in the near region than the rigid surface model. This effect is consistent with the energy dissipation into soil for compaction (plastic deformation).

Effect of deployment in sand

Numerical analysis was performed to investigate the effect of deployment. When the charge is flush or buried the pressure and impulse distribution to the side is reduced. The main affected area is directly above the charge. The pressure obtained from the explosion of buried charges can reach up to 60 % higher in magnitude than the surface-laid charge. The maximum pressure is obtained at distances of 300 and 400 mm above the surface. However, a more pronounced effect of deployment is observed on the specific impulse. The impulse from buried charges was up to 8 times higher than the surface-laid charge. The highest impulse is obtained for distances between 300 and 500 mm. It is noted that this distance is typical of the ground clearance of (armoured) vehicles [3].

7.1.5 Concluding remarks

Incident overpressures and impulses were calculated for a mine using a range of cell sizes and two different equations of state for the detonation products. Simulations led to the conclusion that the ideal gas equation of state is not suitable for modelling an explosion at close range. The JWL equation of state, although superior in some respects, also fails to give satisfactory results in the whole range of interest of this study. The surface on which the mine is laid influences the near region. Although time of arrival and maximum overpressure were not affected, specific impulse decreased up to 23 % for the sand surface model at observed distances.

Although this is a preliminary study, it was found that the method of charge deployment is significant. The specific impulse from explosions of buried charges is up to 8 times higher compared to the surface-laid charge.

These preliminary results were pivotal in influencing the decision to study various deployments of mines, and buried mines in particular. As a consequence, soil properties need to be analysed to make any form of comparison. Thus, to validate the deployment effect, small-scale experiments conducted by Bergeron *et al.* [22] were chosen and numerically recreated.

7.2 Small-scale explosion in dry sand

The second study was undertaken to ascertain the sand model derived by Laine *et al.* [82] and analyse the simulation of the explosion of buried charges. With the aim of validating the numerical results, the simulation setup recreated the experiments of Bergeron *et al.* [22]. The experiments are briefly described in Chapter 6, Section 6.2. Two categories of simulations were performed:

- *Deployment effect:* The small charge was either buried or laid flush in dry sand. For completeness, the numerical predictions obtained using LS-DYNA (Wang [121]) are included in our discussions. Blast-wave and displacement parameters are compared with experiments. The results are presented in Section 7.2.2. These results have been submitted for review to the *Journal of Impact Engineering* [47].
- *Sensitivity of the setup:* The advantage of a numerical simulation is that many variations of a particular experiment setup can be run without incurring the same costs as in experiments. This is utilised in the sensitivity study, which forms one of the important features of this thesis, where the effect of the change in the setup is thoroughly investigated. In particular, the effect of the transducer location and the position of detonation point is analysed. The results are described in Section 7.2.3.

7.2.1 Setup of small-scale explosion in dry sand

A two-dimensional axi-symmetric model was developed using the multi-material solver (Euler) in AUTODYN. The following cases were investigated:

- a buried charge at the depth of 30 mm, referred as $DOB = 30$ mm,
- a flush charge with its top surface level with the ground surface, referred as $DOB = 0$ mm.

The mine was represented by 100 g charge of C-4, which was described by the Jones-Wilkins-Lee equation of state [32]. Measuring points were set at distances of 300 mm and 700 mm above the ground. These configurations are depicted in Figure 7.10. A summary of the model setup is presented in Table 7.5.

In the initial stage, a mesh sensitivity study was conducted using cell sizes of 4, 2, 1 and 0.5 mm. The values of maximum overpressure and specific impulse converged at cell sizes of 1 mm and 0.5 mm. Therefore, the remainder of the simulations were performed using a 1 mm cell size.

The sand was modelled as a porous material (Laine *et al.* [82]). This sand model consists of an EOS describing the compaction, a granular strength model, expressing the yield surface dependence on pressure, and assumes negligible tensile strength. This model was derived for sand having dry density of $1,574 \text{ kg.m}^{-3}$ and average water content of 6.57% [82].

The material input parameters for AUTODYN and LS-DYNA models are presented in Table 7.6. The equations of state and yield functions for sands are illustrated in Figure 7.11. For details on sand models refer to [82] and [121].

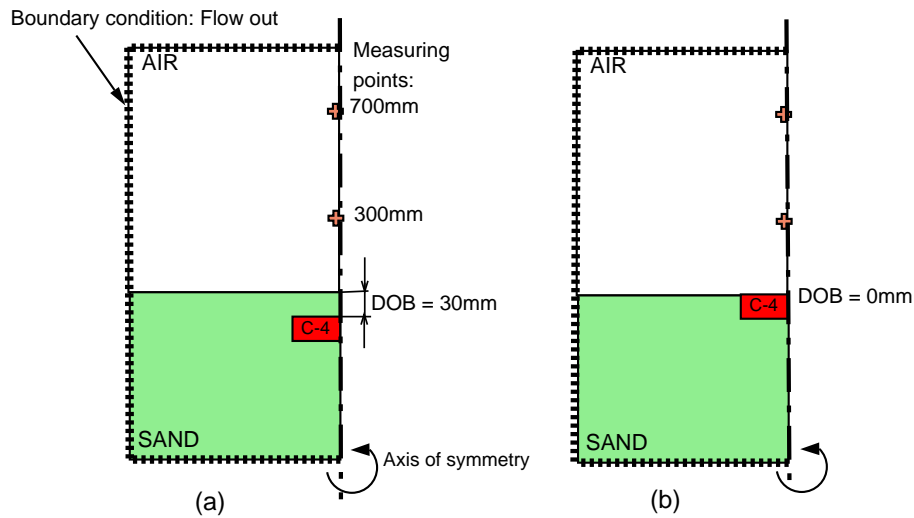


Figure 7.10: Mine deployment – simulation configuration: (a) buried charge, (b) flush charge. (Not to scale.)

7.2.2 Deployment effect in dry sand

The numerical results are compared with the experimental data of Bergeron *et al.* [22]. Also, the numerical results of Wang [121] performed using the LS-DYNA software are presented and discussed. For both the mine deployments, the results of the predictions can be subdivided as follows:

- A. *Blast-wave parameters* describe blast wave propagation through air and consist of time of arrival, maximum overpressure and specific impulse measured at the distances of 300 mm and 700 mm.
- B. *Displacement parameters* describe the displacement of materials with respect to time in terms of height of ejecta front, crater diameter, height and width of detonation products cloud.

Table 7.5: Model description for small-scale explosion in dry sand.

		Notes
	2D axi-symmetric model	
Solver	Euler	
Mesh dimension [mm]	$(-700, 1000) \times (0, 500)$	$(x_1, x_2) \times (y_1, y_2)$
Cell size [mm]	1	4, 2, 0.5 for mesh sensitivity analysis
Boundary conditions	Flow out	
Detonation point	centre	
Gravity x-axis	- 9.80665	
Explosive dimension [mm]	TNT $\phi 64 \times 20$	100 g
EOS	JWL	
Surrounding material	Air	
EOS	Ideal gas	
Soil	Sand	Laine <i>et al.</i> [82]
Deployment	(i) flush: DOB = 0 mm (ii) buried: DOB = 30 mm	
Measured parameter	Maximum pressure Specific impulse Time of arrival	

Table 7.6: Input parameters for material modelling.

AIR: the ideal gas EOS									
	ρ [kg.m ⁻³]	γ [-]	E_{INT} [kJ.kg ⁻¹]	Notes					
AUTODYN	1.225	1.4	206.82	Internal energy corresponds to temperature of 15°C					
LS-DYNA	1.290	1.4	193.80	Internal energy corresponds to temperature of 0°C					
C-4: the Jones-Wilkins-Lee EOS									
	ρ [kg.m ⁻³]	D [m.s ⁻¹]	p_{CJ} [kPa]	E [kJ.m ⁻³]	A [kPa]	B [kPa]	R_1 [-]	R_2 [-]	ω [-]
AUTODYN	1,601	8,193	28×10^6	9×10^6	609.77×10^6	12.95×10^6	4.5	1.4	0.250
LS-DYNA	1,601	8,193	28×10^6	9×10^6	609.97×10^6	12.95×10^6	4.5	1.4	0.250
SAND:									
	ρ [kg.m ⁻³]	Equation of state		Strength model			Failure criteria		
AUTODYN	2,640 (max), 1,674 (initial)	<i>Compaction EOS:</i> Piecewise linear functions of (a) density vs. pressure and (b) density vs. soundspeed		<i>MO Granular:</i> Piecewise linear functions of (a) stress vs. yield (Mohr-Coulomb law), and (b) density vs. shear modulus ($G_1 = 76.9$ MPa)			<i>Hydro tensile limit:</i> -1 kPa		
LS-DYNA	1,800 (initial)	<i>Soil and foam failure:</i> Piecewise linear function of volumetric strain vs. pressure, Bulk unloading modulus $K = 30$ MPa		Piecewise linear function of stress vs. yield (Mohr-Coulomb law), Shear modulus $G = 63.9$ MPa			<i>Tensile limit:</i> -6.9 kPa		

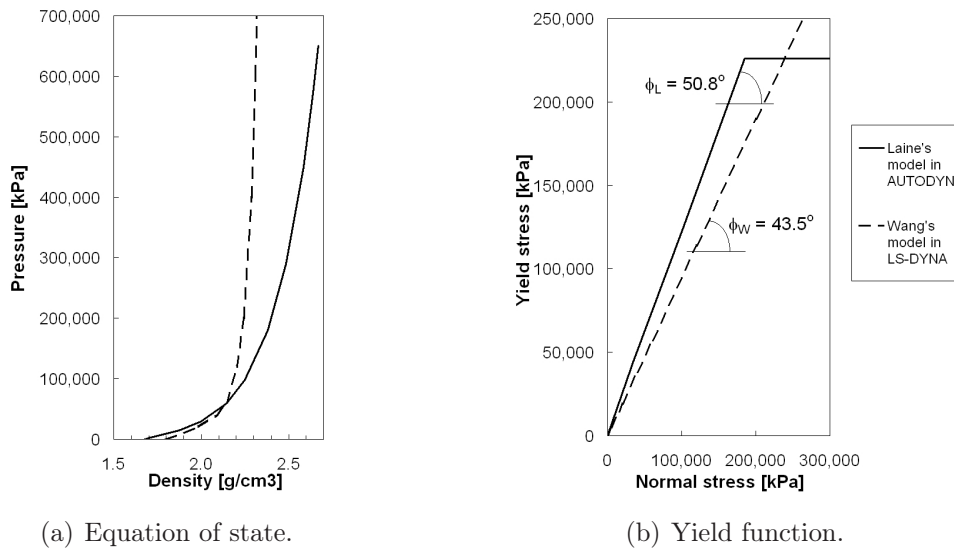


Figure 7.11: Material models for sand derived by Laine et al. [82] and Wang [121] used in AUTODYN and LS-DYNA, respectively.

A. Blast-wave parameters

The blast-wave parameters: time of arrival, maximum overpressure and specific impulse, for both the simulation setups and distances obtained from experiments and numerical simulations are presented in Table 7.7. These are graphically represented in Figure 7.12. Error bars in the figures represent the highest and lowest measured data.

Time of arrival. Time of arrival of the blast-wave front at the two measuring points is shown in Figure 7.12(a) for both the mine deployments. At a distance of 300 mm, the AUTODYN prediction for a buried charge produced a value 20% higher than the average measured value. In the case of a flush charge, AUTODYN predicted a time of arrival which was 20% underestimated. At 700 mm distance, the predictions of time of arrival are in good agreement with the measured data for both mine deployments. The LS-DYNA predictions for all four cases are in good agreement.

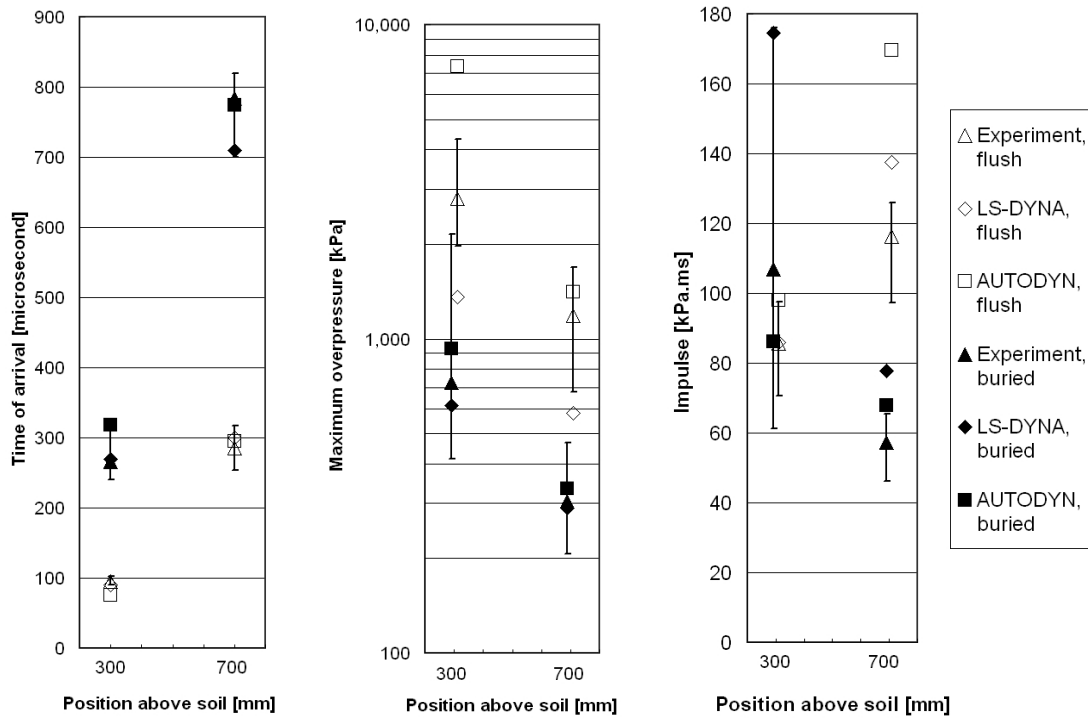
Overpressure. Figure 7.12(b) illustrates maximum overpressure at the two measuring locations for both the mine deployments. The measured maximum overpressure is characterised by wide variance in the data (showed as an error bar in

Table 7.7: Blast-wave parameters for different deployments in dry sand for 100 g C-4 charge.

Position above soil [mm]	Time of arrival [μs]					
	BURIED, DOB = 30 mm			FLUSH, DOB = 0 mm		
	Measured	LS-DYNA	AUTODYN	Measured	LS-DYNA	AUTODYN
300	266	270	318	94.8	90	76
700	784	710	774	285.6	300	295
	Maximum overpressure [kPa]					
	BURIED, DOB = 30 mm			FLUSH, DOB = 0 mm		
	Measured	LS-DYNA	AUTODYN	Measured	LS-DYNA	AUTODYN
300	724.8	613.3	929.7	2 797	1 359	7 380
700	304.5	290.1	334.1	1 189	580.8	1 409
	Specific impulse [kPa.ms]					
	BURIED, DOB = 30 mm			FLUSH, DOB = 0 mm		
	Measured	LS-DYNA	AUTODYN	Measured	LS-DYNA	AUTODYN
300	106.8	174.5	86.1	85.8	86	98.0
700	57.2	77.9	68.0	116.4	137.5	169.6

Figure 7.12). Except for the flush charge at 300 mm distance, the predicted values fall within the range of the measured values. The greatest AUTODYN overestimation (about 164%) was obtained for the flush charge at 300 mm distance. At the same distance, the AUTODYN prediction for the buried charge produced a value 28% higher than the average measured value. At 700 mm distance, the maximum overpressure was about 10% and 18% higher than the average measured values for the buried and flush charges, respectively. For the flush mine, the LS-DYNA results were about 50% lower compared with the average measured values for both the distances.

Specific impulse. Specific impulse at the two measuring points is depicted in Figure 7.12(c). At 300 mm distance, the AUTODYN buried charge underestimated experimental impulse by 19% and LS-DYNA overestimated by 63%. At the same distance, the AUTODYN flush charge gave 14% higher impulse than the experiments. At 700 mm distance for both the deployments, the AUTODYN and LS-DYNA numerical predictions are not within the range of the measured values and are overestimated. The AUTODYN numerical results for the buried and flush mines, are about 19% and 46% respectively higher than the average measured values.



(a) Time of arrival (b) Maximum overpressure (c) Specific impulse

Figure 7.12: Blast-wave parameters for both the mine deployments at measuring points of 300 mm and 700 mm above the ground surface.

B. Displacement parameters

Material displacements with regards to time were extracted from the simulation analyses and are presented in this section. Since soil is displaced upwards after detonation, the height of ejecta, and the crater diameter, were gathered. Expansion of the detonation products after breaking through the soil was characterised in terms of the height and width of the detonation products cloud. Displacement parameters were obtained “by hand” from plots of the material location.

Ejecta. Vertical soil displacement with respect to time is plotted in Figure 7.13. The detonation products break out through the soil at $201 \mu\text{s}$. At this time, soil ejecta reaches the maximum height of 174 mm (average experimental value). The numerical predictions of the soil displacement versus time showed a similar trend as the measured data. The height of ejecta obtained from AUTODYN underestimated the experimental value by about 16% and the LS-DYNA simulation produced a value that is 11% higher. In view of the difficulty in modelling soil behaviour, both numerical results are in reasonably good agreement.

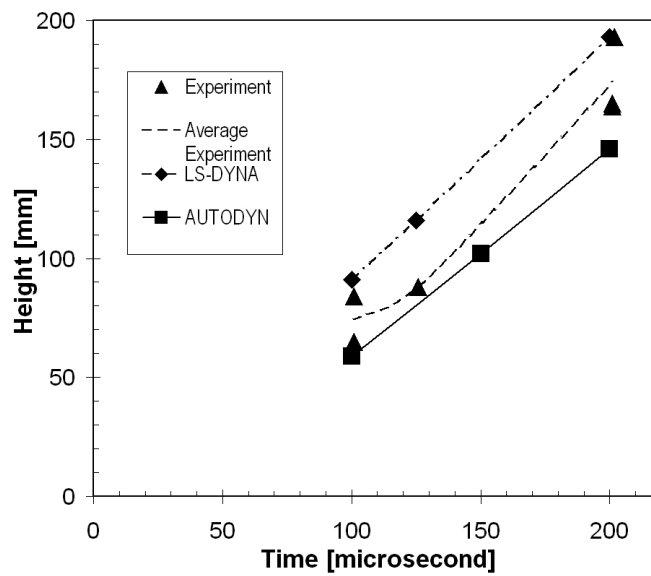
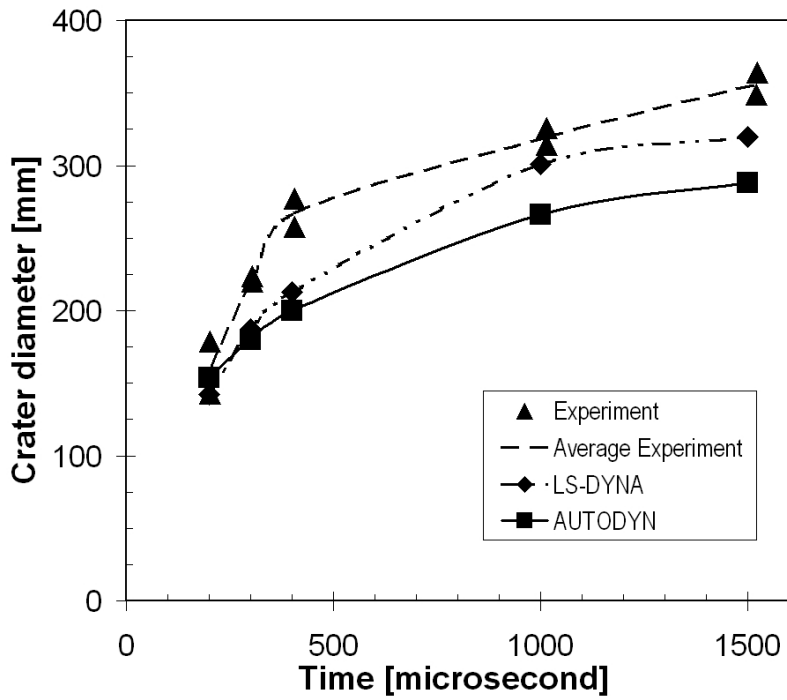
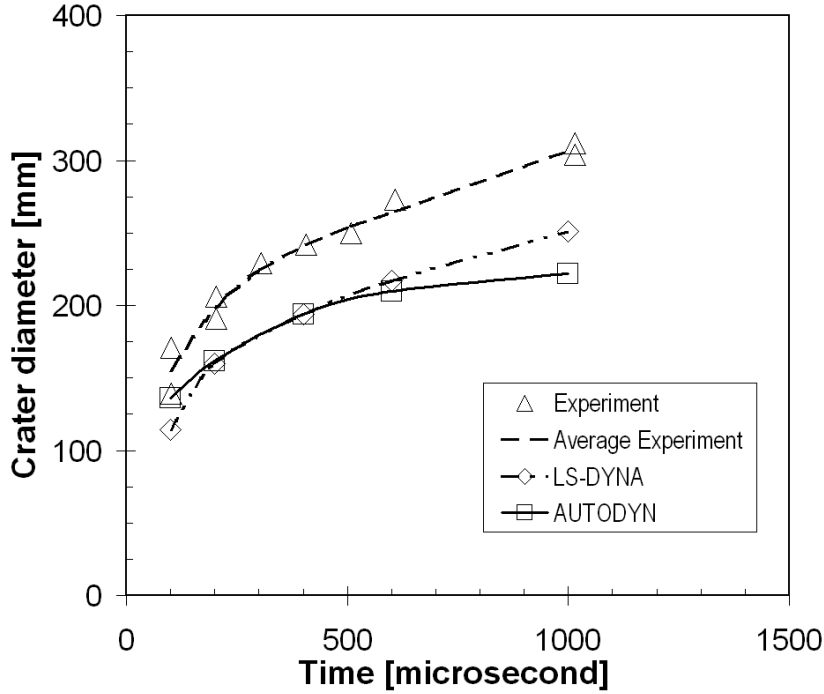


Figure 7.13: Time development of the height of ejecta caused by the explosion of 100 g C-4 in dry sand.



(a) Buried charge.



(b) Flush charge.

Figure 7.14: Time development of the width of crater caused by the explosion of 100 g C-4 in dry sand.

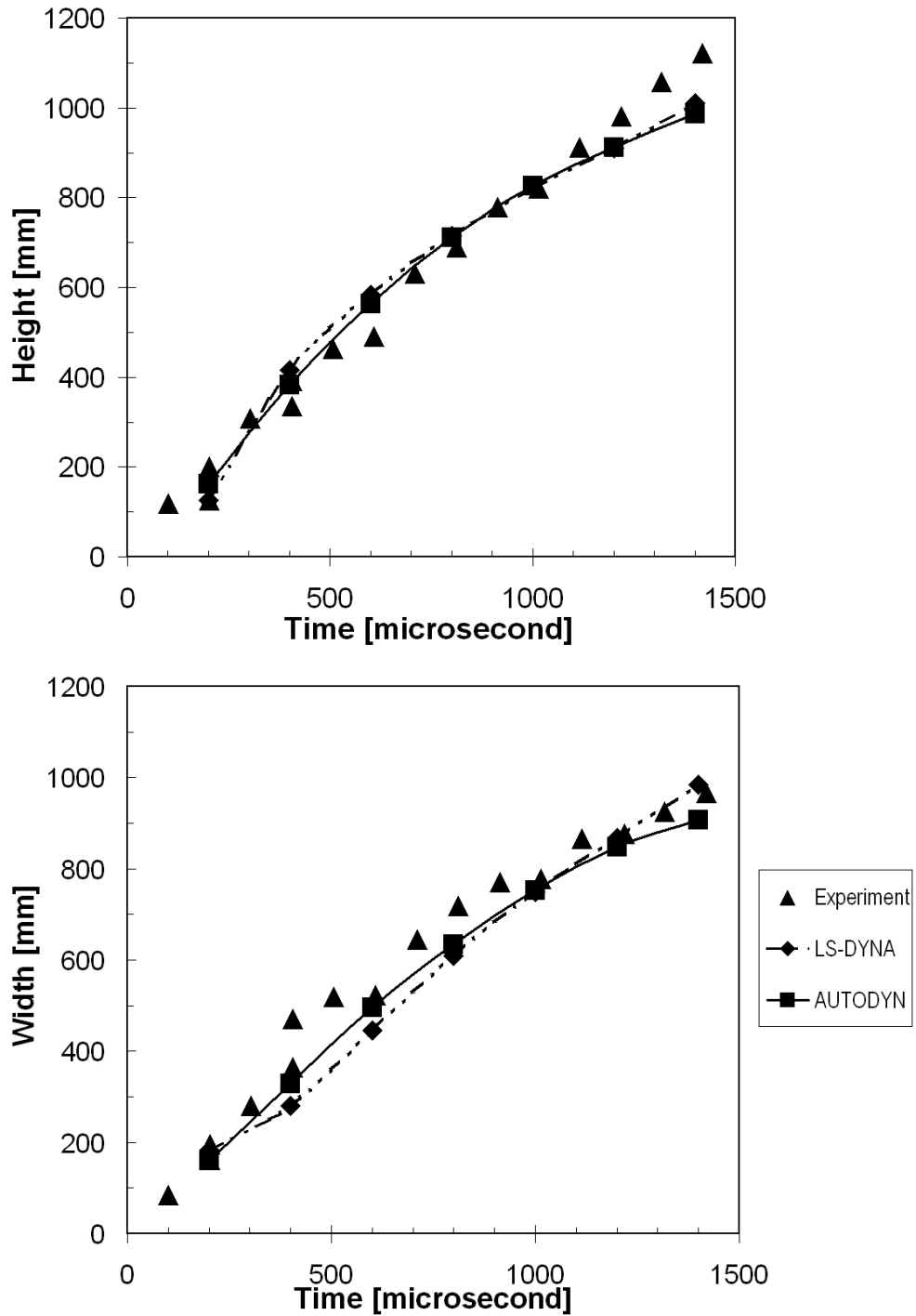


Figure 7.15: Time development of the detonation product cloud caused by 100 g C-4 buried in dry sand.

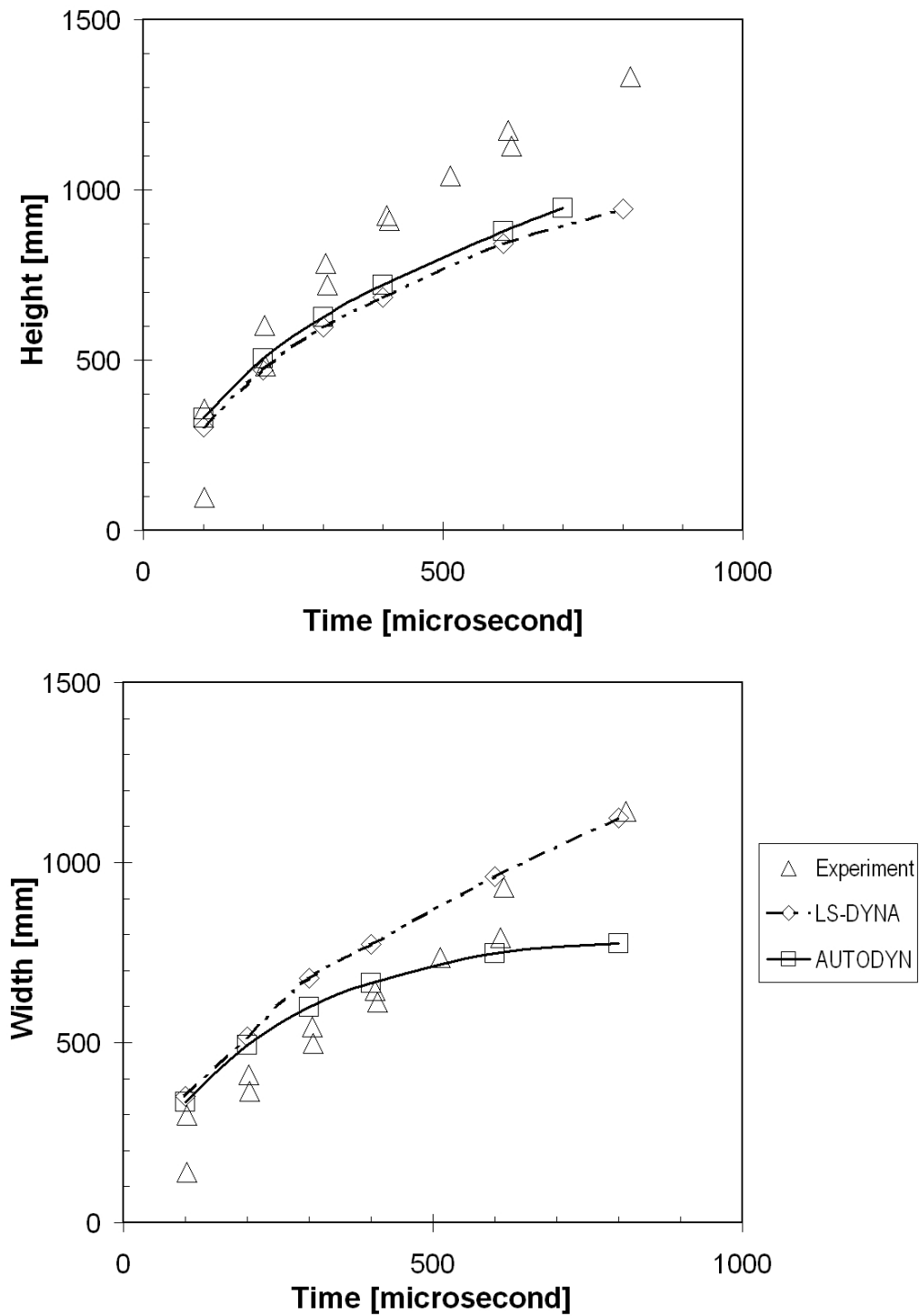


Figure 7.16: Time development of the detonation product cloud caused by 100 g C-4 laid flush in dry sand.

Crater. Crater formation with respect to time for the buried and flush mines is presented in Figure 7.14. A similar trend in crater formation was observed for the experiments and the numerical simulations. The final crater diameter for both the mine deployments was smaller compared to the experimental data for both the numerical tools employed. In the case of the buried charge, the experiments resulted in a crater diameter of 357 mm, while the AUTODYN result yielded a diameter of 288 mm, an underestimation of 19 %. The crater diameter obtained using AUTODYN for the flush charge is underestimated by about 28 %. The LS-DYNA crater diameters for the buried and flush charges are underestimated by 10 % and 19 %, respectively.

Detonation products cloud. The height and width of the detonation products cloud for the buried and flush charges are illustrated in Figs 7.15 and 7.16, respectively. In the case of the buried charge, the height and width of the detonation products cloud obtained using LS-DYNA and AUTODYN are in good agreement with the experimental data. The predictions for the flush charge were underestimated by about 30 % at 800 μ s.

7.2.3 Sensitivity analysis of the setup parameters

It will be recalled from Figure 7.12, that the measuring errors encountered in the experiments vary from 20 % to 80 %. As an explanation, Bergeron *et al.* [22] suggest that this variation (inconsistence) is due to the highly stochastic physical process in the investigated area. Furthermore, Held [62] also argues that the stochastic process and severe condition in the near-field of the explosion make measurements using pressure transducers unfeasible in order to obtain the intended parameters.

The recorded discrepancies in experiments raise questions regarding the sensitivity of the setup. Hence, a sensitivity analysis of the simulation runs is presented in this section. The sensitivity analysis investigates the influence of small differences in setup on the resulting blast-wave parameters. The advantage of using numerical simulations to study mine explosions is that the computational costs for re-runs is the only real costs when the experimental setup is varied. The measuring gauges, their position and number, can be varied in each simulation run. In contrast, the physical experimental setup is constrained by parameters such as the physical mounting for transducers. Therefore, numerical simulations are cost effective when compared with the cost of conducting experiments. Once the results are validated against the experimental results, it is possible to predict how credible the results obtained from a numerical simulation will be within tolerance bands. The sensitivity parameters are shown in Figure 7.17 and are as follows:

- A. *Position of detonation point* – The charge is initiated either on the top, middle or bottom of charge (referred as TOP, CENTRE and BOTTOM, respectively) as shown in Figure 7.17(a).
- B. *Transducer vertical location, Y* – distance of the transducer position above the ground; the investigated range is from 280 to 320 mm with increments of 10 mm.
- C. *Transducer horizontal location, X* – horizontal distance of the transducer from the symmetric axis; the analysed deviation ranges from 0 to 20 mm with increments of 2 mm.

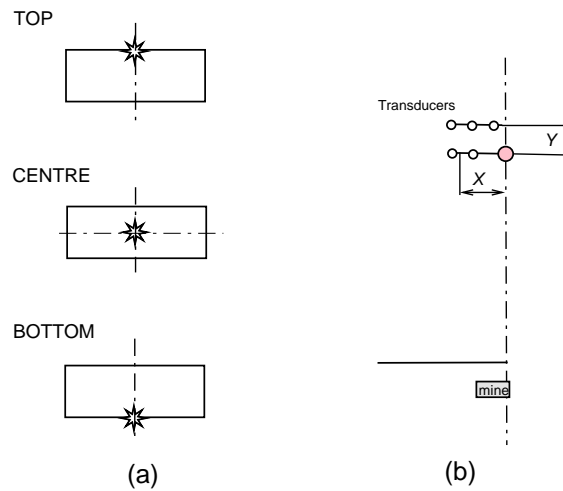


Figure 7.17: Sensitivity parameters: (a) Position of detonation point, (b) Position of transducers: X horizontal and Y vertical deviations.

From the descriptions of the experiments it is known that the recommended optimal setup is CENTRE initiation and the transducer is located on the symmetric axis at a distance of 300 mm above the ground. The AUTODYN model, as presented in Section 7.2.1, was used with the necessary changes in the position of detonation point for each case, with added measurement gauges in the locations described. A 1 mm mesh size was used for all the test runs.

The baseline for the sensitivity analysis is CENTRE position for detonation point, while default X and Y locations of the transducer are 4 mm and 300 mm, respectively. Therefore, the sensitivity coefficients can be expressed as follows for detonation point position:

$$S_{DPi}^f = \frac{f(i) - f(\text{CENTRE})}{f(\text{CENTRE})} \quad (7.2)$$

and for transducer deviations:

$$S_{Xi}^f = \frac{f(i) - f(4)}{f(4)} \quad (7.3)$$

$$S_{Yi}^f = \frac{f(i) - f(300)}{f(300)} \quad (7.4)$$

where $f(i)$ is either the pressure or impulse of the respective model configuration i .

A. Sensitivity of detonation point position

Figures 7.18 and 7.19 depict the maximum overpressure and specific impulse for different detonation point positions. The TOP model gives higher maximum overpressure and impulse than the CENTRE and BOTTOM models for all distances from the symmetric axis. The TOP model generates maximum pressure that is 10 % to 33 % higher, with increasing distance from the symmetric axis, when compared to the CENTRE model. The difference in maximum pressure between TOP and BOTTOM models reaches up to 52 % at 20 mm distance from the symmetric axis. The TOP yields about 9 % higher specific impulse than the BOTTOM model, within all the observed region. Clearly, the TOP model has the potential to generate more damage than the other models. Predictions of maximum pressure and specific impulse exhibit similar trends for all the distances between 280 and 320 mm above the ground.

In practice, the detonation point cannot be controlled to the degree that is made possible by numerical simulation. The simulation results point out that choice of detonation point position is not trivial when modelling mine explosions. Maximum pressure is significantly influenced by the detonation point position, although specific impulse is not so considerably affected.

B. Sensitivity of transducer vertical location

Figures 7.20 and 7.21 present maximum overpressure and specific impulse, respectively, for CENTRE models. The highest and lowest blast-wave parameters are predicted at 280 mm and 320 mm distance above the ground, respectively. The difference in the maximum pressure for different vertical location is not significant for distance from the symmetric axis greater than 12 mm. The vertical deviations affect the specific impulse more than the maximum pressure. For instance, maximum pressure differs by about 10 % at the most in the observed region, while the difference in specific impulse is up to 30 %.

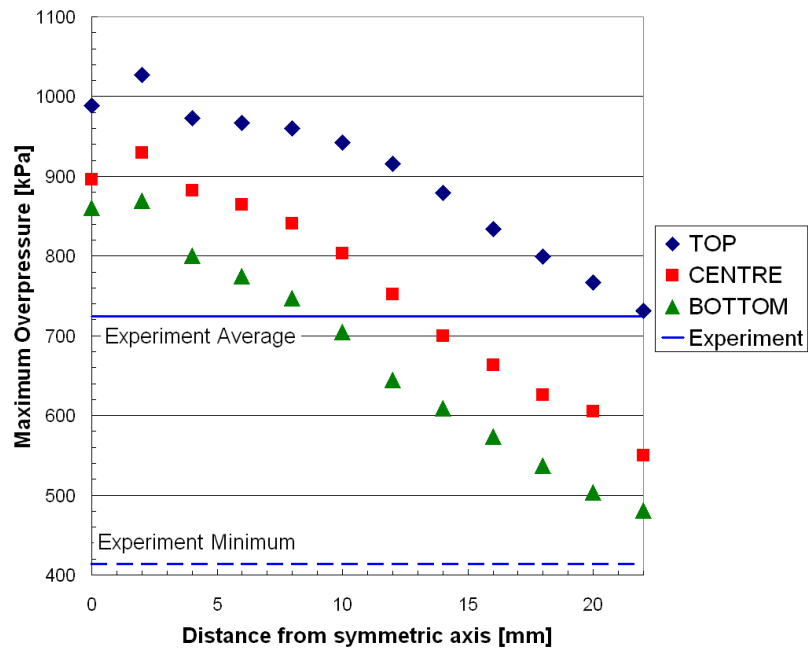


Figure 7.18: Sensitivity of detonation point position: pressure with respect to horizontal position of transducers at 300 mm above the ground.

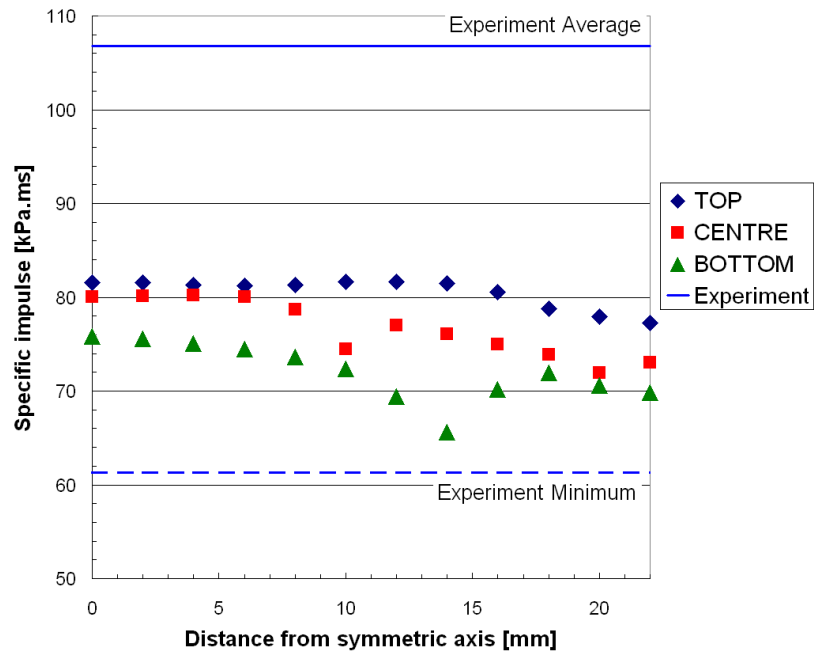


Figure 7.19: Sensitivity of detonation point position: specific impulse with respect to horizontal position of transducers at 300 mm above the ground.

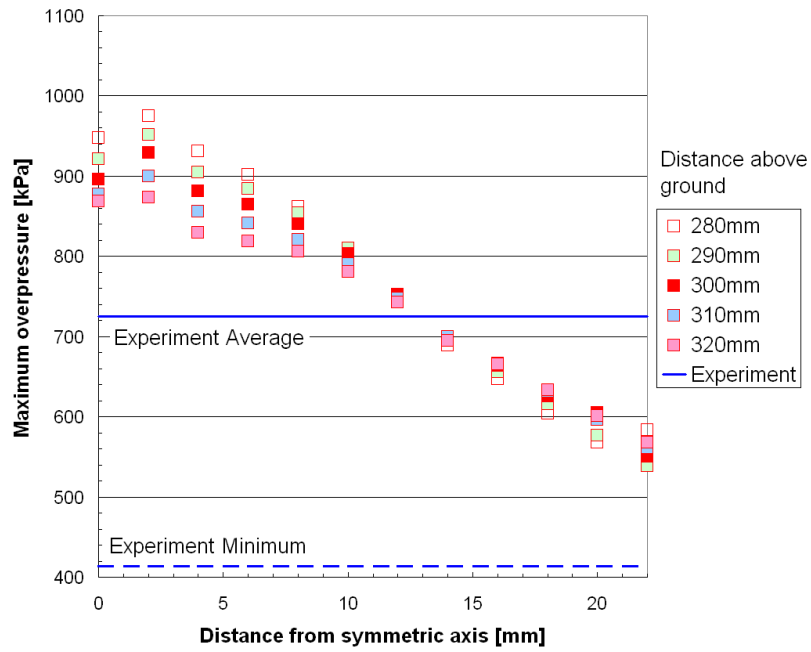


Figure 7.20: Sensitivity of transducer vertical deviation: pressure with respect to transducer horizontal deviation, charge initiated in the CENTRE.

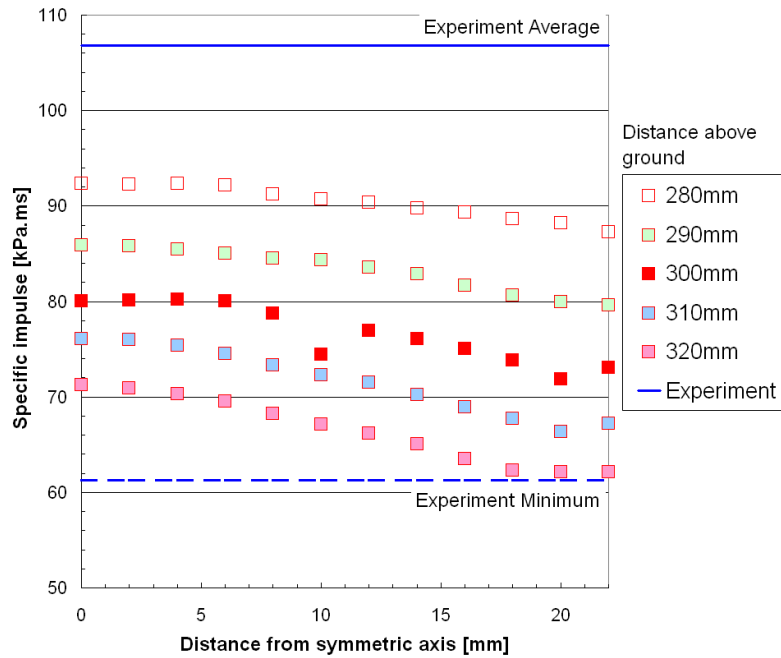


Figure 7.21: Sensitivity of transducer vertical deviation: specific impulse with respect to transducer horizontal deviation, charge initiated in the CENTRE.

C. Sensitivity of transducer horizontal location

Analysing Figures 7.18 and 7.20 with respect to horizontal deviation, it can be observed that the maximum pressure decreases markedly with increasing distance from the symmetric axis. A 10 mm change in horizontal distance reduces the maximum pressure by 20 %. The specific impulse is less affected by the horizontal deviation than the maximum pressure, as shown in Figures 7.19 and 7.21. The specific impulse decreases by 5 % at every 10 mm horizontal intervals.

7.2.4 Discussions

Deployment effect

The numerical predictions of the blast-wave parameters obtained using AUTODYN are more consistent with measured data at 700 mm distance than at 300 mm distance. This is consistent with our previous findings that the convergence of numerical results with experiment occurs with increased range from the charge centre [50]. Since the blast output is commonly assessed in terms of scaled distance³, the simulations discussed here, where 100g of C-4 is assessed at 300 and 700 mm distances, correspond to scaled distances of 0.636 and 1.484 m.kg^{-1/3}, respectively.

Since it is intended that numerical simulations might be used as a tool to improve the design of vehicles and demining equipment, it is important to consider the results with this in mind. When determining the most severe load, conservative estimates are preferred to non-conservative ones. The numerical predictions of the damage factors with respect to the experiments are graphically summarised in Figure 7.22. Generally, damage to a target can be caused by the following modes [58]:

- (a) *Overpressure* is responsible for damage if the vibration period of the target is short relative to positive phase duration. The discrepancy between the AUTODYN and measured maximum overpressures varied from 10 to 164 %, but in overestimation. In the case of LS-DYNA, the results differed with measured data by 5 to 51 %, but in underestimation, and therefore on this evidence the LS-DYNA results would provide an unsafe basis for protective design.
- (b) *Specific impulse* governs damage if the vibration period of the target is long relative to the positive phase duration. The AUTODYN and LS-DYNA predictions are overestimated in all the cases. The exception is the AUTODYN prediction for the buried charge at 300 mm distance which is underestimated

³Scaled distance is defined as $Z = R/W^{1/3}$, where R [m] is the distance from charge centre and W [kg] is the TNT equivalent charge mass.

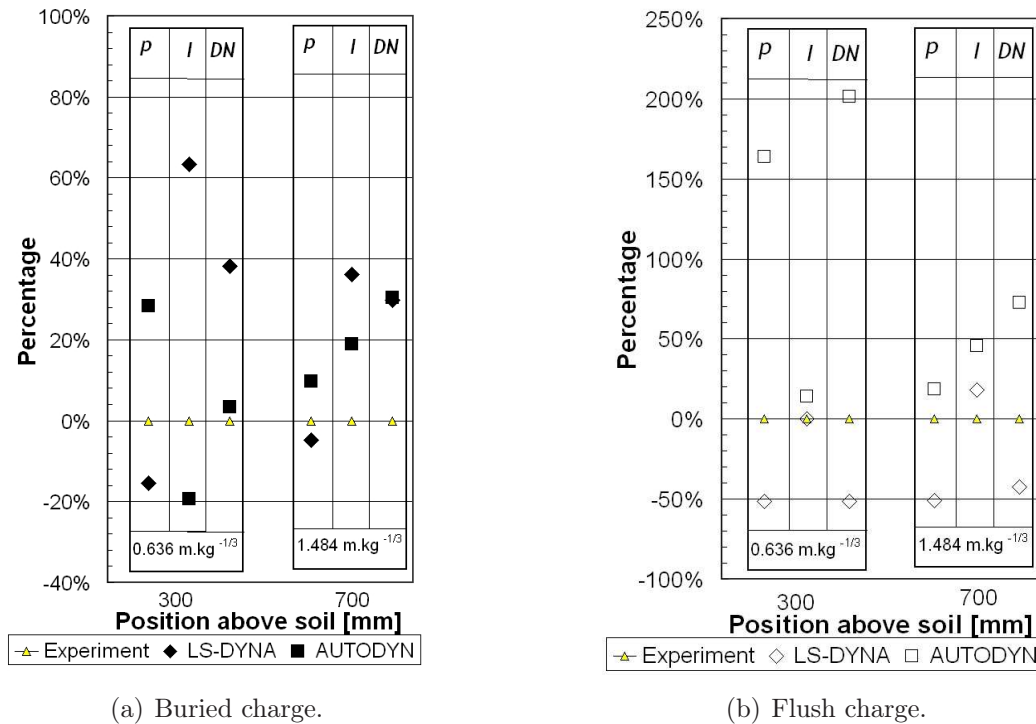


Figure 7.22: Evaluation of predicted damage factors, where p_{max} is the maximum overpressure, I is the specific impulse and DN is the damage number.

by about 19%. The AUTODYN and LS-DYNA predictions would form a reasonable basis for protective design.

- (c) In the iso-damage model, a combination of maximum overpressure p_{max} and specific impulse I is responsible for the damage. It is expressed by *Damage number*⁴. Considering a simplified damage number, the numerical predictions are overestimated by 30% for the buried charge at both the distances. The exception is the AUTODYN prediction at 300 mm distance, whose discrepancy with measured value is only 3%. In the case of the flush charge, AUTODYN predictions for both the distances are overestimated by 201 and 72%, respectively. LS-DYNA underestimated damage number by about 51 and 42%, respectively.

The difference between AUTODYN and LS-DYNA results can be attributed to differences in the *material models*. This difference is pronounced in the area of high

⁴Damage number is defined as $DN = (p - p_{cr})(I - I_{cr})$ [58]. Neglecting critical values p_{cr} and I_{cr} then damage number can be approximately expressed as $DN = I.p_{max}$

pressures (see Figure 7.11). There is a difference between the initial and “maximum” density, and the slope of the yield surface. In addition, the shear modulus in AUTODYN increases with sand compression (from 77 to 37,347 MPa). This change influences the shear component of the velocity by which the shock wave propagates in the sand. The shear modulus is constant in LS-DYNA (equal to 63.9 MPa). Derivation of the sand model used in AUTODYN is explained in detail by Laine *et al.* [82]. However, the sand model in LS-DYNA is from an internal report and the sand description (such as, moisture content and particle size distribution) is not presented.

When working with proprietary software, their internal workings (algorithms) are normally hidden from the user and therefore it is difficult to comment on efficacy of the models⁵. Overall, the solution methodologies are similar. Both AUTODYN and LS-DYNA simulations employed an *Eulerian mesh*⁶ which are solved in *two* steps. The first step is a Lagrangian step where the mesh follows the material flow and distorts. The second step is an advection step where the solution is mapped from the deformed mesh back onto the initial mesh. Furthermore, both software model the explosion process in a similar way, where a fraction of the explosive energy is inserted into the cell at the arrival time of the detonation wave.

Sensitivity of the setup

Insight into the overprediction of the maximum pressure came from the sensitivity study. The sensitivity analyses are summarised in Figure 7.23. The upper band represents the TOP model at 280 mm distance and the lower band is formed by the BOTTOM model at 320 mm distance. The maximum pressure varies from 33 to 44 % and specific impulse differs from 60 to 66 %, within the band.

By comparing the sensitivity analysis results with the experimental data we can observe the following: the maximum pressure is overpredicted by 41 % and underestimated by 32 % with respect to the average experimental value. The band of specific impulse lies between the average and minimum value of experimental data. In the other words, the best fit underpredicts the average experimental data by 5 %, the worst by 44 %.

The maximum pressure responds more sensitively than the specific impulse when setup parameters are varied. A 10 mm change in the horizontal distance decreases the maximum pressure by 20 %. As a consequence, the maximum pressure actually coincides with the average experimental value at 13 mm horizontal distance.

In practice, the detonation point cannot be controlled to the degree that is made possible by numerical simulation. The simulation results indicate that choice of

⁵Any comparison, that can be made, is only available from the manuals.

⁶In Eulerian mesh, materials flow through the spatially fixed mesh.

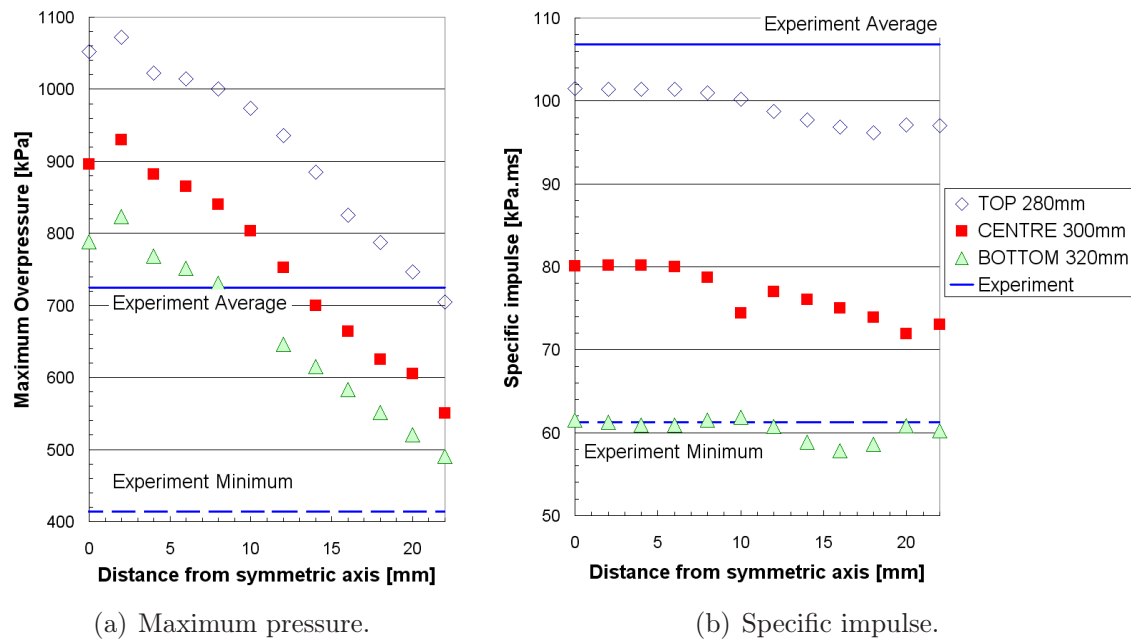


Figure 7.23: Sensitivity analysis of the setup parameters: the band of the results. Note that the maximum experimental values can be seen in Figure 7.12.

detonation point position is not trivial when modelling mine explosions, as maximum pressure is significantly influenced by the detonation point position (up to 52%), although specific impulse is not so considerably affected.

It can be concluded that the maximum pressure is considerably influenced by detonation point position and horizontal deviation. Whereas the specific impulse is more affected by change in vertical distance.

The experiments, the anecdotal evidence [22] and numerical simulation results lead to the conclusion that the blast-wave parameters measured by a pressure transducer do not capture the soil contribution to the loading caused by impinging soil ejecta. Furthermore, the parameters, in particular, maximum pressure, are very sensitive to the setup.

7.2.5 Concluding remarks

Blast-wave parameters (at the symmetry axis) and material displacement parameters were investigated for two mine deployments (buried and flush mines) in sand. The maximum overpressure and specific impulse predictions obtained using AUTODYN are in reasonable agreement with the experimental data, while LS-DYNA underestimated the maximum pressure values. The displacement parameters ob-

tained from both codes show good agreement with the experimental data, and it can be concluded that the *sand model* used is acceptable for explosion simulations of mines deployed in dry sand.

By analysing the soil-blast interaction in studies, it can be inferred that the value of the pressure magnitude is not sufficient to capture the effect of the explosion phenomena in the soil. In particular, the energy transferred to the soil, that forms clumps and moves upwards, does not contribute to the pressure measured by pressure transducers. This becomes relevant when dealing with soils having high moisture content (Bergeron *et al.* [19]). Therefore, different measuring methods for capturing the effect of soil contribution to the loading of the structure are proposed, such as the Mine Impulse Pendulum [19, 30]. The aim is to recreate these experiments, so as to assimilate the advantages discussed in our numerical simulations, along with the cohesive soil modelling.

7.3 Cohesive soil model validation using MIP

This section forms the principal part of this thesis. It is a comprehensive study, and the following tasks were undertaken:

- devise a soil model that allows moisture content to be varied,
- study the performance of several types of high explosives,
- evaluate several methods of mine deployment and
- assess the influence of soil properties towards the explosion process.

These studies combined with a numerical model of cohesive soil for varying soil composition form the major contribution of this thesis.

It will be recalled that, in the previous analyses, a sand model was derived for a particular composition (6.57% moisture content) and it was observed that there is no existing methodology to extend this sand model to different soil compositions. In Chapter 5, a methodology has been developed that derives the soil model for any given soil composition. In order to ascertain the validity of this methodology, comparison of the numerical results with experimental data is required. For the validation of soil model, the following is required:

- i. *Explosion experiment*: of HE charges buried in soil. Equal importance needs to be given to soil analysis, and consistency in the setup is paramount. The soil parameters (at least, moisture content) must be known for each trial.

Table 7.8: *MIP experiments matrix, distance above surface 400 mm.*

Deployment	Sand	Prairie soil	Steel
Surface-laid		C-4	C-4
Flush (DOB = 0 mm)		C-4	
Buried at 50 mm	C-4	C-4 TNT Comp-B	
Buried at 100 mm		C-4	

- ii. *Soil properties:* The physico-mechanical properties shall be determined for the same soil in which explosion experiments were carried out.

These two points will allow validation of the soil model. The experimental work [19, 30] conducted at DRDC-Suffield, Canada is highly beneficial for this research. The mine impulse pendulum (MIP) experiments are a thorough analysis of the effect of soil properties (principally, moisture content) on the impulse delivered to a horizontal pendulum. The experiments focussed on prairie soil, which is described as a sandy, silty clay, i.e., cohesive type soil. The table presenting the experimental matrix is re-written here as Table 7.8.

For an introduction to the experiment details and findings refer to Chapter 6, Section 6.3. Full details are in [19, 30]. The soil properties are given in Appendix D and are used to derive the soil model in Chapter 5.

Preliminary results, including the methodology of soil model derivation was disseminated in the *7th International Conference on Shock and Impact Loads on Structures* [49].

7.3.1 Setup of the MIP model

A two-dimensional axi-symmetric model was developed using multi-material solver (Euler) in AUTODYN to investigate the effect of:

- soil properties – sand and prairie soil of different phase compositions,
- methods of deployment – the charge is surface-laid, buried at the depth of 50 or 100 mm,
- types of explosives – the charge is C-4, TNT or Composition B.

A summary of the model setup is presented in Table 7.9. The mine was represented by 1 kg charge of high explosive⁷, which was described by the Jones-Wilkins-Lee equation of state [32]. Air was assumed to be an *ideal gas*. The numerical procedure was carried out in two steps (Chapter 4, Figure 4.5). In the first step, the high explosive charge is detonated. The detonation products expand, forcing soil to move upwards. In the second step, a plate was added to the model before the expanding gases and soil reached the height where the plate was located. The bottom of the plate was at 400 mm distance above the surface⁸. The automatic interaction is activated between Euler and Lagrange solver. Figure 7.24 depicts the modelling steps and shows the progress of the calculations using pressure contour.

The plate represents the horizontal pendulum arm in the experimental setup. The properties of the plate are equivalent to the properties of the mine impulse pendulum. The properties maintained are (i) the surface area which the explosion acts on, and (ii) moment of inertia. The derivation of the plate dimensions is described in Appendix C. The plate was modelled as a single Lagrangian element. The plate used IRON-ARMCO material model from AUTODYN library. The plate transfers the explosion energy into linear motion. The impulse delivered to the plate includes the kinetic energy of soil lumps impinging on the plate. The plate acts as a “momentum trap”. Neither the experiments nor this thesis studied the deformation of the plate. In other words, the impulse delivered to the plate captures the impulse produced by the air and by the soil. In previous studies, the impulse produced by the air only was considered. The value of delivered impulse is extracted from the AUTODYN history graph termed as **Momentum – plate**.

The prairie soil modelling was subdivided into several groups and is discussed in detail. The proposed methodology for soil model derivation is then benchmarked against Laine’s sand model. Lastly variations in explosives as well as the mine deployments were studied. This section presents the results in the order shown:

⁷This was varied during the course of this study. Charge mainly consisted of C-4. TNT, Composition B were also used.

⁸Corresponding to average vehicle ground clearance.

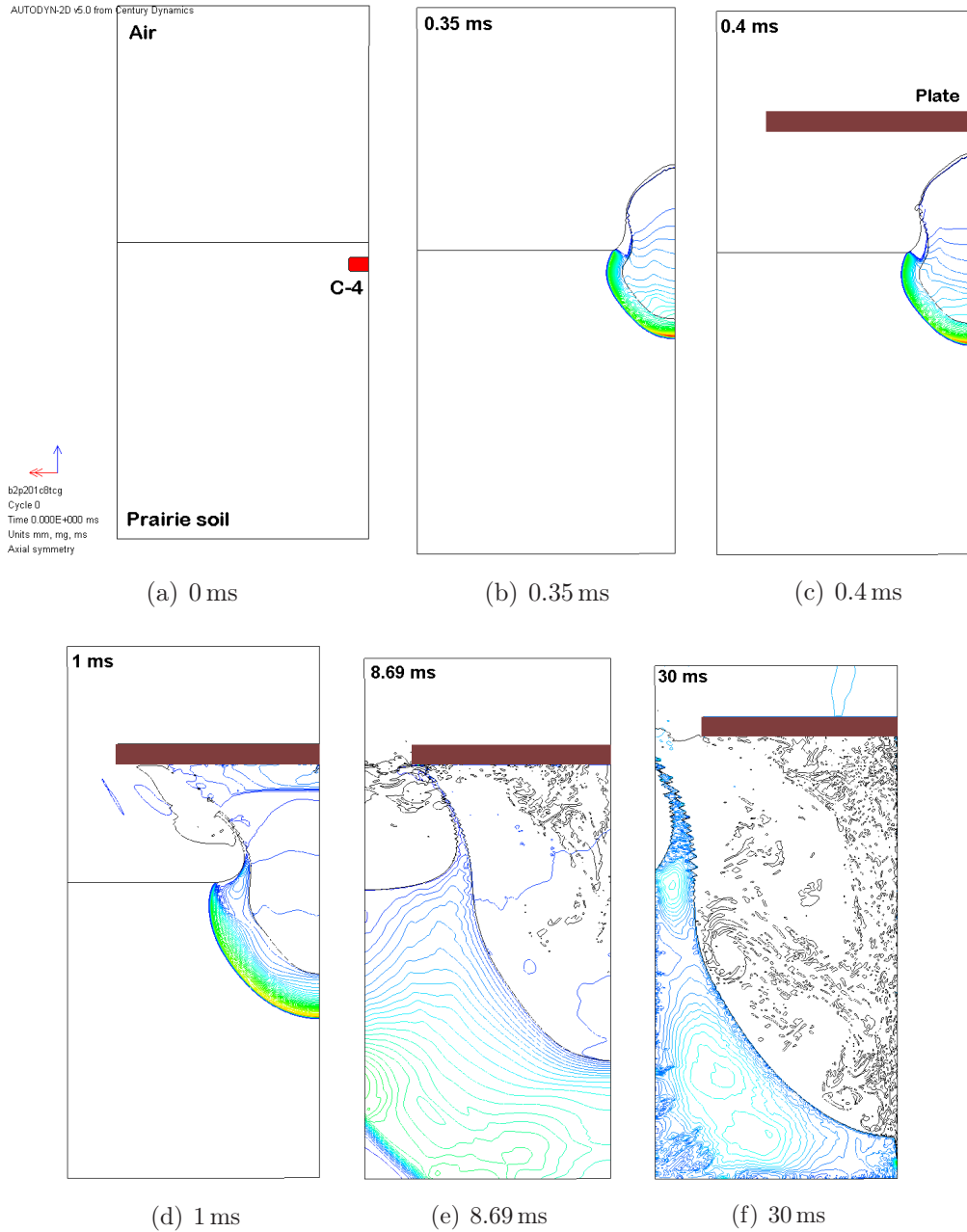


Figure 7.24: The modelling phases of the MIP experiments. (a, b) 1st step: without plate, (c) 2nd step: inserting the plate, (d, e, f) Pressure contours are shown.

Table 7.9: Model description of the recreated mine impulse pendulum experiments.

		Notes
	2D axi-symmetric model	
Solver	Euler	
Mesh dimension $((x_1, x_2) \times (y_1, y_2))$ [mm]	$(-1000, 800) \times (0, 850)$	
Cell size [mm]	6, 4 or 2	
Boundary conditions	Flow out	
Detonation point	Centre of the charge	
Gravity x-axis	- 9.80665	
Explosive EOS	(1) C-4 (2) Composition B (3) TNT JWL	
Surrounding material EOS	Air Ideal gas	
Soil	(i) Prairie soil (ii) Sand	refer to Section 5.3 and Table 7.11 Laine <i>et al.</i> [82] and refer to Section 5.4
Deployment	(a) rigid surface (b) surface-laid: DOB = -5 mm (c) buried: DOB = 50 mm (d) buried: DOB = 100 mm	
Plate mesh dimension [mm] D_{clc} clearance [mm]	Iron-Armco Lagrange, 1 element $\phi 1, 376 \times 68.76$ 400	AUTODYN library [32] automatic coupling Euler with Lagrange 806 kg distance above the ground
Measured parameter	Impulse delivered to the plate	

Validation of the prairie soil numerical model

1. *Rigid surface* – the C-4 charge was placed on a *rigid surface*. This setup allows us to verify the modelling procedure itself, as soil uncertainties are not included.
2. *Prairie soil* – the C-4 charge was buried at the depth of 50 mm in prairie soil. Prairie soil models are analysed for the following sensitivity parameters:
 - (a) Mesh size sensitivity
 - (b) Poisson's ratio
 - (c) Yield surface
 - (d) Failure criterion
3. *Sand* – the C-4 charge was buried at the depth of 50 mm in sand. The following sand models were studied:
 - (a) Sand model for sand of 6.57% moisture content, derived by Laine *et al.* [82],
 - (b) Sand models derived from a combination of prairie soil methodology and Laine's sand. Sand with varying moisture content.
4. *Explosives* – the following 1 kg charges were buried at the depth of 50 mm in prairie soil:
 - (a) C-4
 - (b) TNT
 - (c) Composition B
5. *Deployment* – In addition to the 50 mm overburden, the following deployments in prairie soil were analysed for C-4 charges:
 - (a) Surface-laid
 - (b) Buried at 100 mm

7.3.2 Rigid surface model

This was the first simulation which modelled the MIP. In the corresponding experimental setup, the charge rested on a steel bed. The bed represents a surface of perfect reflection. In AUTODYN, it was recreated as a rigid surface model. This setup enables us to evaluate the two-step modelling procedure for recreation of the MIP experiments, as soil behaviour is not involved. In particular, the load imparted to the plate, which is a substitute for the horizontal pendulum, is considered. The results are presented in Table 7.10. Meshes of 4 and 1 mm cell size were analysed. The predicted impulse overestimated the experimental data by 6 % and 13 %, respectively.

Table 7.10: *Impulse delivered to the plate caused by the explosion of 1 kg C-4 charge laid on the rigid surface.*

Overburden	Soil	Mesh size	Impulse	Difference to experiments
[mm]		[mm]	[Ns]	[%]
surface-laid	rigid	4	2 150	6
surface-laid	rigid	1	2 275	13

The simulation is in good agreement with the experimental data. This demonstrates that the plate characteristics are reasonable. The modelling procedure was also proved feasible. The next task is *to incorporate models of prairie soil*.

7.3.3 Prairie soil model and its sensitivity analysis

In this section, the soil models are validated. The modelling itself is one of the key features of this thesis because the soil model allows us to study soil with varying moisture content. As the experiments were mostly conducted using a 1 kg C-4 charge buried at 50 mm in prairie soil, this was taken as a benchmark. As with any other numerical modelling study, the effect of mesh size was analysed first. Once reasonable agreement with experiments was established, evaluation of the assumptions in soil model derivation was undertaken. In particular, investigation of the effect of Poisson's ratio, yield surface and failure criterion. These analyses also show the effect of each parameter of the soil model on overall soil behaviour. The various combinations of simulation runs are summarised in Table 7.11. The basic model serves as a baseline and other runs are compared against this model. Friction angle, φ , and cohesion, c , were varied throughout. Soil as an incompressible material forms

one of the case studies. Various limits for hydro-tensile failure criterion, p_{MIN} , were also investigated.

Table 7.11: *Parameter analysis conducted on the prairie soil model. (φ is the friction angle, c is the cohesion.)*

No.	Effect of	Yield surface		p_{MIN}	Poisson's ratio	Note
1.	Basic model	φ	c	c	$\nu = f(\alpha_{s0}, \alpha_{w0}, \alpha_{a0})$	
2.	Poisson's ratio	φ	c	c	$\nu = 0.499$	incompressible
3.	Yield surface	φ_{max}	c	c	$\nu = f(\alpha_{s0}, \alpha_{w0}, \alpha_{a0})$	
4.	Yield surface	φ	c_{max}	c_{max}	$\nu = f(\alpha_{s0}, \alpha_{w0}, \alpha_{a0})$	
5.	Yield surface	φ_{max}	c_{max}	c_{max}	$\nu = f(\alpha_{s0}, \alpha_{w0}, \alpha_{a0})$	
6.	Yield surface	φ_{triax}	c_{triax}	c_{triax}	$\nu = f(\alpha_{s0}, \alpha_{w0}, \alpha_{a0})$	triaxial parameters
7.	Failure criterion	φ	c	0	$\nu = f(\alpha_{s0}, \alpha_{w0}, \alpha_{a0})$	
8.	Failure criterion	φ	c	$5c$	$\nu = f(\alpha_{s0}, \alpha_{w0}, \alpha_{a0})$	

A. Mesh sensitivity

Numerical simulations are approximate solutions of the equations defining the problem, i.e., predictions are of certain computational accuracy. Therefore, the accepted practice is to run the simulations using several mesh sizes and accept only those results that converge to the experimental values (within acceptable tolerance levels). This is the purpose of this study.

In every simulation of MIP, the mesh employed was gradually spaced in both x - and y - directions in order to keep the runtime manageable. Fixed mesh sizes of 6, 4, and 2 mm were used for the regions that were most affected by the explosive process. Throughout the following discussions on the MIP model, when reference is to mesh sizes the description given above is assumed. The mesh size chosen also determines time-cost for the model. For example, the 6 mm mesh size models took about a day to complete, while the 2 mm mesh size models ran for 7 days or more.

Table 7.12 and Figure 7.25 show the results of the simulations. The soil conditions of the experiment have been recreated, and there are two options for comparing the results: (i) to compare numerical results with individual experimental results of a particular setup, and (ii) to fit a curve to the experiments and compare results with this trendline.

It was found that the curve fit approach led to the smoothing of experimental errors and yielded a quadratic curve⁹. The simulation results were compared against

⁹However, it can not be concluded that the results are dependent on a quadratic function.

the fitted curve. The key observations are as follows: Simulations with 6 mm mesh size overestimate the quadratic fit by 10 to 20 %. The numerical results converge when using mesh sizes of 4 and 2 mm. However, all the numerical results agree reasonably well with the experiments. As a consequence, it was decided to perform all further sensitivity analyses on the 6 mm mesh size, as completion time of the simulations was acceptable (1 day vs 7 days) and the sensitivity of the simulations was maintained.

Table 7.12: *Mesh sensitivity: impulse delivered to the plate caused by the explosion of 1 kg C-4 buried at 50 mm in prairie soil.*

1 kg C-4, Prairie soil, DOB = 50 mm, $D_{clc} = 400$ mm			
Moisture content	Mesh size	Impulse	Difference to quadratic fit of experiments
[%]	[mm]	[Ns]	[%]
7.7	6	3 416	18
	4	2 549	-12
	2	2 898	0
9.8	6	3 578	18
	4	3 202	6
	2	3 426	13
15.0	6	4 585	29
	4	3 246	-9
	2	3 601	1
17.5	6	4 783	23
18.2	6	4 908	23
20.1	6	4 836	12
	4	4 388	2
	2	4 590	7
20.2	6	4 839	12
20.5	6	4 825	10
23.2	6	5 255	8
28.7	6	6 098	0
	4	5 296	-13
	2	5 297	-12

B. Influence of Poisson's ratio

For representing the strength model in AUTODYN, the relationship between the shear modulus and density is needed. The shear modulus is calculated using the bulk

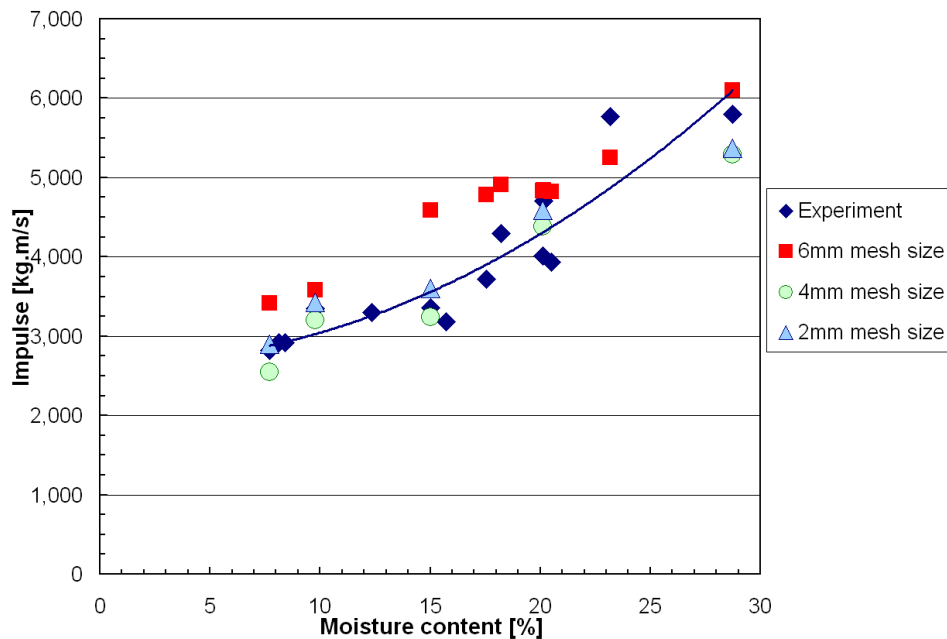


Figure 7.25: Mesh sensitivity: the influence of mesh size on the impulse delivered to the plate. [1 kg C-4, Prairie soil, DOB = 50 mm, $D_{clc} = 400$ mm]

modulus and Poisson's ratio. The bulk modulus is determined from the equation of state. Poisson's ratio corresponds to the soil behaviour. We consider two cases:

- i. *Compressible soil:* $\nu = f(\alpha_{s0}, \alpha_{w0}, \alpha_{a0})$

The soil behaves like a compressible material. Dry soil is more compressible than wet. Therefore, the relationship among the soil phases was used to determine Poisson's ratio (Eq. 5.24) that corresponds to the observed trend. In MIP simulation, Poisson's ratio varies from 0.2196 to 0.3670.

- ii. *Incompressible soil:* $\nu = 0.499$

In this model it is assumed that during the rapid loading soil behaves like an incompressible material, as there is no time for air to be pressed out from the voids.

Table 7.13 presents the results. As shown in Figure 7.26, the influence of Poisson's ratio is not significant. In some cases, the difference between the models of different Poisson's ratio is 1%, with the maximum difference being 8%. The remaining models studied were derived using Poisson's ratio that is based on soil phase composition.

Table 7.13: *Poisson's ratio: impulse delivered to the plate caused by the explosion of 1 kg C-4, charge buried at 50 mm in prairie soil.*

1 kg C-4, Prairie soil, DOB = 50 mm, $D_{clc} = 400$ mm				
Moisture content	Mesh size	Impulse		Difference between models
		$\nu = f(\alpha)$	$\nu = 0.499$	
[%]	[mm]	[Ns]	[Ns]	[%]
7.7	6	3 416	3 690	8
9.8	6	3 578	3 620	1
15.0	6	4 585	4 629	1
20.1	6	4 836	5 218	8
28.7	6	6 098	6 341	4

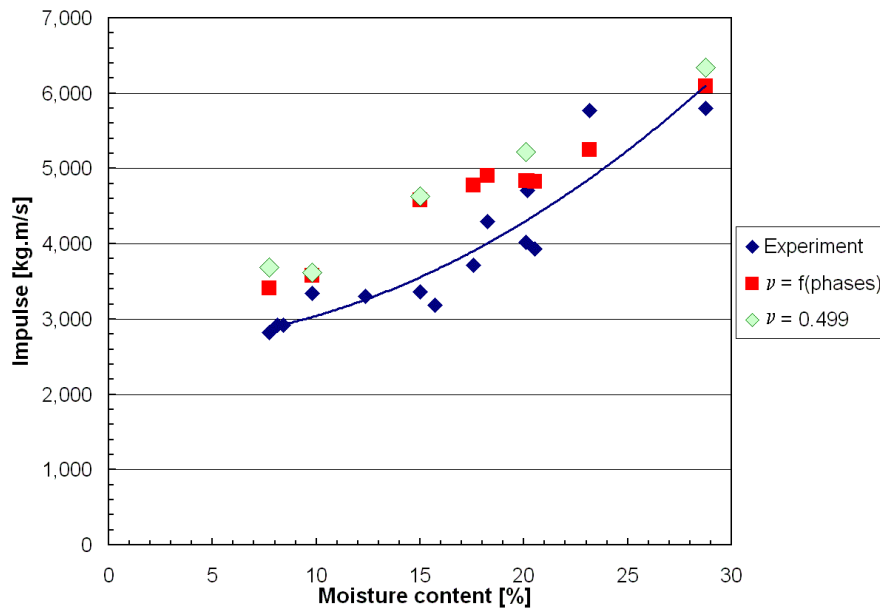


Figure 7.26: *Poisson's ratio: influence of Poisson's ratio on the impulse delivered to the plate. [1 kg C-4, Prairie soil, DOB = 50 mm, $D_{clc} = 400$ mm]*

C. Influence of yield surface

A material's resistance to shear is determined by its yield surface. This is part of the strength model. For soil, yield surface is given by a linear relationship between normal and yield stress. The friction angle, φ , is the slope and the cohesion, c , is the intercept of this linear relation. For demonstration purposes, analyses of the influence of friction angle and cohesion were performed on the prairie soil having 15% moisture content. The yield surface does not change significantly when cohesion is varied with the moisture content, and friction angle is kept constant (recall Figure 5.5). Table 7.14 presents the analysed values along with results. Figure 7.27 graphically represents results. The observations are:

- i. *Slope*: A six-fold increase of friction angle resulted in a 37% decrease in the impulse compared to the basic model (see Table 7.11).
- ii. *Cohesion*: Impulses decreases by about 7% when the cohesion is increased by a factor of 3.7.
- iii. *Slope and cohesion*: For the model with maximum friction angle and cohesion the impulse decreased by 38%. The prairie soil model of 17.5% moisture content was run with the friction angle and cohesion obtained from triaxial tests (omitting the first circle, Figure 5.3). In this case, the increase of friction angle and cohesion by 2.2 and 8.9 times, respectively, predicted the impulse about 14% lower than the basic model.

The friction angle assumption is based on the trendline of statistical data. The value obtained from the triaxial test of prairie soil agrees well with the trendline. We believe that the derived friction angle is a reasonable representation of prairie soil. In future analyses, care must be taken to determine friction angle, as it considerably influences the soil behaviour. Uncertainties remain about the assumptions made for cohesion, but the cohesion does not significantly affect the results.

D. Influence of failure criterion

Soil cannot sustain large tensile stresses, therefore the hydro-tensile failure criterion was employed. In the basic model analysis, the limit of the hydro-tensile criterion was set as $p_{MIN} = -c$, where c is the cohesion. The underlying idea is that failure occurs when soil cohesion becomes negative, i.e. no longer sticking. As before, a model of soil having 15% moisture content was used for investigating the sensitivity of the tensile limit:

Table 7.14: Yield surface: impulse delivered to the plate caused by the explosion of 1 kg C-4, charge buried at 50 mm in prairie soil.

1 kg C-4, Prairie soil, DOB = 50 mm, $D_{clc} = 400$ mm					
Moisture content	Mesh size	Yield surface		Impulse	Difference between models
		friction angle	cohesion		
[%]	[mm]	[°]	[kPa]	[Ns]	[%]
15.0	6	4.27	16.32	4 585	0
15.0	6	26.22	16.32	2 890	-37
15.0	6	4.27	60.57	4 259	-7
15.0	6	26.22	60.57	2 833	-38
17.5	6	4.27	12.82	4 783	0
17.5 triax	6	9.25	114	4 108	-14

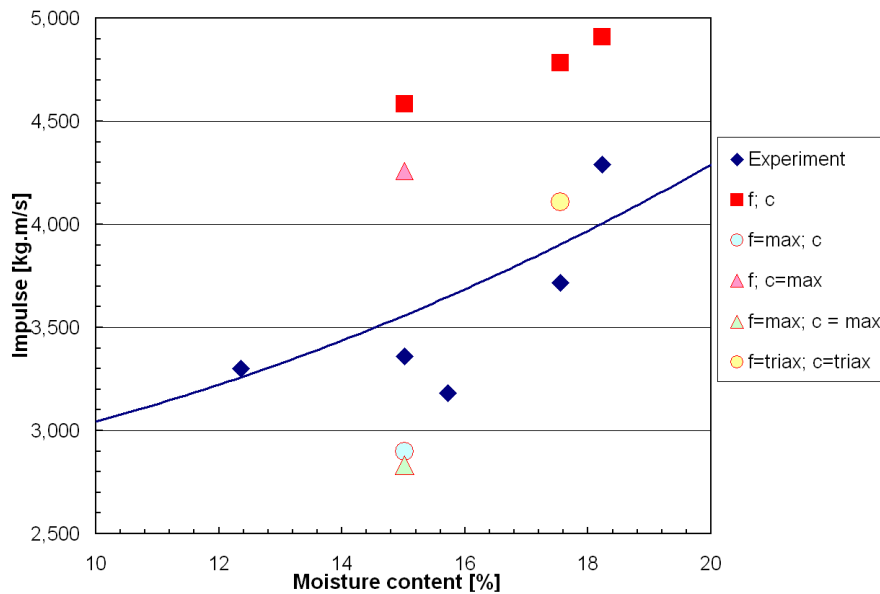


Figure 7.27: Yield surface: influence of yield surface parameters on the impulse delivered to the plate. [1 kg C-4, Prairie soil, DOB = 50 mm, $D_{clc} = 400$ mm]

- i. $p_{MIN} = -1 \text{ kPa}$
- ii. $p_{MIN} = -5c$

Table 7.15 and Figure 7.28 present the results. It can be observed that there is no significant change in the impulse when the hydro-tensile limit is changed. Even when the hydro-tensile limit is increased 5-fold, the corresponding impulse increases by 1%. While reducing it to -1 kPa (representing zero), the impulse decreases by 5%. Further analyses (for different setups) are performed with the hydro-tensile limit $p_{MIN} = -c$.

Table 7.15: *Failure criterion: impulse delivered to the plate caused by the explosion of 1 kg C-4, charge buried at 50 mm in prairie soil.*

1 kg C-4, Prairie soil, DOB = 50 mm, $D_{clc} = 400 \text{ mm}$				
Moisture content	Mesh size	p_{MIN}	Impulse	Difference
[%]	[mm]	[kPa]	[Ns]	[%]
15.0	6	$-c = -16.3$	4 585	0
15.0	6	-1	4 343	-5
15.0	6	$-5c = -81.6$	4 654	1

7.3.4 Derived sand models

The methodology that was used to derive the prairie soil model was applied to sand. Sand properties for the MIP experiments were unavailable, so the model data derived by Laine *et al.* [82] and statistical data (Vrtek [119]) were used. The sand models were described in Chapter 5, Section 5.4. The following were considered:

- i. Laine's sand model which was derived for sand having moisture content of 6.57%.
- ii. Sand models derived based on soil composition.

Both sand models mentioned above use the same material components in AUTODYN., i.e., Compaction EOS, Granular strength model, and hydro-tensile failure criterion. The present sand model differs to Laine's in the values of sound-speed and shear modulus (refer to Figure 5.6).

Table 7.16 and Figure 7.29 present the results of the simulations. The sand models agree well with the experimental data for moisture content 0.5 and 6%. For 16% moisture content, the numerical results underestimated the experiments by 30%.

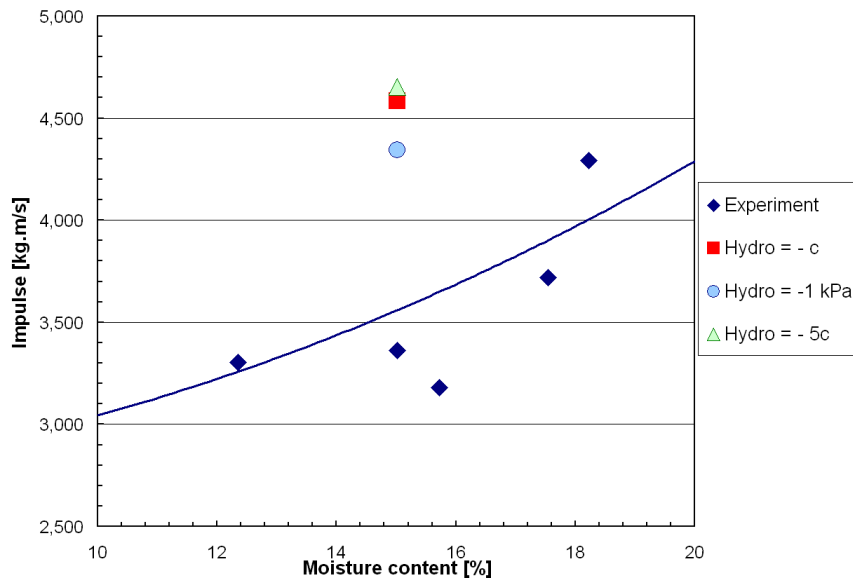


Figure 7.28: Failure criterion: the influence of hydro-tensile limit on the impulse delivered to the plate. [1 kg C-4, Prairie soil, DOB = 50 mm, $D_{clc} = 400$ mm]

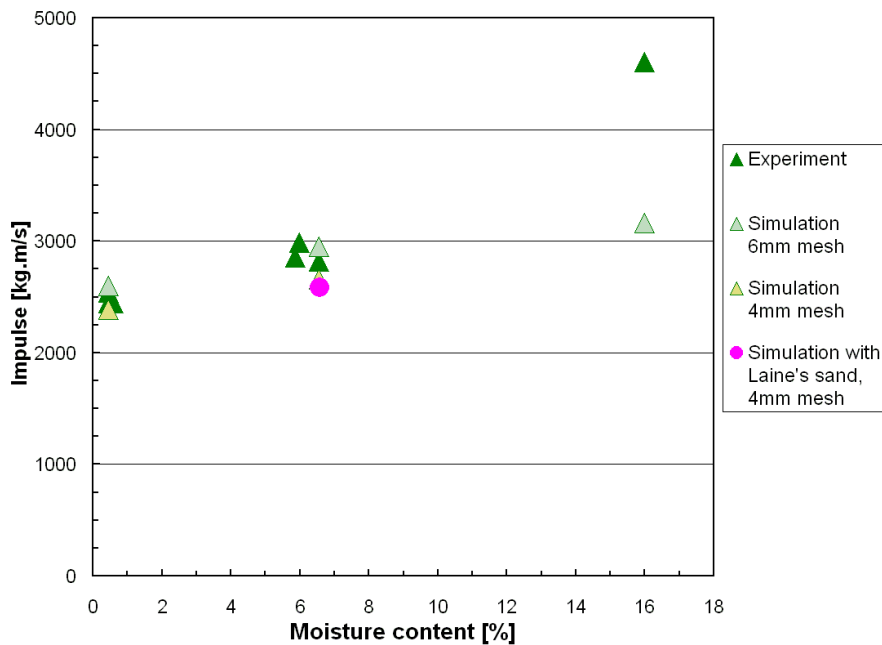


Figure 7.29: Sand models: the influence of sand properties on the impulse delivered to the plate. [1 kg C-4, Sand, DOB = 50 mm, $D_{clc} = 400$ mm]

Table 7.16: *Sand models: impulse delivered to the plate caused by the explosion of 1 kg C-4 buried at 50 mm in sand.*

1 kg C-4, Sand, DOB = 50 mm, $D_{clc} = 400$ mm				
Soil	Moisture content	Mesh size	Impulse	Difference to experiments
	[%]	[mm]	[Ns]	[%]
Sand	0.5	4	2 600	6
Sand	6.57	4	2 586	8
Laine		2	2 455	13
Sand	6.57	4	2 953	5
Sand	16.0	4	3 165	31

7.3.5 Effect of explosives type

The general applicability of the numerical model is considered. The reason is that modelled soil behaviour should be independent of the high explosive type. High explosives differ in the heat of explosion, maximum pressure and detonation velocity, and this in turn influences the damage to the target structure. Therefore, the experiments and simulations are used to analyse the effect of the different explosive charges. In addition to the C-4 charges, Composition B and TNT (both of 1 kg weight) are also investigated.

Table 7.17 and Figure 7.30 present the findings. Models using Composition B underestimated experiments by 11 to 20 %. Simulation with TNT charges yielded about 40 to 49 % higher impulse than the experiments. It is to be noted that in one case, a TNT model predicts about 90 % higher impulse than experiments. The large discrepancy is on account of the comparing values with inconsistent values that were obtained during multiple experiment trials for the same moisture content (see Figure 7.30). The correspondence with DRDC-Suffield that followed, specified that only 930 g TNT was detonated instead of 1 kg in the model. Therefore, the simulation was repeated for charge of 930 g TNT (see Table 7.17). During the modified run, the overestimation decreased from 49 % to 39 %. Since simulations have behaved consistently in all other previous cases, and it is suggested that the TNT explosion process has been represented and modelled more thoroughly in the model than the actual experimental behaviour. The reasons for this are explained in greater detail, during the discussions.

Table 7.17: High explosives: impulse delivered to the plate caused by the explosion of 1 kg HE buried at 50 mm in prairie soil.

1 kg HE, Prairie soil, DOB = 50 mm, $D_{clc} = 400$ mm				
Moisture content	Mesh size	Explosive	Impulse	Difference to experiments
[%]	[mm]		[Ns]	[%]
8.2	6	Composition B	2 484	-11
8.7	6	Composition B	2 500	-16
10.9	6	Composition B	2 377	-20
9.3	6	TNT	2 345	49
9.3	6	TNT (930 g)	2 189	39
9.5	6	TNT	2 402	90
9.9	6	TNT	2 254	40
7.7	6	C-4	3 416	21
9.8	6	C-4	3 578	7

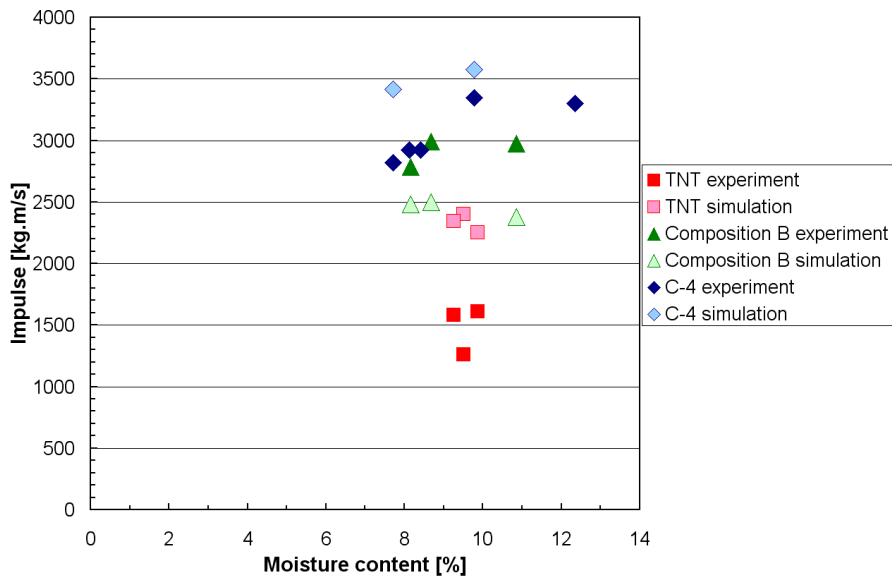


Figure 7.30: High explosives: influence of high explosive type on the impulse delivered to the plate. [1 kg C-4/TNT/Composition B, Prairie soil, DOB = 50 mm, $D_{clc} = 400$ mm]

7.3.6 Effect of deployment in prairie soil

Having validated the soil model against different HE charges, the mine deployment is considered. Anecdotal evidence [22] indicates that buried charges can inflict more damage. By ascertaining this, the model extensibility for different methods of deployment is demonstrated. Two cases are analysed. The charge was laid on the surface or buried at the depth of 100 mm. Table 7.18 presents the results for both deployments.

Surface-laid charge. Figure 7.31 depicts the results. The impulse obtained from the surface-laid charges is not considerably influenced by the soil moisture content. The numerical simulation confirms this trend. The numerical simulation underpredicts the experiments by 3 to 15 %. Recalling the rigid surface results (Table 7.10), it is observed that the surface type, prairie soil or rigid surface, does not affect the total impulse delivered to the pendulum.

Charge buried at 100 mm. Figure 7.32 shows the results. The numerical simulations agree well with experimental data for the whole range of moisture content (7 to 25 %). The predictions overestimated experiments by 0 to 10 %. The 32 % overestimation is caused due to a low (inconsistent) value from the experiment. The experimental value is clearly under the trendline. For clarity, it is mentioned that the numerical and experimental impulse for 25 % moisture content coincides in Figure 7.32.

7.3.7 Discussions

The validity of the proposed model has been proved by subjecting it to numerous validation runs, and by comparing the output with results from the MIP experiments. In every stage of validation, results confirmed the soil behaviour exhibited by the experiments across the range of moisture. In addition, by conducting a parametric study of soil parameters, the components that affect the soil behaviour under the explosion process, have been identified.

Cohesive soil: Prairie soil

Extensive analysis was conducted of the different components of the prairie soil model. Furthermore, the prairie soil model was exposed to several different setups, in particular, deployments and high explosive charges. It was shown that the numerical results are consistent with experiments across the entire range of moisture content.

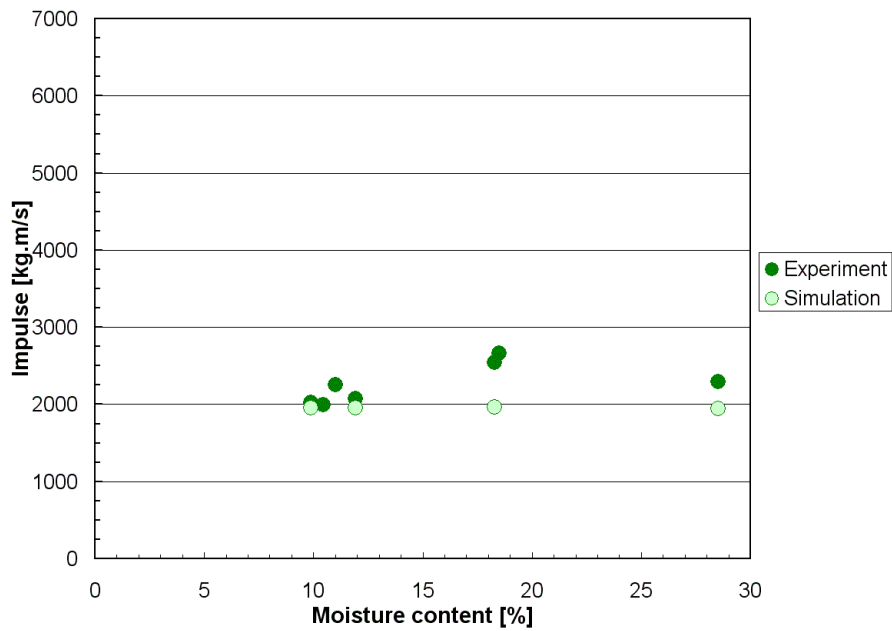


Figure 7.31: Surface-laid charge: impulse delivered to the plate. [1 kg C-4, Prairie soil, DOB = -50 mm, $D_{clc} = 400$ mm]

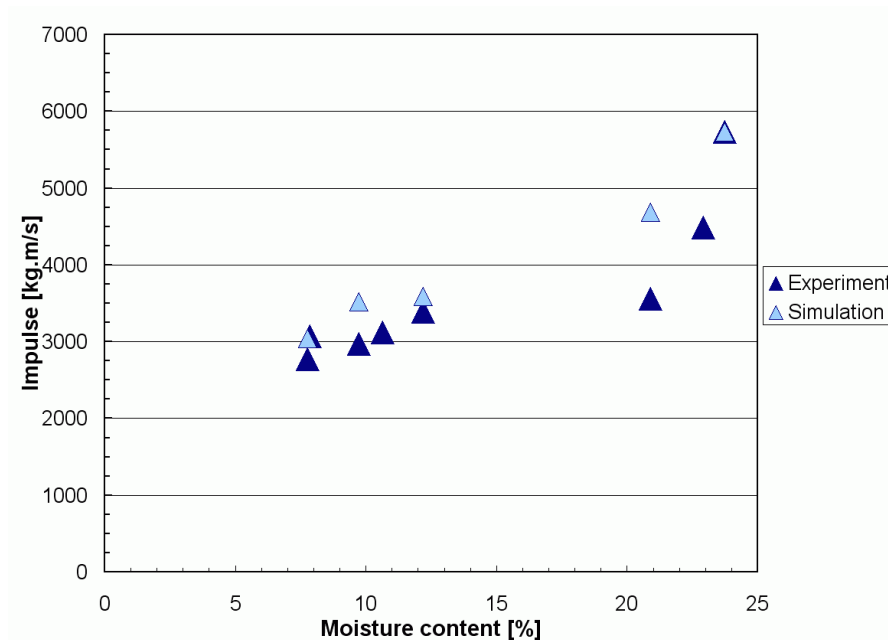


Figure 7.32: Charge buried at 100 mm: impulse delivered to the plate. [1 kg C-4, Prairie soil, DOB = 100 mm, $D_{clc} = 400$ mm]

Table 7.18: *Deployment: impulse delivered to the plate caused by the explosion of 1 kg C-4 for various deployment in prairie soil.*

1 kg C-4, Prairie soil, $D_{clc} = 400$ mm			
Moisture content	Mesh size	Impulse	Difference to experiments
[%]	[mm]	[Ns]	[%]
Charge surface laid			
9.9	4	1 953	-3
	2	1 938	
11.9	4	1 954	-6
18.3	4	1 962	-23
28.5	2	1 942	-16
Charge buried at the depth of 100 mm			
7.8	6	3 044	10
9.7	6	3 523	18
12.2	6	3 591	6
20.9	6	4 686	32 _{exp. low}
23.7	6	5 732	0

A significant observation of this proposed soil modelling methodology is that the model is able to track the experimental behaviour. In other words, explosions in soil having high moisture content results in higher loading (impulse) in both experiments and simulations. The accuracy of the model results are such that it was possible to track experimental inconsistency successfully, such as in the TNT case. Also, the model is extensible enough to allow a parametric study of the soil properties and their influence on mine explosion output.

Influence of soil properties. The influence of soil parameters towards the dynamic loading is summarised:

- *Poisson's ratio:* Although two opposite assumptions of soil behaviour, compressible and incompressible, were investigated, it can be concluded that Poisson's ratio does not influence the prediction.
- *Yield surface:* The soil strength is expressed by the friction angle and cohesion, which are determined from triaxial tests. The study shows that friction angle is dominant in soil strength behaviour. The change in friction angle considerably affects the numerical prediction. The cohesion slightly influences the soil response.

- *Hydro-tensile failure criterion:* This criterion is based on the knowledge that soil cannot sustain large tensile stresses. The actual value does not play an important role in the soil behaviour. It is suggested that this is due to the fact that the soil is subjected to the compression and tension occurs in very small region.

High explosive charges. The model was extended to different high explosive charges. The simulations employing C-4 and Composition-B agreed reasonably well with experiments. Simulations using TNT charges overpredicted the experiments by about 40%. Through discussions with DRDC-Suffield, it was concluded that this is caused by the incomplete detonation of TNT during the experiments. During experiments, the observed trend was that the TNT experiments were the dirtiest ('powder marks') when compared with the other explosives. This can be interpreted as black burnt marks of non-detonated explosive. A similar observation was made in Joynt [76] who has also concluded that the black coloured marks observed in his experiments are non-detonated explosive.

Deployment. Three methods of deployment in prairie soil were investigated, namely, surface, buried at 50 and 100 mm. The numerical predictions for all three deployments agree well with the experimental results. The impulse obtained from the explosion of a surface-laid charge does not significantly change with increasing moisture content. In contrast, charges buried in wet prairie soil yield up to two times higher impulse compared to dry soil. Charges buried in dry prairie soil yield about 46 % higher impulse compared with a surface-laid charge. The difference between charges with 50 and 100 mm overburden is not significant.

Cohesionless soil: Sand

The aim was to extend the sand model derived by Laine *et al.* [82] for different moisture content. Laine's sand model, and consequently the presented model, were derived using soil laboratory test data for different sand than was used in the experiments. The modelling methodology for deriving the equation of state for sand was applied, but there was insufficient soil laboratory test data for sand having high moisture content. Thus, the prediction for sand having 16 % moisture content underpredicts the experimental value. However, the dry and damp sand was modelled successfully. These numerical predictions agree well with the experiments.

Although the present model has lower sound velocity than Laine's sand model, both simulations of sand having 6.5 % moisture content agree well with experiments.

The reason being, that Laine measured the longitudinal and shear components of velocity during the laboratory test, whereas in the present study the velocity was determined from calculations based on uniform material. Although the difference in sound velocity is not pronounced in this output, it is suggested, that this is the part of modelling that can be improved.

Loading: Total versus specific impulse

The MIP experiments capture the soil contribution to the loading. The measured parameter by the pendulum, i.e. impulse delivered to the pendulum arm, represents the overall total impulse acting on the area of pendulum plate. In this case, the active area is $1,200 \times 1,200$ mm. It is apparent, that the area directly above the charge is subjected to a higher loading than the total load recorded by the pendulum. This is another example of where the numerical simulation complements the experiments. Since here is good agreement between experimental and numerical results, the loading along the plate can be considered.

Figure 7.33 depicts the specific impulse with respect to the distance from the plate centre. The specific impulse was extracted from fixed measurement points located at 400 mm distance above the ground. The specific impulse was determined by the integration of pressure-time history. In other words, the specific impulse captures only air contribution to the loading, whereas total impulse is the impulse produced by the soil and air. The specific impulse yields higher value than the MIP impulse for distances of up to 300 mm from symmetric axis. The specific impulse actually reaches up to three times higher value than the total impulse. In the worst scenario (soil of 28.7% moisture content), the total impulse is only 5,297 kN.msec, whereas the specific impulse is 10,818 kPa.ms. On the other hand, the specific impulse underestimates up to three times the total impulse at 600 mm distance from symmetric axis.

This difference between the total and specific impulses will affect the design of vehicle (structure or equipment) in two ways:

- (a) *Undersize design* in the area close to the mine explosion. Vehicle parts designed to sustain the total impulse will be more damaged. The larger material deformation, or even tearing to pieces, can lead to more injuries to the crew.
- (b) *Oversize design* in the area distance away from the explosion. Although the structure will sustain the loading, the additional dimension and weight of the vehicle part can affect the operational behaviour (such as speed of travel, floating, total height of the vehicle).

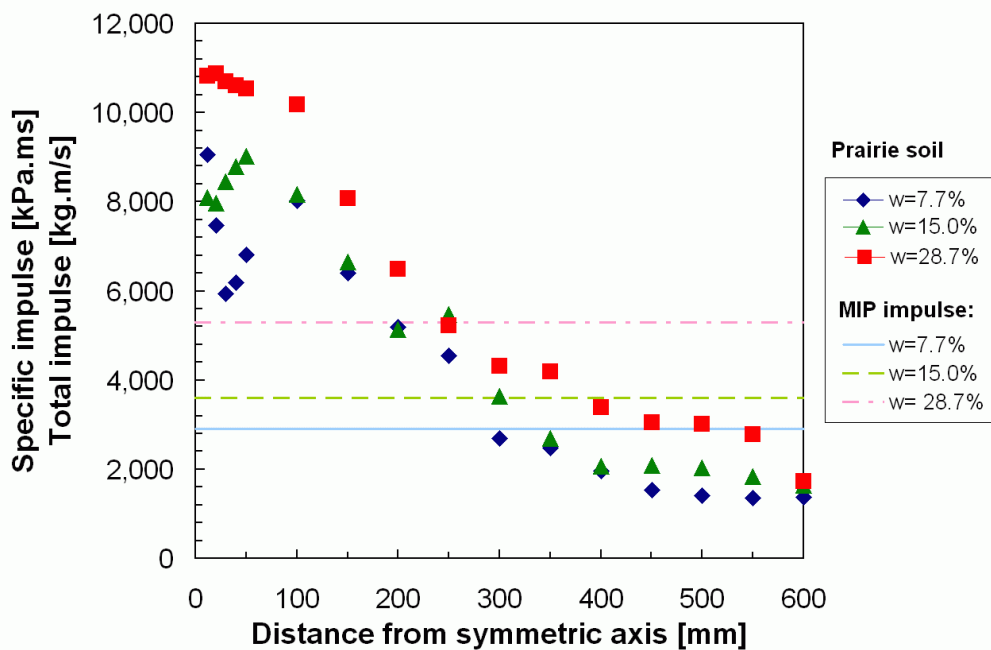


Figure 7.33: Specific impulse versus distance from symmetric axis and the MIP total impulse delivered to MIP. [1 kg C-4, Prairie soil, DOB = 50 mm, $D_{clc} = 400$ mm]

7.3.8 Concluding remarks

A numerical model of prairie soil, which represented cohesive soil, was validated for different modelling setups. In particular, types of explosive and methods of deployment were also considered. The impulse delivered to the pendulum was analysed. It was shown that the numerical results are consistent with experiments across the entire range of moisture content. The parametric study conducted on the soil model indicates that care must be taken when determining the friction angle from the soil laboratory tests. The friction angle is a major parameter that influences the modelled soil behaviour and thus, explosion output. It was shown that the proposed methodology for deriving a soil model is reliable and predicts mine explosion output in soil of varying moisture content. The soil model that captures the soil behaviour for varying moisture content is the principal element of this research. The reliability of numerical predictions with respect to real explosion behaviour was one of the aims of the research.

7.4 Summary

- ◆ Three sets of simulations were presented. In each case, the numerical predictions were validated with experimental work. Each simulation brings new insight to mine explosion process.
- ◆ The simulation progressed from a simple blast model, through sensitivity analysis of the setup parameters, up to the complex model that included the soil model for varying moisture content.
- ◆ Comprehensive validation of the derived cohesive soil numerical model was demonstrated.

Chapter 8

Discussions and future directions

THIS CHAPTER IS A summary of all the work presented in the body of this thesis. Briefly, the chapter covers the rationale and the salient features of the modelling approaches and presents the directions for future work:

- modelling of high explosive,
- modelling of cohesive soil — validation, advantages, future,
- scaling law,
- mine explosion output (loading).

8.1 Modelling high explosives

The literature survey has shown several options for analytical description of explosion processes. These include equations of state and detonation theories. Therefore, a study was undertaken to ascertain modelling of explosion process in AUTODYN. A review of numerical simulation of mine explosions has shown that Jones-Wilkins-Lee and *ideal gas* EOS are commonly employed (refer to Table 2.1). A simple model of explosion in air was analysed and compared with experiments. The JWL and *ideal gas* EOS were used as these equations are commonly used for this purpose. The details are presented in Chapter 7, Section 7.1.

The *ideal gas* EOS is not suitable for modelling explosions in close-range. This is evident when obtaining pressure or impulse values. In contrast, Fairlie *et al.* [44] showed that *ideal gas* EOS does not significantly affect the impulse delivered to the

plate in mine explosion studies when compared with simulations using JWL EOS. Therefore, it was concluded to use JWL EOS for detonation products in further studies. The model using JWL EOS produced reasonable agreement with experiments. The results obtained from JWL and *ideal gas* EOS converged at distances above $Z = 0.37 \text{ m.kg}^{-1/3}$. This suggests that the numerical procedures dealing with detonation process and shock wave propagation in AUTODYN are feasible and are sufficiently reliable to be used in mine explosion studies.

8.2 Modelling cohesive soils

This is the principal element of this research. The methodology that was proposed for deriving the soil model employs standard soil laboratory test procedures. The modelling methodology is based on the soil compositions, and in particular, on the relative volume of the relevant phases. The methodology was comprehensively and extensively validated by benchmarking against experimental data.

8.2.1 Modelling methodology for soil

Instead of developing a soil model from scratch, it was decided to use a combination of existing features to determine the techniques that would be applicable to this study. It was concluded that the following AUTODYN features accurately represent cohesive soil behaviour from a soil mechanics standpoint:

- (a) Equation of state: **Compaction**
- (b) Strength model: **Granular**
- (c) Failure model: **Hydro-tensile limit**

In addition, these modelling features have also proved suitable to model reliably sand behaviour under explosion (see Section 7.2 on sand model by Laine *et al.* [82]). The next phase was to provide input parameters for these AUTODYN relations.

For derivation of the soil model, soil statistical data (Vrtek [119]) and prairie soil laboratory test data (DRDC's work [4, 6, 5]) were utilised. Both data are based on standard laboratory procedures to determine soil mechanical properties. The main difficulty was to find a way in which to extend the prairie soil laboratory data for different moisture contents. A survey of existing literature yielded Henrych's proposal [67]. Henrych suggested that the equation of state for soil is formed by EOS for respective soil phases in their proportional representation. Thus, this approach enables determination of a model for any soil type. The pressure-density curves (refer

to Figure 5.2) obtained from this calculation correspond with commonly observed soil behaviour. For example, dry soil is more compressible than wet soil. This is represented by a slowly rising curve in the low pressure area. In contrast, the curve of wet soil is steep from the outset.

In the course of this study, it was found out that a similar approach was taken by other researchers, namely Donahue *et al.* [42] and Wang *et al.* [122]. Donahue *et al.* [42] employs a *mixed material cell* feature in CFD calculation, i.e. the respective soil phases are inserted into the cell, and each soil phase is described by its equation of state. The EOS parameters (and its derivation) are not given. In CFD, there is no strength and failure model. The Donahue's numerical results for soil having high moisture content overestimated by 37% the experiments by Hlady *et al.* [68]. Wang *et al.* [122] modelled the explosion in unlimited soil (without interaction with atmosphere). The soil model was not derived, the soil parameters presented in Henrych [67] were used.

From analysis of soil statistical data, it was observed that the friction angle depends on the void ratio. This can be explained due to the fact, that the amount of probable contacts among the solid particles determines the friction properties. This relationship was used for extrapolating the friction angle (a parameter of yield surface) to data for different moisture content.

The literature does not contain a relationship for Poisson's ratio as a function of cohesive soil properties. The Poisson's ratio determines the material compressibility, and is a parameter needed for calculating the shear modulus (in the strength model). A relationship was derived for use in this study, based on the soil compressibility as a function of the compressibility of its respective phases. This relationship predicts the Poisson's ratio corresponding to overall values found in literature.

The applied hydro-tensile failure criterion directly corresponds to the soil mechanics theory that soil cannot sustain large tensile stresses.

The treatment of soil by decomposing it into its constituent phases is unique to this study and has not been attempted before in numerical simulations. This approach has proved feasible, as verified by the behaviour observed in soil. Although other relevant approaches confirm the soundness of this applied technique, it can be seen that none of them attempt to model soil in the same level of detail as the present approach.

8.2.2 Validation of soil models

Extensive analyses were carried out in order to validate the derived soil models for different setups. The simulations with prairie soil models were compared with

results obtained from Mine impulse pendulum experiments. In the first step, the assumptions in model derivation were analysed for a particular setup. Then, simulations were performed for different setups that include different depths of burial and type of high explosive. Chapter 7, Section 7.3 presents details.

A. Change in soil model parameters

As some assumptions were made when deriving the soil model, the sensitivity of these assumptions was analysed. The details are presented in Chapter 7, Section 7.3.3.

- *Poisson's ratio*: Modelling was done on the basis that the Poisson's ratio either (i) represents a compressible material (related to the soil composition), or (ii) corresponds to incompressible material. The numerical simulations show that the Poisson's ratio has very slight effect on the impulse delivered to the pendulum. Although the compressibility of soil is an important parameter in static loading [99], it does not play a significant role in dynamic loading (i.e., explosion in soil bounded by a free surface).
- *Yield surface*: The material strength is represented by its yield surface. The yield surface determines the onset of plasticity in a material. From the analysis of soil statistical data [119], it was observed that the yield surface varies considerably with change in friction angle. This was subsequently confirmed in the numerical simulations. The impulse delivered to the plate changes considerably with the variation in friction angle. Change in cohesion does not affect the numerical predictions significantly.
- *Failure criterion*: The hydro-tensile limit failure criterion used in this analysis is based on the theory of soil mechanics that soil cannot sustain large tensile stresses. The onset of failure is taken to be the point when cohesion becomes negative ($p_{MIN} = -c$). The actual limit does not affect the mine explosion output. From numerical analysis, we observe that a 5-fold increase in tensile limit did not result in a significant change in impulse.

B. Change in deployment

The applied methodology for soil model derivation has the ability to reproduce the soil behaviour for different deployment methods. The charge was surface-laid, or buried at the depth of 50 and 100 mm. The models simulated behaviour of the soil having moisture content in the range from 7% to 28%. For each deployment, the numerical simulations confirmed the soil behaviour exhibited by the experiments across the range of moisture contents.

C. Change in high explosives charges

The response of the prairie soil model was also validated for different high explosive charges. In addition to C-4, charges of TNT and Composition B were used. The prediction agrees reasonably well for C-4 and Composition B compared with experiments. The numerical results are overpredicted for TNT charges by about 40%. Although it should be noted, that the experiments underperformed the numerical simulation. The explanation of this difference is in the behaviour of TNT. In order that the TNT charge develops a strong detonation, care must be taken to initiate the charge otherwise the explosion energy is released gradually (i.e., step-by-step evolution of detonation) and the after-burning of the detonation products occurs. Incomplete detonation can influence the dynamic pressure (Dewey [38]). Since TNT experiments were “dirtier” than the other charges, incomplete detonation is a likely explanation. This phenomenon was also noticed during mine experiments conducted by Joynt [76]. Joynt observed the black burnt marks on the ground. He also attributed the marks to the incomplete detonation of explosive. Although TNT is probably the most well known explosive, it is not the best explosive to conduct experiments (with small charges) for validation of numerical simulation.

8.2.3 Advantages of proposed methodology

The proposed methodology is based on the soil phase composition that enables extension of the model to different soil types. The methodology was extensively validated for sandy silty clay of *low plasticity*, i.e. prairie soil. However, it can be argued that, in nature several types of soil exist with each one exhibiting different properties. More specifically, using soil classification schemes, cohesive soil is divided into two categories: silt and clay. These are further subdivided with respect to plasticity into: low, intermediate, high, very high and extremely high (Chapter 3). The scope for data collection and for conducting of soil tests is endless. Since the methodology proposed in this thesis uses standard soil laboratory tests, *extending this study*, i.e., the effect of other soil properties on mine explosion output now reduces to

using soil laboratory tests, which were conducted by accredited labs for civil engineering and geology purposes, for the derivation of soil models of different plasticities as well as composition.

The relevance of soil tests can be briefly summed up as follows: By nature, each soil test is designed to determine a specific parameter of soil. Although primarily, the parameters determined from triaxial tests are the friction angle and cohesion, for

EOS derivations, the triaxial test data are used before it is evaluated as friction angle and cohesion. In particular, the total stress and density of the sheared specimen are needed for the determination of the EOS of the solid phase. Similarly, the soil statistical data (Vrtek [119]) provide the friction angle and cohesion (which were used for yield surface analyses). The report also provided oedometric test data (which is useful in civil engineering studies), but not sufficient to determine the EOS for the solid phase. However, the EOS needs the unevaluated triaxial test data specifically, and those are not presented in the report.

8.2.4 Directions in modelling soil

When applying the proposed methodology to the sand model, it was observed that the measured sound velocity [82] was higher than the velocity calculated (see Figure 5.6). However, the predictions of the impulse delivered to the plate were very similar. In other words, the value of sound velocity does not influence loading of the plate at the near distance.

Concerns arise on the reliability of the prediction when the structure is in contact with soil¹. Joynt [77] argues that the shock wave travels through the fastest possible path. In that case, the difference in the calculated and measured soundspeed can cause inaccurate material response. Therefore, the future directions of soil model improvement are briefly described as follows:

The soil behaviour at *small-strain* deformation is a recent research area being investigated for dynamic loading such as earthquakes and vibration in soil (refer to Viggiani *et al.* [117] and Mašín *et al.* [90]). Within this theory, the bulk and shear moduli, and consequently sound velocity, in small-strain deformation region are higher than those parameters measured by standard triaxial tests. The bulk and shear moduli decrease with the increasing deformation reaching the standard values. It is argued that in contact explosion, the soil deformation is of small-strain type. The proposed methodology is based on soil mechanics theory of large deformation.

From initial analysis, it was determined that in order to capture the soil behaviour that includes the small-strain deformation during the contact explosion, the features provided by AUTODYN are not sufficient. Thus, users' subroutines need to be written to conduct any form of preliminary investigation into this phenomenon. This is a very brief presentation on emerging technologies in soil modelling and mine explosion research. This has been included to serve as a pointer to areas of future research in this field.

¹In vehicle scenario, the tyres are in contact with the ground.

8.3 Comments on scaling

The focus of this thesis is to propose a feasible and widely applicable numerical model that accurately replicates explosion in soil bounded by a free surface. More specifically, a model that includes soil behaviour with the ability to vary moisture content. However, in the course of investigating² scaling laws we have determined that:

- Conventional existing models and laws derived for air blast are not sufficient to capture the dynamics of scaling fully, in the case of buried charges.
- A newer model that either extends currently existing models, or is built from scratch, is needed to assist the effort in scaling. This is beyond the scope of this thesis.

These two issues will be elaborated upon in this section. So far, experimental and numerical studies which predominantly used 0.1 and 1 kg charges of C-4 have been presented in this thesis. This amount of explosive is considerably smaller than that present in an anti-tank blast mine. An anti-tank mine consists of 8 to 13 kg TNT. In order to draw conclusions on a typical anti-tank mine scenario, the following two issues need to be addressed:

- A. conversion of C-4 to TNT, and
- B. extrapolation of the output caused by 1 kg to 10 kg charge.

A. TNT equivalence

This relation is commonly used in the blast community for converting the effect of different explosives to a standard baseline. Different types of conversion factors have been used for the conversion of the actual mass of the charge into TNT equivalent mass. The TNT equivalents are explained in the following examples:

TNT equivalence (specific energy) is based on mass specific energy of the explosive and TNT, i.e., Q_{C-4}/Q_{TNT} . For example, 1 kg of C-4 converts to 1.078 kg of TNT.

TNT equivalent pressure factor 1.37 means that 1.37 kg of TNT makes the same maximum pressure as 1 kg of C-4.

²instigated (no pun) by DSTL during a presentation

TNT equivalent impulse factor 1.19 means that 1.19 kg of TNT makes the same impulse as 1 kg of C-4.

Table 8.1 presents the TNT equivalence for air blast and buried charge. The data presented in Section 7.3.5 was used to determine the TNT equivalent pressure and impulse factors for a charge buried at 50 mm in prairie soil. It is apparent that the TNT equivalent factor for buried charges is not consistent with the factor for air blast. Considering the experimental data for a buried charge, it is found that 5 kg C-4 delivers the same impulse to MIP as 10 kg TNT. Although in air blast, 5 kg C-4 produces the same impulse as (only) 6 kg TNT.

Therefore, the TNT equivalence should be used with care when dealing with buried charges. Williams *et al.* [127] also indicates that TNT energy release equivalence factor does not apply for buried charges. TNT equivalence may not be appropriate in all cases and the issue could be further investigated as a separate topic of research.

Table 8.1: *TNT equivalent factors for air blast and buried charges.*

High explosive	Specific energy [15]	Air blast [115]		Prairie soil, $w \approx 9.8\%$, DOB = 50 mm, 1 kg HE			
		Pressure	Impulse	Impulse (MIP) Experiment	Impulse (MIP) Simulation	Pressure at 400 mm	Specific impulse at 400 mm
C-4	1.078	1.37	1.19	2.10	1.53	1.21	1.16
Composition B	1.148	1.11	0.98	1.83	1.05	0.71	0.96

B. Scaling law

The scaling law presents an equivalent approach to scale *up* or *down* the explosion effect of the charges. It will be recalled that the Hopkinson-Cranz scaling law is represented by:

$$\lambda = \frac{R_2}{R_1} = \frac{I_2}{I_1} = \frac{t_{p2}}{t_{p1}} = \left(\frac{W_2}{W_1} \right)^{1/3}$$

Applying this relationship to the data of 0.1 and 1 kg (Section 7.2 and 7.3), the scaling factor, given by the ratio of the mass of explosive is given as

$$\lambda_w = \left(\frac{W_2}{W_1} \right)^{1/3} = \left(\frac{1}{0.1} \right)^{1/3} = 2.15$$

Table 8.2: *Introduction to the scaling problem. Charge deployed in dry sand (Laine's model). S and E denotes numerical simulation and experimental results, respectively.*

Explosive	Weight [kg]	DOB [mm]	Distance above ground [mm]	Maximum pressure [kPa]	Specific impulse [kPa.ms]	Scaling max. pressure [-]	Scaling specific impulse [-]
C-4	0.1	0	300	E 2 797	E 86	7.46	9.81
C-4	1	0	300	S 20 859	S 844		
C-4	0.1	30	300	E 725	E 107	3.77	7.49
C-4	1	30	300	S 2 732	S 801		
C-4	1	50	300 (plate)	S 4 568	S 2 004	1.00	1.94
C-4	1	50	300	S 4 574	S 1 034		

and the scaling factors for maximum pressure and specific impulse respectively, for 30 mm overburden (not scaled), is:

$$\lambda_p = \frac{p_2}{p_1} = \frac{2732}{725} = 3.77$$

$$\lambda_I = \frac{I_2}{I_1} = \frac{801}{107} = 7.49$$

It can be observed that the scaling factors calculated using the scaling law are not coherent. The scaling factors are summarised in Table 8.2. It is noted that the overburden and distance above the ground were not scaled as required. The other factor to be considered, is that the gravity (gravitational constant g) is not scaled in these experiments. For details on similarity methods see [16].

It can be observed, that the shock-wave parameters depend on the overall measurement condition. Two different measurement conditions were considered, in particular, the parameters are measured in free air or under plate. The maximum pressure is the same in both cases, but the specific impulse under the plate is two times higher than in free air (see Table 8.2).

From this initial assessment, it can be concluded that the procedure of scaling needs to be addressed in greater detail. The research area needs to be analysed by means of extensive simulation work and must be supported with experimental evidence.

8.4 Mine explosion output

The pertinent question in mine explosion studies is by which parameters to characterise the explosion process of buried charges? It has been shown that, soil significantly contributes to loading on the structure (vehicle). Therefore, the requirement is to capture (a) blast effects (high pressure in air) and (b) soil contribution (transferring energy of soil lumps and stones). In addition, the parameters should be consistent, when measured and simulated, and serve as a reliable loading input for design of structures.

This thesis deals with two approaches that have been attempted by experimenters:

- A. pressure transducers, and
- B. mine impulse pendulum.

In this section, these measurement techniques, with their advantages and shortcomings, are discussed and alternatives that might overcome these shortcomings are suggested.

A. Pressure transducers

Bergeron *et al.* [22] used pressure transducers to record the pressure-time history, and consequently obtained the specific impulse. This parameter is determined for a single spatial position (largely governed by the physical constraints of the fixtures). The pressure transducers record only the air blast pressure. The soil energy is not captured. Conversely, when soil lumps (or stone) impinge on the transducer, the transducer is damaged (adding to the cost of experiments). Furthermore, Bergeron experienced a large variation in the measured parameters. This difference was up to 80 %. This is perhaps the reason why Held [59] asks “What do we actually measure?”. Also, Blaney *et al.* [26] states that the “maximum pressure measurements are not always the most reliable data (particularly for cased charges)”.

This numerical study has shown that the maximum pressure is highly sensitive to the distance from the symmetric axis³. A difference of 10 mm from symmetric axis decreases the maximum pressure by about 20 % (Figure 7.23). On the other hand, the specific impulse does not exhibit significant variations with change in setup (Section 7.2).

³In numerical simulation, the symmetric axis receives special treatment, as it can cause the instability/diffusion in its near region. From private communication, AUTODYN believes that their treatment of symmetric axis is correct and should not bring any significant error to the calculation.

B. Mine impulse pendulum

The mine impulse pendulum was designed to capture the energy transferred from the soil to the pendulum arm. The measured impulse delivered to the pendulum is the overall *total* impulse acting on the area of pendulum plate. In this case, the active area is $1,200 \times 1,200$ mm. It is apparent that, the area directly above the charge is subjected to a higher loading than what is recorded. The numerical simulation shows that the specific/local impulse in the plate central region can reach up to three times higher value than the total impulse delivered to the plate (Figure 7.33). This difference between the total and specific impulses could significantly affect the design of a vehicle. Designing vehicles to sustain the total impulse value alone could cause rupture of the chassis and vehicle fragments and explosive gases could enter the crew compartment. Thus, the probability and severity of injuries to the occupants increases. This is also the reason why experiments will always be required to validate the local specific impulse.

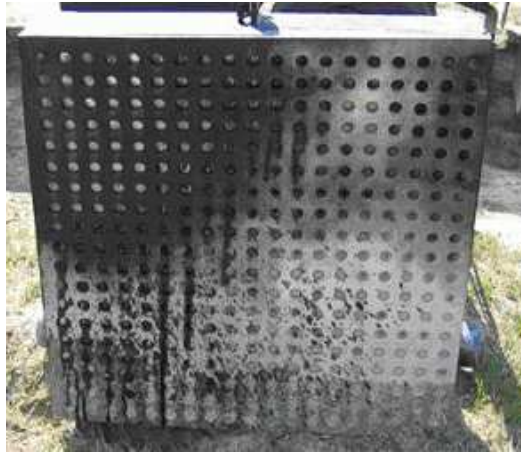
8.4.1 Directions in experiments

It is an acknowledged fact that it is difficult to conduct data acquisition on explosion trials [22, 40, 59]. And it is twice more difficult to measure these parameters in the near region (in other words, inside the fireball) where high temperature and high pressure gasses are very turbulent with soil lumps flying all around. Within this environment, local impulse needs to be measured. Techniques, that can measure the same, are analysed with increasing improvement in data quality levels.

Pressure transducers often get hit and destroyed. This means repeating the trial, and, consequently, adding to the cost of experimental trials. In addition, hot explosive gases in near region, makes the measuring virtually impossible [59].

Momentum gauges were proposed to overcome the shortcomings of pressure transducers. They are commonly used to determine impulse distribution near HE charges by Held [59, 61, 62, 63, 64]. This method also overcomes the problems of material calibration.

The initial work in measuring local impulse was carried out during mine boot experiments (Joynt [76]). The *dimple gauge* was placed in the boot at ankle-height to determine the impulse transferred to the leg. Joynt [78] has enlarged his measuring method to Fine Impulse Structure (FIS), that captures the local and global impulse caused by the explosion of 7 kg TNT. The FIS is a pendulum-type structure fitted with deformable gauges to obtain 361 values of specific local impulse in one trial (see Figure 8.1). The initial results with the fine impulse structure shows the pronounced difference in specific impulse distribution on the plate. In Figure 8.1 (b), the places



(a) The anvil of the dimple gauge.

	1	2	3	4	5	6	7	8	9	10	11	12	13	14	15	16	17	18	19
1	0.00	0.00	0.00	0.00	0.00	0.00	0.00	0.00	0.00	0.00	0.00	0.00	0.00	0.00	0.00	0.00	0.00	0.00	0.00
2	0.00	0.00	0.00	0.00	0.00	0.18	0.00	0.00	0.00	0.00	0.00	0.00	0.00	0.00	0.00	0.00	0.00	0.00	0.00
3	0.00	0.00	0.00	0.00	0.00	0.30	0.28	0.35	0.20	0.90	0.00	0.00	0.00	0.00	0.00	0.00	0.00	0.00	0.00
4	0.00	0.00	0.00	0.32	0.00	0.40	0.36	0.25	0.00	1.35	1.30	1.00	0.75	0.54	0.00	0.00	0.00	0.00	0.00
5	0.00	0.00	0.24	0.00	0.00	2.00	0.82	1.52	2.35	0.38	1.05	0.45	0.14	1.17	0.30	0.00	0.00	0.00	0.00
6	0.00	0.00	0.00	0.42	0.77	1.80	1.10	1.70	1.90	0.84	0.90	1.33	0.03	0.02	0.02	0.00	0.00	0.00	0.00
7	0.00	0.00	0.00	0.00	0.00	0.60	1.15	1.24	1.20	0.10	0.60	0.20	0.20	0.11	0.99	0.00	0.00	0.00	0.00
8	0.00	0.00	0.00	1.60	0.35	1.10	1.62	2.95	3.70	3.80	2.50	1.80	2.45	0.62	1.65	0.00	0.00	0.00	0.40
9	0.00	0.00	0.00	0.40	0.80	1.33	1.00	1.10	1.40	3.18	1.20	3.10	3.00	0.95	0.55	0.30	0.30	4.00	0.90
10	1.60	X	X	2.00	2.90	1.90	1.30	2.30	3.90	4.20	3.40	2.75	X	X	X	1.15	X	0.40	0.10
11	0.40	0.32	0.65	0.00	1.90	X	X	X	2.50	1.80	4.65	3.00	X	3.00	3.00	0.75	3.80	0.72	0.62
12	1.80	X	0.00	3.30	1.15	X	X	X	0.00	X	X	1.05	X	4.60	2.40	X	1.25	0.45	
13	1.80	X	0.00	0.25	1.34	X	X	X	0.00	X	3.85	X	2.90	1.10	1.25	1.15	0.17	1.50	0.55
14	0.00	0.00	X	0.30	1.20	0.35	1.42	0.90	1.20	2.50	1.50	1.90	1.44	0.58	0.50	X	0.00	0.00	0.00
15	2.10	0.00	0.00	0.05	0.10	0.00	1.90	0.62	2.15	1.30	X	1.47	1.50	1.12	0.27	X	0.80	0.80	0.00
16	0.00	0.00	0.12	0.75	0.10	0.00	0.45	0.50	3.00	0.20	2.20	0.75	0.40	1.60	2.55	0.75	0.62	0.30	0.05
17	0.00	0.20	0.50	0.30	0.13	0.00	0.30	0.78	0.62	0.23	1.75	0.54	0.25	0.42	0.30	0.50	0.43	0.16	0.00
18	0.90	0.00	0.00	0.00	0.00	0.00	0.00	0.25	0.00	0.05	0.62	0.02	0.00	0.00	0.10	0.25	0.90	0.00	0.00
19	0.90	0.00	0.00	0.00	0.00	0.00	0.00	0.00	0.00	0.00	0.00	0.00	0.00	0.00	0.00	0.00	0.00	0.00	0.00

(b) Scorecard. The numbers written corresponds to the deflection of the dimples.

Figure 8.1: Fine impulse structure captures the total impulse delivered to the trolley, and local impulse in the small areas (protrusions). Reproduced from Joynt [78].

of high impulse are marked black, with low impulse in white.

The disadvantage of deformable gauges is that the material used, needs to be manufactured to a high quality in order to ensure uniform mechanical properties of the plates. The material needs to be calibrated, i.e., the relationship between the deformation and impulse needs to be determined. Therefore, the author of this thesis proposes *crusher gauges* as an alternative measurement tool instead. Since crusher gauges are commonly used to measure maximum pressure in gun barrels (internal ballistics), its manufacturing is standardised and thus cost-effective. A crusher gauge is a copper cylinder whose deformation is related to the maximum pressure. A bespoke fixture will be needed in order to hold these gauges in place during the trials. This idea could be further investigated as a separate topic of research.

8.5 Summary

- ◆ The modelling of cohesive soil and its validation was discussed. The advantage of modelling methodology allows the extensibility of this approach.

- ◆ The direction in modelling soil was presented for future work.
- ◆ Scaling law and experimental difficulties were demonstrated.

Freedom is not worth having if it does not include the freedom to make mistakes.

— Mahatma Gandhi (1869 - 1948)
Spiritual leader and India's founding father

Chapter 9

Conclusions

THE THESIS BEGAN with a question: “How effective and realistic is numerical analysis study of mine-explosion going to be”? In the course of the investigations, the question has been addressed by the following means:

- (a) In Chapter 5, the methodology for deriving a cohesive soil model was proposed that was implemented using AUTODYN. The soil model is based on the soil composition. In other words, soil behaviour that takes into account varying moisture content is represented as a numerical model. Standard laboratory soil tests are used to determine the soil properties. This is cost-effective and can be easily transferable to any type of soil.
- (b) In Chapter 7, the simulation results were presented which were compared with experimental data. The research progressed from simple models of air blast to the complex models of explosions in soil. A comprehensive validation of the soil model was performed. The model was extensively validated for different setups, such as deployment methods and high explosive charges. The feasibility of the proposed modelling methodology was demonstrated. Sensitivity analysis of the setup was conducted to show the capability of numerical analysis. A parametric study was conducted to study the effect of soil parameters on overall behaviour – to demonstrate the versatility of numerical analysis. Overall, the numerical results have always been in good agreement with the experimental data.
- (c) In Chapter 8, the important findings from running the numerical simulations of mine explosions are presented and discussed briefly. The advantages of the

approach proposed in this thesis are listed here. Important topics, such as scaling law, are discussed in detail. Alternative modelling approaches (in the form of new and emerging technologies) are also suggested as future work on this area.

The investigation shows that soil properties significantly influence mine explosion output. The output caused from the explosion in wet cohesive soil can be twice as high than from charges buried in dry soil. Therefore, it is important to study the soil properties along with the explosion parameters. The proposed methodology for soil derivation gives the option to implement the particular soil into numerical simulations (cf., prairie soil model, sand model). Thus, numerical simulations and experiments can complement each other and contribute to enhancement of vehicle design.

The author would like to mention that a special interest group (made of UK, USA, Canada and Australia) was established to coordinate research on mine protection of vehicles. It is also known that, within this group, there is a lot of information exchange on mine explosion investigation (both numerical and experimental). However, the reports are only available for researchers having the nationality of one of the participating nations.

Since it does not matter how hard you have worked, research never ends and always brings more questions than answers. This research is no exception. Here, are some ideas that shall build up on the work as it stands, and improve the understanding of mine explosion in soil.

- **Lagrangian soil:** Simulations in which soil is modelled using a Lagrange solver can bring further insight into mine explosion loading. This is enabled due to new AUTODYN feature of automatic coupling between Lagrange and Euler solvers. This procedure enables us to differentiate between blast and soil loading on a structure. In addition, Lagrangian soil can employ **stochastic distribution** of failure criterion. This feature corresponds to the non-uniform distribution of soil parameters throughout the soil mass. This non-uniformity is caused by stones, roots etc.
- **Non-linear elastic model:** This area, which is relatively new in soil mechanics, covers the soil behaviour at very small strain. The reason for proposing this model is that sound velocity will play an important role in the contact explosion (such as tyre-soil). This is probably a more challenging task as it will involve the development of bespoke users' subroutines in AUTODYN. A very brief overview is given in Section 8.2.4.

- ***Scaling law:*** The analysis of loading (output) caused by the explosion of charges buried in soil covers two cases. The presented work in this thesis is with charges of 0.1 and 1 kg C-4, which is considerably lower than the high explosive charge in an anti-tank mine (about 10 kg TNT). The extensibility of the loading predictions for different explosive weights can be a subject of extensive simulation work supported with experimental evidence. This issue is introduced in Section 8.3.
- ***Experimental work:*** The experimental techniques that capture soil contribution to the loading, in terms of the specific (local) and total impulse could be developed. The soil properties and consistency in setup should be observed including measuring the moisture content for each trial. Refer to Section 8.4.

The above list is by no means complete. For instance, after prediction of loading, the next step is to investigate the response of vehicle. This includes the study of structural and kinematic response and the attenuation materials.

Bibliography

- [1] *Textbook of ballistics and gunnery*, vol. 1. Her Majesty's Stationery Office, London, UK, 1987. pp. 806. 1.3
- [2] *Jane's Mines and Mine Clearance 1997-98*, 2nd ed. Jane's Information Group Limited, Coulsdon, UK, 1997. (document), 1.2, 1.4, 1.3, 7.1
- [3] *Jane's armour and artillery 1999-2000*. Jane's Information Group Limited, Coulsdon, UK, 1999. 1.3, 7.1, 7.1.4
- [4] One dimensional consolidation tests. Tech. Rep. Project no. BX02777, AMEC Earth and Environmental Limited, Edmonton, Canada, December 2003. 5.2, 8.2.1
- [5] Direct shear tests and specific gravity of soil. Tech. Rep. Project no. BX02777, AMEC Earth and Environmental Limited, Edmonton, Canada, February 2004. 5.2, 8.2.1
- [6] Triaxial undrained tests (cup). Tech. Rep. Project no. BX02777, AMEC Earth and Environmental Limited, Edmonton, Canada, January 2004. 5.2, 8.2.1, D.2
- [7] ICASUALTIES. Iraq coalition casualty count. <http://icasualties.org/>, November 2005. 1.1
- [8] ABSIL, L. H. J., VERBEEK, H. J. AND WEERHEIJM, J. Combined experimental and numerical study of mine detonations in the vicinity of vehicles. In *15th International symposium on the Military Aspects of Blast and Shock* (DRDB, Defence Research Establishment Suffield, Banff, Canada, September 1997). 2.1, 2.1, 2.2.2

- [9] ADAMÍK, V. AND BUCAR, J. Modelování kumulativní nálože kódem LS-DYNA-3D [modelling of shaped charge using code LS-DYNA-3D]. In *ANSYS user's meeting* (Čejkovice, The Czech Republic, 1999). 1.3
- [10] ADUSHKIN, V. V. Effect of the density and moisture content of a sandy soil on the dimensions of a pothole with an underground explosion. *Fizika Goreniya i Vzryva* 15, 3 (May-June 1979), 107 – 116. 1.3
- [11] AKERS, S. A., PHILLIPS, B. A., AND WINDHAM, J. E. Numerical simulation of three small-scale structure-medium-interaction experiments. In *9th International Symposium on Interaction of the Effects of Munitions with Structures* (Berlin, Germany, May 1999), vol. Closed session, pp. 66 – 73. NATO RESTRICTED. 2.3
- [12] ALEM, N. M., AND STRAWN, G. D. Evaluation of an energy absorbing truck seat for increased protection from landmine blast. Technical report, U.S. Army Aeromedical Research Laboratory, Fort Rucker, USA, January 1996. 1.2, 2.1
- [13] AMBROSINI, R. D., *et al.*. Size of craters produced by explosive charges on or above the ground surface. *Shock Waves* 12, 1 (2002), 69 – 78. 1.3, 2.3
- [14] ANDERSON, W. F., WATSON, A. J., AND GOTT, M. B. Development of a large diameter split Hopkinson pressure bar to study compression wave transmission through soils. In *8th International Symposium on Interaction of the Effects of Munitions with Structures* (McLean, USA, April 1997), pp. 1073 – 1082. 5
- [15] BAKER, W. E., *et al.*. *Explosion hazards and evaluation*, vol. 5 of *Fundamental studies in engineering*. Elsevier Science Publishers, Amsterdam, The Netherlands, 1983. ISBN 0-444-42094-0. 2, 2.3, 6.1, 6.1, 8.1
- [16] BAKER, W. E., WESTINE, P. S., AND DODGE, F. T. *Similarity methods in engineering dynamics: theory and practice of scale modeling*, 2nd ed., vol. 12 of *Fundamental studies in engineering*. Elsevier Science Publishers, Amsterdam, The Netherlands, 1991. pp. 384, ISBN 0-444-88156-5. 8.3
- [17] BARNES, G. E. *Soil mechanics: Principles and practice*, 2nd. ed. Palgrave, New York, 2000. pp. 493, ISBN 0-333-77776-X. 3.2, 5.3.3, A
- [18] BENSON, D. J. Computational methods in Lagrangian and Eulerian hydrocodes. *Computer Methods in Applied Mechanics and Engineering* 99 (1992), 235 – 394. 4

- [19] BERGERON, D. M., AND TREMBLAY, J. E. Canadian research to characterise mine blast output. In *16th International Symposium on the Military Aspects of Blast and Shock* (Oxford, UK, September 2000), pp. 501 – 511. 1.2, 1.3, 1.4, 2.1, 2.1.1, 2.2, 5, 6, 6.2, 6.3, 7.2.5, 7.3, 7.3
- [20] BERGERON, D. M., *et al.*. Numerical and experimental study of in-soil explosions from a multiphase perspective. In *8th International Symposium on Interaction of the Effects of Munitions with Structures* (McLean, USA, April 1997), pp. 11 – 34. 1.2, 6, 6.2
- [21] BERGERON, D. M., *et al.*. Assessment of foot protection against anti-personnel landmine blast using a frangible surrogate leg. In *UXO/Countermine forum* (New Orleans, USA, April 2001). 2.1
- [22] BERGERON, D. M., WALKER, R., AND COFFEY, C. Detonation of 100g anti-personnel mine surrogate charges in sand: A test case for computer code validation. Technical report DRES-SR-668, Defence Research Establishment Suffield, Canada, October 1998. (document), 1.2, 1.4, 2.1, 2.1.1, 2.2, 2.1, 6, 6.2, 6.4, 7.1.5, 7.2, 7.2.2, 7.2.3, 7.2.4, 7.3.6, 8.4, 8.4.1
- [23] BERNDT, E. R., DULBERGER, E. R., AND RAPPAPORT, N. J. Price and quality of desktop and mobile personal computers: a quarter century of history. <http://www.nber.org/~confer/2000/si2000/berndt.pdf>. b
- [24] BERRY, P. L., AND REID, D. *An introduction to soil mechanics*. London: McGraw-Hill Book Company, 1987. pp. 317, ISBN 0-07-084164-0. (document), 3.2, 3.2, A
- [25] BIRD, R. Protection of vehicles against landmines. *Journal of Battlefield Technology* 4, 1 (March 2001). 1.1, 1.2, 2.1, 2.1
- [26] BLANEY, E. J., AND OHRT, A. P. Surrogating sub-scale munitions with simple cased cylinders for airblast prediction purposes. In *18th International symposium on the Military Aspects of Blast and Shock* (Bad Reichenhall, Germany, September 2004). 2.1.1, 8.4
- [27] BRITISH STANDARDS INSTITUTION. *BS 1377 : 1990 – British Standard methods of test for soils for civil engineering purposes*, 1990. 3.1.4, 3.3, 3.3, 5, A, A.2(c)
- [28] BRODE, H. L. Numerical calculations of blast waves. Technical report P-1933, The RAND Corporation, Santa Monica, USA, February 1960. pp. 15. 2

- [29] BROWN, W. B. Critical review of theories of steady non-ideal two-dimensional detonation of condensed explosives. Hybrid Stress Blast Model Project, April 2002. 2, 2.2.1
- [30] BUES, R., HLADY, S. L., AND BERGERON, D. M. Pendulum measurement of land mine blast output, Volume 1: Theory and implementation. Technical report DRES-TR-01-200, Vol. 1, Defence Research Establishment Suffield, Canada, December 2001. (document), 2.1, 2.1.1, 6, 6.3, 6.3.1, 6.10, 6.11, 7.2.5, 7.3, 7.3
- [31] CENTERS FOR DISEASE CONTROL AND PREVENTION (CDC). Landmine-related injuries, 1993-1996. *Morbidity and Mortality Weekly Report* 46, 31 (August 1997), 724 – 726. 1.1
- [32] CENTURY DYNAMICS. AUTODYN *user's documentation*. Horsham, UK, 1998. (document), 1.4, 4.1, 4.2, 4.3, 4.4, 7.2.1, 7.3.1, 7.9, B.2
- [33] CHASSILLAN, M. VBCI. In *9th European Armoured Fighting Vehicle Symposium* (Shrivenham, UK, March 2004). 1.2
- [34] CHENG, Q. H., *et al.*. Response of a box-like structure to near-by explosion. In *International Symposium on Defence Construction* (Singapore, April 2002), Defence Science and Technology Agency, Singapore. 1.2, 2.2, 2.1, 2.2.2
- [35] COFFEY, C. G., ROSEVEARE, J., AND TORRANCE, K. . Development of the DRES Large Scale Facility. Technical report DRES CR 2000-102, Defence Research Establishment Suffield, Canada, 1998. 2.1, 6.3
- [36] COLLINS, G. S. An introduction to hydrocode modelling. http://www.lpl.arizona.edu/~gareth/publications/sales_2/download/intro.pdf, August 2002. 4
- [37] COURTNEY-GREEN, P. R. *Ammunition for the land battle*, vol. 4 of *Land warfare: Brassey's new battlefield weapons systems and technology series*. Brassey's Defence Publishers, 1991. pp. 227, ISBN 0-08-035807-1. 1.3
- [38] DEWEY, J. M. TNT equivalency of explosive sources. In *18th International symposium on the Military Aspects of Blast and Shock* (Bad Reichenhall, Germany, September 2004). 8.2.2
- [39] DICK, R. D., *et al.*. Small scale cratering experiments II: sand. *FRAGBLAST – International Journal of Blasting and Fragmentation*, 2 (1998), 269 – 294. 2.3

- [40] DIRLEWANGER, H. Comparison of different pressure transducers and related numerical simulations. In *9th International Symposium on Interaction of the Effects of Munitions with Structures* (Berlin, Germany, May 1999), pp. 629 – 636. 2.1.1, 8.4.1
- [41] DOBRATZ, B. M., AND CRAWFORD, P. C. LLNL explosive handbook: Properties of chemical explosives and explosive simulants. Technical report UCRL-52997-Chg.2, Lawrence Livermore National Laboratory, California, USA, January 1985. 2.2.1, 2.2.1, 4.5
- [42] DONAHUE, L., LINK, R., AND HLADY, S. L. Numerical modelling of soils subjected to explosive loading. In *18th International symposium on the Military Aspects of Blast and Shock* (Bad Reichenhall, Germany, September 2004). 8.2.1
- [43] DORN, M. R., REES, S. J., AND DOCTON, M. K. Improving vehicle resistance to blast. In *8th European Attack and Survivability of AFV's Symposium* (Shrivenham, UK, March 1999). 2.1, 2.2.2
- [44] FAIRLIE, G., AND BERGERON, D. Numerical simulation of mine blast loading on structures. In *17th International symposium on Military Aspects of Blast and Shock* (Las Vegas, USA, June 2002). 1.2, 2.2, 2.1, 7.1.1, 8.1
- [45] FICKET, W., AND DAVIS, C. W. *Detonation*. University of California Press, 1979. pp. 386, ISBN 0-520-03587-9. 2, 2.2.1
- [46] FINGER, M., *et al.*. The effect of elemental composition on the detonation behaviour of explosives. In *6th Symposium of Detonation* (Coronado, USA, October 1976). 2.2.1, 4.5
- [47] FIŠEROVÁ, D., *et al.*. Numerical simulations as a reliable alternative for landmine explosion studies: The AUTODYN approach. *Journal of Impact Engineering*. submitted, under review. 7.2
- [48] FIŠEROVÁ, D., *et al.*. Evaluating numerical approaches in explosion modelling using a surface-laid mine. *Journal of Battlefield Technology* 7, 2 (July 2004), 1 – 5. 7.1
- [49] FIŠEROVÁ, D., *et al.*. The use of numerical simulations to analyse soil behaviour and the contribution made to target effects by soil, following the explosion of buried mines. In *7th International Conference on Shock and Impact Loads on Structures* (Perth, Australia, December 2005). 5, 7.3

- [50] FIŠEROVÁ, D., *et al.*. Systematic study of simulated mine explosions using AUTODYN. In *6th International seminar on New trend in research of energetic materials* (Pardubice, The Czech Republic, April 2003), University of Pardubice. 7.1, 7.2.4
- [51] FRIEDRICH, T., AND BUCHER, K. Experimental and numerical investigation of soil compaction due to pressure pulse loading. In *18th International symposium on the Military Aspects of Blast and Shock* (Bad Reichenhall, Germany, September 2004). 5
- [52] GREUTER, A. MOWAG – mine protection solution LAV's PIRANHA/EAGLE IV. In *9th European Armoured Fighting Vehicle Symposium* (Shrivenham, UK, March 2004). 1.2
- [53] GU, Q., LEE, F. H., AND CHEE, K. H. Numerical simulation of explosive-induced cratering. In *11th International Symposium on Interaction of the Effects of Munitions with Structures* (Mannheim, Germany, May 2003). 2.3
- [54] GUPTA, A. D. Modeling and analysis of transient response in a multilayered composite panel due to explosive blast. In *20th International Symposium on Ballistics* (Orlando, USA, September 2002). 2.2, 2.1
- [55] HECHTER, B. The value of landmine protection simulation in vehicle design. In *9th European Armoured Fighting Vehicle Symposium* (Shrivenham, UK, March 2004). 1.2
- [56] HEFFERNAN, J. Pentagon announces specific plan to use mines in Iraq. http://www.banminesusa.org/news/946_pentagon.htm, March 2003. 1.1
- [57] HEISER, R., AND MUREK, CH. Hydrocode calculations of the penetration of concrete. In *8th International Symposium on Interaction of the Effects of Munitions with Structures* (McLean, USA, April 1997), pp. 435 – 446. 2.2
- [58] HELD, M. Blast waves in free air. *Propellants, Explosives, Pyrotechnics*, 8 (1983), 1 – 7. 7.2.4, 4
- [59] HELD, M. A simple technique of measuring the blast effect of realistic warheads. In *12th International symposium on the Military Applications of Blast Simulation* (Gramat, France, September 1991), pp. 731 – 740. 2, 8.4, 8.4.1
- [60] HELD, M. Blast efficiency measurements. *Propellants, Explosives, Pyrotechnics*, 24 (1999), 286 – 290. 2.1.1

- [61] HELD, M. Diagnostic of momentum distribution and damage contour of non spherical high explosive charges. In *9th International Symposium on Interaction of the Effects of Munitions with Structures* (Berlin, Germany, May 1999), pp. 637 – 645. 8.4.1
- [62] HELD, M. Blast moments of detonating HE charges in the near field. In *4th Asia-Pacific Conference on Shock and Impact Loads on Structures* (Singapore, November 2001), pp. 13 – 26. 2, 2.1.1, 7.2.3, 8.4.1
- [63] HELD, M. Momentum distribution of anti-tank mines. In *20th International Symposium on Ballistics* (Orlando, USA, September 2002). 2, 2.1, 2.1.1, 8.4.1
- [64] HELD, M. Blast contour of cylindrical charges with different length to diameter ratios. In *11th International Symposium on Interaction of the Effects of Munitions with Structures* (Mannheim, Germany, May 2003). 8.4.1
- [65] HELD, M., AND TAN, G. E. B. Radial blast loads of confined cylindrical charges. In *11th International Symposium on Interaction of the Effects of Munitions with Structures* (Mannheim, Germany, May 2003). 2.1.1
- [66] HENRY, F. D. C. *The design and construction of engineering foundations*, 2nd ed. Chapman and Hall Ltd., London, UK, 1986. ISBN 0-412-12530-7. 5.3.2
- [67] HENRYCH, J. *The dynamics of explosion and its use*. Development in civil engineering, 1. Elsevier Science Publishers, Amsterdam, The Netherlands, 1979. pp. 558, ISBN 0-444-99819-5. 1.3, 2, 2.2.1, 2.3, 3.2.4, 5.3.1, 5.3.1, 5.3.2, 6.1, 8.2.1
- [68] HLADY, S. L. Effect of soil parameters on landmine blast. In *18th International symposium on the Military Aspects of Blast and Shock* (Bad Reichenhall, Germany, September 2004). 1.3, 2.1, 2.1.1, 6, 6.3.3, 8.2.1
- [69] HLADY, S. L., AND LAYCOCK, J. W. Affect of soil conditions on landmine blast output: Piston trials. Technical report, Defence Research Establishment Suffield, Canada, 2005. *in progress*. 2.1
- [70] HOLLAND, S. The application of the TABRE attenuation system to vehicles for enhanced underside blast protection. In *10th European AFV Attack And Survivability Symposium* (Shrivenham, UK, May 2001). 2.1

- [71] HORÁK, Z., KRUPKA, F., AND ŠINDELÁŘ, V. *Technická fyzika*. Praha: SNTL, 1960. p.1436. 5.3.1
- [72] HULTON, F. G., AND ENSTOCK, L. K. The direct measurement of close-in loading. In *9th International Symposium on Interaction of the Effects of Munitions with Structures* (Berlin, Germany, May 1999), pp. 217 – 224. 2.1.1
- [73] HUNTINGTON-THRESHER, W. K. E., AND CULLIS, I. G. TNT blast scaling for small charges. In *19th International Symposium of Ballistics* (Interlaken, Switzerland, May 2001), pp. 647 – 654. 7.1.4
- [74] JACKO, M., AND BELLA, V. The simulation of charge detonation action on armour plate. In *IVth International Armament Conference* (Waplewo, Poland, 2002), pp. 281 – 287. 2.1
- [75] JAKY, J. Pressure in sillos. In *2nd International conference on Soil mechanics and foundations engineering* (Rotterdam, 1948), vol. 3, pp. 103 – 107. 5.4.2
- [76] JOYNT, V. Buried landmines: Damage capability of buried landmines. Lecture at *Survivability of light armoured vehicles course*, Cranfield University, Shrivenham, UK, October 2003. 1.3, 2.1, 2.1.1, 7.3.7, 8.2.2, 8.4.1
- [77] JOYNT, V. Using shockwave manipulation against buried landmines. Lecture at *Survivability of light armoured vehicles course*, Cranfield University, Shrivenham, UK, October 2003. (document), 2.1.1, 2.1, 8.2.4
- [78] JOYNT, V. Mine and side blast protection from IED's. Lecture at *Survivability of light armoured vehicles course*, Cranfield University, Shrivenham, UK, November 2004. (document), 2.1, 2.1.1, 8.4.1, 8.1
- [79] KINGERY, C. N., AND BULMASH, G. Airblast parameters from TNT spherical air burst and hemispherical surface burst. Technical report ARBRL-TR-02555, US Army, Armament Research and Development Center, Ballistic Research Laboratory, Aberdeen Proving Ground, USA, April 1984. 2, 6.1, 6.1.1, 6.1.2
- [80] KINNEY, G. F., AND GRAHAM, K. J. *Explosive shocks in air*, 2 nd. ed. Springer-Verlag, 1985. pp. 269, ISBN 3-540-15147-8. 2, 6.1
- [81] KRAUTHAMMER, T., LIM, J., AND OH, G. J. Lessons from using precision impact test data for advanced computer code validations. In *10th International Symposium on Interaction of the Effects of Munitions with Structures* (San Diego, USA, May 2001). 2.2

- [82] LAINE, L., AND SANDVIK, A. Derivation of mechanical properties for sand. In *4th Asia-Pacific Conference on Shock and Impact Loads on Structures* (Singapore, November 2001), pp. 361 – 368. 1.3, 1.4, 2.2, 2.1, 2.3, 5, 4, 5.4, 5.4.1, 5.4.2, 7.1.1, 7.1, 7.1.3, 7.2, 7.2.1, 7.5, 7.11, 7.2.4, 7.9, 3a, 7.3.4, 7.3.7, 8.2.1, 8.2.4
- [83] LAINE, L., *et al.*. Numerical simulation of anti-tank mine detonations. In *12th APS Topical group Conference on Shock Compression of Condensed Matter* (Atlanta, USA, June 2001). 1.2, 2.2, 2.1
- [84] LAMBE, T. W., AND WHITMAN, R. V. *Soil Mechanics, SI Version*. Series in Soil Engineering. John Wiley and Sons, 1979. pp. 553, ISBN 0-471-02261-6. 3.2, 5.3.2, 5.3.2
- [85] LEONG, E. C., *et al.*. Response of buried structures subjected to below ground explosion. In *11th International Symposium on Interaction of the Effects of Munitions with Structures* (Mannheim, Germany, May 2003). 2.3
- [86] LIVERMORE SOFTWARE TECHNOLOGY CORPORATION, USA. *LS-DYNA user's documentation*. <http://www.lstc.com/>. 6.2
- [87] LUONG, M. P. Energy dissipating capacity of soils. pp. 1289 – 1292. 3.2.4
- [88] MADER, C. L. *Numerical modeling of explosives and propellants*, 2nd ed. CRC Press LLC, 1998. pp. 256, ISBN 0-8493-3149-8. 2, 2.2.1
- [89] MADSHUS, C., AND KAYNIA, A. M. Ground response to propagating air blast. *Norwegian Geotechnical Institute*, 201 (1997). ISBN 82-546-0180-1. 2.3
- [90] MAŠÍN, D., AND HERLE, I. Numerical analyses of a tunnel in London clay using different constitutive models. In *5th International Symposium TC28 Geotechnical Aspects of Underground Construction in Soft Ground* (Amsterdam, The Netherlands, 2005). 5.4.2, 8.2.4
- [91] MEYERS, M. A. *Dynamic behaviour of materials*. John Wiley and Sons, New York, 1994. pp. 668, ISBN 0-471-58262-X. 2
- [92] NAKAYAMA, Y., *et al.*. Soil cratering by surface explosions of cylindrical TNT charges. *FRAGBLAST – International Journal of Blasting and Fragmentation*, 3 (1999), 51 – 58. 2.3
- [93] NELL, S. Test and evaluation of landmine protected wheeled vehicles. In *9th AFV Symposium* (Shrivenham, UK, 2000). 1.2, 2.1

- [94] NIEKERK, B. . Land mine protection – dealing with the uncertainties. In *10th European AFV Attack And Survivability Symposium* (Shrivenham, UK, May 2001). 1.2, 2.1, 2.1, 2.1, 2.2.2
- [95] NYKL, FRANTIŠEK, *et al.*. Rázové vlny ve vzduchu [shock-waves in air]. Tech. rep., Výzkumný ústav průmyslové chemie, Pardubice, The Czech Republic, 1987. 1.3
- [96] ORAN, E. S., AND BORIS, J. P. *Numerical simulation of reactive flow*, 2nd ed. Cambridge University Press, 2001. pp. 529, ISBN 0-521-58175-3. 2.2.1, 4, 4.1
- [97] PERSSON, J. C. Scaled testing of mine protection - a cost effective tool for mine protection development. In *8th European Armoured Fighting Vehicle Symposium* (Shrivenham, UK, March 2003). 2.1, 2.1, 2.2.2
- [98] PERSSON, P., HOLMBERG, R., AND LEE, J. *Rock blasting and explosives engineering*. CRC Press, Inc., Boca Raton, 1994. pp. 540, ISBN 0-8493-8978-X. 2, 2.3
- [99] POTTS, D. M., AND ZDRAVKOVIĆ, L. *Finite element analysis in geotechnical engineering: Theory*. Thomas Telford Publishing, London, UK, 1999. pp.440. ISBN 0-7277-2753-2. 8.2.2
- [100] POTTS, D. M., AND ZDRAVKOVIĆ, L. *Finite element analysis in geotechnical engineering: Application*. Thomas Telford Publishing, London, UK, 2001. pp.427. ISBN 0-7277-2783-4. 5.3.2, 5.3.2
- [101] RAVID, M., AND ZIV, D. Protection and survivability of light AFV and support vehicles. In *9th European Armoured Fighting Vehicle Symposium* (Shrivenham, UK, March 2004). 1.2
- [102] RHIJNSBURGER, M. P. M. Overview of the use of LS-DYNA in close-in explosive problems at TNO-PML. In *11th International Symposium on Interaction of the Effects of Munitions with Structures* (Mannheim, Germany, May 2003). 2.1
- [103] SADD, M. H., HOSSAIN, M., AND ROHANI, B. A study of explosive wave propagation in granular materials with microstructure. Technical report SL-86-35, Department of the Army, US Army Engineer Waterways Experiment Station, Vicksburg, USA, September 1986. 1.3

- [104] SCHLEIN, O., AND LAGALÉE, A. Global landmine crisis: The problem. *United Nations Association of the USA* (2000). <http://www.landmines.org/GlobalCrisis/TheProblem/TheProblem-all.htm>. 1.1
- [105] SKAGGS, R., *et al.* Blast loading measurements by the vertical impulse measurement fixture (VIMF). Technical report, US Army Tank-automotive Research Development and Engineering Center, Warren, USA, 2004. *in submission*. 2.1
- [106] SLOAN, C. E. E. *Mine warfare on land*, 1st ed. Brassey's Defence Publishers, London, UK, 1986. pp. 153, ISBN 0-08-031196-2. 1.1, 1.3
- [107] SMITH, D. L., AND KUMMER, R. J. Hydrocode modelling of the misar anti-tank mine. Technical report, Defence Science and Technology Organisation, Melbourne, Australia, 1988. Microfiche: AD-A207740. 1.3
- [108] SMITH, P. D., AND HETHERINGTON, J. G. *Blast and ballistic loading of structures*, 1st ed. Butterworth-Heinemann, Oxford, UK, 1994. pp. 320, ISBN 0-7506-2024-2. (document), 1.3, 2, 2.3, 6.1, 6.2
- [109] SOUERS, P. C., AND KURY, J. W. Comparison of cylinder data and code calculations for homogeneous explosives. *Propellants, Explosives, Pyrotechnics*, 18 (1993), 175 – 183. 2.2.1, 2.2.1, 4.5
- [110] TAN, G. E. B., AND LAM, T. K. Momentum loads from cylindrical explosive charges with different casing thicknesses. In *17th International symposium on the Military Aspects of Blast and Shock* (Las Vegas, USA, June 2002). 2.1.1
- [111] TAN, G. E. B., AND LAM, T. K. Internal blast momentum loads of cylindrical charges with different casing thicknesses. In *18th International symposium on the Military Aspects of Blast and Shock* (Bad Reichenhall, Germany, September 2004). 2.1.1
- [112] TENNANT, D. W., AND LEVINE, H. S. Response and failure of internal structural subsystems under blast and shock loading. *Journal of Pressure Vessel Technology* 116 (November 1994), 409 – 418. 1.3
- [113] TORO, E. F. *Riemann solvers and numerical methods for fluid dynamics: A practical introduction*. Springer-Verlag, Berlin, Germany, 1997. pp. 592, ISBN 3-540-61676-4. 4

- [114] UNKNOWN. Resistance in Chechnya (photos). http://johnw.host.sk/photo/resistance_in_chechnya.htm. downloaded 8. 11. 2005. 1.2
- [115] US ARMY ENGINEER WATERWAYS EXPERIMENT STATION. *CONWEP*. Vicksburg, USA, December 1991. (document), 1.4, 6, 6.1, 6.3, 7.1.2, 8.1
- [116] VÁVRA, P. *Teorie výbušnin*. Univerzita Pardubice, 2002. 2.2.1
- [117] VIGGIANI, G., AND ATKINSON, J. H. Stiffness of fine-grained soil at very small strains. *Geotechnique* 45, 2 (1995), 249 – 265. 5.3.1, 5.4.2, 8.2.4
- [118] VOVK, A. A., AND DEMESHCHUK, L. I. Applied geodynamics of explosions. *International Journal of Fluid Mechanics Research* 23, 1 & 2 (1996), 116 – 121. ISSN 1064-2285. 1.3, 2.3
- [119] VRTEK, F. *Mechanika zemin: Inženýrská geologie a hydrologie v praxi. (Soil mechanics: Engineering geology and hydrology in practice)*, 1998. (document), 5, 5.1, 5.1, 5.1, 5.3, 5.3.2, 5.3.4, 5.4, 7.3.4, 8.2.1, 8.2.2, 8.2.3
- [120] WALTERS, W. P., AND ZUKAS, J. A. *Fundamentals of shaped charges*. John Wiley and Sons, 1989. pp. 398, ISBN 0-471-62172-2. 1.3
- [121] WANG, J. Simulation of landmine explosion using LS-DYNA-3D software: Benchmark work of simulation of explosion in soil and air. Technical report DSTO-TR-1168, DSTO, Aeronautical and Maritime Research Laboratory, Melbourne, Australia, June 2001. 1.2, 2.2, 2.1, 6.2, 6.2.3, 7.2, 7.2.1, 7.2.2, 7.11
- [122] WANG, Z., AND LU, Y. Numerical analysis on dynamic deformation mechanism of soils under blast loading. *Soil Dynamics and Earthquake Engineering*, 23 (2003), 705 – 714. 8.2.1
- [123] WESTINE, P. S., *et al.*. Development of computer program for floor plate response from land mine explosions. Technical report No. 13045, US Army Tank-Automotive Command, Warren, USA, 1985. 2.1
- [124] WILKINS, M. L. Calculation of elastic-plastic flow. *Methods of Computational Physics* 3 (1964), 211 – 263. 4.1
- [125] WILLIAMS, K., AND FILLION-GOURDEAU, F. Numerical simulation of light armoured vehicle occupant vulnerability to anti-vehicle mine blast. In *7th International LS-DYNA Users Conference* (Dearborn, USA, May 2002), pp. 6–7 – 6–14. 1.2, 2.2.2

-
- [126] WILLIAMS, K., AND POON, K. A numerical analysis of the effect of surrogate anti-tank mine blasts on the M113. Technical report DREV TM-2000-007, Defence Research Establishment, Valcartier, Canada, March 2000. 2.2, 2.1
- [127] WILLIAMS, K., *et al.*. Validation of a loading model for simulating blast mine effects on armoured vehicles. In *7th International LS-DYNA Users Conference* (Dearborn, USA, May 2002), pp. 6–35 – 6–44. 1.2, 2.1, 2.2.2, 8.3
- [128] ZUKAS, J. A. *Introduction to hydrocodes*. Studies in Applied Mechanics 49. Elsevier Inc., 2004. pp. 313, ISBN 0-08-044348-6. 4
- [129] ZUKAS, J. A., AND WALTERS, W. P. *Explosive effects and applications*. Springer-Verlag, New York, 1998. pp. 431, ISBN 0-387-98201-9. 2, 2.2.1

Appendix **A**

Description of soil laboratory tests

Short description of soil laboratory tests are presented in this Appendix. The tests serve to describe soil unambiguously and determine the mechanical properties. Soil properties were used to derive the soil model (Chapter 5). The tests are in compliance with British Standard BS 1377 [27]. For further details, also refer to books on soil mechanics, such as Berry *et al.* [24], Barnes [17].

A.1 Tests for determining physical properties of soil

To describe soil completely, the following parameters need to be determined: particle size distribution, density, moisture content and Atterberg limits. From these parameters, the other parameters that describe the ratio of different soil phases can be calculated using formulae presented in Table 3.1.

A.1.1 Particle size distribution

Sieving methods. The oven-dried sample of soil is placed on the 20 mm test sieve and sieved. The soil retained on the 20 mm test sieve is then sieved from 73 mm up to 28 mm test sieve. Water is added to the soil passed through the 20 mm test sieve. Wet soil is washed through the 2 mm test sieve with the 63 μm sieve underneath until the water passing the 63 μm sieve is virtually clear. The soil retained on sieves is dried in the oven. The soil is sieved through set of test sieves from 20 mm to 63 μm sizes. The mass of soil retained on each sieve is weighed and recorded. Subsequently, the percentage of soil mass retained on each test sieve is calculated. The obtained measurement results are represented by curve plotted on a semi-logarithmic chart or at a table.

Sedimentation methods. Both methods, *the pipette method* and *the hydrometer method*, require given particle density of soil specimen. Soil suspension is prepared from soil passed through 63 μm test sieve. In the pipette method, pipette sampling taken at given time from shaken cylinder is dried in the oven and weighed. The hydrometer method determines particle distribution by reading on hydrometer immersed in the soil suspension at different time periods.

A.1.2 Density

Three methods are used to determine the bulk density: *linear measurement method*, *immersion in water method* and *water displacement method*. The methods differ in the procedure of determining the volume of soil specimen. In the linear measurement method, the soil specimen forms a regular shape, prismatic or cylindrical, whose volume is easy to calculate. In the immersion in water method, the volume of irregular shaped soil is determined as difference of masses of soil specimen measured in air and when immersed in water. In the third method, the volume is determined by measuring the mass of displaced water after immersing soil specimen into water.

The particle density is determined by using following methods respective to particles size: *gas jar method*, *small pyknometer method* or *large pyknometer method*. The gas jar method is suitable for most soils as the procedure consists of shaking the gas jar with soil sample in the shaking apparatus to evolve air from soil. The particle density of soils containing particles finer than 2 mm is determined by small pyknometer method, because the air is evolved from soil sample by reducing the pressure in the vacuum desiccator. Since the gas jar and small pyknometer methods have low accuracy, the large pyknometer method is normally used with satisfactory results for non-cohesive soil consisting of particles finer than 20 mm.

A.1.3 Moisture content

The moisture content is determined by the *oven-drying method*. The soil sample inserted in an airtight container is placed in the oven to dry at a temperature of about 105 °C to 110 °C. The sample is dry when the difference in successive weighings is less than 0.1 % of the original mass of the sample.

A.1.4 State consistency of soil

Two methods are standardized for determination of the liquid limit, particularly *cone penetrometer method* and *Casagrande apparatus method*. In the cone penetrometer

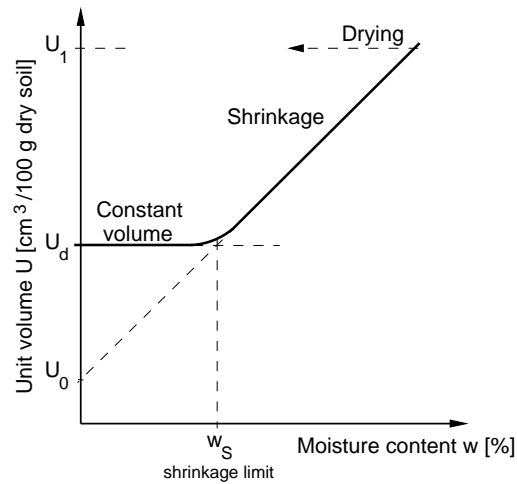


Figure A.1: The shrinkage curve for determining shrinkage limit w_p .

method, the graph expressing dependence of the moisture content and cone penetration to the soil sample is plotted. The liquid limit w_L is referred to the value of the moisture content for 20 mm cone penetration. The Casagrande apparatus method is an alternative method because the results are more inclined to operator's judgement. In this method, the liquid limit w_L is given by the moisture content corresponding to 25 bumps of the Casagrande cup.

The procedure to determine plastic limit consists of moulding and rolling thread from soil. The moisture content of the soil thread, when cracks and crumbles appears, is reported as the plastic limit w_p .

The shrinkage limit is determined by measuring the successive change of specimen volume with decreasing moisture. The test results are expressed by plotting the shrinkage curve. The shrinkage limit is the value of moisture content determined by the intersection of two lines: shrinkage inclined straight line and constant volume horizontal line (see Fig. A.1).

A.2 Tests for determining mechanical properties of soil

The procedures for determining mechanical properties are presented. The direct shear tests and compression tests are laboratory procedures carried out on disturbed soil samples. Strength and stress-strain properties can be measured in situ by *pressuremeter*.

A.2.1 Compression tests

Tests that determine compressive strengths are schematically represented in Figure A.2, and are as follows:

- i. *One dimensional compression test* – for determining the compressibility parameters. Soil specimen is allowed to drain.
- ii. *Unconfined compression test* – for determining compressive strength of the saturated cohesive soil.
- iii. *Triaxial compression test* – for deriving undrained shear strength of cohesive soil with no change in total moisture content. As a variant, the triaxial test can be conducted with *multistage loading*.

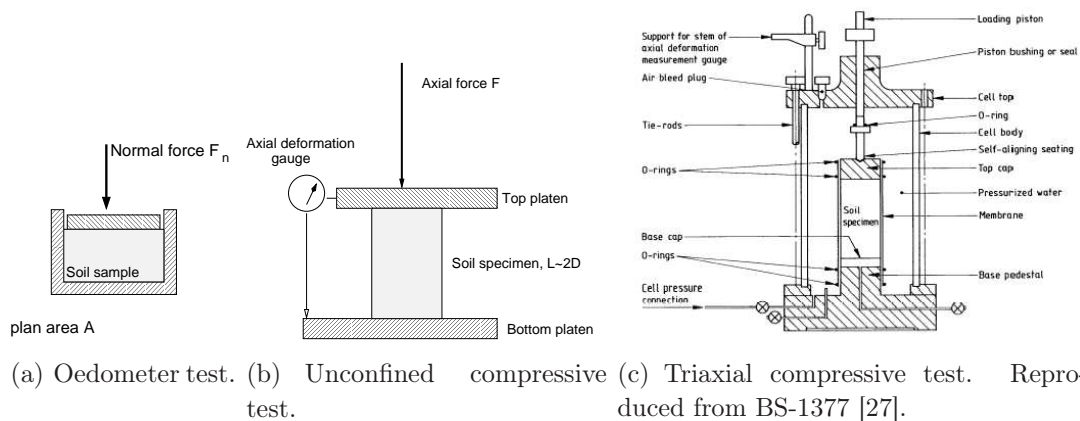


Figure A.2: The schematic representation of compressive strength tests.

i. One dimensional compression test

Other terms for this test are the *oedometer test*, the *confined compression test* and the *consolidation test*. The test is carried out in the consolidation apparatus also known as the oedometer. The disc specimen of soil is laterally confined, i.e., the strain in the horizontal directions is prevented. The soil is subjected to vertical axial compressive force F_n in increments. The schematic representation is in Figure A.2(a). The soil is allowed to drain freely as soil specimen fastens between top and bottom porous discs. The change in the height h of the specimen is recorded in suitable intervals. The oedometer test provides following data:

- plots of void ratio (or vertical compression) against the logarithm of applied pressure,

- plots of compression against the logarithm of time (or square root of time),
- determine the magnitude and rate of the consolidation, which can be expressed by the coefficient of volume compressibility m_v [m²/MN], the coefficient of consolidation c_v [m²/year], the compression index C_c [-] and the swelling index C_s [-], and
- constrained modulus $D = E_{oed} = \Delta p / \Delta \varepsilon$ [Pa], where $\varepsilon = \Delta h / h_0$.

ii. Unconfined compression test

The cylindrical specimens of cohesive soil is only subjected to axial compressive force F_n . The axial deformations with increased applied axial force is recorded until failure occurs. The test principle is illustrated in Figure A.2(b). Compressive stress and strain are calculated from equations:

$$\sigma_1 = \frac{F_n(1 - \varepsilon)}{A_0}; \quad \varepsilon = \frac{\Delta L}{L_0} \quad (\text{A.1})$$

where A_0 is the initial cross-sectional area of the specimen, ΔL is the change in length determined from axial deformations, L_0 is the initial length of the specimen. Stress-strain curve is plotted and failure stress, or 20% strain if it occurs first, is referred as the *unconfined compressive strength*, q_u [Pa]. Two methods are used to determine this: the *Load frame method* in laboratory and the *Autographic method*, which is a portable apparatus intended for in-situ tests.

iii. Triaxial compression test procedure

A cylindrical specimen of cohesive soil is confined by an impervious membrane in order to prevent water drainage. The specimen is placed in a triaxial cell which is pressurized by water (Figure A.2(c)). Strain-controlled axial loading is applied to the specimen while simultaneously being subjected to a constant confining pressure. Readings of applied force F and deformation are recorded until the specimen fails. The maximum value is derived for the deviator stress (i.e., the principal stress difference) which is calculated from equation:

$$(\sigma_1 - \sigma_3) = \frac{F(1 - \varepsilon)}{A_0}; \quad \varepsilon = \frac{\Delta L}{L_0} \quad (\text{A.2})$$

where A_0 is the initial cross-sectional area of the specimen, ΔL is the change in length determined from axial deformations, L_0 is the initial length of the specimen. Then the undrained cohesion c_u is expressed as follows:

$$c_u = \frac{1}{2} \max(\sigma_1 - \sigma_3) \quad (\text{A.3})$$

As $\phi_u = 0$, the undrained cohesion defines the undrained shear strength τ_u , i.e., $\tau_u = c_u$. Tests are conducted to a set of similar specimens subjected to different confining pressures.

Multistage compression test/loading. The specimen is subjected to increased axial load in (usually three) stages, each stage under a different confining pressure. When the maximum stress is imminent, the confining pressure is increased and readings of the applied force and deformation are carried out. The test continues until the maximum deviator stress is clearly defined. The undrained cohesion c_u is calculated by the same way as in single compression test.

A.2.2 Direct shear tests

Direct shear tests determine the parameters describing the soil behaviour under shear loading. Following tests are standardised:

- i. *Laboratory vane test procedure* – vane shear strength τ_v is determined by measuring the torque, i.e., the maximum angular deflection of the torsion spring and the angle of rotation of the vane, applied to shear the cohesive soil sample of the given moisture content.
- ii. *Small shearbox procedure* – effective cohesion c' and effective angle of friction ϕ' is determined for cohesive and cohesionless soil of the given moisture content by this procedure (described below).
- iii. *Large shearbox procedure* – the principle of this method is similar to small shearbox procedure, it is used for the gravelly soil or large sample of soil.
- iv. *Small ring shear procedure* – remoulded cohesive soil is subjected a rotational shear stress while subjected a normal stress. Measured angular displacement is converted to apparent linear displacement. The residual shear strength¹, ϕ'_R , is read off from the plots constructed in similar way, as in the shearbox procedure.

ii. Shearbox test procedure

The soil sample is placed into the shearbox of plan area A . The shearbox apparatus, schematically represented in Figure A.3, is horizontally shifted by applying shear force F_S while subjected to a normal force F_n . The horizontal displacement is recorded within elapsed time. The procedure is repeated under various normal

¹“the shear strength which a soil can maintain when subjected to large shear displacement after the peak strength has been mobilized.”

forces applied. The shear stress and normal stress are calculated from expressions $\tau_f = F_S/A$ and $\sigma_n = F_n/A$, respectively. From each shear stress – horizontal displacement graph, the value of maximum shear stress τ_f is read off. Finally, the effective angle of friction and effective cohesion is derived from the graph of relationship of normal stress σ_n and maximum shear stress τ_f . This evaluation of the test is given in Figure A.4.

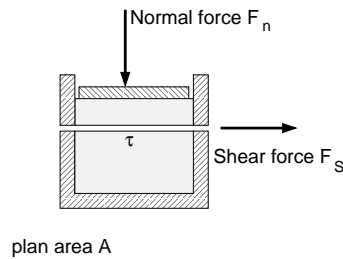


Figure A.3: The schema of the shearbox used in small shearbox tests.

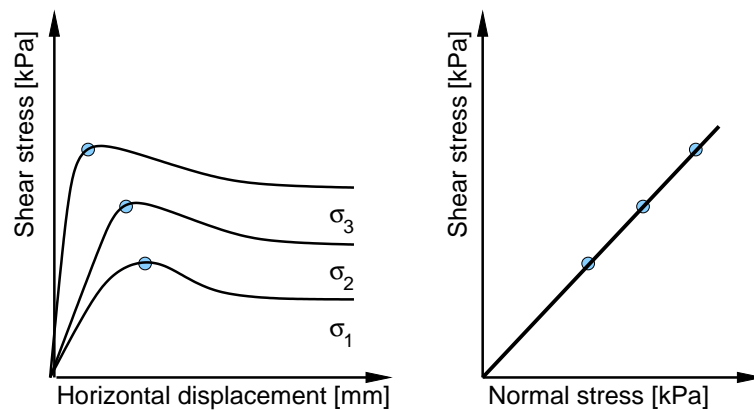


Figure A.4: The evaluation of shearbox test.

A.2.3 Pressuremeter test

The pressuremeter is used for in situ measurements of strength and stress strain properties of all types of soils. The main part of pressuremeter is the probe which is the cylindrical cell fitted with strain gauges on cell circumference. The probe is placed into a borehole at the test depth. The probe is pneumatically or hydraulically inflated. The change in cell diameter is recorded for each pressure increment. The pressuremeter limit pressure p_l and modulus of deformation E_M (termed also as

Ménard modulus) are obtained using the stress-strain curves. The limit pressure p_l is pressure corresponding to the doubling of the volume of the initial cavity. The modulus of deformation E_M is computed from equation:

$$E_M = (1 + \nu) \Delta P \frac{R}{\Delta R} \quad (\text{A.4})$$

where ν is the Poisson's ratio, ΔP is the pressure increment and $\Delta R/R$ is the relative change in cell radius. The principle of this procedure is simple and data are obtained directly, the complexity is given by drilling a borehole with diameter about 75 mm, and imposing working pressure of 4,000 to 20,000 kPa according to the type.

Autodyn features

B.1 Other solvers

With the existence of various structural dynamic applications, different needs arise to be represented in the hydrocode. As AUTODYN tends to cover a wide spectrum of dynamic applications, the following solvers have been implemented, in addition to Lagrange and Euler solvers:

- **Arbitrary Lagrange-Euler (ALE)** is an extension of the Lagrangian approach. As the highly distorted Lagrange mesh can lead to inaccurate solution and even terminate the calculation, a rezoning step must be performed. In Arbitrary Lagrange-Euler solver, the solution is remapped onto a different mesh. This mesh moves independently to the material motion. The material interfaces are treated as Lagrangian grid points. This constrains the ALE approach as the rezoning step has some difficulties at material boundaries. The ALE elements can contain only a single material. The user should have some experience to choose a reasonable specification for mesh movement. Several options for mesh movement are available, such as equipotential, flow averaged, equal spacing in X, Y, I, J or IJ directions. The Arbitrary Lagrange-Euler solver is implemented in AUTODYN-2D and 3D.
- **Smooth particle hydrodynamics (SPH)** is a relatively new technique compared with standard hydrocodes methods (Euler, Lagrange). In the SPH, a set of particles moves in space without boundaries. A particle is a point with assigned mass. The Smooth particle hydrodynamics method contains the potential to model efficiently large deformation of material due to its meshless (gridless) technique. The no-requirement for a numerical grid means that mesh

tangling (large distortion) does not occur. Mesh tangling can cause termination of calculation when the Lagrange solver is employed. The SPH method is a Lagrangian technique. This allows efficient tracking of materials, i.e., no need for convection algorithms and interface tracking methods as in the Euler solver. In addition, the region containing the material can be only modelled compared with the Euler solver. In the Euler solver, the region where materials flow must be modelled thus adding to the computational expense. Smooth particle hydrodynamics solver is implemented in AUTODYN-2D and 3D. The SPH solver can interact with the parts modelled using Lagrange, Arbitrary Lagrange-Euler or Shell solvers.

- **Shell** was implemented into AUTODYN-2D and 3D in order to model thin structural elements. The modelling of a thin structure using the Lagrange solver would be computationally extraordinarily expensive due to the small timestep needed. The Shell solver includes full bending theory. In the Shell solver, it is assumed that the normal stress through the shell is negligible with respect to in-plane stresses and the transverse shear is neglected. The stress distribution is biaxial. In addition, volume change of the shell is not permitted, i.e., the density of the shell is kept constant.

B.1.1 Interface tracking in Euler solver

As the Euler solver allows several materials within a single cell, it is necessary to know the amount of each material in the cell and material interface locations in order to calculate the material transport across a cell. In AUTODYN, two algorithms for interface tracking are available. Both methods derive the surface definitions from the volume fractions of different materials. The choice of tracking algorithms can be made at the field **Controls** → **Transport**. The principles of the methods are as follows:

- **Donor-cell method** – is the simplest interface tracking method. The material interface within the donor cell is reconstructed by analyzing the volume fractions of materials in the two cells adjacent to the face (i.e., one-dimensional donor-acceptor scheme).
- **SLIC** – stands for *Simple Line Interface Calculation* algorithm. This algorithm is also a first order tracking method as Donor-cell method with further improvement. The material presence in three cells (the donor cell, the acceptor cell and the cell behind the donor cell) determines the flux of material. SLIC algorithm is robust and efficient when the materials flow to the normal

of the grid. The algorithm alternates the direction (x, y sweeps) in which the interface is reconstructed. The volume fractions of each materials are determined in a single step. This algorithm is set as default interface technique in AUTODYN.

B.2 Additional features in material modelling

Polynomial EOS

The polynomial equation of state relates pressure p to the compression μ through polynomial function of maximum third order. This is expressed as follows:

$$p = A_1\mu + A_2\mu^2 + A_3\mu^3 + (B_0 + B_1\mu)\rho_0 e \quad (\text{B.1})$$

where A_1, A_2, A_3, B_0, B_1 are coefficients to be defined by user, e is the specific energy, the compression is defined as

$$\mu = \frac{\rho}{\rho_0} - 1 \quad (\text{B.2})$$

The user is prompted to input also reference density ρ_{ref} which equals to the initial density of material ρ_0 , i.e., $\rho_{ref} = \rho_0$.

Linear EOS is a sub-part of the polynomial equation. Only coefficient A_1 is defined, other coefficients are kept zero.

Drucker-Prager strength model

Previously termed as Mohr-Coulomb in AUTODYN, the Mohr-Coulomb criterion is widely used in the soil mechanics. The Mohr-Coulomb strength model linearly relates the yield strength Y to normal stress p by equation:

$$Y = c + p \tan \varphi \quad (\text{B.3})$$

where c is the intercept of y -axis and φ is the slope of the line. The input parameters are the shear modulus, the slope φ and the constant c or piecewise linear relationship between the pressure and the yield stress.

Stochastic option in failure criterion

From AUTODYN version 5 (2004), the Stochastic option in failure was incorporated. This allows to model the material heterogeneity. The failure properties are stochastically distributed in material. Probability of failure is derived from a statistical

distribution as shown in Figure B.1. The algorithm is based on a Mott's distribution that has been used to describe fragment populations obtained by detonating warhead. The Mott's distribution is described by equation for probability of failure at a strain of ε :

$$P = 1 - \exp\left(-\frac{c}{\gamma}e^{\gamma\varepsilon}\right) \quad (\text{B.4})$$

where γ is the stochastic variance, c is the material constant.

The stochastic option can be used with any failure criterion. The material has to be modelled with Lagrange or SPH solvers. The stochastic option is not available for material modelled using Euler solver. This algorithm was successfully used to model “warhead fragmentation” problems. This option has the potential to model the non-uniformity of soil properties that can be attributed to the stones, cluster that are the ‘seeds’ of high pressures and failure.

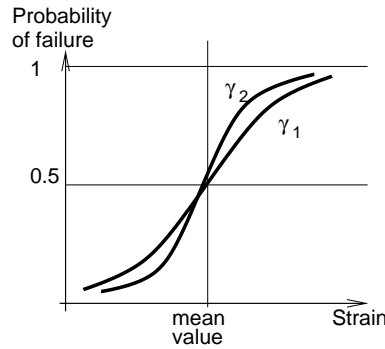


Figure B.1: Stochastic distribution.

Plastic strain failure criterion

The bulk failure occurs when the effective plastic strain exceeds the specified limit. This criterion can be expressed as follows:

$$\varepsilon_{eff}^{pl} < \varepsilon_{eff,max}^{pl} = \text{const.} \quad (\text{B.5})$$

Then, the stress deviator and total stress are set to zero, i.e., $s_{ij} = 0$, $\sigma_{ij} = 0$. The material can not sustain any negative hydrodynamic pressure and any shear strength in post-failure flow. The flow is hydrodynamic. This criterion can be used to model the ductile failure of material.

Cumulative damage failure criterion

Cumulative damage failure criterion was introduced into AUTODYN to model inelastic behaviour of materials such as concrete and ceramics. The strength of these materials can be decreased by the crushing effect. This criterion can be used only with the linear equation of state. Any strength model can be used in conjunction with the cumulative damage criterion. Although, it will be, with the high probability, the Drucker-Prager strength model.

Definition of the damage D is depicted in Figure B.2(a). The damage is set to zero till the effective plastic strain limit ε_{eff1}^{pl} is reached. Then, the damage parameter linearly increases up to the maximum damage value D_{max} . In mathematic notation, it can be written as follows:

$$D = D_{max} \frac{\varepsilon_{eff}^{pl} - \varepsilon_{eff1}^{pl}}{\varepsilon_{eff2}^{pl} - \varepsilon_{eff1}^{pl}} \quad (B.6)$$

The damage factor reduces the bulk modulus, shear modulus and yield strength as the calculation proceeds. The manner is represented in Figure B.2. The yield stress Y is reduced in the following manner:

$$Y_{dam} = Y \left(1 - D \right) \quad \text{for } p > 0 \quad (B.7)$$

$$Y_{dam} = Y \left(1 - \frac{D}{D_{max}} \right) \quad \text{for } p < 0 \quad (B.8)$$

The bulk modulus K and shear modulus G do not change in compressive state, i.e., the hydrostatic pressure p is positive. The bulk modulus, shear modulus and yield stress decreases up to zero by the factor $(1 - D/D_{max})$ when the material is under tension, i.e., the hydrostatic pressure is negative.

Erosion

Erosion overcomes the problem of a large distortion of Lagrange grid. Erosion is not true modelling of a physical phenomenon. Erosion is a numerical procedure that remove the distorted element from the calculation when a strain exceeds a specified limit. An erosion limit can be specified for one of the following strain options:

- *instantaneous effective geometric strain* – increase or decrease upon loading and unloading,
- *incremental effective geometric strain* – monotonically increasing function,

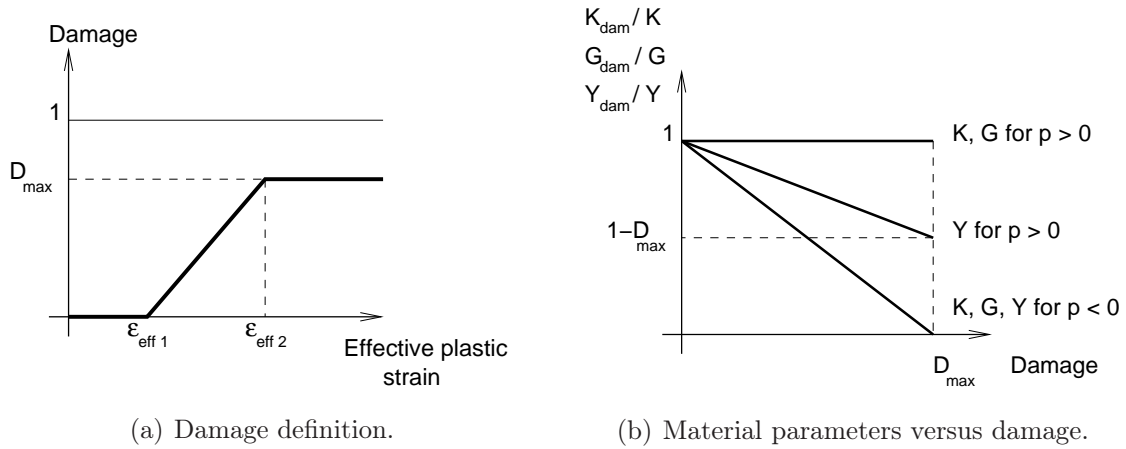


Figure B.2: Definition of cumulative damage failure criterion. After AUTODYN manual [32].

- *effective plastic strain* – monotonically increasing function,
- *user's* defined erosion criterion.

The mass of removed element can be eliminated or retained. When the mass is retained, the conservation of inertia and spatial continuity of inertia are preserved. The mass is distributed to the nodes of the element. The compressive strength and internal energy of material are discarded whether the mass is retained or not.

B.3 Material models used in simulations

Table B.1: Model of air using an ideal gas equation of state.

Parameter	Value	Unit
EOS	Ideal gas	
Reference density ρ_0	1.225	kg.m ⁻³
Adiabatic exponent γ	1.4	–
Internal energy e_0	206.82×10^3	J.kg ⁻¹
Strength model	None	
Failure model	None	

Table B.2: *Model of high explosives using Jones-Wilkins-Lee equation of state.*

Parameter	TNT	C-4	Unit
EOS	JWL	JWL	
Density ρ_0	1,630	1,601	kg.m ⁻³
A	373.77×10^6	609.77×10^6	kPa
B	3.7471×10^6	12.95×10^6	kPa
R_1	4.15	4.5	–
R_2	0.9	1.4	–
ω	0.35	0.25	–
CJ detonation velocity	6,930	8,193	m.s ⁻¹
CJ energy e_0	6.0×10^6	9.0×10^6	J.kg ⁻¹
CJ pressure	21.0×10^6	28.0×10^6	kPa
Autoconvert to ideal gas	Yes	Yes	
Strength model	None	None	
Failure model	None	None	

Table B.3: *Model of Iron Armco.*

Parameter	Value	Unit
EOS	Linear	
Reference density ρ_0	7,890	kg.m ⁻³
Bulk modulus	164×10^6	kPa
Specific heat	452	J.kg ⁻¹ .K ⁻¹
Strength model	Johnson Cook	
Shear modulus	80×10^6	kPa
Yield stress	175×10^3	kPa
Hardening constant	378×10^3	kPa
Hardening exponent	0.32	–
Strain rate constant	0.06	–
Thermal softening exponent	0.55	–
Melting temperature	1,811	K
Strain rate correction	1st order	
Failure model	None	
Erosion model	None	

Appendix **C**

Mine impulse pendulum

Chapter 6, section 6.3 describes the experiments in which the mine blast output is captured by the mine impulse pendulum (MIP). In the subsequent section of this Appendix, the governing equations of the pendulum are described. For the purposes of modelling in 2D, axi-symmetric geometry is assumed throughout and the pendulum's rotational movement is converted into straight-line motion of a plate. The physical parameters of the system have to be maintained in order to reproduce the experiment in a reliable manner. This has also been discussed and presented in the subsequent sections of this Appendix.

C.1 Mine impulse pendulum – rotational movement

The mine impulse pendulum is depicted in Figure C.1(a). The force generated from the explosion is acting on the target plate. This force causes the pendulum arm to move upwards. The gravitational force reacts against this force. Upon reaching the maximum deflection the arm moves back to the initial position. Equilibrium of the forces is satisfied during this motion. The pendulum arm describes a circular arc and exhibits *rotational movement*. The law of conservation of energy has to be satisfied during the pendulum's motion. The total energy equals the sum of kinetic and potential energy at any time. Two points are considered: (1) The kinetic energy is maximum at the beginning of the motion where the gravitational force does not have time to react against the pendulum arm. The potential energy does not change and is equal to zero. (2) The pendulum arm reaches the maximum deflection and starts moving back. At this point, the kinetic energy is equal to zero and the potential energy is maximum. The change in potential energy is given by the change in the

deflection. Mathematically, this can be represented as:

$$E = E_{kinetic} + E_{potential} \quad (C.1)$$

$$\text{at the beginning: } E = \frac{1}{2}J_0\omega^2 + 0 \quad (C.2)$$

$$\text{maximum deflection: } E = 0 + mgr \sin \beta_{max} \quad (C.3)$$

Rewriting, the energy equation becomes

$$\frac{1}{2}J_0\omega^2 = mgr \sin \beta_{max} \quad (C.4)$$

The momentum of the rotational motion is defined as

$$I = \frac{J_0\omega}{R} \quad (C.5)$$

Combining Equations C.4 and C.5, the maximum impulse delivered to the pendulum is

$$I = \sqrt{\frac{2J_0mgr \sin \beta_{max}}{R^2}} \quad (C.6)$$

The meanings of the symbols used and their values, can be found in Table C.1. The impulse is dependent on the angular deflection. This is only the variable that changes with the loading. Other parameters are determined by the dimensions of the pendulum.

The task within the experiments is to measure the angular deflection. Three methods (for verification purposes as well as to ensure the collection of at least *one* value) were used for collecting this data:

- high speed video,
- a scratch gauge – sharp pointer scratches an arc on the aluminium plate,
- a displacement pot – the length of cable retracted with the rising pendulum corresponds to the displacement angle.

C.2 Surrogate MIP – straight-line motion of the plate

The principle is the same as in the MIP. Only, the plate executes a straight-line motion as opposed to the rotational motion of the pendulum arm.

Applying the law of conservation of energy principle again, the equation takes the mathematical form:

$$E = E_{kinetic} + E_{potential} \quad (C.7)$$

$$\text{at the beginning: } E = \frac{1}{2}m_p v^2 + 0 \quad (C.8)$$

$$\text{maximum displacement: } E = 0 + m_p g h \quad (C.9)$$

where h is the maximum displacement of the plate. Rewriting, the energy equation becomes

$$\frac{1}{2}mv^2 = mgh \quad (C.10)$$

The momentum of the straight-line motion is defined as

$$I = mv \quad (C.11)$$

Combining equations C.10 and C.11, the impulse delivered to the plate is the function of the plate's displacement:

$$I = m \sqrt{2gh} \quad (C.12)$$

C.3 Plate parameters equivalent to the horizontal pendulum

For the purposes of being incorporated into the presented numeric model, it is desirable for the pendulum to possess 2D axi-symmetric properties. This is represented in Figure C.1. Also, a *pro rata* calculation has to be made to determine the equivalent mass of the plate, in order to retain the same properties of the original system, i.e., mass and surface area of the plate. It follows that:

I. Mass of the equivalent plate

The impulse of the horizontal pendulum (MIP) has to be equal to the impulse of the plate. The same is valid also for energy.

$$I_{MIP} = I_{plate}, \quad \text{and} \quad E_{MIP} = E_{plate}$$

From the equality of energy

$$\frac{1}{2}J_0\omega^2 = \frac{1}{2}m_{plate}v^2 \quad (C.13)$$

After manipulation in equation C.13, the mass of the plate m_{plate} is determined as

$$m_{plate} = J_0 \left(\frac{\omega}{v} \right)^2$$

and substituting ω , v from impulse relationships C.5 and C.11, the plate mass is determined as

$$m_{plate} = \frac{J_0}{R^2} \quad (C.14)$$

Using parameters of the horizontal pendulum, the plate mass is calculated

$$m_{plate} = \frac{14700}{4.27^2} = 806.23 \text{ kg}$$

Note: Checking with experimental data – I_{MIP} , E_{MIP} – the mass is 806.76 kg

II. Diameter

The other parameter which has to be matched is the surface area which the impulse acts on. Applying axial symmetry in 2D modelling, the plate is of circular profile. Whereas, the active surface of pendulum is of square profile. The area of the pendulum and the plate has to be equal thus

$$\begin{aligned} A_{\square} &= A_{\circ} \\ a^2 &= \pi r_{plate}^2 \\ r_{plate} &= a / \sqrt{\pi} \end{aligned}$$

Then the radius of plate is calculated

$$r_{plate} = 1219.2 / \sqrt{\pi} = 688 \text{ mm}$$

The horizontal pendulum dimensions are in the Table C.1. The plate parameters are summarised in the Table C.2.

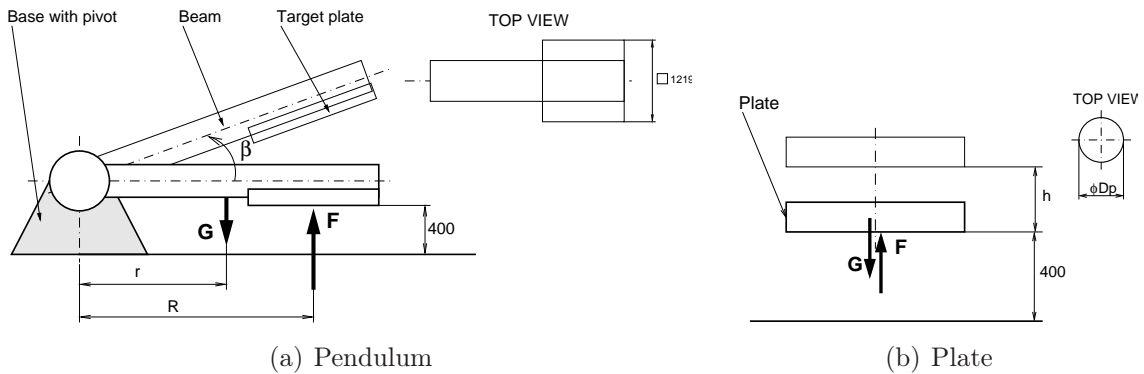


Figure C.1: Schematic pendulum and plate. (Not to scale.)

Table C.1: *Dimension of the mine horizontal pendulum.*

m	mass of the pendulum arm	1480 kg
r	distance from pivot to the centre of gravity of the arm	2.44 m
R	distance from pivot to the application point of the force	4.27 m
J_0	moment of inertia of the pendulum arm about the pivot point	14700 kg.m ²
g	gravitational constant	9.81 m.s ⁻²
β	angle reached by the pendulum arm	

Table C.2: *Dimension of the plate as surrogate MIP.*

m_{plate}	mass of the plate	806 kg
r_{plate}	radius of the plate	688 mm

Prairie soil laboratory data

D.1 Physical properties

Particle size distribution

Sieve analysis showed 100 % of particles passing at 10 mm sieve size and 45 % passing at 0.08 mm. This means that the sample was roughly 45 % fine soil, i.e., silt and clay. Particle size distribution is presented in Table D.1 and graphically represented in Figure D.1. Prairie soil is described as a sandy, silty, low plastic, brown clay containing roots.

Soil composition

For each soil trial, bulk density and moisture content were determined. From the bulk density and moisture content, relative volume of each phase can be calculated, i.e. $\alpha_{s0} + \alpha_{w0} + \alpha_{a0} = 1$, where s, w, a denote the solid, water and air phase, respectively. Figure D.2 shows the relative volume for each MIP trial. Solid particle

Table D.1: *Particle size distribution for prairie soil.*

Sieve size	Percent passing
10.000	100
5.000	98
2.500	97
1.250	95
0.630	92
0.315	82
0.160	63
0.080	45

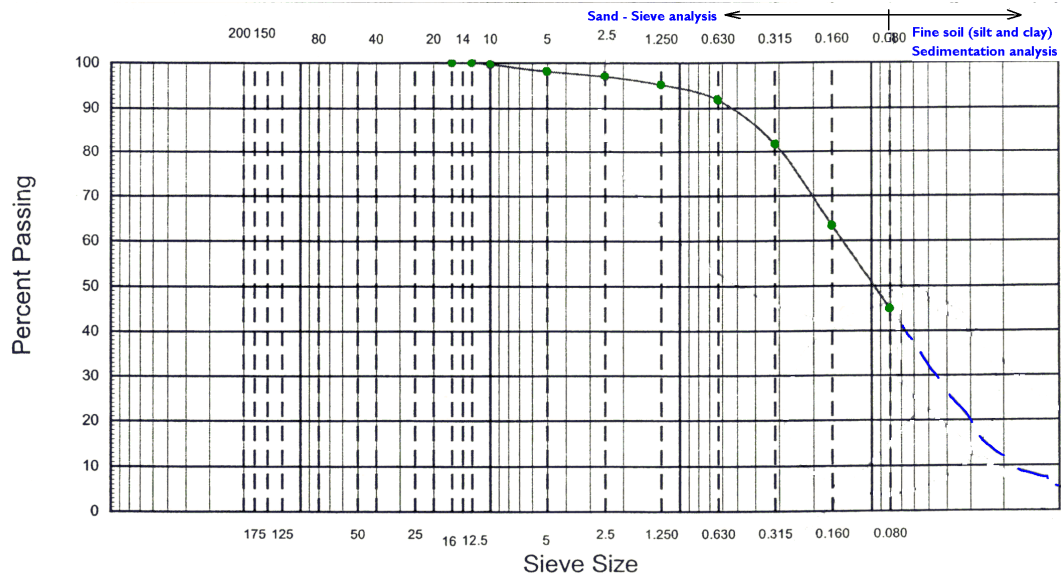


Figure D.1: Grading curve for prairie soil.

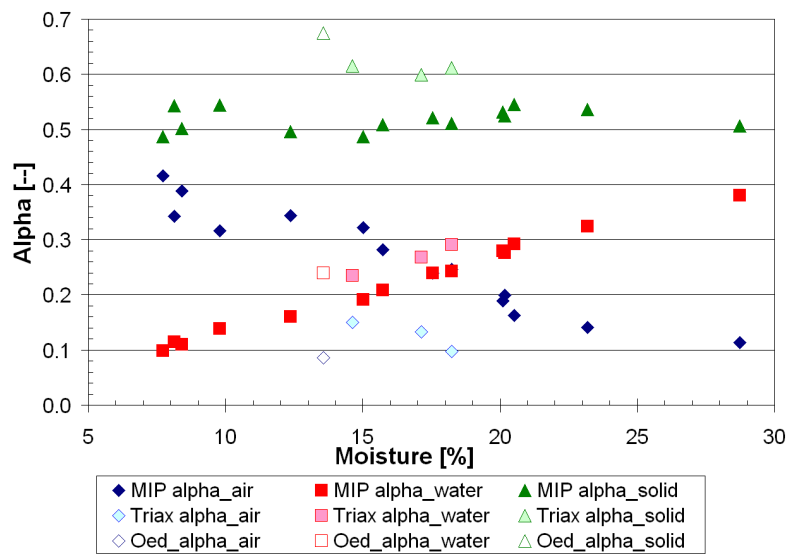


Figure D.2: The composition of prairie soil at the initial stage - MIP trials, triaxial test and oedometer test specimens.

density was 2680 kg.m^{-3} .

D.2 Mechanical properties

Triaxial undrained tests were carried out on three specimens of 14.6, 18.3 and 17.1 % moisture content, respectively. The triaxial test determined the cohesion and friction angle. This is described in detail below.

In *one dimensional consolidation test* (Oedometer), one sample having 13.6 % moisture content was tested. This test determines the oedometric modulus and compression parameters with respect to time (several hours/days). These test data were not used in soil model derivation as water was allowed to drain. This condition does not correspond with the soil behaviour under the explosion process.

Direct shear test determined the effective cohesion and effective friction angle. These test data were not used in soil model derivation as the total cohesion and total friction angle shall be used to represent soil behaviour under undrained condition, that occurs during explosion process.

Evaluation of triaxial tests

From the triaxial test, the friction angle and cohesion can be obtained by plotting the Mohr's circle. Then the cohesion and friction angle are parameters of the line tangent to the Mohr's circles. The determination is as follows:

1. The values of stress when the specimen failed are extracted (see Table D.3).
2. The Mohr's circle are drawn in the *normal stress-* and *shear stress-* coordinate system. The centre of the circle has coordinates $(\sigma_3 + \frac{1}{2}(\sigma_1 - \sigma_3), 0)$ and radius is given by $\frac{1}{2}(\sigma_1 - \sigma_3)$.
3. A line is fitted through the apex points using the least squares method:
 $y = bx + a$
4. As the Mohr-Coulomb criterion is defined as a tangent to the Mohr's circle (and not a secant line), the following correction method is established to obtain the friction angle and cohesion as tangent.

$$\sin \phi = b \quad (D.1)$$

$$c = \frac{a}{\cos \phi} \quad (D.2)$$

The determination of the friction angle and cohesion for prairie soil is graphically represented in Figure D.3. The procedure explained above is applied:

Triaxial test data were extracted from the AMEC laboratory report [6] and are presented in Table D.3. Mohr's circle for total stress were drawn as in Figure D.3.

Table D.2: *Prairie soil properties at the initial and final stage of triaxial tests.*

Parameter	Unit	Specimen no. I		Specimen no. II		Specimen no. III	
		Initial	Post-shear	Initial	Post-shear	Initial	Post-shear
Density	kg.m ⁻³	1841	2062.7	1887	2062.7	1832	2097.4
Dry density	kg.m ⁻³	1606	1695.2	1596	1695.2	1564	1750.6
Moisture content	%	14.6	21.7	18.3	21.7	17.1	19.8

Table D.3: *Stresses at triaxial tests for prairie soil.*

Specimen No.	Total stress [kPa]		
	σ_1	σ_3	$\sigma_1 - \sigma_3$
I.	1439.306	1038.029	401.276
II.	2418.454	1554.043	864.411
III.	3033.357	1998.562	1034.795

Line was fitted through the apex points (dashed blue line) in the form:

$$y = 0.2521x - 98.942, R^2 = 0.9738$$

Corrected parameters are determined using Equations D.1 and D.2 are given as follows :

$$\begin{aligned} \text{friction angle: } \sin \phi &= 0.2521, \phi = 14.6^\circ \\ \text{cohesion: } c &= \frac{-98.942}{\cos 14.6} = -102 \text{ kPa} \end{aligned}$$

As can be observed, the obtained cohesion is negative and this is not feasible for cohesion parameter. The first circle was obtained for specimen of lower moisture content (14.6%) compared with the remaining specimen (18.3 and 17.1%). The first circle is visible smaller than the other circles. It was assumed that this caused the unfeasible results and the first circle was neglected in the repeated calculation of friction angle and cohesion. A line was fitted through the apex points (dashed-dot green line) in the form:

$$y = 0.1608x + 112.76, R^2 = 1$$

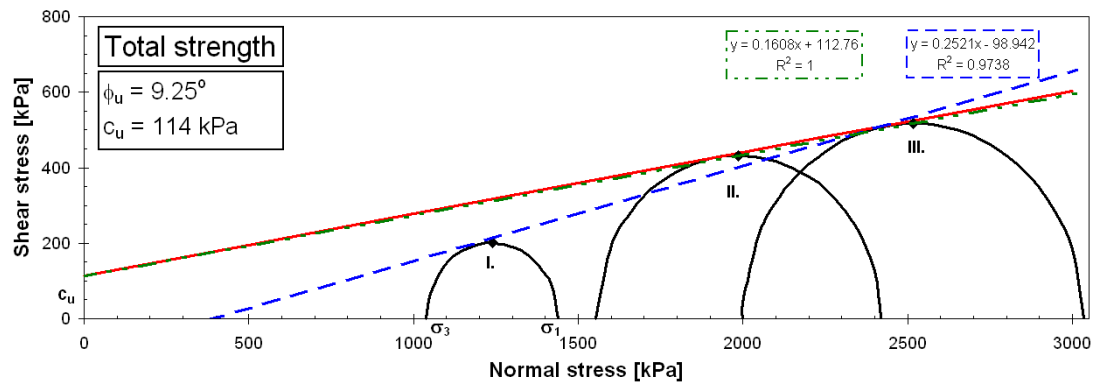


Figure D.3: Calculation of the friction angle and cohesion for prairie soil.

Corrected parameters were determined and are plotted in red solid line:

$$\text{friction angle: } \sin \phi = 0.1608, \phi = 9.25^\circ$$

$$\text{cohesion: } c = \frac{112.76}{\cos 9.25} = 114 \text{ kPa}$$

Prairie soil modelling

Chapter 5 presents the methodology for the derivation of a cohesive soil model. These AUTODYN material models were used throughout the simulations:

- ❖ Equation of state: **Compaction**
- ❖ Strength model: **Granular**
- ❖ Failure model: **Hydro-tensile limit**

The relations used in the model derivations are summarised in Table E.1. A sample model calculation, for prairie soil having 7.7% moisture content is presented in Table E.2. The calculations are described forthwith. The equations refer to those in Table E.1 and references to columns are for Table E.2.

Given

During the MIP trial the following soil properties were measured:

Moisture content: 7.7%

Bulk density: 1368 kg.m⁻³

- Calculate relative volumes of soil phases using equations 1, 2 and 3:
 $\alpha_{a0} = 0.41541$, $\alpha_{w0} = 0.098$ and $\alpha_{s0} = 0.48659$.

Calculation for EOS: $p = f(\rho)$

- *Pressure vs. density:* columns B and C are inserted into AUTODYN
 - Calculate α_{sp} , α_{wp} and α_{ap} (columns D, E and F) for pressure values in column B using equations 5, 6 and 7.
 - Calculate bulk density ρ (column C) using equation 4.

Calculation for strength model

- *Pressure vs. yield stress*: columns B and L are inserted into AUTODYN
 - Calculate yield stress Y (column L) using equation 14: cohesion and friction angle were determined from the relationships presented in Figure 5.4, in this case $c = 21.59$ kPa and $\phi = 4.27^\circ$.
- *Shear modulus vs. density*: columns H and C are inserted into AUTODYN
 - Calculate bulk modulus K using equation 8 (column G)
 - Calculate Poisson's ratio ν using equation 10, in this case: $\nu = 0.35 \cdot 0.48659 + 0.4999 \cdot 0.098 + 0.0001 \cdot 0.41541 = 0.2193$.
 - Calculate shear modulus G using equation 9 (column H)

Calculation for EOS: $\rho = f(v)$

- *Density vs. soundspeed*: columns C and K are inserted into AUTODYN
 - Calculate velocity components v_L and v_S using equations 11 and 12 (columns I and J)
 - Calculate soundspeed velocity v using equation 13 (column K)

Failure model

- *Hydro-tensile limit*: $p_{MIN} = -c$, in this case $p_{MIN} = -21.59$ kPa

Table E.1: Summary of equations for deriving cohesive soil model.

Eqn.	Parameter	Equation	Notes	Refer in text
1	α_{a0}	$\alpha_{a0} = A_v = n(1 - S_r)$	$e = \rho_s/\rho_d - 1$, $n = e/(1+e)$, $S_r = w\rho_s/e$	Tab. 3.1
2	α_{w0}	$\alpha_{w0} = n - A_v$		Tab. 3.1
3	α_{s0}	$\alpha_{s0} = 1 - \alpha_{w0} - \alpha_{a0}$		Eq. 3.1
4	Density	$\rho = \frac{\rho_0}{\alpha_{sp} + \alpha_{wp} + \alpha_{ap}}$		Eq. 5.13
5	Solid	$\frac{\alpha_{sp}}{\alpha_{s0}} = 1.514347 (p - p_0)^{-0.050123}$	$p_0 = 101.3 \text{ kPa}$	Eq. 5.16
6	Water	$\alpha_{wp} = \alpha_{w0} \left[\frac{p - p_0}{\rho_{w0} c_{w0}^2} k_w + 1 \right]^{-1/k_w}$	$k_w = 3$, $\rho_{w0} = 1000 \text{ kg.m}^{-3}$, $c_{w0} = 1415 \text{ m.s}^{-1}$	Eq. 5.11
7	Air	$\alpha_{ap} = \alpha_{a0} \left(\frac{p}{p_0} \right)^{-1/k_a}$	$k_a = 1.4$	Eq. 5.10
8	Bulk modulus	$K = \frac{p_2 - p_1}{\varepsilon_2 - \varepsilon_1}$		Eq. 5.20
9	Shear modulus	$G = K \frac{3}{2} \frac{1 - 2\nu}{1 + \nu}$		Eq. 5.21
10	Poisson's ratio	$\nu = 0.35\alpha_{s0} + 0.4999\alpha_{w0} + 0.0001\alpha_{a0}$		Eq. 5.24
11	Longitudinal velocity	$v_L = \sqrt{\frac{3 K (1 - \nu)}{\rho (1 + \nu)}}$		Eq. 5.18
12	Shear velocity	$v_S = \sqrt{\frac{G}{\rho}}$		Eq. 5.19
13	Velocity	$v = \sqrt{v_L^2 - \frac{4}{3}v_S^2}$		Eq. 5.17
14	Yield	$Y = c + \sigma \tan \phi$		Eq. 3.11

Table E.2: Derivation of model for prairie soil with 7.7% moisture content.

A	B	C	D	E	F	G	H	I	J	K	L
	Pressure	Bulk density	Solid	Water	Air	Bulk modulus	Shear modulus	Longitudinal velocity	Shear velocity	Velocity	Yield stress
	p	ρ	α_{sp}	α_{wp}	α_{ap}	K	G	v_L	v_S	v	Y
	[kPa]	[kg.m ⁻²]	[-]	[-]	[-]	[kPa]	[kPa]	[m.s ⁻¹]	[m.s ⁻¹]	[m.s ⁻¹]	[kPa]
1	101	1,368.0		0.09800	0.41541	5,457	3,764	87.5	52.5	63.2	29
2	2,000	2,097.9	0.50473	0.09800	0.04934	41,521	28,635	194.9	116.8	140.7	171
3	5,000	2,261.3	0.48132	0.09800	0.02564	113,341	78,167	310.2	185.9	223.9	395
4	10,000	2,365.7	0.46464	0.09800	0.01563	261,854	180,590	460.9	276.3	332.7	768
5	20,000	2,459.6	0.44866	0.09800	0.00953	485,361	334,735	615.5	368.9	444.2	1,515
6	30,000	2,511.4	0.43960	0.09800	0.00713	713,308	491,941	738.4	442.6	532.9	2,262
7	40,000	2,547.1	0.43329	0.09800	0.00581	944,593	651,450	843.7	505.7	609.0	3,008
8	50,000	2,574.3	0.42846	0.09800	0.00495	1,178,336	812,654	7937.4	561.9	676.6	3,755
9	60,000	2,596.3	0.42455	0.09800	0.00435	1,413,962	975,156	1022.4	612.9	738.0	4,501
10	70,000	2,614.8	0.42128	0.09800	0.00389	1,651,085	1,138,690	1100.9	659.9	794.6	5,248

Hoping for the best is not a viable way forward.

Timothy A. Rose

It takes a wise man to come up with proverbs. . .
All fools can do, is to simply quote them!

P M Jeyaraman